Jan Schulze

Adjoint based jet-noise minimization

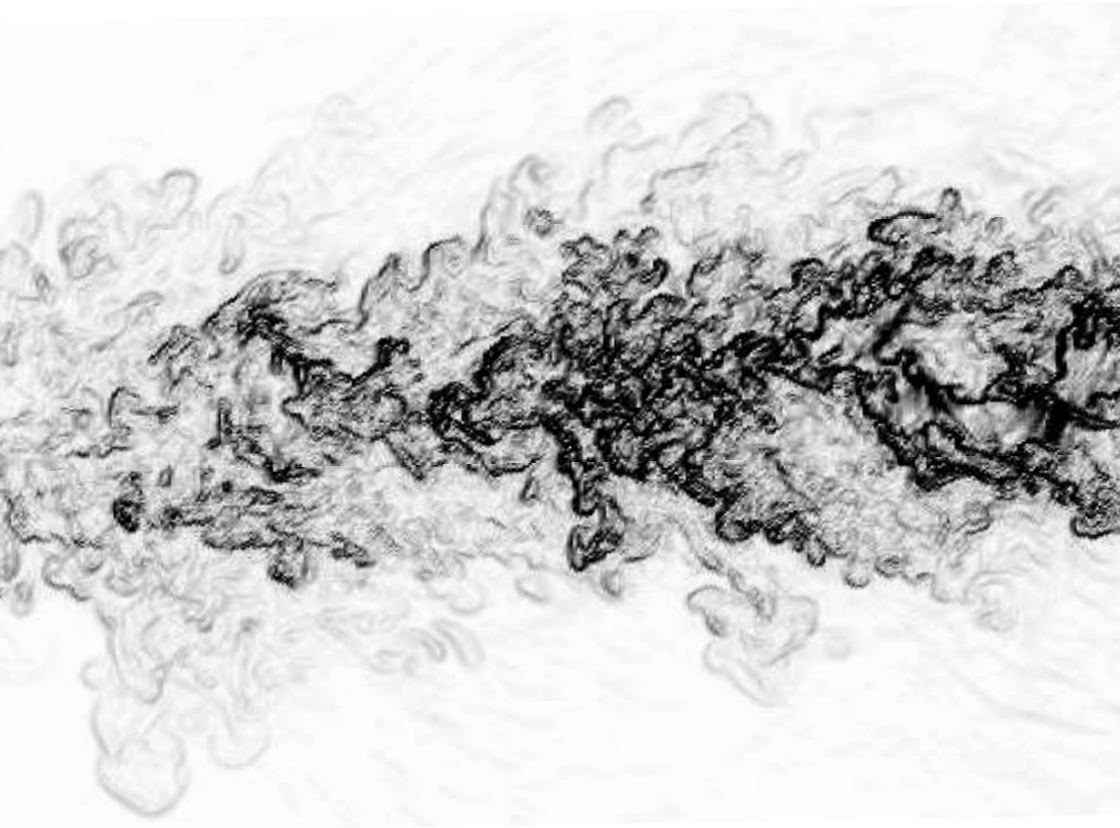

cfd | caa

Technische Universität Berlin

Jan Schulze

Adjoint based jet-noise minimization

Bibliografische Information der Deutschen Nationalbibliothek.
Die Deutsche Nationalbibliothek verzeichnet diese Publikation in der Deutschen Nationalbibliografie; detaillierte bibliografische Daten sind im Internet über http://dnb.dnb.de/ abrufbar.

Universitätsverlag der TU Berlin 2013
http://www.univerlag.tu-berlin.de

Fasanenstr. 88 (im VOLKSWAGEN-Haus), 10623 Berlin
Tel.: +49 (0)30 314 76131 / Fax: -76133
E-Mail: publikationen@ub.tu-berlin.de

Zugl.: Berlin, Technische Universität, Diss., 2012
1. Gutachter: Prof. Dr. Jörn Sesterhenn
2. Gutachter: Prof. Dr. Christophe Bogey
Die Arbeit wurde am 22. Oktober 2012 unter Vorsitz von Prof. Dr. Michael Möser erfolgreich verteidigt.

Druck: docupoint GmbH Magdeburg

Cover design: Rosi Wahl
Satz: Dieses Dokument ist gesetzt mit KOMA-Script und LaTeX

ISBN 978-3-7983-2494-7 (Druckversion)
ISBN 978-3-7983-2495-4 (Onlineversion)

Zugleich online veröffentlicht auf dem Digitalen Repositorium der Technischen Universität Berlin:
URL http://opus.kobv.de/tuberlin/volltexte/2013/3871/
URN urn:nbn:de:kobv:83-opus-38719
http://nbn-resolving.de/urn:nbn:de:kobv:83-opus-38719

Zusammenfassung

Freistrahlen (engl. Jets) mit einer komplexen Stoßzellen-Struktur treten in vielen technischen Anwendung auf. Die meisten Überschallfreistrahlen in der Luftfahrt sind nicht perfekt angepasst, auch nicht solche aus sorgfältig gestalteten konvergent-divergenten Düsen. Die Anpassung an den Umgebungsdruck erfolgt in einer Abfolge von schiefen Verdichtungsstößen, die mit den freien Scherschichten interagieren und Lärm erzeugen. Dabei strahlt die Interaktion von Stoß und Scherschicht einen breitbandigen Lärm ab. Dies kann die dünne Scherschicht am Düsenaustritt anregen und eine Rückkopplungsschleife bilden, die einen diskreten Ton namens *Screech (dt. Kreischen)* hervorruft. Beide Komponenten sind aus strukturellen und umgebungsbedingten Gesichtspunkten unerwünscht (z. B. Kabinenlärm). Screech-Töne erzeugen Schalldruckpegel von 160 dB und darüber hinaus.

Der Fokus der vorliegenden Arbeit liegt in der Minimierung von Überschall Jet-Lärm, insbesondere in der Minimierung von Jet-Screech. Da Screech – ein Phänomen, das noch nicht in allen Einzelheiten verstanden ist – durch die Geometrie der Jet-Düse beeinflusst wird, soll ein poröses Material an der Düse angebracht werden, um den Rückkopplungsmechanismus zu unterdrücken. Dadurch wird ebenfalls der Screech-Ton unterdrückt. Es ist keineswegs klar, wie die charakteristischen Eigenschaften des porösen Materials beschaffen sein sollten, um den Lärm zu minimieren. Zu diesem Zweck wird ein Optimierungsverfahren, basierend auf adjungierten Methoden, angewandt, um die Materialeigenschaften in Bezug auf den Lärm zu optimieren.

Abstract

Jets with complex shock-cell structures appear in numerous technological applications. Most supersonic jets used in aeronautics will be imperfectly adapted in flight, even those from carefully designed convergent–divergent nozzles. The adaption to the ambient pressure takes place in a sequence of oblique shocks which interact with the free shear layers and produce noise. The shock/shear-layer interaction emanates a broadband noise component. This may trigger the thin shear layer at the nozzle exit, forming a feedback loop which results in a discrete noise component called *screech*. Both components are undesirable from structural and environmental (cabin noise) points of view. Screech tones produce sound pressure levels of 160 dB and beyond.

The focus of the present thesis lies in the minimization of supersonic jet-noise and in particular in the minimization of jet-screech. Since screech – a phenomenon which is not yet understood in all details – seems to be affected by the presence of the jet-nozzle, a porous material will be added to the nozzle exit to suppress the feedback mechanism. Thus, to minimize the emanated noise. It is by no means clear how the shape an characteristic properties of the porous material should be. To this end, an optimization technique, based on adjoint methods, will be applied to optimize the material with respect to the emanated noise.

Preface

The present work addresses the problem of adjoint based minimization of supersonic jet noise. It started in 2006 with the DFG Sub-Project SP2 (Shock-Induced Noise in Supersonic Jets) at the Technical University in Munich, initiated by Jörn Sesterhenn with the French partners Daniel Juvé, Christophe Bailly and Peter Schmid, and was finished six years later at the Technical University in Berlin. Adjoint based optimization is a fairly recent and very active research field not only in the academic environment but also in the industry. Different approaches dealing with the numerical and mathematical difficulties were developed within the last years helping to popularize this method. Still, many questions are unsolved. This work will provide an insight in the method of adjoint based optimization of a supersonic jet. A new and promising approach to optimize a porous medium to suppress jet noise is applied and validated. The purpose of this research project is to discuss the feasibility of such an approach and to help to improve the understanding of adjoint based methods and the physics of supersonic jet noise generation.

The development of this thesis would not have been possible without the guidance of my two supervisors Jörn Sesterhenn in Munich and Berlin and Peter Schmid in Paris. Their support in any issues concerning the numerical, mathematical or physical part of this work was essential for its outcome.

As part of the Cotutelle I had the opportunity to visit the research group at the École Polytechnique (LadHyX) in Paris. I was fortunate to meet my colleagues Shervin Bagheri, François Gallaire and Fulvio Martinelli. Furthermore I wish to thank my colleagues in Munich, Alex Barbagallo, Christoph Mack and Olivier Marquet for the many suggestions and discussions. And finally my colleagues in Berlin, Jens Brouwer, Flavia Cavalcanti Miranda, Mathias Lemke and Julius Reiss for creating the nice and inspiring working environment.

Financial support by the Deutsche Forschungsgemeinschaft (DFG) and the Deutsch–Französische Hochschule (DFH) and computational time at the

Leibnitz Rechenzentrum (LRZ) and the Norddeutscher Verbund für Hoch- und Höchstleistungsrechnen (HLRN) is particularly acknowledged. I also like to thank the DEISA Consortium (co-funded by the EU, FP6 project 508830), for support within the DEISA Extreme Computing Initiative.

Last but not least I want to thank my family, my sister Rosi who always gave me a homelike atmosphere and a place to live both in Paris and Berlin, my parents Sieglinde and Armin for their support and finally Anna for her care and patience.

Munich, Jan Schulze
March, 2013

Contents

List of Tables

List of Figures

List of Algorithms

I

Computing supersonic jet noise

1

Introduction

Supersonic jets can be found in a variety of technical applications like in civil- or military aircraft. The most famous supersonic civil aircraft, the *Concorde*, reached Mach numbers of up to 2.23, using a turbojet engine. It is worthwhile to point out that high speed aircraft are extremely loud. The noise pollution of urban areas close to an airport is a common problem and responsible for night flying restrictions and other noise mitigation programs. During take-off and climb, the loudest noise sources are not the mechanical parts of the jet-engine but the aeroacoustic noise sources of the exhaust jet. This is especially true for supersonic jets. During landing, airframe noise, generated by e. g. landing gears and flaps can be the dominant noise sources.

In 1952 Lighthill came up with his famous M^8 law for jet noise. This law for the mean acoustic power is a function of the jet Mach number M_j and the jet diameter D and reads:

$$\langle \rho'^2 \rangle \sim \rho_0^2 M_j^8 \frac{D^2}{R^2} \tag{1.1}$$

with the density of the ambient fluid ρ_0 and the distance R from the jet to the observer. It states that the acoustic power radiated by the jet is proportional to the eighth power of the jet Mach number. The dependence of the jet diameter D to the acoustic power is quadratic. This law is only valid for small Mach numbers $M_j \ll 1$. Supersonic jets scale with M_j^3 [see e.g. Goldstein, 1976]. The corresponding law reads:

$$\langle \rho'^2 \rangle \sim \rho_0^2 M_j^3 \frac{D^2}{R^2} \tag{1.2}$$

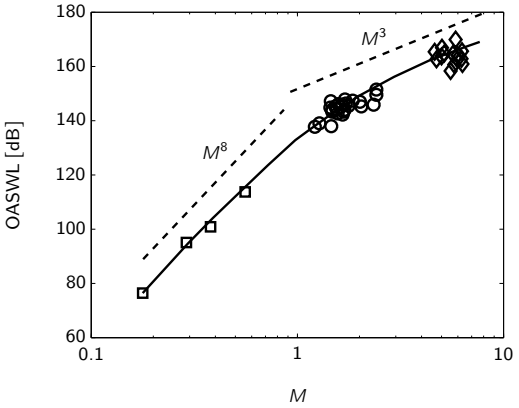

Figure 1.1: Overall sound power level as a function of the Mach number [adapted from Ffowcs Williams, 1963]. (———) theory; (- - - - - -) M^8- and M^3-law, respectively; □ subsonic flows ($M < 0.8$); ○ supersonic turbo jet engines; ◇ supersonic rockets.

Both laws, for the sub- and supersonic jet, could be observed in several experiments. An example presenting the overall sound power level (OASWL) for different jets, ranging from sub- to supersonic, can be found in Fig. 1.1 with measurements adapted from Ffowcs Williams [1963]. The OASWL and the acoustic power are linked with the logarithmic law $L = 10\log_{10}(P/P_0)$, with the acoustic power P as in Eq. (1.1) or (1.2) and a reference power P_0 (here: $P_0 = 10^{-13}\,\mathrm{W}$).

The reduction of supersonic jet noise is a matter of particular concern. Most supersonic jets used in aeronautics will be imperfectly expanded in flight, even those from carefully designed convergent-divergent nozzles. As a result, shocks form in the jet core to adapt the flow to the ambient pressure and produce additional noise sources. This thesis is concerned with the prediction and reduction of supersonic jet noise. In the following introduction, the physical phenomenon of supersonic jets and their noise sources will be presented.

1.1 Physics of a supersonic jet

Most supersonic jets are imperfectly expanded. What this means is that the pressure at the nozzle exit is either below or above the ambient pressure.

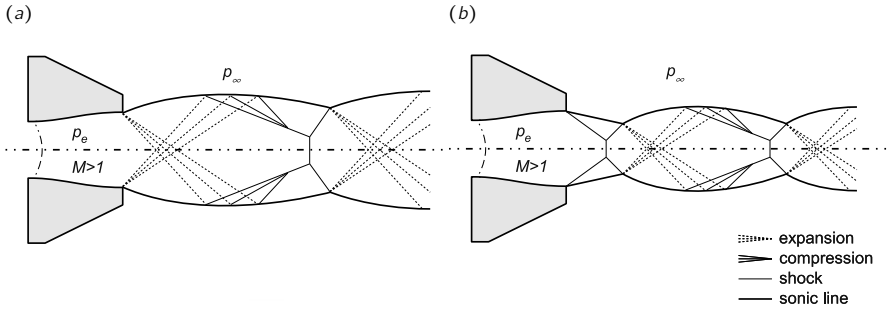

Figure 1.2: Sketch of a supersonic jet for different pressure ratios. (a) over-expanded $p_e < p_\infty$; (b) under-expanded $p_e > p_\infty$.

The former jets are called over-expanded whereas the latter ones are under-expanded. Only when the pressure at the nozzle exit is equal to the ambient pressure the jet would be perfectly adapted, or running under design conditions. This phenomenon can only be found in supersonic jets. The pressure at the nozzle exit of a subsonic jet is always equal to the ambient pressure.

In an imperfectly expanded jet, oblique shocks adapt the flow to the ambient pressure forming a regular shock cell pattern. Prandtl [1904] was the first to observe this phenomenon. At the nozzle exit of an under-expanded jet, an expansion fan is initiated to decrease the pressure discrepancy inside and outside the nozzle. Once the expansion fan is passing the jet core, it is reaching the opposite side of the jet, the mixing layer. As the outside of the jet is subsonic, neither an expansion fan nor a shock may exist. To this end, the expansion fan is reflected at the sonic line as a compression fan back into the jet core. This phenomenon is repeated several times downstream the jet forming a regular pattern of shock cells (cf. Fig. 1.2(a)). For high Mach number jets, a normal shock (Mach disk) may appear at the end of the first shock cell and create a region of mixed sub- and supersonic flow. Mach disks appear at fully expanded Mach numbers above $M_j \gtrapprox 2$. Within the present numerical study, Mach numbers in the range of $1 \leq M_j \leq 2$ will be investigated and the influence of the Mach disk will not be considered.

During the operation of a supersonic turbofan, shock cells can be clearly visible without complex visualization techniques. They appear as bright areas in the jet core. The reason for this is the high temperature inside a shock cell, especially when passing a normal shock (Mach disk). It ignites any excess fuel

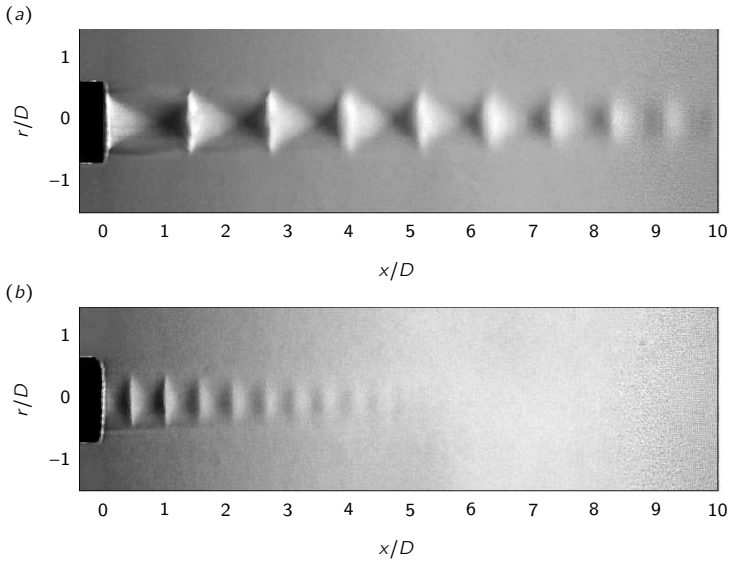

Figure 1.3: Schlieren visualization of an under-expanded jet with a convergent nozzle ($M_d = 1$) for two different nozzle pressure ratios [Schulze, 2011]. (a) $M_j = 1.45$. (b) $M_j = 1.11$.

present in the exhaust plume. Due to the bright shining combustion inside the shock cells, they are also referred to as *shock diamonds.*

In the over-expanded case (cf. Fig. 1.2(b)) the pressure at the nozzle exit is below the ambient pressure initiating a oblique shock at the nozzle lip. Together with the oblique shock from the opposite side if the nozzle they may end up in a vertical shock (Mach disk, again depending on the pressure ratio and Mach number and will not be considered here) increasing the overall pressure. From that point on, the shock cell structure is similar to the one of the under-expanded jet (cf. Fig. 1.2(a)).

In Fig. 1.3 a Schlieren visualization of an under-expanded jet for two different nozzle pressure ratios is presented for a convergent nozzle [Schulze, 2011]. Panel (a) corresponds to a fully expanded jet Mach number of $M_j = 1.45$ and panel (b) to $M_j = 1.11$. This Schlieren technique visualizes density gradients in the stream-wise direction and highlights the shock cell structure (knife-edge orientation is perpendicular to the jet axis as in a variety of experimental studies, like Yu & Seiner [1983]). One can see from this experimental investigation that the shock cell spacing is increasing with the jet Mach number.

over-expanded	ideally expanded	under-expanded
$M_j < M_d$	$M_j = M_d$	$M_j > M_d$
$D_j < D$	$D_j = D$	$D_j > D$
$p_e > p_\infty$	$p_e = p_\infty$	$p_e < p_\infty$

Table 1.1: Features of a supersonic jet with different stages of expansion. Over-expanded, ideally expanded and under-expanded..

Tam et al. [1985] found a generalized relation based on the theory of Prandtl [1904] and later Pack [1950] to obtain the pressure distribution in the shock cells. Based on that theory an approximation for the shock cell length can be obtained:

$$L_s \approx \pi \left(M_j^2 - 1\right)^{\frac{1}{2}} \frac{D_j}{\sigma_1} \tag{1.3}$$

with the fully expanded jet Mach number M_j, the fully expanded jet diameter D_j and the first root of the zero order Bessel function $\sigma_1 \approx 2.404826$. The fully expanded values depend on the order of expansion. For an ideally expanded jet the fully expanded jet Mach number M_j is equal to the jet exit Mach number. The latter one is also referred to as the jet design Mach number M_d and only dependent on the cross section ratios inside the Laval nozzle. The same holds true for the jet diameter $D_j = D$ with the nozzle exit diameter D. In the under- or over-expanded jet, the values differ. Both the fully expanded jet Mach number and diameter for an under-expanded jet are larger than the design Mach number and jet diameter, respectively. For an over-expanded jet it is the other way round. In Tab. 1.1 these features are summarized. Assuming an isotropic expansion inside the nozzle, an expression for the fully expanded values can be obtained. The fully expanded jet Mach number can be expressed based on the ratio of the reservoir pressure p_r and the ambient pressure p_∞:

$$M_j = \left(\frac{2}{\gamma - 1}\left(\left(\frac{p_r}{p_\infty}\right)^{\frac{\gamma-1}{\gamma}} - 1\right)\right)^{\frac{1}{2}}, \tag{1.4}$$

with the ratio of specific heats γ (here: $\gamma = 1.4$). The reservoir pressure p_r and the pressure at the nozzle exit p_e are related as follows:

$$\frac{p_r}{p_e} = \left(1 + \frac{\gamma - 1}{2} M_d^2\right)^{\frac{\gamma}{\gamma-1}} \tag{1.5}$$

Combining Eq. (1.4) and (1.5) we obtain an expression for the fully expanded jet Mach number M_j as a function of the pressure ratio at the nozzle exit:

$$M_j = \left(\frac{2}{\gamma - 1} \left(\left(\frac{p_e}{p_\infty} \right)^{\frac{\gamma-1}{\gamma}} \left(1 + \frac{\gamma - 1}{2} M_d^2 \right) - 1 \right) \right)^{\frac{1}{2}} \tag{1.6}$$

The fully expanded jet diameter D_j is related to the jet diameter D and was found by Tam & Tanna [1982] based on the condition of conservation of mass flux:

$$D_j = D \left(\frac{1 + \frac{1}{2}(\gamma - 1) M_j^2}{1 + \frac{1}{2}(\gamma - 1) M_d^2} \right)^{\frac{\gamma+1}{4(\gamma-1)}} \left(\frac{M_d}{M_j} \right)^{\frac{1}{2}} . \tag{1.7}$$

As we can see from Eq. (1.6), the fully expanded jet Mach number depends on the pressure ratio at the nozzle exit and the design Mach number. The latter one only depends on the geometry inside the nozzle and is independent on the pressure. One can distinguish between two types of nozzles: convergent and convergent-divergent nozzles. In the convergent case, the diameter of the nozzle is being reduced from the reservoir with the smallest diameter at the nozzle exit. As in a Laval nozzle the Mach number at the smallest diameter is equal to one, the design Mach number of a convergent nozzle is always sonic ($M_d = 1$). If we neglect shocks in the Laval nozzle, the gas is accelerated in the divergent part of a convergent-divergent nozzle. Hence, the design Mach number of a convergent-divergent nozzle is always supersonic ($M_d > 1$).

The cross section area A and the Mach number M in a Laval nozzle are related as follows:

$$\frac{A}{A_0} = \frac{M_0}{M} \left(\frac{1 + \frac{\gamma-1}{2} M^2}{1 + \frac{\gamma-1}{2} M_0^2} \right)^{\frac{1}{2} \frac{\gamma+1}{\gamma-1}} \tag{1.8}$$

based on an arbitrarily condition M_0 with the cross section A_0. An exemplary geometry of a round convergent-divergent Laval nozzle is presented in Fig. 1.4 with an inlet Mach number of $M = 0.25$ and a design outlet Mach number of $M_d = 1.5$. The shape is based on a cubic spline one for each the convergent and the divergent part of the nozzle and chosen such that the diameter at the outlet is equal to one.

For the same parameters as in Fig. 1.4 a planar nozzle is presented in Fig. 1.5. One can see that the hight of the nozzle inlet is larger as for the round nozzle, yet with the same coss-section area. Based on this geometry, the flow inside the round nozzle of Fig. 1.4 can be computed with a

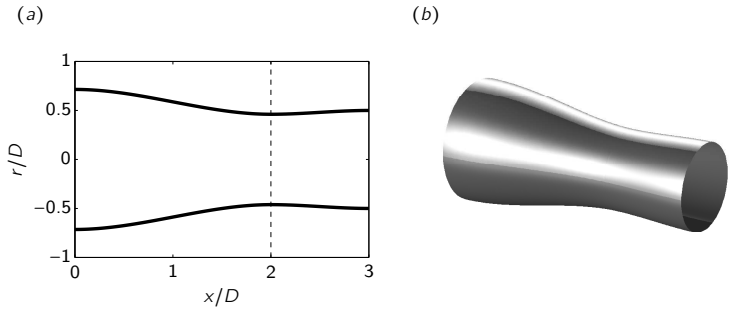

Figure 1.4: (a) Geometry of a round convergent-divergent Laval nozzle for an inlet Mach number of $M = 0.25$ and a design outlet Mach number of $M = 1.5$. Smallest diameter at $x/D = 2$ with the diameter D measured at the outlet. Convergent and subsonic part for $0 < x/D < 2$; Divergent and supersonic part for $2 < x/D < 3$. (b) Three-dimensional view.

one-dimensional isentropic theory. Assuming a reservoir pressure and temperature of $p_r = 734\,\mathrm{kPa}$ and $T_r = 300\,\mathrm{K}$, respectively, the state in the nozzle is defined. In Fig. 1.6 the flow inside the nozzle is presented. Based on the reservoir conditions, the fully expanded Mach number is $M_j = 1.96$ with a pressure ratio of $p_e/p_\infty = 2.0$. Hence, the nozzle runs in under-expanded condition. The smallest diameter in the figure is marked with a dashed line. At this point the accelerated flow reaches $M = 1$ which can be seen in panel (f). The Mach number is increasing monotonously from sub- to supersonic conditions and reaches the design Mach number of $M_d = 1.5$ at the nozzle exit.

The reservoir temperature is chosen to be equal to the ambient temperature ($T_r = T_\infty = 300\,\mathrm{K} = 26.85\,^\circ\mathrm{C}$). Inside the nozzle the temperature is decreasing due to the acceleration of the fluid to an exit temperature of $T_e \approx 209.5\,\mathrm{K}$ ($= -63.65\,^\circ\mathrm{C}$) which is below the ambient temperature (cf. panel (a)). If the temperature of the surrounding fluid is equal to the reservoir temperature the jet is referred to as a cold jet. Hot jets, on the other hand, exhibit a higher reservoir temperature of the jet than the ambient fluid. As we will see later, one of the dominant noise sources of a supersonic jet – the *screech* phenomenon – is decreasing with increasing temperature [see amongst others, Krothapalli et al., 1997, Rosfjord & Toms, 1975, Shen & Tam, 2000, Tam et al., 1994]. To this end, we restrict to cold jets in the present investigation.

As well as the temperature, the density is monotonously decreasing to satisfy the assumption of an ideally gas (cf. panel (b)). The local speed of

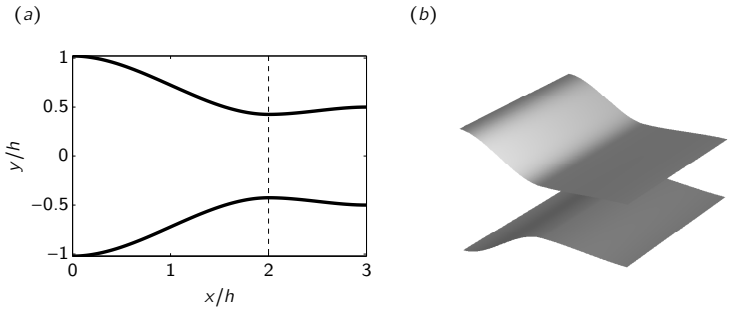

Figure 1.5: (*a*) Geometry of a planar convergent-divergent Laval nozzle for an inlet Mach number of $M = 0.25$ and a design outlet Mach number of $M = 1.5$. Smallest height at $x/h = 2$ with the height h measured at the outlet. Convergent and subsonic part for $0 < x/h < 2$; Divergent and supersonic part for $2 < x/h < 3$. (*b*) Three-dimensional view.

sound is a function of the temperature ($c = \sqrt{\gamma RT}$, with the specific gas constant R) and hence decreasing (cf. panel (e)). In panel (d) the streamwise velocity is presented and, based on the Mach number and local speed of sound, increasing monotonously inside the nozzle. For an ideally expanded nozzle or a nozzle at design point, the gas is leaving the nozzle with the design Mach number and keeps this level in the jet core until it interacts with the ambient fluid and adapts its velocity. In the imperfectly expanded jet the picture looks different. Depending on the value of expansion, the gas is either accelerating or decelerating. An under-expanded jet is accelerating the gas and an over-expanded jet is decelerating the gas when leaving the nozzle.

The area where the flow is not affected by the ambient fluid is referred to as the potential core. Its length is one of the most significant differences of sub- and supersonic jets [see Nagamatsu et al., 1969]. In subsonic jets the length of the potential core is independent on the jet Mach number and about as long as four times the jet diameter as assumed by Lighthill [1963] (valid in the Mach number range of $0 < M_j < 0.7$). However, the potential core of a supersonic jet is depending on the jet Mach number and probably on the value of expansion. For a fully expanded supersonic jet one can identify that the higher the jet Mach number, the longer the potential core. In Fig. 1.7 an exemplary result of the potential core length is presented as a function of the Mach number. In addition to this the length of the sonic area – the area, where the flow in the jet is supersonic – is presented for supersonic Mach numbers. As an example, the potential core of a $M_j = 2$ jet is about

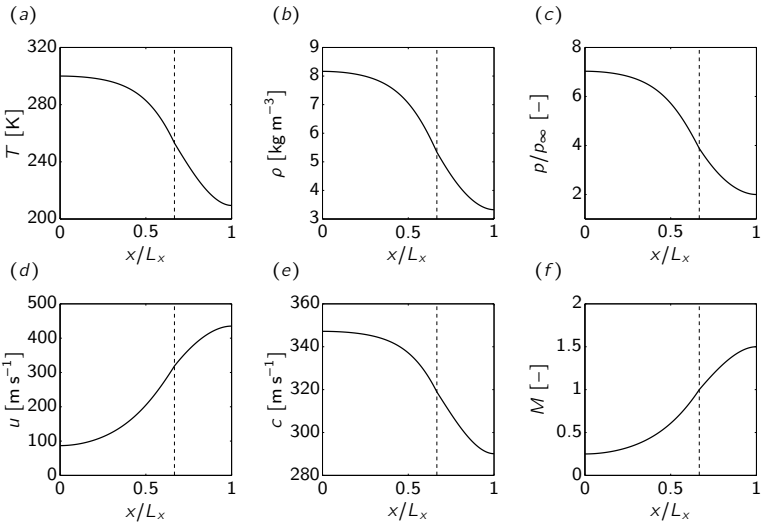

Figure 1.6: Flow inside a round convergent-divergent Laval nozzle for an inlet Mach number of $M = 0.25$ and a design outlet Mach number of $M = 1.5$ (cf. Fig. 1.4). Smallest diameter at $x/L_x = 2/3$ (- - - - - -). Pressure ratio at the outlet: $p/p_\infty = 2.0$; corresponding to a fully expanded Mach number of $M_j = 1.96$ and a reservoir temperature and pressure of $T_r = 300\,\mathrm{K}$ and $p_r = 734\,\mathrm{kPa}$, respectively (cold jet, under-expanded). (*a*) Temperature; (*b*) Density; (*c*) Pressure; (*d*) Velocity; (*e*) Local speed of sound; (*f*) Mach number.

as long as ten jet diameters and the length of the sonic area is about as long as twenty jet diameters. Empirical results on supersonic jets show that the length of the potential core scales with $M^{0.9}$ and the length of the sonic area with M^2 [see Nagamatsu & Horvay, 1969]. For the sub- and supersonic jet, the potential core is surrounded by the mixing layers and finally followed by the fully developed jet.

In the following section we will see that the value of expansion, or the difference of the fully expanded Mach number M_j and the design Mach number M_d, is particular important for the noise generation mechanism in a supersonic jet.

1.1.1 Three sources of noise

The noise of a supersonic jet differs in many aspects from the one of a subsonic jet. One of the first observations is that the noise intensity – the overall sound pressure level (OASPL) – is several orders larger than the one of a subsonic

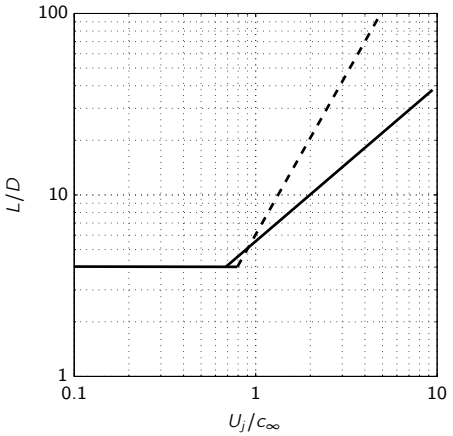

Figure 1.7: Length of the jet potential core (———) and length of the supersonic area (- - - - - -) as a function of the jet Mach number. Supersonic jet assumed to be ideally expanded. Data adapted from Nagamatsu et al. [1969].

jet. Another observation is the distinct spectrum of supersonic jet noise. Whereas the spectrum of a subsonic jet usually contains one wide peak, the noise spectrum of a supersonic jet can exhibit sharp peaks and broadband components. In addition to that the noise components of a supersonic jet show strong directional characteristics compared to its subsonic counterpart.

Two essential phenomena are responsible for these differences. The first one are large coherent structures in the jet convecting with supersonic phase velocity and the second one are the shock cells in the jet core. The former one can also occur in high temperature subsonic jets [Seiner, 1984, Viswanathan, 2004] where the phase velocity is supersonic with respect to the cold ambient fluid. The second phenomenon is restricted to purely supersonic jets. In the following a brief overview on supersonic jet noise will be presented. An extensive overview of supersonic jet noise can be found in Seiner [1984], Tam [1995] and with the focus on jet screech in Raman [1998, 1999b].

The aeroacoustic noise of a supersonic imperfectly expanded jet can be divided in three parts, *turbulent mixing* noise, *broadband shock-associated* noise and the *screech tones*. The latter two noise components are only present in imperfectly expanded jets. Turbulent mixing noise is the dominant noise source in subsonic jets but shows some additional effects in supersonic jets, as we will see later. In Fig. 1.8 a typical noise spectrum of an imperfectly

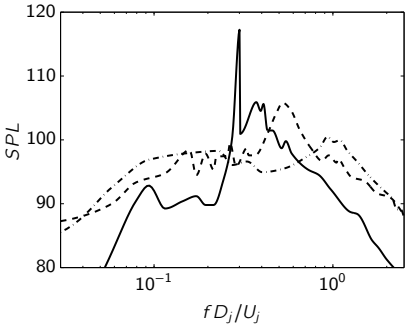

Figure 1.8: Noise measurements of an under-expanded supersonic jet with convergent-divergent nozzle. Design Mach number M_d = 1.5, jet Mach number M_j = 1.672. SPL over Strouhal number measured at different nozzle inlet angles: Θ = 30° (———), Θ = 90° (- - - - - -), Θ = 120° (-·-·-·-·-). [Data from Norum & Seiner, 1982a, p. 172].

expanded supersonic jet, measured by Norum & Seiner [1982a], is presented. The supersonic jet of this specific case is under-expanded with a convergent-divergent nozzle. Hence, the design Mach number is supersonic (M_d = 1.5) with a fully expanded jet Mach number of M_j = 1.672.

Visualized is the sound pressure level (SPL) as a function of the Strouhal number Sr. Both, the x- and y-axis are quasi logarithmic. The Strouhal number is applied logarithmic on the axis and the sound pressure level is a logarithmic law:

$$SPL = 20 \log_{10} \left(\frac{p'_{\mathrm{rms}}}{p_{\mathrm{ref}}} \right) \tag{1.9}$$

with the RMS value of the acoustic pressure fluctuations p'_{rms} and a fixed reference value $p_{\mathrm{ref}} = 2 \cdot 10^{-5}\,\mathrm{Pa}$. The Strouhal number is a dimensionless frequency f, scaled with the fully expanded jet diameter D_j (cf. Eq. (1.7)) and the fully expanded jet velocity $U_j = M_j c_j$ (cf. Eq. (1.6)):

$$Sr = \frac{f D_j}{U_j} \tag{1.10}$$

Note, that the definition of the Strouhal number is not unique in the literature. In some references [like Seiner, 1984] instead of using the fully expanded jet diameter D_j, the nozzle exit diameter D is chosen which can alter the Strouhal number of up to 20 % and more (depending on the expansion).

The three curves in Fig. 1.8 correspond to three measurement angles. One in the upstream direction of the jet ($\Theta = 30°$), one in the normal direction ($\Theta = 90°$) and one in the downstream direction ($\Theta = 120°$) with the angle Θ measured from the upstream direction. One can observe a strong directivity of the noise with several peaks. Each of the three noise components can be identified in the spectrum. The most prominent feature is the peak measured in the upstream direction ($\Theta = 30°$) with a frequency of $Sr \approx 0.3$ and an amplitude of 117.3 dB. This peak corresponds to the screech tone. It is more than 10 dB louder than all other peaks in the spectrum.

Listening further in the downstream direction, normal to the jet axis ($\Theta = 90°$), the peak of the screech tone vanished and an other component, the broadband shock-associated noise, becomes the dominant noise source. The peak of this source is less sharp than the screech tone and of higher frequency ($Sr \approx 0.53$). It is also visible in the upstream signal and in the downstream signal with increasing frequency when increasing the observation angle ($Sr \approx 0.4$ and $Sr \approx 0.95$, respectively). As we will see later, this is due to a Doppler shift of convecting sources. In addition to this, the peak amplitude of the broadband component in the upstream and normal direction of the jet is about 5 dB louder than in the downstream direction.

The turbulent mixing noise is of low frequency and low amplitude (20 – 30 dB less than the screech tone) and can be detected at all three observation angles. It is characterized by a wide and flat hill with a wide peak in the spectrum. The frequency reaches from the largest wave length up the screech frequency and beyond. Contrary to the screech tone and the shock-associated noise the amplitude of the mixing noise is increasing with the observation angle.

1.1.1.1 Turbulent mixing noise

Turbulent mixing noise is caused by the large and small scale turbulent structures in the jet mixing layers. Large scale structures are the dominant sources whereas the small scale structures induce the background noise.

Turbulent mixing noise is of low frequency and is dominant in the range of $0.1 < Sr < 0.25$ [Tam, 1995]. It is obvious from Fig. 1.8 that the dominant part of turbulent mixing noise is radiated in the downstream direction. In the normal and downstream direction ($\Theta = 90°$ and $\Theta = 120°$) the turbulent mixing noise is up to 10 dB louder than in the upstream direction. In Fig. 1.9 the OASPL is measured as a function of the observation angle Θ for the same jet as in Fig 1.8. A distinct increase of the noise level is visible for observation angles larger that 125° (gray area). The two curves in that figure illustrate a

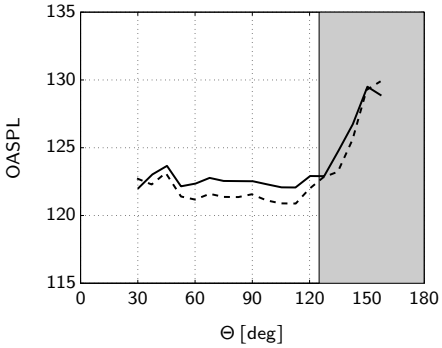

Figure 1.9: Noise measurements of an under-expanded supersonic jet with convergent-divergent nozzle. Design Mach number $M_d = 1.5$, jet Mach number $M_j = 1.672$ (same case as in Fig. 1.8). Overall SPL as a function of the observation angle Θ measured from the upstream direction. Gray area ($\Theta > 125\,\text{deg}$) dominated by turbulent mixing noise. (———) without screech tone (tab inside the nozzle); (- - - - - -) with screech tone (no tab). [Data from Norum & Seiner, 1982a, p. 44f.].

case with screech and one without screech (to suppress the screech, a tab is included inside the nozzle [see Norum & Seiner, 1982a, p. 196]). As we will see later, the screech tone is dominant in the upstream direction and does not affect the dominant turbulent mixing noise.

The dominant noise sources in a supersonic jet are the large scale turbulent structures in the jet. They are convected downstream in the mixing layers of the jet and can reach a supersonic phase velocity (here the convection velocity with respect to the ambient fluid). Once the phase velocity is supersonic, intense noise is radiated in the form of Mach waves. The first to observe Mach wave was Lighthill [1954] when he studied supersonically convecting sources. Later on, the underlying theory was added by Phillips [1960] and Ffowcs Williams [1963]. In Fig. 1.10, a sketch of the noise generation mechanism is presented. The large coherent turbulent structures are modeled as a sinusoidal instability wave with the wavelength as two consecutive eddies. They are convected with the phase velocity c_p. In the ambient fluid, the speed of sound is constant and given by c_∞. Now, if $c_p > c_\infty$ a Mach wave radiation will occur with the propagation angle $\theta = \arccos(c_\infty/c_p)$. Tam et al. [1992] found that the peak Strouhal number of the emanated Mach waves is corresponding to the most amplified instability wave.

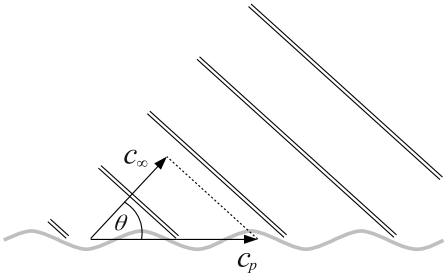

Figure 1.10: Mach wave radiation of a high speed jet with supersonic phase velocity c_p with respect to the ambient speed of sound c_∞. Angle of radiation $\Theta = \arccos(c_\infty/c_p)$. Mach wave: (═══); Instability wave: (———).

1.1.1.2 Broadband shock-associated noise

Broadband shock-associated noise is caused by the interaction of downstream propagating large scale structures and the quasi periodic shock cell structure in the jet plume. Harper-Bourne & Fisher [1973] were the first to derive a theory on shock-associated noise and to identify the importance of the quasi periodic shock cells. In their model they account for the Doppler shift of the convecting sources which is associated with the convecting Mach number M_c and can be expressed by the factor $(1-M_c\cos\Theta)^{-1}$. This shift is clearly visible from Fig. 1.8 where the peaks of the broadband noise components are shifted to higher frequencies as the observation angle is increasing. For moderate pressure ratios the directivity of the broadband noise is found by Norum & Seiner [1982b] to be faced mainly in the upstream direction. Only for high pressure ratios the noise component shows omnidirectional characteristics.

Despite the decrease of the noise intensity in the downstream direction, Seiner [1984] concludes that for observation angles Θ larger than 75°, the broadband noise component will be the dominant noise source. In addition to that Norum & Seiner [1982a] observe at least one secondary peak with less than twice the peak Strouhal number Sr_{BB}. Based on their data one can approximate the second peak at $Sr_{2BB} \approx 1.9 Sr_{BB}$.

Harper-Bourne & Fisher [1973] found that the acoustic intensity scales with

$$I \sim \left(M_j^2 - M_d^2\right)^2 \tag{1.11}$$

up to the point where a Mach disk forms in the jet plume [see Seiner & Norum, 1979]. Hence, the broadband shock-associated noise intensity scales

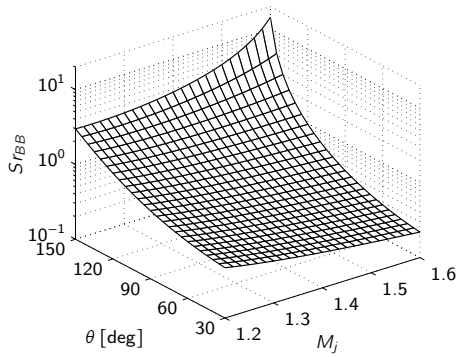

Figure 1.11: Peak Strouhal number Sr_{BB} of broadband shock-associated noise as a function of the observation angle Θ and the fully expanded jet Mach number M_j. Theory based on Eq. (1.13).

with the shock strength. Based on a stochastic model, a theory to predict the spectra of broadband shock-associated noise has been proposed by Tam [1987]. He decomposed the quasi periodic shock cell structure into several time independent modes and superimposed the interaction of the instability wave with the distinct modes to a spectrum of broadband shape. In a one-dimensional analysis one obtains for the peak Strouhal number of the broadband shock-associated noise:

$$\frac{f_{BB}D_j}{u_j} = \frac{u_c D_j}{L_s(1+\frac{u_c}{c_\infty}\cos\Theta)u_j} \tag{1.12}$$

with the shock cell spacing L_s and the convective velocity of the large scale structures u_c. Under the assumption that the convective velocity is $u_c = 0.7u_j$ and the shock spacing as defined in Eq. (1.3) we get:

$$\frac{f_{BB}D_j}{u_j} = \frac{0.54}{(M_j^2-1)^{\frac{1}{2}}(1+0.7M_j\cos\Theta)}. \tag{1.13}$$

Hence, the peak Strouhal number of broadband shock-associated noise is only depending on the fully expanded jet Mach number M_j and the observation angle Θ. Note, that this relation is only valid for $M_j > 1$.

In Fig. 1.11 the dependence of the peak Strouhal number Sr_{BB} on the observation angle Θ and the fully expanded jet Mach number M_j is presented. One can observe on the one hand that the frequency is increasing with the

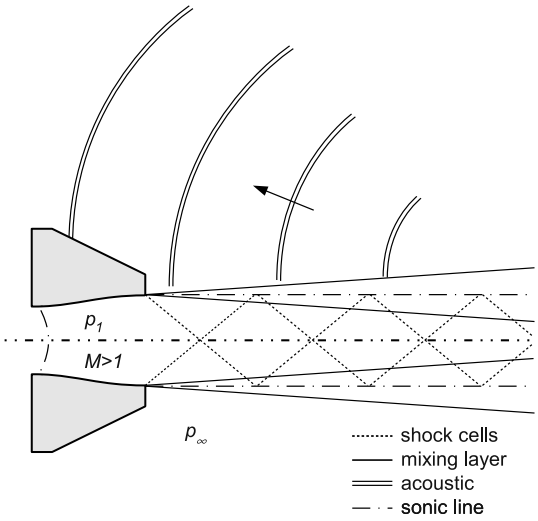

Figure 1.12: Schematic view of the interaction of shock and turbulent mixing layer in a jet with emanated noise. Upstream traveling acoustic waves are impinging at the nozzle and exciting new instabilities in the thin mixing layer to close a feedback loop (screech).

observation angle due to the Doppler shift and on the other hand that the frequency range is increasing with the Mach number. Due to the latter fact, the Strouhal number is decreasing with the Mach number in the upstream direction but increasing with the Mach number in the downstream direction.

1.1.1.3 Screech tones

Powell [1953a,b] was the first to observe screech tones. In his pioneering work on choked jet nozzles above the design point he observed a dominant peak in the spectrum which he called to be a *powerful whistle* or *screech*. He identified that this peak may dominate the spectrum over mixing noise and broadband shock associated noise.

As an explanation to this phenomenon, he correctly suggested that an acoustic feedback mechanism is causing these discrete tones. In Fig. 1.12, the screech noise generation process is presented in a sketch of a supersonic jet including the jet nozzle. Upstream propagating acoustics are impinging on the nozzle lip and forcing instabilities in the thin mixing layer at the nozzle exit. These Kelvin–Helmholtz instabilities are convected downstream and

growing rapidly in the mixing layer of the jet. Subsequently, they are interacting with the repeating shock cell structure and emanating noise. As for the broadband shock-associated noise, these acoustics are emanated mainly in the upstream direction and transported outside the jet towards the nozzle. Once they reach the nozzle, new instabilities embryo and the feedback mechanism is closed.

Experimental investigations on screech tones has been performed by a host of researchers like Davies & Oldfield [1962a,b], Krothapalli et al. [1986], Mclaughlin et al. [1975], Nagel et al. [1983], Norum [1983], Seiner [1984], Seiner & Norum [1979], Tam & Tanna [1982], Westley & Woolley [1975] and more recently by Alkislar et al. [2003], Gutmark et al. [1990], Panda [1998, 1999], Panda et al. [1997], Ponton & Seiner [1992], Powell et al. [1992], Raman [1997a, 1999a], Yu et al. [1998], Zaman [1999]. A detailed overview over the research in jet screech from the beginnings with Powell in 1953 can be found in Raman [1999b]. In the experiments on screech tones, sound pressure levels of up to 160 dB could be observed. From Fig. 1.8, one can see that the screech tone is discrete in its frequency. This discrete and intense acoustic of 160 dB correspond to a RMS value of the pressure fluctuation of $p_{\mathrm{rms}} = 2000\,\mathrm{Pa}$. On a surface of one square meter (like e.g. the vertical tail of an airplane) these pressure fluctuations are responsible for RMS loads of 2000 N. It is reported in Hay & Rose [1970], Seiner [1994], Seiner et al. [1987] that screech tones are responsible for structural damage and fatigue failure of airplane.

Powell [1953b] also observed that screech tones are not Doppler shifted. Independent on the observation angle, the screech frequency is constant. This leads to the conclusion that the source of screech tones is not convected and hence linked to the quasi periodic shock cell structure. Despite the independence on the frequency, the screech amplitude is strongly dependent on the observation angle. Whereas in the upstream direction, the screech tone is the dominant noise source, it is not detectable in the downstream direction (cf. Fig. 1.8 for $\Theta = 30°$ and $\Theta = 120°$).

One of the most important observations of Powell [1953b] on his research on axisymmetric (round) and two-dimensional (rectangular) jets, is the dependence of the screech Strouhal number Sr_S on the fully expanded jet Mach number M_j. For rectangular jets, he observed a smooth variation of the Strouhal number when modifying the Mach number. More precisely, the Strouhal number decays monotonously with an increasing jet Mach number. A typical behavior of this phenomenon is presented in Fig. 1.13(b) based on measurements from Panda et al. [1997]. In his experiments, he used a rectangular jet with an aspect ratio of the nozzle of 5:1 and varied the Mach number in the range from $1.1 \leq M_j \leq 1.85$. The Strouhal number (here based

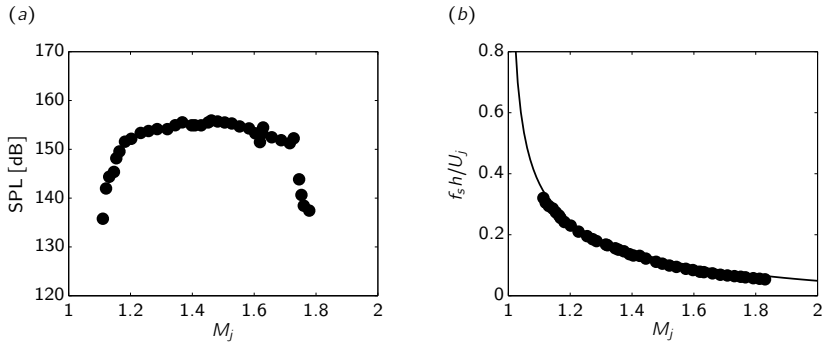

Figure 1.13: Screech amplitude and frequency of a rectangular jet versus the fully expanded jet Mach number M_j [measurements from Panda et al., 1997]. Aspect ratio of the nozzle 5:1 with the smaller dimension h. (a) Screech amplitude versus the fully expanded jet Mach number. (b) Dominant screech frequency as a function of the jet Mach number M_j. (———) analytical solution of Tam [1988] with $u_c = 0.5u_j$.

on the smaller height of the rectangular nozzle h) is decreasing from 0.3 to a value below 0.1 with a smooth behavior. One can show that the inverse of the Strouhal number (the wavelength of the acoustic) scales nearly linear with the Mach number [see e.g. Seiner, 1984].

The corresponding peak amplitudes of the screech tones are presented in Fig. 1.13(a). One can see that the amplitude strongly varies with the Mach number. One might imply that the amplitudes are increasing with the Mach number as the M^3 law postulates the OASPL. In fact the SPL is increasing rapidly in the lower Mach number range ($1.1 \leq M_j \leq 1.2$) from 135 dB to more than 150 dB. From this point on the slope is less steep until the amplitude reaches its maximum with 155 dB at a Mach number of about $M_j = 1.5$. A further increase of the Mach number up to $M_j = 1.7$ leads to a slow decrease in the amplitude back to 150 dB. After that, the amplitude drops drastically to 130 dB at the upper limit of a Mach number of $M_j = 1.8$. From this picture it is evident that the screech tone for rectangular jets is limited to the Mach number range of $1.1 \leq M_j \leq 1.8$. Other experiments observe screech tones for rectangular jets up to $M_j = 1.9$ [see Panda et al., 1997]. The reason for the cessation of screech at high Mach numbers will be given later.

For axisymmetric (round, cylindrical) jets the data of Powell [1953b] showed discrete jumps in the Strouhal number. Compared to the case of a rectangular jet the curve is not smooth. These jumps are now referred to as *screech*

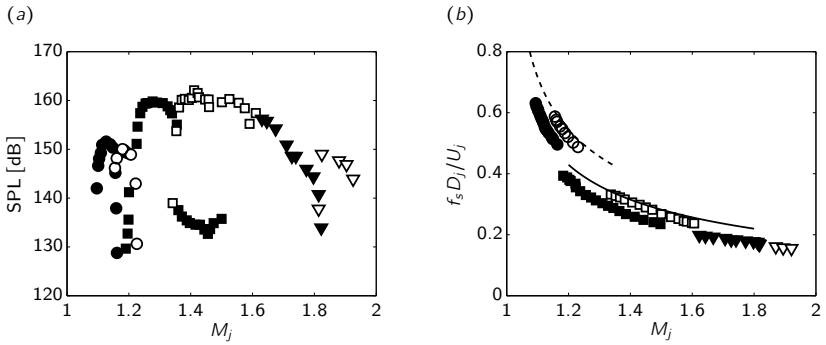

Figure 1.14: Screech amplitude and frequency of a circular jet versus the fully expanded jet Mach number M_j for different screech modes [measurements from Panda et al., 1997]: A1 ●; A2 ○; B ■; C □; D ▼; E ▽; (*a*) Screech amplitude versus the fully expanded jet Mach number. (*b*) Dominant screech frequency as a function of the jet Mach number M_j. Analytic solution for mode A (- - - - - -) and analytical solution for mode C (———) by Massey [1997].

modes (before that: *screech stages*). It was first reported by Davies & Oldfield [1962a,b] that the screech modes are overlapping and that they can exist simultaneously or switch randomly from the one to the other mode. A typical behavior of this phenomenon is presented in Fig. 1.14(*b*) based on measurements from Panda et al. [1997]. Up to now, five different screech modes are reported and labeled in alphabetic order: A (A1 and A2), B, C, D and E. Mode A can de separated in two modes with a similar behavior. All five modes can be identified in Fig. 1.14(*b*) including the fact that they are indeed overlapping for some Mach number regimes. Each mode represents a typical instability of the jet. These are: *toroidal*, *helical* or *flapping* whereas the latter one is a superposition of two counter-rotating helical modes. In Fig. 1.15 an attempt is made to visualize the three different instability modes. Panel (*a*) toroidal, panel (*b*) helical and panel (*c*) flapping as superposition of two helical modes (gray). The y- and z-axis represent the jet exit plane (normal to the jet axis x). The t-axis represents the time or alternatively the x-axis. One can define the black lines in the figures as the path of an acoustic wave front. The only existing dominant mode in a two-dimensional jet is the flapping mode whereas it is not caused by helical modes.

During screech, the jet undergoes strong oscillations, based on the three instabilities. Mode A is known to be toroidal, mode B is flapping, mode C is helical, mode D is flapping and mode E is unknown. An exhaustive

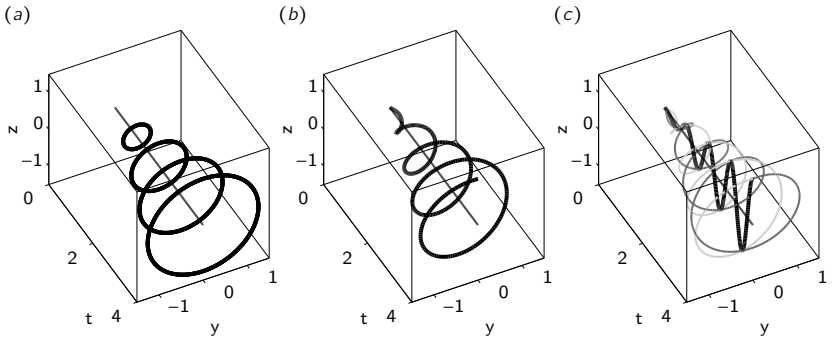

Figure 1.15: Instability modes in a jet (acoustic modes). y-z-plane normal to the jet axis. t-axis: time (or x-axis). (a) toroidal (axisymmetric) mode (A-mode; A_1: unstable, A_2: stable); (b) helical mode (C-mode: stable); (c) flapping mode (superposition of two counter-rotating helical modes (gray)) (B, D-mode, B: unstable, D: unstable), flapping plane: z-t. [see Merle, 1956, Powell et al., 1992, for more information about the stability of the seperate modes].

description of the screech modes A-D can be found in Powell et al. [1992]. The first to observe the additional E mode was Panda et al. [1997]. Further on Powell et al. [1992] summarizes that mode A1 is unstable and A2 is stable. Mode B is very unstable, mode C on the other hand very stable and mode D again very unstable and not always visible. The same holds true for mode E. A similar result could be found by Yu & Seiner [1983] as they observe that the helical mode is more stable than the toroidal mode at least for Mach numbers in the range of $1.25 < M_j < 2.24$. Westley & Woolley [1975] mention that the helical mode rotates with the same frequency as the corresponding screech tone. The same holds true for the toroidal and flapping mode.

Mode A (A1 and A2), the toroidal (axisymmetric) mode, only exists for the lower Mach number range ($1.1 \leq M_j \leq 1.25$) whereas the unstable mode A1 exists only in the lower bound of that interval. In a small region in the middle of the Mach number interval the modes are overlapping and may exist simultaneously or switch randomly back and forth. In such a case, the jet would emanate two screech tones with similar amplitude but two sharp frequencies. One with a Strouhal number of about $Sr = 0.5$ corresponding to mode A1 and one with a Strouhal number of about $Sr = 0.6$ corresponding to mode A2.

Mode B (flapping) exists for higher Mach number as mode A in the range of $1.17 \leq M_j \leq 1.5$ with a corresponding Strouhal number range from $0.25 \leq Sr \leq 0.4$. This mode overlaps the stable mode C which exists in the Mach

number range from $1.3 \leq M_j \leq 1.6$. Mode C is of higher frequency as mode B and exists without a neighboring mode in the small range from $1.5 \leq M_j \leq 1.6$. What follows is mode D and E up to Mach numbers of $M_j = 1.9$. They do not overlap each other which might imply that they are of similar structure.

In Fig. 1.14(a) the corresponding amplitudes of the screech tones are presented. One can observe that on the one hand the amplitudes vary with the jet Mach number, similar as for the rectangular jet, and that each mode exhibits different amplitudes. Modes A1 and A2 are comparable small in their amplitude. Sound pressure levels of 140 - 150 dB could be measured. A higher SPL can be gained for mode B with a peak value of 160 dB. This is followed by mode C with the highest amplitude and a peak value of 162 dB. It is interesting to note that in the overlapping area of mode B and C, the amplitude of mode B drops to a value of about 132 dB which is a difference of 30 dB. Finally, mode D and E exhibit less acoustic energy than the latter two ones at which mode D drops rapidly from 155 dB down to 133 dB and the SPL of mode E is around 145 dB.

Despite the dominant peak values of the screech tone of one individual mode, additional subharmonics of that specific mode can exist. The amplitude of these modes is usually smaller than the one of the fundamental frequency. A detailed description of additional subharmonics can be found in Powell et al. [1992].

For a numerical experiment, mode instabilities and the so related randomly back and forth switching of the individual states is extremely expensive. To capture the separated modes for a statistically converged result, the experiment needs to be simulated for a long time. To this end, we will focus in our axisymmetric jet computations on the helical mode C as it is very stable. Furthermore we avoid an overlapping of other unstable modes. Thus, the remaining Mach number range is $1.5 \leq M_j \leq 1.6$. The benefit of this Mach number range is also that the corresponding screech amplitude is very powerful (in the order of 160 dB). Hence, a Mach number in the middle of $M_j = 1.55$ will be used for axisymmetric (round) jet noise simulations. For two-dimensional (rectangular) jets only one stable mode does exist [Note, that Gutmark et al., 1990, observed a symmetric mode for rectangular jets for Mach numbers slightly above chokeing ($1 \leq M_j \leq 1.15$) which we will not consider here]. Hence, the Mach number can be chosen arbitrarily. To validate the present numerical method, a Mach number range of $1 \leq M_j \leq 2$ will be investigated for the planar jet.

As we have seen in Fig. 1.13(b) and 1.14(b) the screech frequency, both for the axisymmetric and rectangular jet, depends on the fully expanded Mach number M_j. In fact, the screech frequency is depending on the shock cell

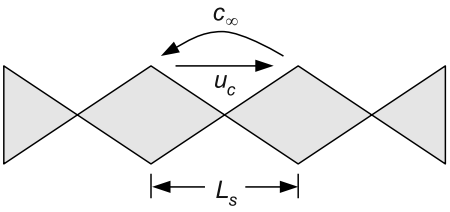

Figure 1.16: Sketch of the mechanism involved in predicting the screech frequency. L_s: shock cell spacing; c_∞: ambient speed of sound; u_c: convection velocity of the large scale structures (eddies).

spacing which is also a function of the jet Mach number (cf. Eq. (1.3)). The screech frequency can be approximated as the sum of the times to transport a large coherent structure from one shock cell to the next one plus the time an acoustic wave needs for the same distance. In Fig. 1.16 a sketch of the the mechanism involved in predicting the screech frequency is presented with the shock cell spacing L_s, the ambient speed of sound c_∞ and the convection velocity of the large scale structures u_c. With this assumption, the screech frequency can be obtained by computing the sum:

$$T_s = \frac{L_s}{u_c} + \frac{L_s}{c_\infty}$$

and finally the Strouhal number:

$$\frac{f_s D_j}{u_j} = \frac{u_c D_j}{L_s(1 + M_c)u_j} \tag{1.14}$$

with the convection Mach number $M_c = u_c/c_\infty$. Note, that above equation can be also obtained by setting the observation angle Θ in Eq. (1.12) to zero.

Equation (1.14) can be modified by including the length of the shock cell spacing L_s based on Eq. (1.3) and the empirical observation that the convection Mach number is about 0.7 times the jet Mach number ($M_c = 0.7M_j$). In addition to that, it is assumed that the shock cell spacing at the location of the screech source (usually at the third to fifth shock cell) is about 20 % smaller than expected by Eq. (1.3). With these assumptions and Crocco's relation, it is straightforward to find an expression for the screech frequency

only depending on the jet Mach number and the temperature ratio of the ambient fluid T_∞ and the reservoir temperature T_r, as proposed by Tam et al. [1986]:

$$\frac{f_s D_j}{u_j} = \frac{0.67}{\left(M_j^2 - 1\right)^{\frac{1}{2}}} \left(1 + \frac{0.7 M_j}{\left(1 + \frac{\gamma - 1}{2} M_j^2\right)^{\frac{1}{2}}} \left(\frac{T_r}{T_\infty} \right)^{-\frac{1}{2}} \right)^{-1} \tag{1.15}$$

Note, that the assumption by Tam et al. [1986] that the convective Mach number is 0.7 times the jet Mach number is not consistent in the literature. Powell et al. [1992] propose different values for the individual modes: 0.64 (mode A), 0.68 (mode B), 0.8 (mode C) and 0.75 (mode D). Similar results are proposed by Panda et al. [1997]: 0.67 (mode A), 0.58 (mode B), 0.66 (mode C) and 0.69 (mode D). These differences indicate that it is difficult to predict the convection Mach number [see also Gao & Li, 2010]. Furthermore, the convection velocity of the disturbances is not constant in a specific jet as the disturbances are accelerated right after passing a shock and decelerated as they approach a shock [see Raman, 1999b]. Improvements in the screech prediction formula, taking into account the individual modes of axisymmetric jets can be found e. g. in Gao & Li [2010], Massey [1997], Panda et al. [1997] and Powell et al. [1992]. An estimation of the screech frequency for rectangular jets can be found in Tam [1988].

In most experimental studies, the Reynolds number is in the order of 10^6. As we will see later, such high Reynolds numbers are unfavorable for direct numerical investigations, based on the state of art high performance computers. In the present numerical investigation on planar and axisymmetric jet screech, a Reynolds number of $Re = 5000$ is chosen. The remaining question is, to which extent the Reynolds number influences screech tones. High Reynolds number flows contain more small scale turbulent fluctuations. These fluctuations will contribute to the shock-associated noise and will be responsible for additional broadband components of high frequency. The screech frequency is obviously depending on the shock cell spacing which is independent on the Reynolds number. Hu & McLaughlin [1990] show that the small scale turbulent structures are irrelevant to screech tones. They investigated a low Reynolds number under-expanded jet ($Re_D = 8000$) and compared the results to a high Reynolds number case ($Re \approx 10^6$). It is demonstrated that the large scale fluctuations and the shock cell spacing are responsible for screech tones and independent on the Reynolds number. Only the broadband shock associated noise components are reduced for the low Reynolds number jet.

We have seen that the prediction of the screech frequency is straightforward and, depending on the screech mode, can be approximated using empirical results for the convection Mach number. In contrast to that is the prediction of the screech amplitude. Up to now, no theory for the prediction of the screech amplitude is available not even an empirical. The difficulty in predicting the screech amplitude is its strong dependency on the surrounding environment. Most sensitive to screech tones is the geometry of the nozzle, since it is responsible for the receptivity process – the coupling of acoustic and hydrodynamic instabilities. Raman [1997a] observed that increasing the nozzle lip t of a rectangular jet with $t/h = 0.2$ to $t/h = 2$ increases the SPL from 130 dB up to 148 dB measured in a distance of $10h$ normal to the nozzle exit. This is a drastic increase of 18 dB by only changing the nozzle exit lip, a part which does not directly influence the jet flow. Other researchers like Glass [1968] indicate that screech tones can be enhanced by an acoustic reflector upstream the nozzle. The reflector can be placed such that the reflected acoustic waves amplify the acoustic fluctuations at the nozzle exit by means of a positive superposition of upstream and downstream propagating waves and therefore enhance the receptivity process. The same reflector can be placed upstream the nozzle to suppress screech tones by means of noise cancellation at the nozzle exit as reported by Nagel et al. [1983], Norum [1984]. Hence, the change of the surrounding environment, like reflecting surfaces or the design of the nozzle have a significant impact on the screech tone amplitude which makes its prediction a challenging task. In addition to that, initial conditions, like a turbulent or laminar boundary layer inside the nozzle, a swirl in the flow or the velocity distribution in the nozzle exit plane (depending on the contour of the nozzle contraction) may influence the individual screech modes [Powell et al., 1992]. Especially the position of the neutral plane of the flapping mode may be exited randomly as reported by Seiner et al. [1986b].

One could expect that the screech amplitude is linked to the shock strength, as a certain shock amplitude is necessary to produce screech and strong screech tones need strong shocks, but indeed the link between shock strength and screech amplitude is very weak [see amongst others Raman, 1998]. The shock strength is increasing monotonously [nearly linear; see Raman, 1997a] with the jet Mach number whereas the screech amplitude is first increasing up to a maximum value and then again decreasing (cf. Fig. 1.13(a)). In the following section some techniques to influence supersonic jet noise and in particular jet screech will be addressed.

1.1.2 Mechanism of jet noise reduction

As we have seen, supersonic jet screech can be responsible for a loud and discrete noise source. In the early years of jet screech research it was thought that screech tones do not exist in full scale aero-engines due to the non-uniformity of the flow and the complex geometry of the nozzle. However, the experiments of Jungowski [1979] demonstrate that even a non-uniform flow does excite screech tones. It is furthermore reported in Hay & Rose [1970] and Seiner et al. [1987] that screech tones are responsible for structural damage and fatigue failure of airplane. To this end, the understanding and finally the reduction of screech tones is a matter of particular concern. In the last decades several techniques were developed to influence screech tones. Their main idea is based on the cancellation of the feedback loop by means of active and passive devices. In the following some active and passive devices will be presented, beginning with the passive ones.

Acoustic reflector Glass [1968] was the first to observe that a passive acoustic reflector can be used to enhance screech tones. He placed the reflector in an upstream position of the nozzle such that impinging acoustic waves (broadband shock-associated noise) are reflected back in the downstream direction of the jet. These downstream wave are superimposed with the upstream propagating waves and forming a standing wave with stationary nodes and anti-nodes. Is the reflector located such that the position of an anti-node matches that of the nozzle exit, the feedback loop will be amplified. This phenomenon was also studied recently by Kweon et al. [2006] where they could show that the jet mixing (here equivalent to screech) can be enhanced by a reflector placed at the nozzle exit. On the other hand, if the reflector is located such that the position of a node matches that of the nozzle exit, the feedback loop will be canceled. The latter phenomenon was investigated by a series of researches beginning with Nagel et al. [1983] and Norum [1984]. It was also studied recently by Khan et al. [2004]. Based on the theory that the anti-nodes and nodes of a standing wave can influence screech, the location of the reflector to amplify and to cancel screech can be given. Assuming the screech wave length to be λ_s and the fact that at the surface of the reflector is an anti-node, the position for screech amplification and cancellation is at

$$x = \begin{cases} -\dfrac{n}{2}\lambda_s & \text{amplification} \\ -\dfrac{2n+1}{4}\lambda_s & \text{cancelation} \end{cases} \tag{1.16}$$

with an integer number $n = 0, 1, 2, ...$ The wave length can be approximated by Eq. (1.15) and with the constant speed of sound in the ambient fluid we get: $\lambda_s = c_\infty / f_s$.

Harper-Bourne & Fisher [1973] also used an acoustic reflector to amplify screech tones. In addition to that they added a sound absorbing foam (porous material) on the surface of the reflector. Compared to the reflector without the foam, the screech tone was reduced but remained higher than a jet without reflector. The effect of the reflector coated with foam in this experiment is that the acoustic waves are reflected less efficient as in the case for a solid reflector. Hence, the standing wave is damped and the amplification of the screech tone is reduced. Still, as the screech tone of the jet with porous reflector is louder than a jet without reflector, the damping properties of the porous material are not optimal. Similar results were obtained by Kweon et al. [2005]. In an experimental study, they investigated the influence of a porous reflector (based on grass wool and polyurethane foam) compared to a metal (solid) reflector. They found that the reflector with sound-absorbing material reduces the screech tone up to 13 dB an the OASPL up to 5 dB compared to the metal reflector.

Nozzle lip Based on Eq. (1.16) it is evident that a thick nozzle amplifies screech tones. At the nozzle exit ($x = 0$) a thick nozzle acts as a reflector and hence amplifies screech (for $n = 0$). This phenomenon has been reported by numerous researchers. Norum [1983] was one of the first to investigate the dependence of the nozzle lip thickness. In his experiment the peak screech tone could be reduced by 13 dB with a nozzle of "zero" lip thickness. He also investigated more complex nozzle configurations, like asymmetric nozzles, nozzles with a tab and also solid and porous reflectors. He concluded that a large reduction of the screech tone can be gained from modifications of the jet exit geometry, although the extent of this reduction is mode dependent.

Ponton & Seiner [1992] noticed that despite the amplification of the screech tone for a thick nozzle lip, the two remaining noise components (mixing noise and broadband shock-associated noise) are affected as well. They also observed that the existence of the individual screech modes varies in the Mach number range with a modification of the nozzle lip. In particular, for a thin-lipped nozzle the B mode cannot be detected at high Mach numbers. Furthermore, an increase of the nozzle lip thickness caused a decrease of the screech Strouhal number for the A and B mode and an increase for the C mode.

In a recent numerical study by Kim & Lee [2007] the trend of an increase

of the screech tone by a thicker nozzle lip of an axisymmetric jet could be simulated based on the Euler equations. In a similar numerical study by Kim & Nakamura [2006] the influence of the nozzle shape of a rectangular jet was investigated. They observed a reduction of the dominant screech tone for a non-uniform nozzle geometry.

Raman [1997b] studied jet screech in rectangular supersonic jets with spanwise non-uniform exits. He also observed that a non-uniform exit (here: spanwise-oblique) produced weaker screech tones than a uniform exit. In addition to that, the Mach number range to exhibit screech tones was reduced for non-uniform nozzles.

To summarize the influence of the nozzle lip thickness to supersonic jet noise and in particular screech tones: the thicker the nozzle the louder the screech. This strong influence of the surrounding environment makes the prediction of the screech amplitude complicated [Seiner, 1984]. Raman [1998] notes that when mounting a screech suppression device (like a reflector) care should be taken not to increase the nozzle lip thickness.

Chevrons, Tabs, etc. It is well known that non-uniform flows can be responsible for screech tone cancellation. Especially for axisymmetric jets, the non-uniformity influences the individual modes of the jet (A-E) and hence the corresponding screech tone. Norum & Seiner [1982a] used in their experimental investigation on screech tones a small tab inside the nozzle to suppress screech. The small rectangular shaped protrusion extended $0.063D$ into the jet with a width of $0.125D$ (with the jet diameter D). By adding this small device at the nozzle exit the screech tone could be suppressed leading to a peak noise level reduction of more than 13 dB. A similar investigation was performed recently by Clement & Rathakrishnan [2006].

A more advanced geometry was used by Munday et al. [2011]. They added chevrons to reduce supersonic jet noise. Chevrons are used especially in subsonic jets and can be found at many civil aeroplanes like the recently developed Boeing 747-8 (first flight in 2010[1]. They are based on a sawtooth shaped geometry placed at the nozzle exit to influence the mixing behavior in the shear-layer. For supersonic jets, they are responsible for a non-uniform flow and have been shown to reduce or suppress screech by more than 20 dB.

Porous material As we have seen already, a porous material can influence screech [cf. Harper-Bourne & Fisher, 1973]. The porous material can be added on a passive acoustic reflector to act as a sound absorbing material. In

[1] `http://boeing.com/`

this case, the screech amplification of the acoustic reflector can be reduced. A recent investigation on this topic is reported by Khan et al. [2008]. They use a porous reflector at the nozzle exit to reduce the sound pressure at this point. This prevents the unstable disturbances at the nozzle exit to be exited and the loop of the feedback mechanism disappears. Hence, the screech tone can be canceled. In their investigation, they use a porous material with a porosity of $\phi = 0.4$ (a definition of the porosity is given in Sec. § 3). Further comments on the porous material investigated are not given.

Besides on the surface of acoustic reflectors, the porous material can be also placed in the jet core as a porous center-body [first observed by Maestrello, 1979]. Seiner et al. [1980] indicate that a porous plug can eliminate shock-associated noise (and hence screech) and reduce jet mixing noise. More than 20 dB of peak SPL reduction can be gained. The porous plug used in this investigation extended two jet diameters into the jet core and eliminated the shock cells since the porous material allows a smooth adjustment of the pressure gradient in the flow. They conclude that the noise reduction of the porous plug is particular dependent on the porosity and the length of the plug. Similar results could be found by Kibens & Wlezien [1985].

Active devices In the previous paragraphs, the effect of passive devices, like acoustic reflectors, chevrons or a porous material, on jet screech reduction is presented. Besides the passive approach, active devices can be used to reduce screech tones. Krothapalli et al. [2003] used water injection in high-speed jets to reduce supersonic jet noise. They achieved a OASPL reduction of up to 6 dB. A similar approach is investigated by Munday et al. [2011]. They use fluidic injection and fluidically enhanced chevrons to reduce jet screech. They could gain a reduction of up to 20 dB for a fluidic injection configuration.

Kim et al. [2011] use plasma actuators, distributed uniformly at the nozzle exit of contoured and conical axisymmetric nozzles. They could reduce or even suppress the screech tone most likely due to weakening of naturally occurring structures by forcing. In Chen et al. [2002] it is reported that adding a swirl to the jet flow can eliminate screech tones of under-expanded jets. They mention that the swirl in the jet can be responsible to reduce the length of the shock containing core and hence reduce screech tones.

1.2 Objective of this thesis

As we have seen in the previous section, supersonic jet noise is a matter of particular concern. In the presence of jet screech, it can be responsible for

structural damage and fatigue failure of airplanes, like it has been reported for the USAF F-15 fighter and the B-1B bomber [see Seiner, 1994]. Up to now, jet screech is not understood in all details. No analytical or even empirical prediction formula for the correct screech amplitude could be found. The environmental influences on jet screech, like the shape of the nozzle, play an important role. By a modification of the nozzle geometry or other external devices, like an acoustic reflector, jet screech can be reduced. The performance of the screech reduction strongly depends on the specific device.

The objective of the present thesis is to find a device which not only reduces screech, but minimizes it. To this end, a passive device, based on a porous material, is added to the nozzle exit to influence the screech feedback mechanism and finally to eliminate the screech tone. Porous media can be characterized by the porosity and the permeability. As the choice of the optimal porous material (the optimal porosity and permeability) to minimize jet screech is by no means clear, an optimization technique will be used to identify the optimal material properties. In this context, a numerical investigation on supersonic jet noise is performed to identify the phenomenon of jet screech. Both, planar and axisymmetric jets are studied. In a second step, an optimization algorithm based on the adjoints of the compressible Navier–Stokes equations is derived and used to optimize the parameters of the porous material at the nozzle exit to minimize jet screech.

Thesis overview This thesis is divided in two parts. The first part deals with the numerical computation of supersonic jet noise. It starts with the present introduction, explaining the physics of a supersonic jet in chapter § 1. This is followed, by presenting the governing numerical method of computing supersonic jet noise. In chapter § 3, the theory of computing flow in porous media is presented including the derivation and validation of the porous flow equations. This chapter is closed with some numerical examples. Finally, at the end of the first part, in chapter § 4, the results of the supersonic jet noise computations are presented.

The second part deals with the numerical minimization of supersonic jet noise. In its first chapter § 5, the underlying theory of adjoint based optimization techniques is presented and validated with some examples. Results of the minimization of supersonic jet noise with porous media is presented in chapter § 6. In the last chapter § 7, the thesis is summarized with the main results of the present investigation.

At the end of the thesis an appendix contains some additional information and derivations.

2

Theory of computing supersonic jet noise

A supersonic jet is a complex flow. The physical process acting on vastly different length and time scales are a commonplace observation for this application. On the one hand, the propagation of long-wave acoustics ($\mathcal{O}(10^{-2}\text{m})$ – $\mathcal{O}(10^{-1}\text{m})$) in the far field, like the mixing noise of low frequency or the roll-up of a large vortex ($\mathcal{O}(10^{-1}\text{m})$) in the mixing-layer, are comparatively large scales. In contrast to that are small scale turbulent eddies in the order of the Kolmogorov scale ($\eta \approx \mathcal{O}(10^{-5}\text{m})$, for $Re \approx 10^6$) or oblique or even vertical shocks with a length scale in the order of the mean free path ($\mathcal{O}(10^{-7}\text{m})$). Different temporal scales originate e. g. in areas behind a bluff body, like the nozzle, with a large separation zone ($M \approx 0$) compared to the downstream transported acoustics in the supersonic jet core ($M \gg 1$).

Besides the vastly varying time and length scales, one also has to account for different amplitudes in the flow. These arise in particular in the acoustic pressure fluctuations. The ambient pressure is in the order of $\mathcal{O}(10^5\text{Pa})$. Depending on the noise level, an acoustic wave fluctuates from $\mathcal{O}(10^{-4}\text{Pa})$ at 20 dB up to $\mathcal{O}(10^1\text{Pa})$ at 120 dB. Propagating the quiet noise with 20 dB causes a difference of 12 orders of magnitude in the pressure. It is needles to say that this type of flow configuration causes a great challenge in computational resources as well as numerical methods.

In the last decades different classes of methods developed with increasing complexity to compute turbulent flows. Beginning with the three-dimensional *(Un)steady Reynolds Averaged Navier–Stokes (URANS)* followed by the *Large Eddy Simulation (LES)* and finally the *Direct Numerical Simulation (DNS)*.

In addition to that, several subclasses and hybrid approaches combining the individual methods emerged. A brief overview of the different classes and subclasses can be found in Spalart [2000].

Reynolds averaged Navier–Stokes simulations do not compute the Navier–Stokes equations but their Reynolds averaged counterpart with the cost of an additional statistical turbulence model. This method comes with the least computational effort and needs, based on a high Reynolds number computation, like the flow past an aeroplane, about 10^7 grid points to resolve the computational domain. To adjust the statistical turbulence model a lot of empirical information of the flow-case needs to be available. The second class, the Large Eddy Simulation, applies a low-pass filter to the Navier–Stokes equations and hence resolves on the large scales (eddies). To close the system of equations, a sub-grid scale model needs to be included. The computational effort of this method is larger than the one of URANS computations and one needs for the computation of the high Reynolds number example about 10^{12} grid points to resolve the large scales. Finally, the Direct Numerical Simulation, comes without any modeling and hence needs to resolve both the largest and the smallest scales (Kolmogorov length-scale) of the turbulent flow. To resolve the high Reynolds number flow past an aeroplane, a total of about 10^{16} grid points need to be included in the computational domain. It is therefore on the one hand the most expensive method but on the other hand the most accurate one. State of the art high performance computers (HPC), with a peak performance of more than one Petaflop/s and several hundred Terabyte of main memory, are capable to handle about 10^9 grid points. Even for LES, the high Reynolds number flow can not be resolved on the state of the art computers. Hence, the numerical computation, especially the DNS is limited to moderate to low Reynolds number flows as the number of grid points scales with the Reynolds number, like:

$$N_L \approx \frac{L}{\eta} \approx Re_L^{3/4}; \quad \text{with } Re_L = \frac{UL}{\nu}$$

in one direction. The smallest length-scale, the Kolmogorov scale η, and the largest length-scale L determine the number of grid points and can be replaced with the Reynolds number, based on the characteristic velocity U, the corresponding length L and the kinematic viscosity ν. In three dimensions, the total number of grid points is:

$$N_L \approx Re_L^{9/4}$$

Based on the maximum number of grid points of state of the art computations (10^9) the largest resolvable Reynolds number is $Re_{\max} = 10^4$ for a DNS [see

also Kim et al., 1987]. To give an example on a supersonic jet computation based on that Reynolds number and the assumption that the fluid is air under standard conditions, the diameter of the jet would be 0.27mm (based on $M_j = 1.55$ and $T_0 = 20°C$). In the present application a Reynolds number of 5000 is chosen which corresponds to a diameter of 0.14mm. This is about the thickness of a human hair. According to that, DNS is still linked to simple flow geometries and academic cases. It is proposed by Spalart [2000] that a high Reynolds number DNS will be available in the year 2080 and a high Reynolds number LES in the year 2045.

Above mentioned methods are capable to compute the aeroacoustic noise directly, yet with different accuracy. Direct Numerical Simulation (DNS), which resolves all scales, capture the aeroacoustic noise field without any approximations and provide the full spectrum of the generated noise with the drawback of low Reynolds number limitations.

Large Eddy Simulation, model the effect of the small scales and hence fail in the prediction of high-frequency noise components. These missing or under predicted high-frequency spectral components in LES jet noise computations can be highly annoying to the human ear [2-3 kHz, see Bodony & Lele, 2005] and are the most important components in noise regulation. In addition that, the choice of the sub-grid model in the LES is of particular importance to the predicted noise. Bogey & Bailly [2005] show that the results obtained by a selective filter as sub-grid model are quantitatively closer to experimental data than the ones obtained by the widely used dynamic Smagorinsky model by Moin et al. [1991]. They explain this behavior with the lowered effective Reynolds number of the jet computation by means of the eddy viscosity. A reduction of a factor of 50 between the effective Reynolds number of the dynamic Smagorinsky model and the one using a compact/selective filter can be observed.

Mathew et al. [2006, 2003] show that an explicit filter applied to the flow field can be used as sub-grid-scale modeling alone. They apply the filter between every integration step of any DNS algorithm to obtain a LES and conclude that the solution tends uniformly towards the DNS once the grid is refined and the filter cut-off is shifted to higher wave numbers.

A direct prediction of aeroacoustic noise by URANS computations presents the lowest level of flow details and spatial/temporal accuracy. This method is only capable to predict the noise of the largest flow scales and fails in the prediction of broadband components, like shock induced noise [see Wang et al., 2006].

However, the computational domain of any direct approach is limited and usually only contains the hydrodynamic fluctuations and the acoustic near-

field. To propagate the waves into the acoustic far field or to apply it to URANS computations, hybrid methods can be used. These methods use some kind of source information, either in a volume containing the hydrodynamic (noisy) fluctuations (Lighthill), or on a surface enclosing the fluctuations (Linearized Euler Equations (LEE), Ffowks-Williams-Hawkins (FWH)). The latter ones, using the sources, distributed on a surface, can only be applied to methods capable to compute the noise directly (LES or DNS). An application of these hybrid methods to a two-dimensional shear layer can be found in Schulze et al. [2007].

2.1 State of the art

In the following three paragraphs, an overview of the recent achievements in the numerical simulation of supersonic jet noise, and in particular in supersonic jet screech, is outlined and divided in the three major direct methods, beginning with the DNS, followed by the LES and finally the URANS method. The numerical investigations are summarized in Tab. 2.1 and sorted in chronological order.

Direct Numerical Simulation The first direct numerical simulation of supersonic jet noise was reported by Freund et al. [2000]. They computed a Re_D = 2000 jet based on a fully expanded jet Mach number M_j = 1.92 under design condition. Hence, no shocks and no screech was present, only the Mach wave radiation in the acoustic near field could be observed. For the spatial discretization they used a 6th order compact scheme proposed by Lele [1992] and a 4th order Runge–Kutta method for the time integration. Most following research projects on jet noise based on DNS and LES use this combination of spatial and temporal discretization. The jet is computed on a cylindrical grid containing about 21 million grid points without including the nozzle directly. Instead, they use a inlet velocity profile to model the presence of the nozzle.

One year later, Freund [2001] applied the DNS on a M_j = 0.9 subsonic jet with a Reynolds number Re_D = 3600 and a slightly increased spatial resolution (26 million grid points). In this study, they could compare their results to experimental data by Stromberg et al. [1980] and showd a good agreement in terms of mean flow, noise-spectra and -directivity.

Supersonic jet screech was first reported by Manning [1999], Manning & Lele [1998, 2000]. Instead of computing the whole jet and its acoustic field, they investigated the interaction of a shock wave impinging on a supersonic

mixing-layer in two dimensions. The emanated dominant noise component is caused by a "leakage" of the shock tip in the ambient subsonic region once a vortex passes the shock resulting in a loud and sharp acoustic wave. Similar results on two-dimensional shock containing supersonic mixing-layers could

Author	Year	Method	Screech	Geom.
Shen & Tam	1998	URANS	■	○
Freund et al.	2000	DNS	□	○
Freund	2001	DNS	□	○
Al-Qadi & Scott	2003	LES	■	▭
Imamoglu & Balakumar	2003	LES	■	○
Loh et al.	2003	ILES	■	○
Hashimoto et al.	2004	LES	■	○
Lee et al.	2004	Euler Eq.	■	○
Li & Gao	2004	URANS	■	○
Fujimatsu & Misu	2005	Euler Eq.	■	○
Bodony et al.	2006	LES	□	○
Gao & Li	2006	URANS	■	○
Berland et al.	2007	LES	■	▭
Kim & Lee	2007	URANS	■	○
Ray & Lele	2007	URANS	□	○
Singh & Chatterjee	2007	LES	■	○
Schulze et al.	2009	DNS	■	▭
de Cacqueray	2010	LES	□	○
Shur et al.	2010	LES	■	○
Gao & Li	2011	LES	■	○
Kurbatskii	2011	URANS	■	○
Munday et al.	2011	LES	■	○
Manning & Lele	1998	DNS	ML	2D
Suzuki & Lele	2003	DNS	ML	2D
Schulze et al.	2007	DNS	ML	2D
Schaupp et al.	2008	DNS	ML	3D

Table 2.1: Overview of the numerical investigation on supersonic jet noise. Fields marked with a ■ include the prediction of screech tones; else (□) mixing- and shock-associated noise. Investigated nozzle geometry: ○ (round jet); ▭ (planar jet). ML: Shock containing Mixing-Layer.

be observed by Suzuki & Lele [2003]. Schulze et al. [2007] included several hybrid approaches (Linearized Euler Equations (LEE), Ffowcs-Williams and Hawkins (FWH) and Lighthill) to the two-dimensional mixing-layer to propagate the noise in the acoustic far-field. They conclude that FWH besides LEE are in good agreement to the DNS data and capable to propagate noise of supersonic flow cases. Later, Schaupp et al. [2008] extended the shock containing mixing-layer in three dimensions and conclude that the proposed method is suitable for capturing the acoustic field generated in the interaction region of shock and mixing-layer.

A DNS on a turbulent planar jet including screech could be observed by Schulze et al. [2009a]. They computed an under-expanded planar jet, periodic in the transverse direction, with a Reynolds number of $Re_D = 8000$ and a fully expanded jet Mach number $M_j = 1.4$. The thin computational domain contains more than 8 million grid points and is based on a Cartesian domain stretched in the stream-wise and transverse direction to refine the grid in the turbulent region. The nozzle is modeled by a velocity profile as in the work of Freund and does not include the solid nozzle itself. As the sensitivity of the instabilities of the mixing-layer to upstream propagating acoustics seems to be amplified by the presence of the nozzle an artificial forcing of the mixing-layer is applied to close the screech feedback loop. To this end, two "microphones" measure the noise in the upstream direction (close to the artificial nozzle exit) and apply this signal, together with a model spectrum, containing the most unstable instability and its subharmonics, to a small fringe region in the mixing-layer. With this technique, a good agreement with the theoretically expected screech frequency can be observed whereas the screech amplitude is under-predicted. The discrepancy in the screech amplitude is probably related to the empirically adjustable gain of the artificial forcing of the mixing-layer. A DNS including nearly 300 million grid points without artificial forcing (zero gain) showed no screech component in the spectrum [see Schulze & Sesterhenn, 2010a, Schulze et al., 2009a].

Large Eddy Simulation LES prediction of supersonic jet noise was first reported by Al-Qadi & Scott [2003, 2001]. They use a planar jet with a Reynolds number based on the fully expanded jet height of $Re_{h_j} = 178000$ and the fully expanded jet Mach number $M_j = 1.44$ of a convergent nozzle (design Mach number $M_d = 1$). Their Cartesian domain contains more than 5 million grid points and is stretched to refine the shear layers. To treat the sub-grid scales, a compact low pass filter is applied together with a second order TVD based dissipation to treat shocks.

A screech containing LES of a round jet was first reported by Imamoglu & Balakumar [2003] based on a fifth order Weighted Essentially Non Oscillatory (WENO) spatial discretization and a third order total variation diminishing (TVD) Runge–Kutta scheme for the time advancement. The fully expanded jet Mach number is $M_j = 1.43$ with a sonic design Mach number. Shock cell structure and screech frequency are in agreement to experimental data without comparing the screech amplitude.

Loh et al. [2003], Loh & Hultgren [2006] use a second order finite volume method to simulate screech of a round nozzle with an unstructured hexahedral grid with a second order time integration. Based on a fully expanded jet Mach number $M_j = 1.42$ they observe the flapping B-mode.

The helical C-mode was investigated by Hashimoto et al. [2004] with a LES of a round jet and a Mach number of $M_j = 1.7$ with a design Mach number of $M_d = 1.33$ (under-expanded, convergent-divergent (CD) nozzle). Spatial discretization is performed with a fourth order WENO scheme and a third order Runge–Kutta method for the time advancement. Their grid contains more than six million grid points with a Reynolds number of $Re = 580000$

In 2006, Bodony et al. simulate the noise radiation of a $M_j = 2.2$ round jet with a design Mach number of $M_d = 1.95$ (under-expanded). In this Mach number regime screech tones are not present and only shock associated and mixing noise can be observed. Based on the fully expanded jet Mach number and jet diameter a Reynolds number of $Re = 394000$ is adjusted using a cylindrical grid containing one million grid points.

A round over-expanded jet ($M_j = 1.49$, $M_d = 2.0$) was investigated, as well as an under-expanded jet ($M_j = 1.19$, $M_d = 1.0$), by Singh & Chatterjee [2007] using a WENO scheme.

Using an explicit spectral-like filtering of the flow variables, Berland et al. [2006, 2007] aim to minimize the dissipation on the resolved scales by adjusting the filter close to the grid cutoff wavenumber. Thereby, the effective Reynolds number of the inlet condition can be maintained [Bogey & Bailly, 2005]. In their investigation on planar under-expanded jet screech computation they simulate a Reynolds number of $Re_h = 60000$ based on the jet height and the fully expanded jet Mach number $M_j = 1.55$ (convergent nozzle, $M_d = 1$). A total of 16 million grid points are used on a Cartesian grid discretized with explicit fourth order schemes in space and time. To avoid numerical instabilities at discontinuities, like shocks, they apply a selective filter [Bogey et al., 2009]. Their results on screech frequency and amplitude are in good agreement to analytical and experimental data. The observed discrepancies are addressed to the computational geometry and initial shear layer thickness.

Later, de Cacqueray [2010], de Cacqueray et al. [2011] computed a high supersonic round jet with a fully expanded jet Mach number $M_j = 2.83$ at over-expanded conditions with a design Mach number $M_d = 3.3$. This Mach number regime is outside the range where screech can be observed, hence only shock associated noise and turbulent mixing noise is considered. The Reynolds number, based on the jet exit conditions, is set to $Re_D = 94000$ and simulated with the same methods as in the previous mentioned work using 27 million grid points. Spectral acoustic properties are in good agreement with experimental data. Using the acoustic analogy based on the Linearized Euler Equations (LEE) the acoustic information could be extrapolated into the acoustic far-field.

Based on the FWH analogy, Shur et al. [2010] used a $M_j = 1.36$ round and under-expanded jet, to capture the far-field acoustics including the screech tone. Recently, Gao & Li [2011] computed the axisymmetric mode of a round $M_j = 1.19$ under-expanded jet with roughly ten million grid points. A wide range of Mach numbers ($1.22 \leq M_j \leq 1.71$) is investigated recently by Munday et al. [2011] for a round over- and under-expanded jet. They use a nozzle including chevrons to reduce jet screech based on a finite element code including 11 million grid points.

Unsteady Reynolds Averaged Navier–Stokes The first investigation to apply a URANS to jet screech computations was performed by Shen & Tam [1998]. They observed both axisymmetric screech modes (A1 and A2) in a Mach number range of ($1.0 \leq M_j \leq 1.2$) with a convergent nozzle. They also investigate the influence of the temperature and the nozzle lip thickness on screech tones in Shen & Tam [2000] and conclude that there is no strong influence of the temperature and lip thickness on screech tones for the low Mach number range. Later, Shen & Tam [2001, 2002] extend the Mach number range up to $M_j = 1.5$ to also capture the flapping B- and helical C-mode. Their results regarding screech amplitude and frequency are in good agreement to experimental data and they found that two screech tones can exist simultaneously at one Mach number. They also mention that the present method is not capable to predict broadband shock associated noise and that empirical constants of the turbulence model need to be adjusted to match the analytical results.

A similar setup was studied by Li & Gao [2004, 2005] in a Mach number range of $1.05 \leq M_j \leq 1.2$ where they could observe the A- and B-mode. To observe also the C-Mode, the Mach number range was extended up to $M_j = 1.6$ in Li & Gao [2007] and the helical behavior could be observed.

Gao & Li [2006] use a similar method and investigate the influence of the screech tone to the initial shear layer thickness for the low Mach number regime (M_j = 1.1). They observe that the a thin shear layer produces a 5 dB louder screech tone than a thick shear layer as the thin shear layer is responsible for steeper velocity gradients and hence stronger shocks. To this end, they propose to reduce screech tones by enhancing the shear layer thickness.

Kim & Lee [2007], Kim & Nakamura [2006] investigate the influence of the nozzle lip to the screech tone and observe that a larger nozzle lip increases the screech frequency. This phenomenon can be explained with an increased momentum thickness for a larger nozzle lip due to the stronger reflections at the thick nozzle lip. The better the reflection properties, the larger the pressure fluctuations at the nozzle exit an hence the larger the momentum thickness. A thicker shear layer will reduce the effective nozzle diameter and therefore increase the screech frequency (reduce the sock cell spacing and reduce the screech wavelength) while keeping the jet Mach number constant (only depending on the nozzle pressure ratio).

Over- and under-expanded jets were investigated by Ray & Lele [2007] and the acoustic field was extrapolated with the LEE method. They found that the higher-frequency sound was missing in their computations which might have its origin in the intense modeling assumptions.

Recently, Kurbatskii [2011] investigated screech with a general purpose second order finite volume CFD code in the Mach number range of $1.3 \leq M_j \leq 1.6$ for a convergent nozzle. He could capture the screech frequency of the B- and C-mode in good agreement to experimental data, while the amplitudes differ with more than 10 dB. In addition to that, he observed an extended Mach number range for the B-mode (up to M_j = 1.6 compared to M_j = 1.4 of the experimental data).

Other methods Besides the three above mentioned classes, another small class emerged using the Euler equations instead of the Navier–Stokes equations. Hence, friction dependent influences are neglected and a comparison to real flows is difficult. Lee et al. [2004] investigate screech tones from an under-expanded axisymmetric jet using the two-dimensional Euler equations with a grid containing a total of 160000 points solved with fourth order schemes in space and time. For the lower Mach number range $1.08 \leq M_j \leq 1.19$ a good agreement to experimental data can be found whereas the influence on the nozzle lip thickness does not match the experimental data. A similar setup is used by Fujimatsu & Misu [2005].

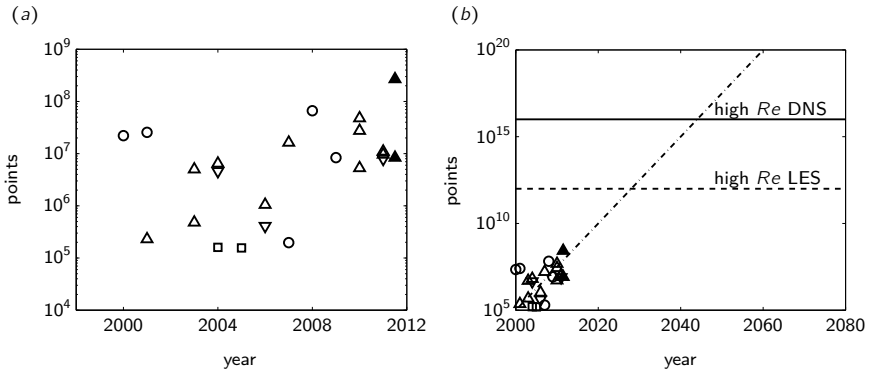

Figure 2.1: Total number of grid points of the numerical investigations of supersonic jet noise within the last decade (a). Divided in numerical method: ○ DNS; △ LES; ▽ URANS; □ Euler equations. Filled symbols: current computations. (b) Data extrapolated (-·-·-·-); Number of grid points for a high Re LES (- - - - - -); Number of grid points for a high Re DNS (———).

Men'shov & Nenashev [2011], Men'shov et al. [2008] use the three-dimensional Euler equations in combination with a linear stability analysis to extract the helical mode of a $M_j = 1.7$ under-expanded jet. A comparison of the numerical results to experimental data shows a strong discrepancy in screech frequency and amplitude although the helical mode is extracted.

In Fig. 2.1(a) an overview of the size of the numerical investigations on supersonic jet noise is presented for the last decade. Despite some spikes, like the DNS computations of Freund [2001], Freund et al. [2000], an exponential growth of the computational expense (total number of grid points) over the last decade is visible. This observation coincides with Moore's law and the exponential growth of the number of transistors which can be placed on one CPU. Extrapolating this trend (cf. panel (b)), one would expect the ability to solve a high Reynolds number jet with an LES (10^{12} points) in 2030 and with a DNS in 2045. This extrapolation is more optimistic than the assumption of Spalart [2000] that a high Reynolds number DNS will be available in 2080. The current LES computations, as presented in Sec. § 4, are marked with a filled symbol. The high resolution case exceeds the recent computations by one order of magnitude but match the exponential trend.

2.2 Equations of motion

As we have seen in the previous introduction, there is a number of methods available in the literature to treat supersonic jet noise computations. In the present application, we will use the three-dimensional compressible Navier–Stokes equations in combination with a high order dissipative upwind scheme applied to the convective terms and a high order central scheme applied to the diffusive terms to solve the flow induced noise directly. As the upwind schemes are dissipative, they behave like a filter applied to the flow variables. To this end, the present method can be classified as a LES with explicit filtering as proposed by e. g. Bogey & Bailly [2009], Mathew et al. [2006, 2003]. However, as the Reynolds number of the investigated jet noise computations is small ($Re_D = 5000$) and the spatial resolution is high, the large scale computations can be considered as an under-resolved DNS as the solution tends uniformly towards the DNS once the grid is refined [see Mathew et al., 2006, 2003].

In the following section the governing equations of motion, as implemented in the present investigation, are presented.

2.2.1 Compressible Navier–Stokes equations

The perturbations of an unsteady fluid flow are described by the Navier–Stokes equations. They are divided in three equations: the mass conservation, the balance of momentum and the balance of energy. All three equations are highly nonlinear and coupled with each other. Following the derivations in Kovasznay [1953], it is possible to decouple the Navier–Stokes equations when one applies a linearization of small perturbations around a base-flow. The three distinctly different modes are: vorticity mode, entropy mode and sound-wave mode. To this end, the three-dimensional compressible Navier–Stokes equations are written in non-conservative pressure p, velocity u_i and entropy s formulation and read:

$$\frac{\partial p}{\partial t} + u_i \frac{\partial p}{\partial x_i} = -\gamma p \frac{\partial u_i}{\partial x_i} + \frac{p}{C_v}\left(\frac{\partial s}{\partial t} + u_i \frac{\partial s}{\partial x_i}\right) \tag{2.1a}$$

$$\frac{\partial u_i}{\partial t} + u_j \frac{\partial u_i}{\partial x_j} = -\frac{1}{\rho}\frac{\partial p}{\partial x_i} + \frac{1}{\rho}\frac{\partial \tau_{ij}}{\partial x_j} \tag{2.1b}$$

$$\frac{\partial s}{\partial t} + u_i \frac{\partial s}{\partial x_i} = \frac{1}{\rho T}\left(-\frac{\partial}{\partial x_i}(-\lambda \frac{\partial T}{\partial x_i}) + \Phi\right) \tag{2.1c}$$

where

$$\tau_{ij} := 2\mu\left(s_{ij} - \frac{1}{3}s_{kk}\delta_{ij}\right) \tag{2.2}$$

$$s_{ij} := \frac{1}{2}\left(\frac{\partial u_i}{\partial x_j} + \frac{\partial u_j}{\partial x_i}\right) \tag{2.3}$$

$$\Phi := \tau_{ij}s_{ij} \tag{2.4}$$

and the Kronecker delta δ_{ij}. The effects of the bulk viscosity are neglected. To close the above set of equations the following thermodynamic relations are used. The fluid is modeled by dry air represented as a perfect gas:

$$p = \rho RT \tag{2.5}$$

with the gas constant $R = 287\ [\mathrm{m^2K^{-1}s^{-2}}]$ and the density ρ. The viscosity is modeled with Sutherland's law

$$\mu = \mu_0 \frac{T_0 + S}{T + S}\left(\frac{T}{T_0}\right)^{3/2} \tag{2.6}$$

using the following constants: $S = 110.4\ [\mathrm{K}]$ (Sutherland's temperature), and T_0 and μ_0 the total temperature and corresponding viscosity, respectively. Heat conductivity is, following Fourier's law, depending on the viscosity:

$$\lambda = \mu\frac{C_p}{Pr}. \tag{2.7}$$

with $\gamma = C_p/C_v = 1.4$, $C_p - C_v = R$ and $Pr = 0.71$.

2.2.2 Characteristic Formulation

The Navier–Stokes equations are written in a characteristic formulation. This has several advantages. First of all, the treatment of the boundary conditions in aeroacoustic applications is fairly easy since the commonly usual recalculation in characteristic variables is no more necessary. For a non-reflecting boundary condition simply the incoming acoustic wave is set to zero. Other boundary conditions like solid walls can be treated in a similar way as for codes written in primitive variables. Secondly, due to the decomposition of the flow equations in waves one can use upwind schemes, where the up- and down-traveling waves are discretized with up- and downwind schemes, respectively. Compared to commonly used central schemes, upwind schemes are numerically dissipative which increases the numerical stability and reduces

the use of additional filtering. The latter one can reduce the computational cost of the code. Anyway, up- and downwind discretization is applied each time the right hand side is evaluated, which is in each sub-step of the used time integration method (e. g. five stage Runge–Kutta). Additional filtering, used in classical implementations, is performed only after one completed time-step, and can be thus less expensive. Due to the fact that the code gains additionally numerical stability, the method of un-centered discretization is used in the present code implementation.

Following Sesterhenn [2000], the three-dimensional characteristic Navier–Stokes equations in p, u, s-formulation can be written as:

$$\begin{aligned}
\frac{\partial p}{\partial t} &= -\frac{\rho c}{2}\left((X^+ + X^-) + (Y^+ + Y^-) + (Z^+ + Z^-)\right) \\
&\quad + \frac{p}{C_v}\left(\frac{\partial s}{\partial t} + X^s + Y^s + Z^s\right) && \text{(2.8a)} \\
\frac{\partial u}{\partial t} &= -\left(\frac{1}{2}\left(X^+ - X^-\right) + Y^u + Z^u\right) + \frac{1}{\rho}\frac{\partial \tau_{1j}}{\partial x_j} && \text{(2.8b)} \\
\frac{\partial v}{\partial t} &= -\left(X^v + \frac{1}{2}\left(Y^+ - Y^-\right) + Z^v\right) + \frac{1}{\rho}\frac{\partial \tau_{2j}}{\partial x_j} && \text{(2.8c)} \\
\frac{\partial w}{\partial t} &= -\left(X^w + Y^w + \frac{1}{2}\left(Z^+ - Z^-\right)\right) + \frac{1}{\rho}\frac{\partial \tau_{3j}}{\partial x_j} && \text{(2.8d)} \\
\frac{\partial s}{\partial t} &= -\left(X^s + Y^s + Z^s\right) + \frac{R}{p}\Phi && \text{(2.8e)}
\end{aligned}$$

with the following abbreviations:

$$\begin{aligned}
X^\pm &:= (u \pm c)\left(\frac{1}{\rho c}\frac{\partial p}{\partial x} \pm \frac{\partial u}{\partial x}\right) && \text{(2.9a)} \\
Y^\pm &:= (v \pm c)\left(\frac{1}{\rho c}\frac{\partial p}{\partial y} \pm \frac{\partial v}{\partial y}\right) && \text{(2.9b)} \\
Z^\pm &:= (w \pm c)\left(\frac{1}{\rho c}\frac{\partial p}{\partial z} \pm \frac{\partial w}{\partial z}\right) && \text{(2.9c)}
\end{aligned}$$

$$X^v := u\frac{\partial v}{\partial x} \quad (2.10a) \qquad X^w := u\frac{\partial w}{\partial x} \quad (2.11a)$$

$$Y^u := v\frac{\partial u}{\partial y} \quad (2.10b) \qquad Y^w := v\frac{\partial w}{\partial y} \quad (2.11b)$$

$$Z^u := w\frac{\partial u}{\partial z} \quad (2.10c) \qquad Z^v := w\frac{\partial v}{\partial z} \quad (2.11c)$$

$$X^s := u\frac{\partial s}{\partial x} \quad (2.12a)$$

$$Y^s := v\frac{\partial s}{\partial y} \quad (2.12b)$$

$$Z^s := w\frac{\partial s}{\partial z} \quad (2.12c)$$

The speed of sound c is computed using the following relation:

$$c = \sqrt{\gamma R T} \quad (2.13)$$

Above equations are valid for Cartesian coordinates, only. The general case of curvilinear grids is presented in the appendix in Sec. § A.

2.3 Discretization

Especially in aeroacoustic applications (CAA) the choice of the temporal and spatial discretization is particularly important. The range of temporal and spacial scales in the aeroacoustic field spans several orders of magnitude. To this end, a high order of accuracy for the discretization is necessary. In the following two sections the methods used for the spatial and temporal discretization are presented.

2.3.1 Space discretization

The spatial discretization in the present work is based on finite differences in an implicit formulation. These compact schemes are modified Padé methods of high order of accuracy using a small stencil. They show a low dispersion error – an important feature especially for aeroacoustic applications. The spectral-like resolution of these methods captures short length scales better than standard finite differences [Lele, 1992]. In the last years, compact finite differences developed to a standard tool not only in the field of aeroacoustics [see amongst many others, Ghosh et al., 2011, Jones et al., 2010, Mitchell

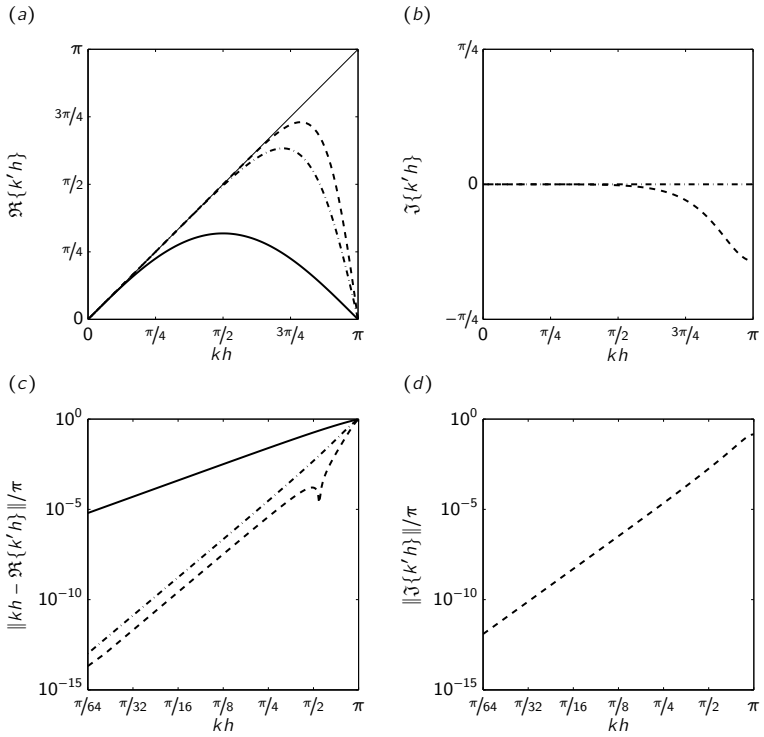

Figure 2.2: Modified wavenumber for the compact fifth order upwind scheme Adams & Shariff [1996] (- - - - - -) and the compact sixth order central schemeLele [1992] (-·-·-·-). (*a*) Dispersion. (*c*) Dispersion error. (*b*) Dissipation. (*d*) Dissipation error.

et al., 1995, Tam & Webb, 1993]. In the following section, two different compact schemes, implemented for the present simulations, will be summarized.

2.3.1.1 Compact schemes

The hyperbolic part of the Navier–Stokes equations is decomposed into plane characteristic waves. Based on the direction of the wave, they are discretized with a fifth order upwind scheme of Adams & Shariff [1996] (CLUD). The remaining terms of the Navier–Stokes equations (heat–flux and friction terms) are of parabolic nature and are discretized with a sixth order central scheme studied by Lele [1992]. Both schemes are characterized by a low dispersion

	Lele [1992]	Adams & Shariff [1996]
α_{-2}	0	0.027844800835984
α_{-1}	$1/3$	0.455868829489
α_0	1	1.0
α_1	$1/3$	0.4774791908094
α_2	0	0.038825537571968
a_{-2}	$1/36$	−0.118727423955
a_{-1}	$7/9$	−0.7482059425882
a_0	0	0.00052666822731662
a_1	$7/9$	0.7184558284235
a_2	$1/36$	0.1479508698924

Table 2.2: Coefficients used for the compact schemes of Eq. (2.14) on a periodic domain (interior points). Central tridiagonal scheme, sixth order: Lele [1992]; Upwind penta-diagonal scheme, fifth order: Adams & Shariff [1996].

error which can be seen in Fig. 2.2(a). In the field of CFD and CAA these schemes with its spectral like resolution have become popular and are used for many aeroacoustic applications.

Central schemes come up with no numerical dissipation (cf. Fig. 2.2(b)). Hence, on an under resolved grid, numerical instabilities can grow. A usual fashion, to handle these instabilities is to filter the solution aver several time–step. In the present investigation the upwind schemes undertake this task. They exhibit a dissipative behavior for high wave numbers (cf. Fig. 2.2(b)) and an additional filter is only necessary for special purposes, like extremely under resolved or discontinuous applications.

Compact schemes, to obtain the first derivative f'_i of a function f_i at the location x_i, whether upwind or central, can be written as:

$$\sum_{\mu=-\mu_l}^{\mu_r} \alpha_\mu f'_{i+\mu} = \frac{1}{h} \sum_{\nu=-\nu_l}^{\nu_r} a_\nu f_{i+\nu} \tag{2.14}$$

with the coefficients α_μ and a_ν. If the coefficients $\alpha_\mu = \alpha_{-\mu}$ and $a_\nu = a_{-\nu}$, one obtains a central scheme and apart from that an upwind scheme. In Tab. 2.2, the coefficients for the two schemes, used for the present discretization on a periodic domain, are presented. As compact schemes are implicit, a system of equations has to be solved to obtain the derivative f'_i of a function f_i at the location x_i. By means of a LU decomposition, followed by one forward and

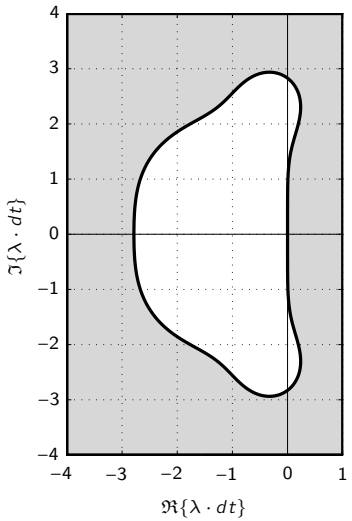

Figure 2.3: Stability map of the fourth order Runge–Kutta time integration. Eigenvalues in the white area are stable; unstable in the gray area.

one backward elimination, the system of equations can be solved efficiently with $\mathcal{O}(n)$ operation. One has to note that for the computation of the derivative, the data of the entire direction has to be accessible. This circumstance makes special demands on the parallelization of the code (cf. § 2.5).

2.3.2 Time discretization

The time integration method is a crucial factor for performance of the code. Its stability properties restrict the time-step and can, depending on the application, slow down the whole performance of the code drastically. Different time integration methods offer different stability maps, in which the eigenvalues and its corresponding modes of the evolution operator can be propagated without numerical instabilities. Due to implementational issues of the parallelization, the time integration is restricted to explicit methods. In the field of CFD the fourth order Runge–Kutta time integration method of Williamson [1980] has established to be one of the standard time integration schemes. Its stability map is presented in Fig. 2.3.

This method is able to capture both acoustic (on the positive and nega-

tive imaginary axis) and damped eigenvalues (on the negative real axis). For most applications in the field of CFD and CAA this stability area is sufficient unless no highly damped eigenvalues appear. The reason for such eigenvalue are either extremely low Reynolds numbers or other numerical effects, usually introduced through source terms. One could be a dissipative shock capturing method, like an artificial hyperviscosity [Cook & Cabot, 2005]. Another alternative is a porous medium. The latter one is implemented in the present code and needs a time integration method with an extended stability area.

In many cases, the source of the temporal stiffness lies in the linear terms of the governing equations. In this case, a more accurate description of the linear solution operator (the matrix exponential for the autonomous case) has the potential to greatly alleviate the time-step restrictions. Due to the large number of degrees of freedom in high-performance fluid simulations, the explicit calculation (and formation) of the matrix exponential is impractical; rather, a significantly lower-dimensional approximation based on iterative techniques is sought. This approximation represents the matrix exponential in a low-dimensional Krylov space using a polynomial ansatz. The Krylov subspace is formed by a repeated application of the linear (or linearized) system matrix to a given starting vector. In this Krylov basis, the matrix exponential can then be computed by direct methods.

The method of integrating a general system of ordinary differential equations (ODEs) using Krylov subspaces techniques is by no means new. It has been shown Hochbruck et al. [1998] that various techniques can be devised that provide approximations of different accuracy and error bounds. A comprehensive review of the techniques and their implementation is given in Gallopoulos & Saad [1992], Saad [1992] and Sidje [1998]. Specific applications to fluid dynamic equations, in particular, the incompressible Navier-Stokes equations, have been reported by e.g. Saad & Semeraro [1991] or Newman [2003] where the linear system matrix has been extracted from a finite-elements discretization combined with a projection method. Numerical software for the implementation of exponential integrators based on Krylov subspaces is also available: the *EXPOKIT*-package provides various implementation and error estimates Sidje [1998].

Although the general techniques has been developed and implemented for general systems of ordinary differential equations and for simplified (incompressible) flow situations, the exponential integration technique based on Krylov subspaces has not yet found wide-spread use in more challenging (compressible) fluid simulations where multi-scale effects combined with commonly used explicit techniques represent the bottleneck for more efficient large-scale simulations. This section will give an overview over the theory of integrating

linear and nonlinear ODEs in time with an exponential Krylov scheme. A more detailed review can be found in Schulze et al. [2009b] which is used as a basis for this section.

2.3.2.1 Theory of Exponential Krylov Time Integration

The exponential time integration with on Krylov subspaces is based on a low-dimensional approximation of the matrix exponential which represents the exact evolution operator for an autonomous linear system. For inhomogeneous problems minor modifications have to be implemented, as will be shown later. To start, however, we will consider the simplest case: the linear and autonomous problem. The linear theory will be applied to the adjoint compressible and porous Navier–Sokes equations as they are linear. The nonlinear theory of the subsequent paragraph unge be applied to the nonlinear compressible and porous Navier–Sokes equations.

Linear equations The solution of the linear and autonomous problem

$$\frac{\mathrm{d}\boldsymbol{u}(t)}{\mathrm{d}t} = \boldsymbol{A}\boldsymbol{u}(t) + \boldsymbol{q}(t), \tag{2.15a}$$

$$\boldsymbol{u}(0) = \boldsymbol{v} \tag{2.15b}$$

with system matrix $\boldsymbol{A}$, state vector $\boldsymbol{u}$, initial condition $\boldsymbol{v}$ and external driving $\boldsymbol{q}$ can formally be written as

$$\boldsymbol{u}(t) = e^{t\boldsymbol{A}}\boldsymbol{v} + \int_0^t e^{(t-s)\boldsymbol{A}}\boldsymbol{q}(s)\,\mathrm{d}s. \tag{2.16}$$

The first term involves the matrix exponential and represents the homogeneous part of the solution, whereas the second term consists of a convolution integral, again involving the matrix exponential, and represents the particular part of the full solution.

We will first consider the homogeneous case, i.e., the case where $\boldsymbol{q} = 0$, for which we need to compute the matrix exponential applied to a vector, $e^{t\boldsymbol{A}}\boldsymbol{v}$. If $\boldsymbol{A}$ is a bounded operator, which is the case for most fluid dynamic equations, the matrix exponential can be defined by a Taylor power series. For an unbounded operator, like an elliptic operator, the meaning of $\boldsymbol{A}$ comes from the mathematical theory of semigroups. A detailed discussion of this topic can be found in Trefethen [2005]. Since the present research project focuses on fluid dynamic equations, the solution of the matrix exponential will be

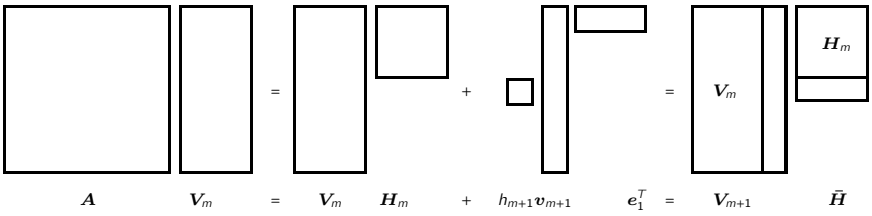

Figure 2.4: Arnoldi decomposition for a square matrix $\boldsymbol{A}$ with m subspaces $\boldsymbol{V}_m$ and the reduced Hessenberg matrix $\boldsymbol{H}_m$.

understood as an expansion series for the remainder of this discussion, like

$$e^{t\boldsymbol{A}}\boldsymbol{v} = \sum_{n=0}^{\infty} \frac{1}{n!} (t\boldsymbol{A})^n \boldsymbol{v}. \tag{2.17}$$

A straightforward approach to construct $e^{t\boldsymbol{A}}$ is thus a truncated form of (2.17). This is in fact the underlying principle of a Runge–Kutta (or any linear multi-step) scheme; in general, Runge–Kutta schemes approximate the first few terms of the above Taylor series expansion, but are not a recommended method – according to Moler & Loan [2003] – to approximate the matrix exponential. Better approximations can be found if we seek a general polynomial approximation of the product of the matrix exponential and a given vector of the form

$$e^{t\boldsymbol{A}}\boldsymbol{v} \approx p_{m-1}(t\boldsymbol{A})\boldsymbol{v} \tag{2.18}$$

with p_{m-1} denoting a general $(m-1)$-degree polynomial.

This approximation problem can be recast by introducing a m-dimensional Krylov subspace based on the starting vector $\boldsymbol{v}$ and the system matrix $\boldsymbol{A}$

$$\mathcal{K}_m = \text{span}\{\boldsymbol{v}, \boldsymbol{A}\boldsymbol{v}, ..., \boldsymbol{A}^{m-1}\boldsymbol{v}\}. \tag{2.19}$$

Our problem thus reduces to finding an element in the Krylov subspace $\mathcal{K}_m$ that best approximates the solution to the homogeneous initial-value problem. To efficiently manipulate the elements of the Krylov subspace we generate an orthonormal basis $\boldsymbol{V}_m = [\boldsymbol{v}_1, \boldsymbol{v}_2, ..., \boldsymbol{v}_m]$ of $\mathcal{K}_m$. This orthonormal basis is obtained by employing the well-known Arnoldi algorithm starting with the initial vector $\boldsymbol{v}_1 = \boldsymbol{v}/\beta$ where $\beta = \|\boldsymbol{v}\|_2$. Besides the orthonormal basis $\boldsymbol{V}_m$, the Arnoldi algorithm also produces an upper $m \times m$ Hessenberg-matrix $\boldsymbol{H}_m$

Input: initial vector $\boldsymbol{v}$
Output: Hessenberg matrix $\boldsymbol{H}$
Ritz vectors $\boldsymbol{V}$

1: $\beta = \|\boldsymbol{v}\|_2$
2: $\boldsymbol{v}_1 = \boldsymbol{v}/\beta$
3: **for** $j = 1$ **to** m **do**
4: $\quad \boldsymbol{p} = \boldsymbol{A}\boldsymbol{v}_j$
5: $\quad$ **for** $i = 1$ **to** j **do**
6: $\quad\quad h_{i,j} = \boldsymbol{v}_i^T \boldsymbol{p}$
7: $\quad\quad \boldsymbol{p} = \boldsymbol{p} - h_{i,j}\boldsymbol{v}_i$
8: $\quad$ **end for**
9: $\quad h_{j+1,j} = \|\boldsymbol{p}\|_2$
10: $\quad \boldsymbol{v}_{j+1} = \boldsymbol{p}/h_{j+1,j}$
11: **end for**

Algorithm 2.1: Arnoldi Decomposition.

which satisfies the relation (see also Fig. 2.4):

$$\boldsymbol{A}\boldsymbol{V}_m = \boldsymbol{V}_m\boldsymbol{H}_m + h_{m+1,m}\boldsymbol{v}_{m+1}\boldsymbol{e}_1^T \tag{2.20}$$

where, for a given k, $\boldsymbol{e}_k$ denotes the k-th unit vector belonging to $\mathbb{R}^m$, and h_{ij} stands for an element of the matrix $\boldsymbol{H}_m$.

The complete Arnoldi algorithm is outlined in Alg. 2.1. For the computation of the matrix $\boldsymbol{H}_m$ and the orthonormalized basis $\boldsymbol{V}_m$ only matrix-vector and scalar products have to be evaluated. As an input the algorithm requires the dimension of the Krylov subspace m, the initial vector $\boldsymbol{v}$ and the system matrix $\boldsymbol{A}$. Alternatively, the algorithm can be rewritten in a matrix-free form such that only the matrix-vector product $\boldsymbol{A}\boldsymbol{v}$ is used without explicitly forming or evaluating the system matrix $\boldsymbol{A}$.

Since we assume an orthonormal basis $\boldsymbol{V}_m$ of $\mathcal{K}_m$, we get $\boldsymbol{H}_m \approx \boldsymbol{V}_m^T\boldsymbol{A}\boldsymbol{V}_m$; in other words, $\boldsymbol{H}_m$ is a projection of the (large) system matrix $\boldsymbol{A}$ onto the Krylov subspace $\mathcal{K}_m$ using the orthonormalized basis $\boldsymbol{V}_m$. We can then form the vector $\boldsymbol{u}_{\text{opt}} = \boldsymbol{V}_m\boldsymbol{V}_m^T e^{t\boldsymbol{A}}\boldsymbol{v}$ which is a projection of $e^{t\boldsymbol{A}}\boldsymbol{v}$ onto $\mathcal{K}_m$. This vector is the best approximation of $e^{t\boldsymbol{A}}\boldsymbol{v}$ among the elements of the Krylov subspace $\mathcal{K}_m$. Furthermore, a reformulation of the optimal vector, using the definition of the orthonormal basis $\boldsymbol{V}_m$, leads to

$$\boldsymbol{u}_{\text{opt}} = \boldsymbol{V}_m\boldsymbol{V}_m^T e^{t\boldsymbol{A}}\boldsymbol{v} = \beta\boldsymbol{V}_m\boldsymbol{V}_m^T e^{t\boldsymbol{A}}\boldsymbol{V}_m\boldsymbol{e}_1. \tag{2.21}$$

The optimal vector still depends on the matrix exponential $e^{t\boldsymbol{A}}$ based on the (large) matrix $\boldsymbol{A}$, which is in practice unobtainable. However, owing to the orthogonality of the basis $\boldsymbol{V}_m$, we can introduce the following approximation

$$\boldsymbol{V}_m^T e^{t\boldsymbol{A}} \boldsymbol{V}_m \approx e^{t\boldsymbol{H}_m} \tag{2.22}$$

and finally rewrite the vector $\boldsymbol{u}_{\text{opt}}$ as

$$\boldsymbol{u}_{\text{opt}} \approx \beta \boldsymbol{V}_m e^{t\boldsymbol{H}_m} \boldsymbol{e}_1, \tag{2.23}$$

or, with the improved approximation including the residual in Eq. (2.20) with $h_{m+1,m}$,

$$\boldsymbol{u}_{\text{opt}} \approx \beta \boldsymbol{V}_{m+1} e^{t\boldsymbol{H}_{m+1}} \boldsymbol{e}_1. \tag{2.24}$$

The original problem — which was to compute $e^{t\boldsymbol{A}}\boldsymbol{v}$ with $\boldsymbol{A} \in \mathbb{R}^{n\times n}$ — has been replaced by evaluating $e^{t\boldsymbol{H}_m}\boldsymbol{v}$ with $\boldsymbol{H}_m \in \mathbb{R}^{m\times m}$ and $m \ll n$. For the reduced problem, the matrix exponential can be computed using highly accurate Padé methods [Moler & Loan, 2003].

It should be mentioned that the Arnoldi algorithm merely requires the *product* of $\boldsymbol{A}$ and $\boldsymbol{v}$ to compute $\boldsymbol{V}_m$ and $\boldsymbol{H}_m$; we thus do not explicitly need to know the system matrix $\boldsymbol{A}$ — which is the case for the present applications.

Contrary to the formulation above, the solution $\boldsymbol{u}(t)$ at a given time t is not computed directly, but rather advanced from the initial condition $\boldsymbol{v}$ via a time-stepping algorithm. The problem to be treated by the exponential time integration thus reduces to an initial-value problem over one time step $[t_n, t_n + \tau]$

$$\boldsymbol{u}(0) = \boldsymbol{v} \tag{2.25a}$$

$$\boldsymbol{u}(t_n + \tau) = e^{(t_n+\tau)\boldsymbol{A}}\boldsymbol{v} = e^{\tau\boldsymbol{A}}\boldsymbol{u}(t_n). \tag{2.25b}$$

For various flow configurations the system of governing equations is non-homogeneous, i.e., the source term $\boldsymbol{q}$ in (2.15) is nonzero. Examples include reacting fluids where the combustion terms are modeled as temperature-dependent source terms, or numerical boundary conditions such as an outflow sponge term that applies a highly dissipative force near the boundary which ensures that no (or negligible) energy is scattered back into the computational domain. In the present case, the linear adjoint Navier–Stokes equations are integrated backwards in time with this method. They contain a source term, arising from the objective function, which drives the adjoint peturbations backwards in time. The general solution for this problem is given in (2.16) and can be rewritten using the solution of the integral term

$$\boldsymbol{u}(t) = e^{t\boldsymbol{A}}\boldsymbol{v} + t\varphi(t\boldsymbol{A})\boldsymbol{q} \tag{2.26}$$

where $\varphi(z) = (e^z - 1)/z$. The resulting method

$$\boldsymbol{u}_{n+1} = e^{\tau \boldsymbol{A}} \boldsymbol{u}_n + \tau \varphi(\tau \boldsymbol{A}) \boldsymbol{q}(t_n), \quad t_{n+1} = t_n + \tau \tag{2.27}$$

is often called the (explicit) exponential Euler method. Exponential time-integration methods of Runge–Kutta type are studied in Hochbruck & Ostermann [2005].

If we use the following manipulation

$$\begin{aligned} \boldsymbol{u}(t_n + \tau) &= e^{\tau \boldsymbol{A}} \boldsymbol{u}(t_n) + \tau \varphi(\tau \boldsymbol{A}) \boldsymbol{q}(t_n), \\ &= (\tau \boldsymbol{A} \varphi(\tau \boldsymbol{A}) + \boldsymbol{I}) \boldsymbol{u}(t_n) + \tau \varphi(\tau \boldsymbol{A}) \boldsymbol{q}(t_n), \\ &= \tau \varphi(\tau \boldsymbol{A})(\boldsymbol{A} \boldsymbol{u}(t_n) + \boldsymbol{q}(t_n)) + \boldsymbol{u}(t_n), \end{aligned} \tag{2.28}$$

the only remaining expensive operation for the inhomogeneous case is to evaluate $\varphi(\tau \boldsymbol{A}) \boldsymbol{v}$ which can be approximated in a similar manner as $e^{\tau \boldsymbol{A}} \boldsymbol{v}$. We therefore obtain

$$\varphi(\tau \boldsymbol{A}) \boldsymbol{v} \approx \beta \boldsymbol{V}_m \varphi(\tau \boldsymbol{H}_m) \boldsymbol{e}_1. \tag{2.29}$$

The Krylov subspace approximation to $\varphi(\tau \boldsymbol{A}) \boldsymbol{v}$ converges toward the exact solution as fast as $e^{\tau \boldsymbol{A}} \boldsymbol{v}$ converges to its exact equivalent, see Hochbruck & Lubich [1997].

Following the formulation in Saad [1992], the function $\varphi(\boldsymbol{Z})$ of a matrix argument $\boldsymbol{Z}$ — or, more precisely, the product $\varphi(\boldsymbol{Z}) \boldsymbol{e}_1$ — can be computed using only one matrix exponential

$$\exp \begin{pmatrix} \boldsymbol{Z} & \boldsymbol{e}_1 \\ \boldsymbol{0} & 0 \end{pmatrix} = \begin{pmatrix} \exp(\boldsymbol{Z}) & \varphi(\boldsymbol{Z}) \boldsymbol{e}_1 \\ \boldsymbol{0} & 1 \end{pmatrix}. \tag{2.30}$$

This expression can be obtained by explicitly deriving the matrix exponential by a Taylor series expansion (cf. also Saad [1992]).

Nonlinear equations The exponential time-integration technique is based on a linear problem given by the system matrix $\boldsymbol{A}$. However, nonlinear governing equations are well within the reach of this technique. In particular, we want to apply the Krylov time-integration method to the nonlinear compressible porous Navier-Stokes equations, which calls for some small modifications. First, the equations have to be linearized about the current state vector, and, secondly, we need an approximation for the resulting Jacobian matrix $\boldsymbol{A}$.

We consider the general nonlinear initial-value problem

$$\frac{\mathrm{d}\boldsymbol{u}(t)}{\mathrm{d}t} = \boldsymbol{f}(\boldsymbol{u}(t)). \tag{2.31}$$

A Taylor expansion of the right-hand side about a given state $\boldsymbol{u}(t_n)$ yields

$$\boldsymbol{f}(\boldsymbol{u}(t)) = \boldsymbol{f}(\boldsymbol{u}(t_n)) + \frac{\partial \boldsymbol{f}}{\partial \boldsymbol{u}}(\boldsymbol{u}(t_n))(\boldsymbol{u}(t) - \boldsymbol{u}(t_n)) + \boldsymbol{r}(\boldsymbol{u}(t)) \tag{2.32}$$

with the remainder term $\boldsymbol{r}(\boldsymbol{u}(t))$and the Jacobian matrix

$$\boldsymbol{A} \equiv \frac{\partial \boldsymbol{f}}{\partial \boldsymbol{u}}(\boldsymbol{u}(t_n)) \tag{2.33}$$

The nonlinear governing equation can then be rewritten in the form

$$\frac{\mathrm{d}\boldsymbol{u}(t)}{\mathrm{d}t} = \boldsymbol{f}(\boldsymbol{u}(t_n)) + \boldsymbol{A}(\boldsymbol{u}(t) - \boldsymbol{u}(t_n)) + \boldsymbol{r}(\boldsymbol{u}(t)). \tag{2.34}$$

Introducing an integrating factor $e^{-t\boldsymbol{A}}$ in Eq. (2.34) and subsequently integrating over the interval $t \in [t_n, t_n + \tau]$, the solution $\boldsymbol{u}(t_n + \tau)$ at the new time-step yields

$$\boldsymbol{u}(t_n+\tau) = \boldsymbol{u}(t_n) + (e^{\tau\boldsymbol{A}} - \boldsymbol{I})\boldsymbol{A}^{-1}\boldsymbol{f}(\boldsymbol{u}(t_n)) + \int_{t_n}^{t_n+\tau} e^{(t_n+\tau-s)\boldsymbol{A}}\boldsymbol{r}(\boldsymbol{u}(s))\,\mathrm{d}s. \tag{2.35}$$

Equation (2.35) still depends on $\boldsymbol{A} \in \mathbb{R}^{n\times n}$ and represents an exact solution to problem (2.31). The integral term in Eq. (2.35) has to be evaluated numerically. Different methods based on quadrature rules like Runge–Kutta and multi-step methods are presented, e.g., in Tokman [2006] and Hochbruck et al. [1998]. Solving this integral term numerically will enhance the accuracy of the time-integration method at the expense of an increase in computational time. More precisely, depending on the specific case and the chosen approximation method for the integral, the computational time for the solution of the integral roughly matches the computational time for the approximated matrix exponential [see Tokman, 2006]. This raises the question whether the inclusion of this integral term is necessary for our specific fluid dynamic equations. It is shown in Schulze et al. [2009b] that omitting the integral is comparable to the error induced by a standard explicit Runge–Kutta method. Methods of this type are referred to as *exponentially fitted Euler methods* Hochbruck

et al. [1998] or *exponential Rosenbrock-Euler methods* Caliari & Ostermann [2009]

Using the same φ-function from the linear, nonhomogeneous case, $\varphi(z) = (e^z - 1)/z$, and setting the integral to zero, we can rewrite Eq. (2.35) and give an approximation for the solution at the new time-step as

$$\boldsymbol{u}(t_n + \tau) \approx \boldsymbol{u}(t_n) + \tau\varphi_1(\tau \boldsymbol{A})\boldsymbol{f}(\boldsymbol{u}(t_n)). \tag{2.36}$$

Employing the approximation of the matrix exponential in the φ-function, we obtain

$$\boldsymbol{u}(t_n + \tau) \approx \boldsymbol{u}(t_n) + \tau\beta \boldsymbol{V}_{m+1}\varphi_1(\tau \bar{\boldsymbol{H}}_{m+1})\boldsymbol{e}_1 \tag{2.37}$$

including the improved approximation with $\bar{\boldsymbol{H}}_{m+1} = \begin{bmatrix} \bar{\boldsymbol{H}} & 0 \end{bmatrix}$.

The Jacobian $\boldsymbol{A} = \frac{\partial \boldsymbol{f}}{\partial \boldsymbol{u}}(\boldsymbol{u}(t_n))$ of the system can be approximated using a first Fréchet derivative. However, we choose to implement the Arnoldi algorithm in a matrix-free form; we thus only need the matrix-vector product $\boldsymbol{Av}$ (see Alg. 2.1) which can straightforwardly be approximated by

$$\boldsymbol{Av} \approx \frac{\boldsymbol{f}(\boldsymbol{u} + \varepsilon \boldsymbol{v}) - \boldsymbol{f}(\boldsymbol{u})}{\varepsilon}. \tag{2.38}$$

The choice of ε in Eq. (2.38) can be influential on the stability of the simulation, in particular, for large systems, and has to be adapted judiciously for each case. For the numerical simulations presented in the next section, we chose the parameter ε according to

$$\varepsilon = \|\boldsymbol{u}\|_2 \sqrt{\varepsilon_{\text{machine}}} \tag{2.39}$$

which yielded satisfactory results.

The present method shows excellent stability properties and is capable to integrate stiff equations, like the porous Navier–Stokes equations of Sec. 3.1. In Fig. 3.2 of Sec. 3.1.4 these properties are presented in detail. In addition to that, the method is able to treat linear equation in an efficient way. This is especially important for the solution of the adjoint equations of Sec. 5.4.1, which are linear.

2.4 Including the nozzle

Supersonic jet screech is very sensitive to the shape of the nozzle geometry and may be even eliminated for certain geometries. Hence, embedding the

nozzle in the computational domain is of particular importance. Especially in computational aeroacoustics, where high order schemes combined with finite differences are used, the inclusion of solid boundaries is a challenging task. Within the last two decades several methods are developed to simulate the presence of solid objects with curved boundaries, like immersed-boundary methods or overlapping (chimera) grids.

In the following, a brief overview of the possible methods to include a nozzle for jet screech computations will be presented, beginning with a low order modeling of the nozzle by a velocity profile, followed by immersed boundary methods and finally chimera grids.

Velocity profile The presence of the nozzle can be modeled by a velocity profile without explicitly including the nozzle geometry in the computational domain. Instead, the velocity profile of the jet at the nozzle exit is modeled and included in the domain as an inlet boundary condition. However, the screech feedback mechanism which is amplified due to the reflections at the solid nozzle lip will not be considered using this approach. It is shown in Schulze et al. [2009a] that a jet with a nozzle modeled by means of a velocity profile only, does not produce screech tones.

When modeling the nozzle with a velocity profile, there is the option to force the screech feedback mechanism artificially [see Schulze et al., 2009a]. To this end, *microphones* (sensors) are placed in the upstream direction of the jet (only positions which amplify screech can be considered; see Eq. (1.16)) to capture the acoustic signal (pressure fluctuations) of the shock-associated jet noise. This signal is then used to force the instabilities in a small fringe region in the mixing layers at the nozzle exit. Hence, the feedback loop is closed and screech tones can be detected. Yet, it is not clear how to adjust the gain when transforming the measured signal into the forcing in the fringe region. To this end, the screech amplitude, in contrast to the screech frequency, can not be predicted properly.

Immersed-boundary These methods can be applied by introducing ghost points inside the solid domain (which is included in the Cartesian computational grid) which are chosen such that the solid pressure boundary condition is satisfied [see Kurbatskii & Tam, 1997]. These methods also include the volume penalization techniques where the velocities inside the solid obstacle are forced to zero for fixed bodies or the velocity of the obstacle if it is moving to satisfy the no-slip condition [Kolomenskiy & Schneider, 2009, Schneider & Farge, 2005]. In the present study, a volume penalization method for the

compressible Navier–Stokes equations is implemented and presented in detail in Sec. § 3.

Overlapping grids The most challenging approach to include a nozzle in the computational domain is based on overlapping grids or also referred to as chimera grids. They use a set of grids, usually containing a curvilinear grid surrounding the solid body which is embedded in a Cartesian grid. The exchange of information between both grids is based on a three-dimensional spatial interpolation.

The interpolation is performed in an interpolation zone close to the boundary of the curvilinear grids. Depending on the order of interpolation, the width of this interpolation zone has to be at lest $n+1$ points, where n is the order of the interpolation. It is proposed by Guenanff et al. [2003] that a fourth order Lagrange interpolation is a good compromise between accuracy and computational cost. Based on a Lagrange interpolation in three dimensions, the values in the interpolation zone are updated within each iteration of the time integration method. Due to the closed feedback loop in the present application (screech) the information of the curvilinear grid and the Cartesian grid needs to be interpolated in both directions. Thus, a two-way coupling has to be applied. To increase the numerical stability of the interpolation method the Lagrange interpolation can be written in a barycentric formulation. For more information on the interpolation procedure in overset grid techniques see Schulze & Sesterhenn [2010a].

The main advantage of overset grid techniques compared to immersed boundary methods is the ability to obtain a smooth grid at the surface of the obstacle and to easily adjust the grid resolution to efficiently resolve the boundary layer. The main disadvantages of overset grid methods is the additional computational time due to the interpolation and the exchange of the interpolated data between the individual grids using MPI interfaces in highly parallelized environments [see Schulze & Sesterhenn, 2010b]. Another disadvantage of overset grid techniques is the creation of spurious waves at the interface of both grids and the increase of numerical dissipation based on the order of interpolation. The latter two phenomena will be addressed briefly in the following.

To this end, the linear convection-diffusion equation is solved on a one-dimensional computational domain with a one-way coupling of two overset grids. Spatial discretization is performed with a sixth order compact finite differentiation by Lele [1992] as used for the Navier–Stokes equations of the present investigation. Due to the interpolation between both overlapping

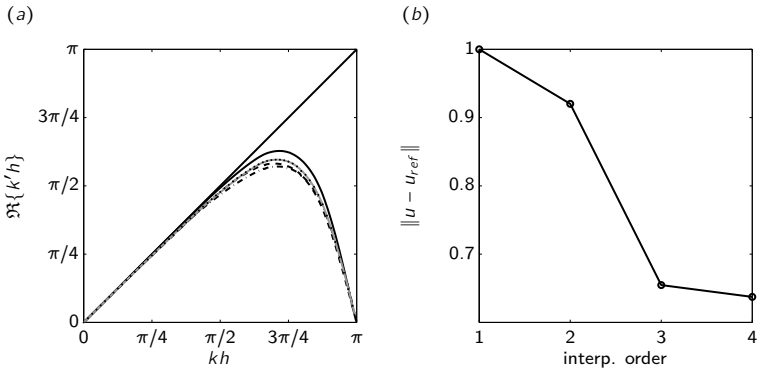

Figure 2.5: (a) Modified wavenumber for the sixth order compact finite differentiation by Lele [1992] for two overlapping grids including interpolation of different order. No interpolation (———); First order interpolation (-·-·-·-); Second order interpolation (- - - - - -); Third order interpolation (———); Fourth order interpolation (· · · · · · · ·). (b) 2-norm of the difference of the sixth order finite differences without interpolation to the one with interpolation. For various interpolation orders.

domains, the dispersion increases with decreasing order of interpolation. In Fig. 2.5(a) the combined modified wave number of the total system including the interpolation is presented as a function of the interpolation order. One can identify that the dispersion of the high wave numbers of a first order interpolation is larger compared to a higher order interpolation and decreasing for a second and third order interpolation. A further improvement of the dispersion error for high wave numbers, when increasing the interpolation order to four, can not be identified. In Fig. 2.5(b) the total error of a wave propagating through both domains is presented as a function of the interpolation order and scaled with the error of a first order interpolation. One can see that the error is decreasing monotonically with the inerplation order. An improvement of more than 25 % can be gained when changing a first order interpolation to a fourth order interpolation. It is also visible from that figure that additional benefit of a fourth order interpolation compared to a third order interpolation is less than 2 %. Combining both observations from panel (a) and (b) a third order interpolation may be a good compromise between accuracy and computational time.

To obtain a deeper inside in the numerical properties of the error related to the interpolation, the eigenvalues and -vectors of the combined differentiation and interpolation operator can be identified. In Fig. 2.6 both, the

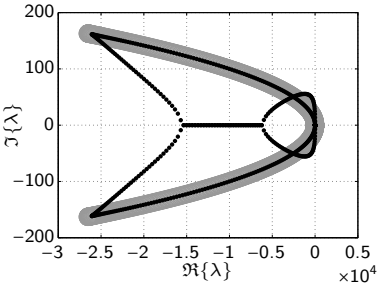

Figure 2.6: Eigenvalues of the linear convection diffusion operator, based on the sixth order compact finite differences by Lele [1992]. Gray circles (○): no interpolation; Black dots (•): fourth order interpolation.

eigenvalues of the discretization operator without interpolation and the combined operator including a fourth order interpolation are presented. Both operators show the characteristic behavior of a convection-diffusion operator. In the combined case, including interpolation, additional eigenvalues appear with both high frequency and low damping and also low frequency and high damping. Two characteristic eigenvalues of the combined operator are presented in Fig. 2.7(a) including their corresponding eigenvector in panel (b). The first eigenvalue is located close to the origin of the imaginary plane and marked with a black circle. The corresponding eigenvector in panel (b) is marked with a black curve. This eigenvalue connects both computational domains with the interpolation zone in the center of the two overlapping domains. No spurious reflections or discontinuities are visible. In contrast to that, is the second eigenvalue investigated. This eigenvalue lies on a branch, caused by the interpolation, and is marked with a gray circle. The corresponding eigenvector in panel (b) (gray curve) shows a solution separated by the two individual grids. On the left domain, the solution is zero whereas the solution on the right domain is characterized by a high frequent wave number with increasing amplitude towards the end of the domain. These modes on the additional branches, arising due to the interpolation, are responsible for spurious reflections at the domain interfaces. In CAA and especially in screech computations where an acoustic feedback is responsible for the dominant noise source, spurious frequencies close to the nozzle (interpolation zone of the curvilinear grid (cf. Schulze & Sesterhenn [2010b] for a possible setup of a nozzle with overset grid techniques) can strongly influence the investigated physical phenomenon.

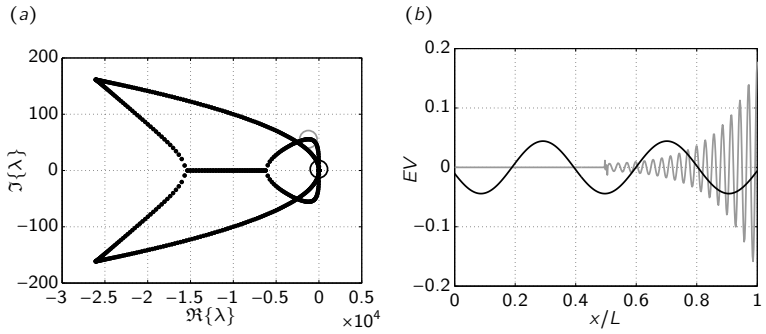

Figure 2.7: Eigenvalues of the linear convection diffusion operator, based on the sixth order compact finite differences by Lele [1992]. Black dots (•): fourth order interpolation. Eigenvalue marked by the gray circle (○) corresponds to the Eigenvector in (*b*) (———). Eigenvalue marked by the black circle (○) corresponds to the Eigenvector in (*b*) (———).

To this end, and due to the increased computational requirements, the method of immersed boundary methods (volume penalization) will be used in spite of the advantages of overlapping grid techniques.

2.4.1 Computational domain

Immersed boundary methods include the geometry as a space depended function in a Cartesian domain. In the present thesis, planar an round jets are investigated. In the round case, the Cartesian domain is non-periodic in all three directions. At the domain boundaries, specific numerical boundary conditions are applied which are addressed briefly in section § 2.4.3. To refine the grid in the areas with small scales, like in the turbulent areas of the jet, a grid stretching is applied in the two transverse directions (y and z; see § 2.4.2). In the planar case, one direction (here z) is supposed to be periodic and neither a grid stretching nor any boundary conditions are applied in that direction.

The definition of the nozzle and the method of immersed boundary methods (volume penalization) is presented in detail in § 3. A sketch of the Cartesian domain including the boundary conditions and the nozzle for the planar and round jet is presented in Fig. 2.8.

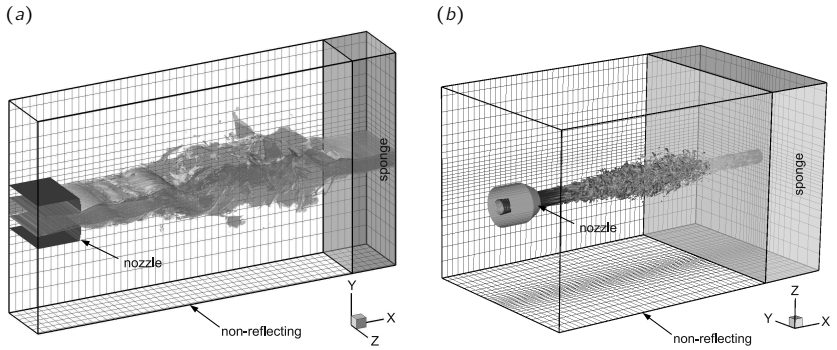

Figure 2.8: Sketch of the Cartesian domain including the boundary conditions (see § 2.4.3) and the nozzle of the planar jet (*a*) and round jet (*b*). Only every tenth grid point is shown.

2.4.2 Grid stretching

As mentioned already, different length scales can be found in a compressible turbulent flow, ranging from the smallest scales, the Kolmogorov length scale [Kolmogorov, 1962], to the largest scales, like a large coherent structure or a large acoustic wavelength. The smallest scales can be found in the turbulent areas, like the mixing-layer of a jet. The acoustic wavelength of a moderate Reynolds number flow is usually larger than the smallest turbulent scales. Audible acoustics lie in the range of 20 Hz to 20 kHz with the smallest corresponding wavelength for 20 kHz. Considering standard conditions (cf. Tab. 2.3) the wavelength for the upper bound of audible frequencies is $\lambda = c/f_{\max} = 17 \cdot 10^{-3}$ m. The smallest turbulent scale in a jet with $Re = 5000$ and a jet diameter of $D = 1$ m is $\eta = 1.7 \cdot 10^{-3}$ m, so one order of magnitude smaller than the smallest audible acoustic wave. Increasing the Reynolds number, this discrepancy becomes even larger (cf. Fig. 2.9). From a numerical point of view it is reasonable to use different spatial resolutions for the different flow regimes.

To this end, a grid stretching is implemented to refine the grid around the jet core and to coarsen the grid in the acoustic near-field. The grid stretching, as proposed by Anderson et al. [1984], can be expressed as:

$$y(\eta) = y_0 + \eta_c \left(\frac{\sinh(\tau_y(\eta - B))}{\sinh(\tau_y B)} + 1 \right) L_y, \tag{2.40}$$

with the offset y_0 and the length of the domain L_y. It is performed in the

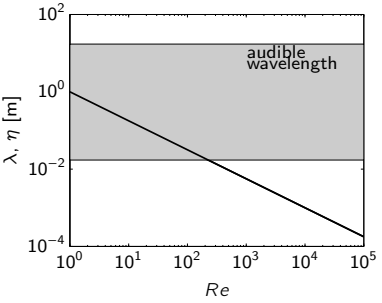

Figure 2.9: Kolmogorov scale for a jet with diameter D = 1m versus the Reynolds number (———). Gray area marks the audible wavelength range (corresponding to 20Hz < f < 20kHz). For a Reynolds number larger than $Re \approx 200$ the smallest turbulent scale is smaller than the smallest audible wavelength.

normal directions (y and z) of the jet with a free parameter τ_y and the center of the refinement η_c. The parameter B is defined as:

$$B := \frac{1}{2\tau_y} \ln\left(\frac{1 + (\mathrm{e}^{\tau_y} - 1)\,\eta_c}{1 + (\mathrm{e}^{-\tau_y} - 1)\,\eta_c}\right).$$

The choice of the two free parameters in the present jet computations is $\tau_y = 5$ and $\eta_c = 0.5$. A showcase of the grid stretching is presented in Fig. 2.10. In panel (a), the grid spacing is visualized, scaled with the equidistant grid spacing $dh = 1/(N-1)$. Hence, values smaller than one represent a refined grid whereas values larger than one a coarse grid. The values reach from 0.41 for the finest grid-spacing to 2.47 for the largest grid-spacing. Each point in this panel marks one grid point (here total number of points $N = 100$). One can see that the points are clustered around the center η_c. In panel (b), the physical space y versus the computational space η is visualized. Note, that all derivatives are evaluated in the computational space, so metric coefficients need to be computed in the transformed coordinates (cf. Sec. § A).

2.4.3 Boundary conditions

According to Colonius & Lele [2004], in CAA the implementation of robust and accurate boundary conditions (BC) is one of the most challenging aspects. A three-dimensional Cartesian domain has six boundaries which we will denote with Xp and Xm for the left and right boundary in the x-direction, respectively. A similar nomenclature exists for the y- and z-direction (cf. Fig. 2.11). In the present study, several numerical boundary

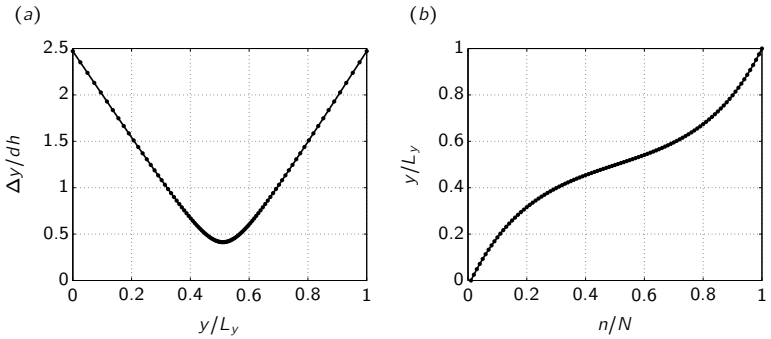

Figure 2.10: Grid stretching to refine the grid in the area of the jet core and to coarsen the grid in the acoustic near-field. Based on Eq. (2.40). (*a*) Grid spacing scaled with the equidistant grid spacing $dh = 1/(N-1)$ with the number of grid points N. Values smaller than one mark a refined grid. (*b*) Physical space versus computational space.

conditions are implemented to treat the aeroacoustic application properly. One can distinguish between two types of boundaries: a solid wall and an in- or outflow. From an acoustic point of view, the main difference between a wall and an outflow are the reflection properties. A solid wall reflects all acoustic waves whereas a perfect in- or outflow shall not reflect any acoustic waves. The latter type of boundary conditions are also referred to as *non-reflecting* boundary conditions.

2.4.3.1 Non-reflecting BC

At a non-reflecting boundary condition, one has to distinguish between a pure acoustic boundary with negligible aerodynamic fluctuations and a boundary where aerodynamic fluctuations dominate the flow. The latter one is typical for an outflow boundary whereas a pure acoustic boundary can be found in the acoustic far-field. These non-reflecting acoustic boundaries are usually based on a decomposition of the flow into characteristic waves [see Hedstrom, 1979]. With the decomposition, it is possible to identify the in- and outgoing waves depending on their sign. The unknown of a characteristic BC is usually the ingoing wave. For a non-reflecting BC the ingoing wave has to be zero such that all acoustic waves are leaving the domain without reflections. In a one-dimensional domain, these BC are exact and in a two- or three-dimensional space a good approximation. The standard approach to implement a non-reflecting BC is to first decompose the flow into characteristic waves, setting the ingoing wave to zero and then to recompute the

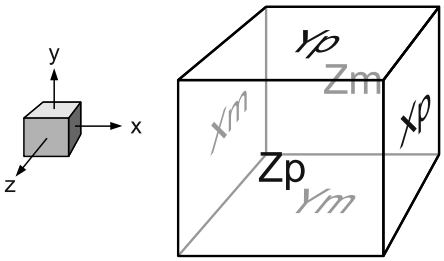

Figure 2.11: Nomenclature of the boundaries of the three-dimensional Cartesian domain. *Xp*lus for the right boundary and *Xm*inus for the left boundary in the x-direction. Similar for the y- and z-direction.

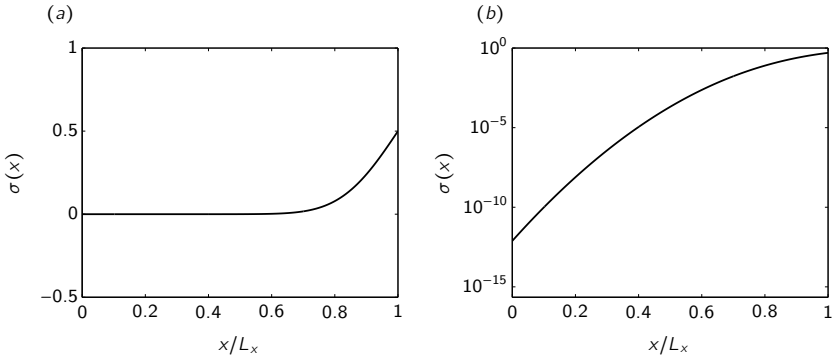

Figure 2.12: (a) Example of the sponge function $\sigma(x)$ of Eq. (2.42) with $L_{Xp} = 0.4L_x$ and $C_{Xp} = L_x$. (b) Logarithmic scaling.

waves into flow variables. In the present case, the flow variables are already decomposed into characteristic waves so that the numerical implementation of this BC is straightforward.

2.4.3.2 Fringe region (sponge)

Outflow boundaries need a special numerical treatment. Besides a reflected acoustic wave from the inside of the computational domain they can be responsible for spurious acoustic waves. The problem arises when large coherent structures, like vortices, are leaving the artificial boundary of the computational domain. They are responsible for loud noise sources once they get truncated by the boundary. To avoid these problems, a damping term is

added in a region upstream the boundary to absorb the aerodynamic fluctuations. Due to its physical interpretation, this BC is also referred to as a *sponge* BC. From a mathematical point of view this additional source term is added to the right-hand side of the Navier–Stokes equations and reads in symbolic form:

$$\frac{\partial \boldsymbol{q}}{\partial t} = \mathcal{N}(\boldsymbol{q}) - \tau_{sp}\sigma(\boldsymbol{x})(\boldsymbol{q} - \boldsymbol{q_0}) \tag{2.41}$$

with the flow state $\boldsymbol{q}$, the right-hand side of the Navier-Stokes equations $N(\boldsymbol{q})$, a spatially varying damping function $\sigma(\boldsymbol{x})$ and some reference state $\boldsymbol{q_0}$. The choice of $\boldsymbol{q_0}$, $\sigma(\boldsymbol{x})$ and the strength of the sponge τ_{sp} has to be done carefully to avoid numerical instabilities and acoustic reflections. Usually the reference state $\boldsymbol{q_0}$ is chosen to be the mean flow field. For linear equations $\boldsymbol{q_0}$ would be zero. The damping function $\sigma(\boldsymbol{x})$ has to be smooth to absorb aerodynamic fluctuations slowly. A fast increase of $\sigma(\boldsymbol{x})$ can be responsible for acoustic reflections. To this end, the damping function has to extend a large area and thus occupies a large area of the computational domain. Points in the sponge have no physical meaning and represent a computational overhead. To increase the computational performance an additional grid stretching can be applied in the area of the sponge (not performed in the present investigation).

The sponge function, as implemented in the present study, can be written as follows:

$$\sigma(x) = \frac{1}{2}\left(1 + \operatorname{erf}\left(\frac{2}{L_{Xp}}\left(x - C_{Xp}\right)\right)\right). \tag{2.42}$$

A sponge region can be also applied to boundaries in the acoustic far-field and can be combined with other numerical BC like the non-reflecting BC of Sec. § 2.4.3.1.

In the present investigation on round an planar jets, the sponge term is added at the outflow boundary Xp (cf. Fig. 2.8). The parameters for both jets are set to: $L_{Xp} = 10D$ and $C_{Xp} = L_x = 25D$ with the diameter/height of the nozzle D and the strength of the sponge $\tau_{sp} = 10^3$. The shape of the sponge function σ is presented in Fig. 2.12 with the present parameters.

2.5 Parallelization

As we have seen in Sec. § 2.6, the Kolmogorov scale is the smallest scale to resolve a DNS for reasonable Reynolds numbers. We have also seen that there is an upper limit for a feasible Reynolds number in the order of 10^4. In

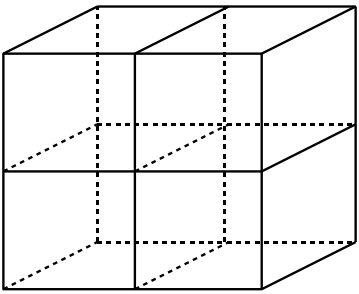

Figure 2.13: Decomposed domain in two dimensions (x and y) of a three-dimensional domain.

most technical applications, like supersonic jets of real aircraft, the Reynolds number is much higher. A real supersonic jet has a Reynolds number of the order of 10^7. To resolve a DNS of such a flow needs approximately $N \approx 10^{17}$ grid points, which corresponds to a memory requirement of approximately one million terabyte. Todays high performance hardware is equipped with about one hundred terabyte of main memory.

To get as close as possible to real flows, the use of high performance computing is indispensable. As high performance computers are parallel computers, the code is parallelized with a domain decomposition approach (cf. Fig. 2.13). Each processor/core solves the Navier–Stokes equations on a small part of the entire domain. Communication between the processors is necessary, especially when computing the derivatives. On the boundaries of a sub-domain the finite difference stencil needs information of the neighboring process. In the present investigation, communication is based on a hybrid approach using the Message Passing Interface (MPI) and the OpenMP libraries. Whereas the OpenMP is intended to communicate only between the cores of one processor/blade to avoid the memory-bottleneck for the memory consuming application. The three-dimensional domain is decomposed in two dimensions (x and y). In this plane, the MPI libraries are the underlying communication routines. In the third direction (z) the OpenMP libraries divide the outer loop in the shared memory of one multicore CPU.

For the case of compact finite differences, where a system of equations needs to be solved, data of an entire direction needs to be accessible. To this end, a special technique, to transform the domain in a certain direction, has to be performed. This method is presented in Fig. 2.14 for the x and y-direction (panels (a) and (b), respectively) and based on the methods in

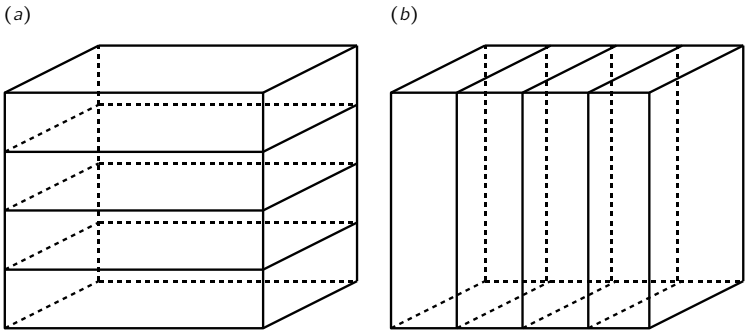

Figure 2.14: Transformation of the decomposed domain in two dimensions (x and y) of a three-dimensional domain. (a) For the discretization in the x-direction. (b) For the discretization in the y-direction.

Eidson & Erlebacher [1995]. All data in the decomposed domain is rearranged to access each process the information in a new sub-domain including one entire direction (x or y). Thereby, the total number of grid point allocated to one process is not changing to allow a balanced work load and to avoid deadlock. Eidson & Erlebacher [1995] mention, that for a periodic direction, the "chained" algorithm can be faster than the present "transpose" algorithm. In the work of Foysi [2005], both algorithm have been investigated, and it could be shown that the performance of both algorithms matches each other. To this end, only the transpose algorithm is implemented in the present code and highlighted in Alg. 2.2.

In Fig. 2.15 the performance of the code is visualized. It has been measured on two platforms with slightly different hardware. On the *HLRB-II*[1] and on the *HLRN-II*[2]. Two different test cases are investigated. A medium scale job with 64 million grid points and a large scale job with one billion grid points. For the medium scale job the code shows a nearly linear scaling on both platforms with up to 1024 cores (cf. Fig. 2.15(a)). In the large scale job an even superlinear scaling can be observed (cf. Fig. 2.15(b)). Due to resource limitations, this job is only measured at the *HLRB-II*.

[1] Leibnitz–Rechenzentrum (LRZ). SGI Altix 4700. `http://www.lrz.de/`
[2] Norddeutscher Verbund zur Förderung des Hoch- und Höchstleistungsrechnens (HLRN). SGI Altix ICE 8200 Plus (ICE2). `http://www.hlrn.de/`

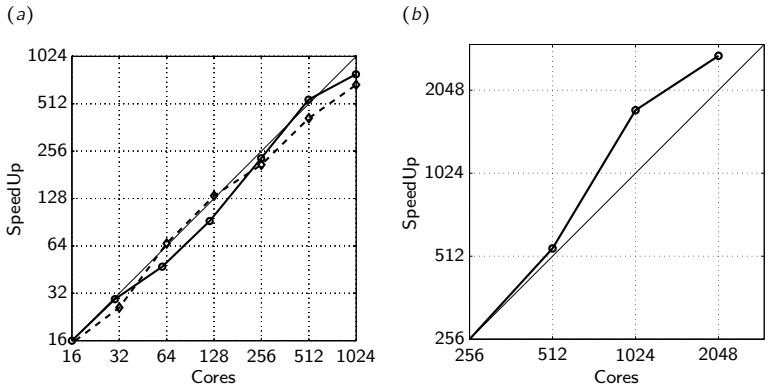

Figure 2.15: Speed-Up of the parallel code, measured on the *HLRB-II* (———) and the *HLRN-II* (- - - - - -). (*a*) Medium scale job with 64 million grid points. (*b*) Large scale job with one billion grid points (only *HLRB-II*).

Quantity	Unit	Value	Description
T_0	$[\mathrm{K}]$	293.15	temperature
p_0	$[\mathrm{Pa}]$	101325	pressure
μ_0	$[\mathrm{kg\,m^{-1}\,s^{-1}}]$	$1.7 \cdot 10^{-5}$	dynamic viscosity
R	$[\mathrm{J\,kg^{-1}\,K^{-1}}]$	287	specific gas constant
γ	$[\cdot]$	1.4	ration of specific heats

Table 2.3: Standard conditions for dry air, used in Fig. 2.16 before the shock (supersonic area).

2.6 Treating shocks

Shocks may appear in supersonic flows when the back pressure is increasing. They are characterized by a nearly discontinuous change in the characteristics of the fluid, like pressure, density and velocities. Especially shocks, which are orientated normal to the flow direction are sharp. Their width is approximately one order larger than the mean free paths of the fluid [Salas & Iollo, 1996]. For dry air under standard conditions (cf. Tab. 2.3) the mean free path of a gas molecule is 68nm = $68 \cdot 10^{-9}$m. In the four panels of Fig. 2.16, the profiles of the density, pressure, entropy and Mach number through a shock are presented. The shock is computed, based on the compressible Navier–

Input: field of one process $\mathbf{u}$
Output: transposed field $\mathbf{u_t}$

```
1: for p = 0 to np − 1 do
2:    m2 = n2/np
3:    for k = 1 to n3 do
4:       for j = 1 to m2 do
5:          for i = 1 to n2 do
6:             tmp1(i, j, k) = u(i, idest ∗ m2 + j, k)
7:          end for
8:       end for
9:    end for
10:   send tmp1 to idest
11:   receive tmp2 from idest
12:   for k = 1 to n3 do
13:      for j = 1 to m2 do
14:         for i = 1 to n2 do
15:            ut(i + idest ∗ n1, j, k) = tmp2(i, j, k)
16:         end for
17:      end for
18:   end for
19: end for
```

Algorithm 2.2: Transpose algorithm for the parallelization.

Stokes equations of the present chapter in one dimension for dry air under standard conditions (see Tab. 2.3). For the velocities, the pressure and the density, the interior shape of a weak shock [Crighton, 1986] is similar to a hyperbolic tangent profile [Taylor, 1910]. Pressure and density are increasing when passing the shock, whereas the velocity is decreasing from supersonic ($M > 1$) to a subsonic state ($M < 1$). The entropy, on the contrary, shows a non monotonically behavior. Its value increases to a maximum in the center of the shock and then decreases to its final value [Morduchow & Libby, 1949]. That the entropy is decreasing, one might notice a violation of the second thermodynamic law. However, the final value of the entropy after passing the shock has increased and the second thermodynamic law, valid for the entire system and not locally, is satisfied.

Following the theory of Taylor [1910], one can obtain an approximation, based on a linear theory, for the shock width. He also provided an expression

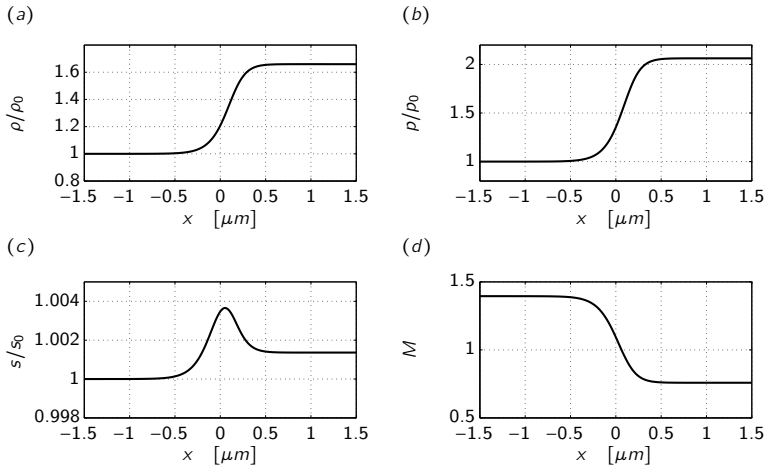

Figure 2.16: Computation of the shock profiles, based on the one–dimensional Navier–Stokes equations. (*a*) Density, (*b*) Pressure, (*c*) Entropy, (*d*) Mach number. The distance is measured in $\mu m = 10^{-6}\ m$. Shock width one order larger than the mean free path of the gas ($10{\cdot}68\ nm = 0.68 \cdot 10^{-6}\ m$).

for the velocity profile in the interior of the shock. A comparison of the linear theory and the results of the one-dimensional Navier–Stokes equations can be found in Fig. 2.17(*a*). The black dots represent the analytic solution and the solid line the numerical results. Both curves are in very good agreement, with only slight deviations in the subsonic part of the shock. Hence, the implemented numerical method is capable to capture resolved shocks. To answer the question, whether the investigated numerical method is able to resolve a sharp shock, two issues need to be addressed. (i) In the numerical experiments of the present work, the Reynolds number (viscosity, dimension) is usually small compared to real flows. What is the relation of shock width and viscosity? (ii) What is the resolution of a DNS?

To answer the first question, the theory of Taylor can be used to obtain an expression for the shock width depending on the dynamic viscosity. To obtain comparable results, instead of using the viscosity as a measure, the Reynolds number is used as a function of the viscosity, only. All other parameters (velocity, density and length-scale) are kept constant with the values of Tab. 2.3 and a length-scale of one meter. Following Taylors theory, the shock width scales linear with the viscosity or linear with the inverse of the

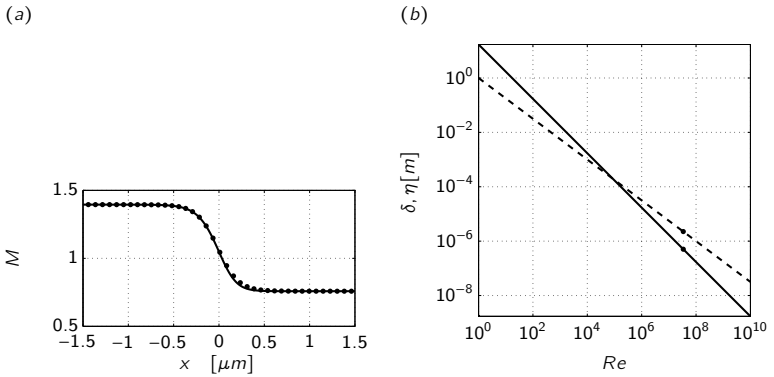

Figure 2.17: (*a*) Comparison of the Navier–Stokes computation with the linear theory of Taylor [1910]. *Black solid curve:* Navier–Stokes computation. *Black dots:* linear theory. (*b*) Shock width δ as a function of the viscosity (Reynolds number, under standard conditions and length-scale one meter) (black solid curve). Kolmogorov scale (dashed curve). Black dots mark the viscosity for dry air ($\mu = 1.7 \cdot 10^{-5}$ [kg m^{-1} s^{-1}]).

Reynolds number:

$$\delta \sim \mu \sim Re^{-1}.$$

The result is presented in Fig. 2.17(*b*) (solid line) where the dot marks the Reynolds number for dry air ($\mu = 1.7 \cdot 10^{-5}$ [kg m^{-1} s^{-1}]). In this point, the shock width is 0.64333 μm.

To answer the second question, the standard method to determine the resolution of the computational domain for a DNS, the Kolmogorov scale, is presented in the same figure (dashed line). The Kolmogorov length scales with [Pope, 2000]:

$$\eta \sim \mu^{3/4} \sim Re^{-3/4}.$$

Compared to the Kolmogorov scale, the shock width (solid line) decreases with a steeper slope, as it scales linear with the viscosity. For Reynolds numbers $Re < 10^5$, the shock width is larger than the Kolmogorov scale. For Reynolds numbers $Re > 10^5$, the shock width is smaller than the Kolmogorov scale [see also Sesterhenn et al., 2005].

Following Pope [2000], the resolution of a DNS or the number of grid points needed to resolve the Kolmogorov scale can be approximated as:

$$N \approx Re^{9/4}.$$

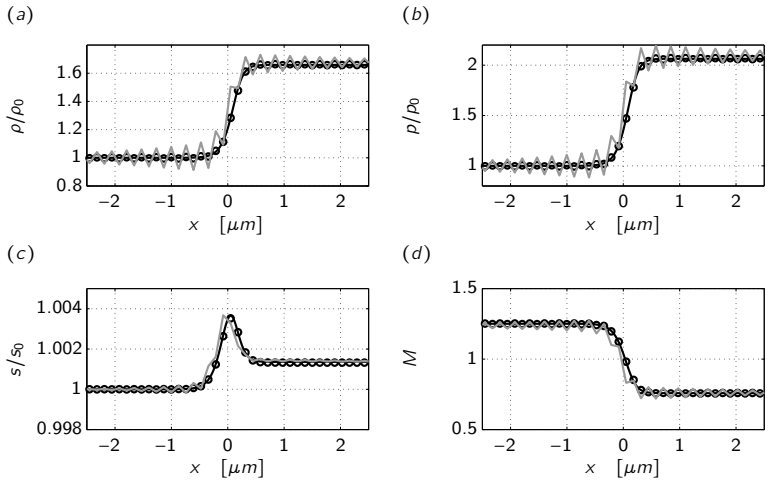

Figure 2.18: Computation of the shock profiles, based on the one–dimensional Navier–Stokes equations with different resolutions and filters. *Black solid line:* Same case as Fig. 2.16 computed with high resolution (approx. 50 points in the shock); no filter used. *Gray solid line:* low resolution (only 7 points in the shock). No filter used. *Black circles:* low resolution (only 7 points in the shock) with shock filter Bogey et al. [2009].

To resolve a cubic domain with an edge length of one meter and a Reynolds number of $Re = 10^4$, about one billion (10^9) grid points are needed. This is at present in 2011 the upper limit for large scale computations in the field of CFD. Hence, the upper limit of the Reynolds number to resolve the Kolmogorov scale is $Re = 10^4$. Consequently, as in this Reynolds number regime, the shock width is larger than the Kolmogorov scale, a DNS will resolve a shock.

However, in many applications with a high Reynolds numbers, it is too expensive to resolve the Kolmogorov scale or even the shock. Under these assumptions, the unresolved shock causes numerical instabilities due to spurious Gibbs oscillations and has to be treated separately. Different numerical methods (so called *shock–capturing methods*) have been designed over the last decades to address this issue, especially in the field of CAA with high order requirements. In the present work, an adaptive spatial filter is used, based on Bogey et al. [2009][3], to filter the spurious Gibbs oscillations. As the filter is adaptive, it detects the location of a shock, by means of the dilata-

[3] with the adjustable parameter $r_{th} = 10^{-5}$ and using the optimized filter F_{opt}

tion of the velocities as a measure, and applies the filter in this area, only. In Fig. 2.18, the same shock as in Fig. 2.16 is computed with a seven times lower resolution. Only seven points remain in the interior of the shock. Without any filter, the numerical result shows strong oscillations around the center of the shock (gray solid line). To compare the result, the high resolution case is presented with the black solid line. Although the under-resolved case shows strong oscillations, the correct shock jump in all quantities is reached. A small displacement of the center of the shock into the supersonic region is visible. In contrast to that, the result treated with the shock filter and the same low resolution, shows a very good agreement with the resolved case (black circles). No oscillations are visible and the correct shock jump and speed are preserved.

3

Theory of computing flow in porous media

In the literature, porous media are not only used to reduce aeroacoustic noise, but can be found in a series of flow control applications. For instance, Bruneau & Mortazavi [2008] controlled the vortex shedding of the flow past a cylinder with a porous coating. In another numerical study by Sandham & Luedeke [2009], the Mack mode was stabilized in a Mach 6 boundary layer flow by means of a porous surface.

The porous medium investigated in the present study, is modeled by a volume force, similar to Darcy's law for incompressible flow. For the present aeroacoustic application the volume force is implemented in the fully compressible Navier–Stokes equations leading to a new set of porous flow equations.

A porous medium can be characterized by only two parameters: the porosity ϕ and the permeability $\boldsymbol{K}$. Whereas ϕ describes the volume ratio of void space V_f to the volume of the whole porous material ($\phi = V_f/V$). Thus, a porosity equal to one represents void space only, and a porosity of zero a solid body, where no fluid can penetrate. The latter extreme causes a singularity in the porous flow equations, thus only values of $0 < \phi \leq 1$ are feasible.

The second parameter $\boldsymbol{K}$ stands for the permeability of the material and

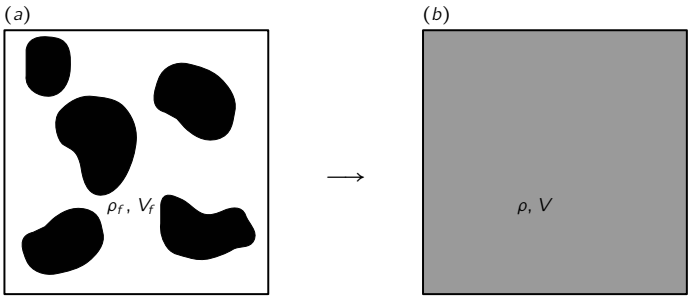

Figure 3.1: Replacing the density of the fluid ρ_f in a real porous medium (a) by the density ρ in a homogenized volume V (b). The porosity is defined as $\phi = V_f/V = \rho_f/\rho$.

is a symmetric and positive definite tensor [see e. g. De Wiest, 1969]:

$$\boldsymbol{K} = \begin{pmatrix} \kappa_{11} & \kappa_{12} & \kappa_{13} \\ \kappa_{21} & \kappa_{22} & \kappa_{23} \\ \kappa_{31} & \kappa_{32} & \kappa_{33} \end{pmatrix}$$

The entries in that tensor can reach values of zero for a material which is not permeable (solid) and infinity for a material with no influence on the fluid (zero drag, void material). To keep the freedom in the design process of the porous medium, the two coefficients ϕ and $\boldsymbol{K}$ are supposed to be functions of space and time. Anyway, since the realization of a time dependent structure of a porous medium for technical applications is hard to realize, only the space dependence will be considered ($\phi = \phi(\boldsymbol{x})$, $\boldsymbol{K} = \boldsymbol{K}(\boldsymbol{x})$).

To include a porous medium in the simulation, the equations of continuity, momentum and energy have to be modified. The main idea is based on a relation found by Darcy [1856] to relate the flow velocities and the pressure gradient with the permeability of the porous medium in a linear way. This relation, called Darcy's law, has been validated in several experiments and reads in the present terminology:

$$\boldsymbol{v} = -\frac{\boldsymbol{K}}{\mu} \nabla \boldsymbol{p}, \tag{3.1}$$

with the so called Darcy velocity $\boldsymbol{v} = \phi \boldsymbol{u}$. This additional volume force is added to the momentum equation and acts like a source term damping all velocities in the porous medium. In addition to that, the density of the fluid

Name	Material	Permeability [m^2]
Panacell 45 ppi	PU-foam	$2.4 \cdot 10^{-8}$
M-Pore Al 45 ppi	Metal-foam	$1.7 \cdot 10^{-8}$
M-Pore PU 45 ppi	PU-foam	$1.1 \cdot 10^{-8}$
Arpro	Synthetic foam	$7.4 \cdot 10^{-10}$
ArmaFoam Sound	Elastomer foam	$1.5 \cdot 10^{-10}$
Oil Rocks	Stone	$1.0 \cdot 10^{-11}$
Sandstone	Stone	$1.0 \cdot 10^{-13}$
Limestone Dolomite	Stone	$1.0 \cdot 10^{-15}$
Granite	Stone	$1.0 \cdot 10^{-17}$

Table 3.1: Permeability for different porous media. Adapted from Bear [1972] and Geyer et al. [2010].

in the porous medium, averaged in an infinitesimal small control volume, will change [Fulks et al., 1971]. It is related to the porosity:

$$\phi = \frac{V_f}{V} = \frac{\rho}{\rho_f}, \tag{3.2}$$

with the density and volume of the fluid, ρ_f and V_f, respectively, and V as the control volume (cf. Fig. 3.1). This second fundamental law for porous media has to be included in the whole derivation of the compressible porous flow equations.

The unit of the permeability is [m^2] and can reach values of a wide range. Darcy used his own unit to measure the permeability, called *darcy*. To convert from darcy to the S.I. area unit, we get: $1\,\text{darcy} = 9.8697 \cdot 10^{-13}\,\text{m}^2$ [see e. g. Bear, 1972]. Although the unit darcy is widely used in the literature, we will keep the S.I. unit in all following derivations. In Tab. 3.1, some examples of existing porous media are given.

In the literature, different ways to include Darcy's law can be found. Especially the choice of the velocities ($\boldsymbol{v}$ or $\boldsymbol{u}$) and the placement of the porosity ϕ is not unique. Most applications deal with the incompressible Navier–Stokes equations where terms simplify [see amongst others, Bruneau & Mortazavi, 2008, Kevlahan & Ghidaglia, 2001, Khadra et al., 2000]. In the compressible case, Liu & Vasilyev [2007] and Kramer et al. [2008] use a set of modified Navier–Stokes equations including Darcy's law. As they use a different formulation for the energy equation, without taking into account the transformation of kinetic energy into entropy, we will present the porous Navier–Stokes

equations for compressible flow, including an equation for the entropy in the following section.

3.1 Porous flow equations

The derivation of the compressible porous flow equations is based on the derivation in Fulks et al. [1971], yet with an additional energy equation. Replacing consequently the density ρ by $\phi\rho_f$ (3.2) and including Darcy's law (3.1), one obtains a set of porous flow equations for compressible fluids, based on the Navier–Stokes equations, including an equation for the energy. In what follows, we will omit the subscript $(\cdot)_f$ and relate all flow variables to the fluid.

3.1.1 Porous mass equation

The density, averaged over the volume V is simply $\rho\phi$ and the porosity can be $0 < \phi \leq 1$. To this end, the modified continuity equation reads:

$$\frac{\partial \phi\rho}{\partial t} + \frac{\partial \phi\rho u_i}{\partial x_i} = 0. \tag{3.3}$$

Although the time dependence of the porous material will not be considered in the optimization algorithm, the general assumption of a space and time dependent material will be used to derive the porous flow equations as they are not restricted to the optimization algorithm ($\phi = \phi(\boldsymbol{x}, t)$). In the present numerical analysis, the governing equations are based on the pressure p, the velocities u_i and the entropy s. To this end, the continuity equation is rewritten using Gibbs fundamental relation which reads:

$$T\mathrm{d}s = \mathrm{d}e - p\,\mathrm{d}\left(\frac{1}{\rho}\right), \tag{3.4}$$

with the specific entropy s, the specific internal energy e and the specific volume $v = 1/\rho$. Again, the density has to be modified for porous media, because only the part of the volume occupied by fluid is considered. With the internal energy $\mathrm{d}e = C_v \mathrm{d}T$ for an ideal gas, one obtains:

$$T\mathrm{d}s = C_v \mathrm{d}T - p\,\mathrm{d}\left(\frac{1}{\phi\rho}\right), \tag{3.5}$$

Note, that ϕ can be a function of space and time and can not be considered as constant. To eliminate the explicit dependence of the temperature from

Eq. (3.5), the modified relation for an ideal gas is applied which reads:

$$p = \phi\rho RT, \tag{3.6}$$

or in a variational formulation:

$$\mathrm{d}p = R(\rho T\,\mathrm{d}\phi + \phi T\,\mathrm{d}\rho + \phi\rho\,\mathrm{d}T), \tag{3.7}$$

with the specific gas constant R. Now, combining Eq. (3.3), (3.5) and (3.7) we end up with a continuity equation, written in pressure and entropy formulation:

$$\frac{\partial p}{\partial t} + u_i\frac{\partial p}{\partial x_i} = -\phi\rho c^2\frac{\partial u_i}{\partial x_i} + \frac{p}{C_v}\left(\frac{\partial s}{\partial t} + u_i\frac{\partial s}{\partial x_i}\right) \tag{3.8}$$

Setting $\phi = 1$ (no porous medium), one obtains the original continuity equation for an undisturbed fluid written in pressure and entropy formulation as in Eq. (2.1a). Consequently, this equation can be used for both, the porous domain and the void domain.

It is interesting to see that this formulation of the continuity equation is no more depending on the variation of the porosity as it is the case for Eq. (3.3). Form a numerical point of view, this is of particular importance, since ϕ can be a discontinuous function in space and time. Its derivative might be undefined and can be responsible for numerical instabilities. Especially in applications with mixed areas of porous media and void space, as in the present application, discontinuities of ϕ arise at every boundary of the porous material.

3.1.2 Porous momentum equation

To obtain the momentum equation, we follow the same strategy as for the continuity equation, by replacing the density with $\phi\rho$. Furthermore, the above mentioned Darcy term (Eq. (3.1)) is added to the right hand side to account for the viscous damping of the velocities in the porous medium, depending on the permeability of the material [as proposed by Wooding, 1957].

Finally, the momentum equation for a compressible fluid, including porous media, can be written as:

$$\frac{\partial u_i}{\partial t} + u_j\frac{\partial u_i}{\partial x_j} = -\frac{1}{\phi\rho}\frac{\partial p}{\partial x_i} + \frac{1}{\phi\rho}\frac{\partial \tau_{ij}}{\partial x_j} - \frac{\mu}{\rho}(K^{-1})_{ij}u_j, \tag{3.9}$$

with τ_{ij} as defined in Eq. (2.2). As for the continuity equation, this equation is also valid in the void domain with no porous medium, by setting $\phi = 1$ and $\boldsymbol{K} \to \infty \cdot \boldsymbol{I}$, with the identity matrix $\boldsymbol{I}$.

3.1.3 Porous energy equation

In the present study, the energy is expressed by the entropy. An expression for the entropy conservation can be obtained by subtracting the kinetic energy from the total energy and using Gibbs fundamental relation together with the conservation of mass. To this end, the equations for continuity (3.8) and momentum (3.9), multiplied by u_i (to obtain the kinetic energy), are combined with Gibbs fundamental relation (3.5), to obtain the entropy equation for porous media.

The total energy equation with modified density can be written as:

$$C_v \frac{DT}{Dt} + \frac{D}{Dt}\left(\frac{1}{2}u_i u_i\right) = \frac{1}{\phi\rho}\frac{\partial}{\partial x_j}\left(-pu_j + u_i\tau_{ij} + \left(\lambda\frac{\partial T}{\partial x_j}\right)\right) \tag{3.10}$$

Multiplying u_i to the momentum equation (3.9) leads to an expression for the kinetic energy, including Darcy's law:

$$\frac{D}{Dt}\left(\frac{1}{2}u_i u_i\right) = -\frac{1}{\phi\rho}u_i\frac{\partial p}{\partial x_i} + \frac{1}{\phi\rho}u_i\frac{\partial \tau_{ij}}{\partial x_j} - \mu\rho(K^{-1})_{ij}u_i u_j \tag{3.11}$$

Subtracting Eq. (3.11) from Eq. (3.10) reads:

$$\phi\rho C_v\frac{DT}{Dt} - p\frac{\partial u_i}{\partial x_i} + \frac{\partial}{\partial x_j}\left(\lambda\frac{\partial T}{\partial x_j}\right) + \Phi + \phi\mu(K^{-1})_{ij}u_i u_j \tag{3.12}$$

Finally, using Gibbs fundamental relation of Eq. (3.5), which can be rewritten in the following form:

$$\phi\rho C_v\frac{DT}{Dt} = \frac{\phi\rho T}{\gamma}\frac{Ds}{Dt} + \frac{1}{\gamma}\frac{Dp}{Dt} \tag{3.13}$$

leads to an expression for the entropy after some standard manipulations and reads:

$$\begin{aligned}\frac{\partial s}{\partial t} + u_j\frac{\partial s}{\partial x_j} = \frac{1}{\rho\phi T}\left(\frac{\partial}{\partial x_j}\left(\lambda\frac{\partial T}{\partial x_j}\right) + \Phi\right)\\ + \underbrace{\frac{\mu}{\rho T}\left(K^{-1}\right)_{ij}u_i u_j}_{①} - \underbrace{\frac{h_s}{\phi}(T - T_s)}_{②},\end{aligned} \tag{3.14}$$

with the dissipation function Φ as defined in Eq. (2.4) and the thermal conductivity λ as defined in Eq. (2.7). In Eq. (3.14), two additional terms, related to the porous medium, can be identified (marked with ① and ②).

The first term has its origin in the momentum equation (3.9) multiplied by $\boldsymbol{u}$, to obtain an expression for the kinetic energy. This term is in fact a $\boldsymbol{K}^{-1}$-norm ($\boldsymbol{u}^T\boldsymbol{K}^{-1}\boldsymbol{u}$), since $\boldsymbol{K}$ is a positive definite tensor, as is its inverse. Hence, it can be positive only and represents the entropy production due to the loss of kinetic energy in the porous medium. This entropy production is responsible for a temperature increase in the porous medium which can lead to particularly high temperatures.

Based on the above equations, the porous medium has the same thermodynamic properties as the fluid. In a technical application the porous medium is based e. g. on an aluminum foam. This foam will have a different heat conductivity and thus a modified temperature. In the present study, we assume a constant temperature of the porous medium T_s which is a good approximation for most metal foams, based on aluminum or even copper. To this end, the second term is added to the entropy equation with $h_s = C_s\tau_s^{-1}T_s^{-1}$. Whereas h_s is a specific heat transfer coefficient with a characteristic time scale and a characteristic specific heat C_s of the porous material. In the present investigation, the parameters are chosen as follows: $C_s = 897\,[\mathrm{Jkg^{-1}K^{-1}}]$ as for Aluminum and $\tau_s = 0.5\,[\mathrm{s}]$. The temperature of the porous medium T_S is equal to the ambient temperature of the fluid T_0 (here $300\,[\mathrm{K}]$).

If the approximation of a constant temperature is not feasible, it might be necessary to solve an additional heat conduction equation for the space and time dependent distribution of the temperature in the porous material. This equation would be a part of the system of coupled equations to solve and would consequently produce a corresponding adjoint equation for the adjoint temperature distribution in the adjoint porous medium which is not considered here.

Finally, the modified Navier–Stokes equations for porous media are closed with the thermodynamic relation for an ideal gas (Eq. (3.6)) and Sutherland's law to obtain the temperature dependent viscosity as in Eq. (2.6). The specific gas constant is $R = C_p - C_v = 287\,[\mathrm{J\,kg^{-1}\,K^{-1}}]$ with a constant ratio of specific heats $\gamma = C_p/C_v = 1.4$ and a constant Prandtl number $Pr = 0.71$.

The difference between the Navier–Stokes equations of Sec. 2.2.1 and the present porous Navier–Stokes equations is restricted to additional source terms and the modified density. Hence, the decomposition of the porous Navier–Stokes equations into characteristic waves can be performed in the same way as described in Sec. 2.2.2. For all following numerical computations, the compressible and porous Navier–Stokes equations of the present chapter will be used, together with the characteristic formulation. In applications, where no porous material is investigated, ϕ is set to one and the permeability is set to infinity with an isotropic behavior.

3.1.4 Numerical Implementation

The porous flow equations of section § 3.1.1–§ 3.1.3 can be implemented using the same methods as in Sec. § 2.3. Anyway, the time integration technique of Sec. § 2.3.2 plays an important role. Depending on the value of the permeability in Eq. (3.9), highly damped eigenvalues may appear in the evolution operator. These eigenvalues will be the most damped eigenvalues of the evolution operator when the Darcy term in the porous momentum equation dominates the convection and diffusion terms. One can obtain an analytical approximation for the porous dominated eigenvalue by only considering the momentum equation with the Darcy term and neglecting the convection and dissipation terms. The dominant term in the porous Navier–Stokes equations (3.8 - 3.14) will be $-\mu/\rho \boldsymbol{K}^{-1}\boldsymbol{u}$. According to that, the corresponding real valued eigenvalue is $-\mu/\rho(\boldsymbol{K}^{-1})_{ij}$ which is scaling with the inverse of $\boldsymbol{K}$. This eigenvalue causes stiff equations and constitutes a restriction to the time-step for standard explicit time integration methods, like Runge–Kutta. Extremely low time-steps and a bad performance are the consequence. In contrast to that, the implemented exponential time integration method based on Krylov subspaces is able to handle these stiff equations. This method, based on the Arnoldi algorithm (cf. Alg. 2.1), captures the largest eigenvalues of the operator including the ones dominated by the porous terms. Hence, these terms can be advanced in time without causing numerical instabilities.

To compare the results of the following sections, a dimensionless value of the permeability is introduced. The unit of the permeability is $[m^2]$ and in the momentum equation its inverse scales with $\frac{\mu}{\rho}$:

$$\frac{\mu}{\rho}\boldsymbol{K}^{-1} \sim \frac{1}{Re_L}\boldsymbol{K}^{-1}$$

to this end, the Reynolds number and the length-scale L are used to obtain an expression for the dimensionless permeability:

$$\boldsymbol{\chi} \coloneqq \frac{L^2}{Re_L}\boldsymbol{K}^{-1}. \tag{3.15}$$

In addition to that, to extract the largest entry of a matrix, the non submultiplicative matrix norm $\|\boldsymbol{A}\|_{\max} = \max\{|a_{ij}|\}$ can be used. Now, a large value of $\boldsymbol{\chi}$ represents a rather solid body, whereas $\boldsymbol{\chi} = \boldsymbol{0}$ is void space. How to choose the value of $\boldsymbol{\chi}$ to obtain the desired properties is validated in section § 3.2.

In Fig. 3.2 an example of the spectrum of the evolution operator is presented. The case is based on a periodic chanel flow with 128 grid points in

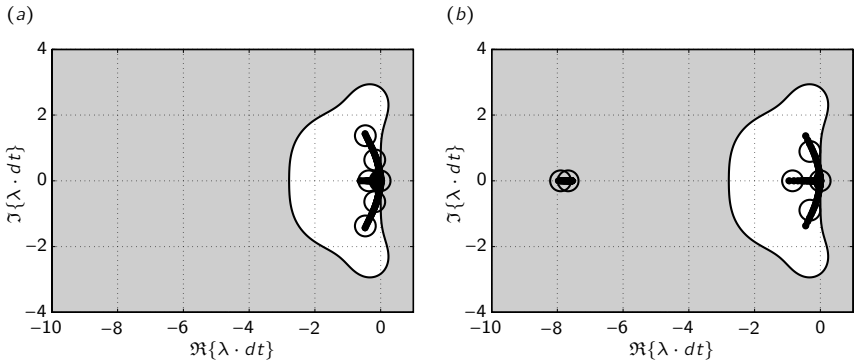

Figure 3.2: Eigenvalues of the evolution operator extracted with a Krylov technique. White area: Stable eigenvalues for fourth order Runge–Kutta. Taken for one time-step of a channel flow with Re = 1000 including a porous medium and CFL = 1 (cf. case 1 of the validation in Sec. § 3.2.1). Black dots • represent the full spectrum (based on full Hessenberg matrix). Circles ∘ represent the eigenvalues of a reduced Hessenberg matrix with m = 6 subspaces (corresponding to 6 eigenvalues). (*a*) No porous medium ($\|\boldsymbol{\chi}\|_{\max} = \frac{L^2}{Re}\|\boldsymbol{K}^{-1}\|_{\max} = 0$). (*b*) Porous medium with $\|\boldsymbol{\chi}\|_{\max} = 2000$.

the wall normal direction. One side of the channel is coated with a porous medium (case 1 of the validation in section § 3.2.1). Panel (*a*) shows the full spectrum for one time-step (black dots) without a porous medium. Here, the values of $\boldsymbol{\chi}$ are set to zero and no damped eigenvalues, related to the porous terms are visible. In addition to that, the spectrum of a reduced Hessenberg matrix, based on six Krylov subspaces, is marked with black circles. One can see that the Arnoldi algorithm captures the largest eigenvalues of the spectrum. In the background, the stability map of a fourth order Runge–Kutta time integration method is shown for comparison, only. Eigenvalues in the white area can be advanced stable in time with a fourth order Runge–Kutta time integration method, whereas eigenvalues in the gray area will cause numerical instabilities. For the present case, a CFL number of CFL = 1 is chosen and all eigenvalues lie in the stable area.

In panel (*b*), the same case is presented, now including the porous coating on one side of the channel. The value of the permeability is chosen such that $\|\boldsymbol{\chi}\|_{\max} = \frac{L^2}{Re}\|\boldsymbol{K}^{-1}\|_{\max} = 2000$. Compared to the case without porosity, several highly damped eigenvalues of the full spectrum appear in the unstable part of the stability map. Again, six eigenvalues of a reduced Hessenberg matrix are marked with black circles. As for the case without porosity, the

largest eigenvalues are captured with the Arnoldi algorithm including the highly damped eigenvalues related to the permeability. Integrating this case with the a CFL number of CFL = 1 and a fourth order Runge–Kutta time integration method, would cause numerical instabilities and finally fail. As the eigenvalues are scaled with the time-step dt one could reduce the time-step (CFL number) by a factor of about four to scale the highly damped eigenvalues in the stable part of the stability map. Consequently, the performance of the overall simulation would be reduced by the same factor of four. Apparently, the chosen value of the permeability is directly linked to the performance of the simulation, when using a standard explicit time integration technique. To represent a solid body with a porous medium, the value of $\boldsymbol{\chi}$ has to be as large as possible. Values of $\|\boldsymbol{\chi}\|_{\max} \approx 10^5$ have shown to be a good approximation for a solid body (cf. § 3.2). This value would cause much smaller time-steps than the one with $\|\boldsymbol{\chi}\|_{\max} = 2000$. The maximum value of $\boldsymbol{\chi}$ or the corresponding CFL number to guarantee a stable porous eigenvalue for standard explicit methods can be approximated in the following way:

The eigenvalue, scaled with the time-step has to be in the order of one (depending on the explicit time integration method):

$$\frac{\mu}{\rho}\boldsymbol{K}^{-1}dt < 1.$$

With the definition of the CFL number: $\mathrm{CFL} = u\,dt/dx$, the Reynolds number: $Re = \rho u L/\mu$ and the approximation of the number of grid points used in one direction: $N = L/dx$, we end up with an expression for the minimal value of the permeability:

$$\|\boldsymbol{K}\|_{\max} > \frac{\mathrm{CFL}\cdot L^2}{Re\cdot N}$$

or for the dimensionless value of the permeability $\boldsymbol{\chi}$:

$$\|\boldsymbol{\chi}\|_{\max} < \frac{N}{\mathrm{CFL}}$$

In the present case, for CFL = 1 and $N = 128$ we get $\|\boldsymbol{\chi}\|_{\max} < 128$ to obtain a numerically stable result. The other way around, a value of $\|\boldsymbol{\chi}\|_{\max} = 10^5$ representing a solid body, causes a CFL number of $\mathrm{CFL} \lessapprox 10^{-3}$ to obtain stable results. Hence, the overall performance of the simulation would decrease by the order of three.

To this end, the time advancement is performed using an exponential integration based on Krylov subspaces. As we have seen in Fig. 3.2, this time

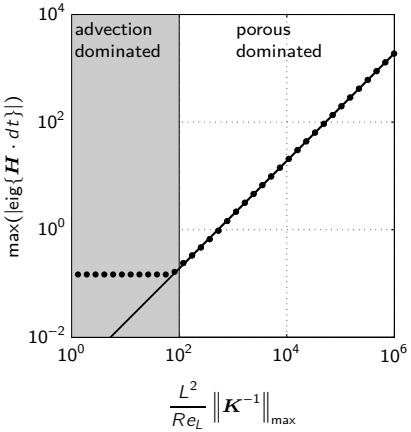

Figure 3.3: Dependency of the minimal eigenvalue of the evolution operator (Ritz value) on the permeability $\boldsymbol{K}$. Numerical measured eigenvalue •, analytical eigenvalue (———). Scaled with the time-step. With the non submultiplicative matrix norm $\|\boldsymbol{A}\|_{\max} = \max\{|a_{ij}|\}$.

integration method is able to capture the highly damped eigenvalues. In the present analysis, a maximum number of 32 subspaces is used to simulate solid like porous materials. Compared to a fourth order five stage Runge–Kutta method, the Krylov technique with 32 subspaces is about six times as expensive. Again, a simulation of a porous medium with solid-like properties, based on the explicit Runge–Kutta method, would be 1000 times as expensive and not feasible for High Performance Computations.

In Fig. 3.3 the dependence of the most damped eigenvalue of the evolution operator, based on the channel flow, mentioned earlier (case 1), is presented. One can see that the most damped eigenvalue starts to converge to its analytical solution ($-\mu/\rho\|\boldsymbol{K}^{-1}\|_{\max}$, solid line) for values of the dimensionless permeability larger than $\|\boldsymbol{\chi}\|_{\max} = 10^2$. This marks the point, where the porous terms dominate the damped eigenvalues of the spectrum. Hence, the values of the permeability can be classified in a convection dominated part ($0 \leq \|\boldsymbol{\chi}\|_{\max} \leq 10^2$) and a porous dominated part ($10^2 < \|\boldsymbol{\chi}\|_{\max} < \infty$). As we will see later, most optimized porous media will exhibit eigenvalues in both regimes.

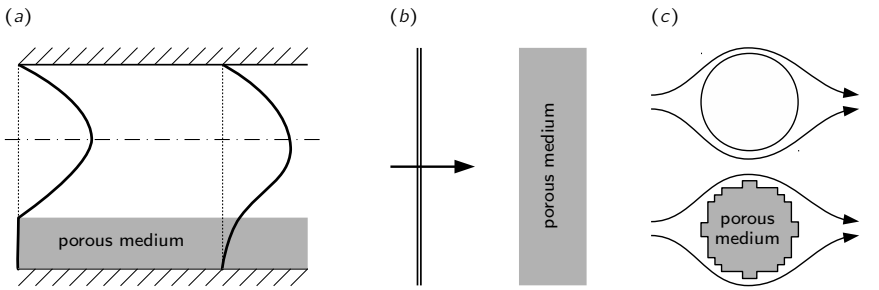

Figure 3.4: Validation cases for porous properties. (*a*) Channel with a porous coating on one side of the channel walls (Sec. § 3.2.1). (*b*) Plane acoustic wave impinging on porous wall (Sec. § 3.2.2). (*c*) Comparison of a porous cylinder with solid properties and a curvilinear cylinder (Sec. § 3.2.3).

3.2 Validation

In the following section, three test cases will be used to investigate the properties of a porous material. The first test-case, in Sec. § 3.2.1, studies the hydrodynamic properties. Especially the feasibility to use a porous material as a solid body will be investigated. To this end, a periodic channel flow is applied with a porous coating on side of the channel walls. A sketch of the flow case is presented in Fig. 3.4(a).

The second case, in Sec. § 3.2.2, deals with the acoustic properties of a porous material. The reflection and absorption of an impinging acoustic wave, depending on its wavenumber, will be shown. In Fig. 3.4(b) the principle setup of the numerical experiment is shown.

Finally, in the third test case in Sec. § 3.2.3, the properties of a porous medium are investigated on a more complex application (cf. Fig. 3.4(c)). The flow past a cylinder, based on a porous material with solid properties, is compared to a cylinder with a curvilinear grid. Instantaneous and mean-flow features are compared.

3.2.1 Hydrodynamic properties

As we have seen already in the beginning of this chapter, a porous material can be characterized by two parameters, the porosity and the permeability. The latter parameter determines the force (pressure) necessary to pass fluid through the material. It can be chosen to either prevent any fluid to pass

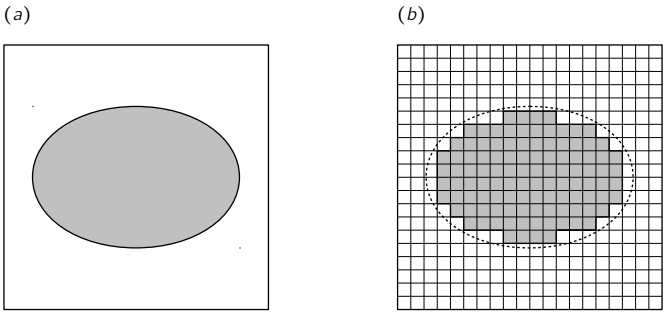

Figure 3.5: (*a*) Shape of a specific geometry. (*b*) Shape of (*a*) represented by the technique of volume penalization.

through the material or to let it pass without any resistance, including all intermediate states. In the first case the permeability is set to $\boldsymbol{K} = 0$ and the porous material represents a solid body. In the second case, the permeability is set to $\boldsymbol{K} = \infty$ and simply represents void space.

The first feature is particularly interesting, since one can easily create complex geometries by placing a porous body with solid properties in the computational domain without transforming the computational grid. A Cartesian grid is used in the background to embed the porous material as a function of the space and eventually also of the time. The solid body encloses a certain number of grid points representing the solid body. Depending on the resolution of the underlying Cartesian grid, the surface of the solid body is as rough as the resolution of the grid. In Fig. 3.5, the basic principle to include a solid body in a Cartesian grid, by means of volume penalization, is shown. In any technical application and experiment, a surface of a solid body in a fluid flow will always show a certain roughness, depending on the fabrication technique. The fabrication tolerance, especially in experimental setups, can be in the order of one tenth of a millimeter.

Considering e. g. a drilled round laval nozzle with a diameter of 10mm in an experimental setup with a fabrication tolerance of 0.1mm. To obtain the same surface roughness in the numerical simulation, the resolution of the embedding Cartesian grid needs 100 points inside the nozzle. The high resolution numerical experiments of Sec. § 4.2 satisfy this property due to a grid refinement in the jet core. One has to mention, that in the usual fashion with curvilinear grids, the surface roughness of the numerical solution

is zero. This influences the turbulence in the boundary layers and special techniques are necessary to trip the laminar boundary layers to obtain a similar turbulence value as measured in the experiment [Bogey & Bailly, 2010].

The technique to include a complex geometry in a Cartesian computational domain is related to immersed boundary methods and is called in this context *volume penalization* [see amongst others, Angot et al., 1999, Arquis & Caltagirone, 1984, Baur et al., 2009, Carbou, 2008, Keetels et al., 2007, Kevlahan & Ghidaglia, 2001, Kolomenskiy & Schneider, 2010, Liu & Vasilyev, 2007, Schneider & Farge, 2005]). To only use the technique of volume penalization to include complex geometries as solid bodies in the computational domain, the porous flow equations can be extended with an additional term including a second derivative of the velocities (*Brinkmann penalization* [see Brinkman, 1949]). This term is similar to the friction terms of the Navier–Stokes equations and adds an artificial viscosity inside the porous material. It reads:

$$\nabla p = -\mu \boldsymbol{K}^{-1} \boldsymbol{v} + \mu' \Delta \boldsymbol{v}, \tag{3.16}$$

where the first term on the right hand side corresponds to Darcy's law of Eq. (3.1) and the second term to the Brinkmann extension. The additional viscosity μ' in the second term my be different from μ, depending on the configuration of the porous material [see Brinkman, 1949, Eq. (19)]. From a numerical point of view, this additional Brinkmann term can be useful to satisfy the non-slip condition at the surface of the solid body as the second derivatives are large in these areas [see Liu & Vasilyev, 2007]. Especially for incompressible, divergence free flows, this can be important [see Kolomenskiy & Schneider, 2009]. If $\boldsymbol{K}$ is close to zero, the first term will dominate Eq. (3.16) even though if the velocity gradients are large. To this end, the Brinkmann extension will only operate for large values of $\boldsymbol{K}$ which corresponds to void space in the porous material. Considering a constant $\mu' = \mu_0$ and a measurable velocity gradient, a drag on the velocity will be present in the porous medium even tough if $\boldsymbol{K} \to \infty$ (void space).

The focus of the present research project is the optimization of porous material to reduce flow induced noise by means of controlling the permeability $\boldsymbol{K}$. To maintain the freedom in the design process, to create areas of void space in regions of porous material, the Brinkmann extension of Eq. (3.16) is not included in this analysis.

To obtain a solid body with the present equations, one has to choose $\boldsymbol{K} \to 0$. The only problem is that we can not choose a permeability of zero due to the related stiffness of the flow equations and the corresponding restrictions of

the time integration method. The remaining question is, how to choose the value of $\boldsymbol{K}$ to obtain on the one hand a porous material with solid properties and on the other hand a balance in computational effort.

To investigate this question a test-case, based on a periodic channel flow is simulated. One side of the channel is a solid wall boundary condition with adiabatic properties and on the other side of the channel a layer of porous material is added to the wall. The layer extends $0.25h$ into the channel (with the height of the channel h). In the wall normal direction, a total of 128 points are used with a grid stretching to refine the mesh at the interface between porous material and the channel flow. The grid stretching is based on Eq. (2.40) with $\eta_c = 0.25h$ and $\tau_y = 5$. All computations are based on the compressible and porous Navier–Stokes equations, integrated with 32 Krylov subspaces in time. Based on the channel height and the initial peak Mach number $M = 0.5$, the Reynolds number is set to $Re_h = 100$. Due to this low value, the high dissipation causes the kinetic energy to decay rapidly in time. The amplitude of the initially parabolic velocity profile, which is defined in the area without porous medium and zero elsewhere, decreases in time and in addition to that, penetrates into the porous material, depending on the choice of the permeability. In the present investigation, five different values of the permeability are chosen. Whereas the permeability is distributed homogeneously in the porous layer and an isotropic behavior of the material is assumed ($\boldsymbol{K} = \|\boldsymbol{K}\|_{\max}\boldsymbol{I}$). Hence, only one scalar value is used to describe the material properties in the present test-case.

A total of five computations are performed with different values of the dimensionless permeability: $\chi = 0$ (void space, no porous material), $\chi = 4 \cdot 10^{-1}$, $\chi = 4 \cdot 10^{0}$, $\chi = 4 \cdot 10^{1}$, $\chi = 4 \cdot 10^{5}$. The simulation starts with the parabolic velocity profile in the area without porous medium ($0.25 \leq y/h \leq 1$). In the area of the porous medium, all velocity components are zero for the initial condition. In Fig. 3.6(a), the velocity profiles are presented after 4000 time-steps, which corresponds to a bulk convection length of $2.34h$. One can see clearly, that the amplitudes of the velocity profiles decayed for all cases by about 40 %. In addition to that, one can see that for most cases, the fluid penetrates the porous material (gray area). The trend is obvious: the smaller the dimensionless permeability, the easier it is to penetrate the material. For the case with no porous material (dash-dotted curve), the largest amplitudes of the velocities inside material can be detected. They decay with increasing permeability and are finally no more detectable in this view for the largest dimensionless permeability ($\chi = 10^5$). From this view, this value can be considered as a solid material, as the typical parabolic shape of the channel flow is maintained and no penetration of the porous material is visible. It is

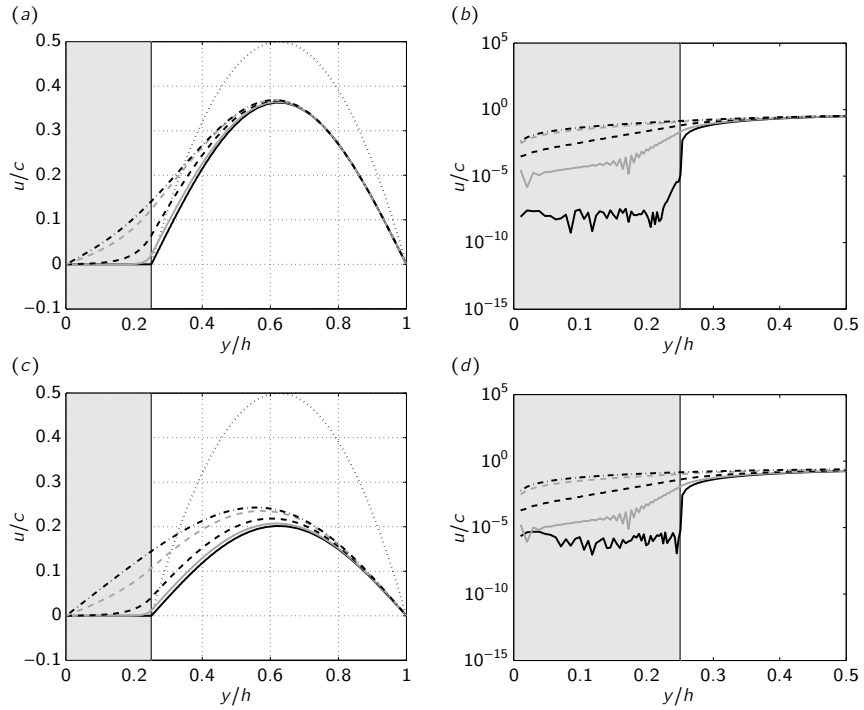

Figure 3.6: Case 1: Channel flow with a porous coating on one side of the channel-walls (gray area, $0 \le y \le 0.25h$) for different permeabilities: $\|\chi\|_{\max} = 4 \cdot 10^5$ (———); $\|\chi\|_{\max} = 4 \cdot 10^1$ (———); $\|\chi\|_{\max} = 4{\cdot}10^0$ (- - - - - -); $\|\chi\|_{\max} = 4{\cdot}10^{-1}$ (- - - - - -); $\|\chi\|_{\max} = 0$ (-·-·-·-). (*a*) and (*b*) taken after 4000 time-steps with logarithmic scaling in (*b*). (*c*) and (*d*) taken after 10000 time-steps with logarithmic scaling in (*d*). Initial condition (· · · · · · · ·) in (*a*) and (*c*) based on a peak Mach number $M = 0.5$. Reynolds number based on the channel height h and the initial Mach number M: $Re = 100$.

interesting to note, that for this high value, a sharp gradient of the velocity profile at the interface between porous material and fluid flow occurs without visible oscillations. This is especially surprising as no additional treatment, like a filter or even shock filter, is applied (except the dissipative upwind schemes).

At a snapshot, taken after 10 000 time-step in panel (*c*), which corresponds to a bulk convection length of $3.90h$, the trend of the previous time-step (*a*) can be confirmed. Still, the velocities of the highest permeability case are not

detectable in this view. In fact, the velocities do not vanish completely. In the corresponding panels (b) and (d), respectively, the velocity profiles are visualized in a logarithmic scaling. For the high permeability case, the velocity components inside the porous medium are in the order of $M = 10^{-6}$ which can be neglected for the present numerical investigation, where supersonic velocities with $M > 1$ dominate the flow.

From this analysis, one can conclude, that from a hydrodynamic point of view, a dimensionless value of the permeability of $\chi = 10^5$ can be considered as a solid body.

3.2.2 Acoustic properties

In the following test case the acoustic properties of a porous medium, based on the porous Navier–Stokes equations of this chapter are investigated. The focus of this investigation lies on the acoustic properties of the interface of a porous medium and void space depending on the permeability of the material. It is well known, that a porous medium can be used as a sound absorber. For example, the walls of any anechoic room can be regarded as a porous medium.

This test case is based on a one-dimensional simulation of a plane acoustic wave impinging, reflecting and transmitting on a porous wall with a varying permeability. In addition to that, the dependence of the wave number of the impinging and reflecting wave is investigated. To measure the deviation of a reflecting wave of a porous wall to a solid wall, a wall boundary condition is implemented at the location of the interface of void space and porous material.

The one-dimensional plane wave is solved on a domain $\Omega \in [0, L]$ with 128 equidistantly spaced grid points. The interface of void space to porous material is located at $x = 3/4L$ with the porous material ranging from $3/4 \leq x/L \leq 1$. As initial condition, the shape of the plane acoustic wave is of Gaussian type and reads:

$$
\begin{aligned}
p(x) &= p_0 + \exp\left(-\left(\frac{x - 3/8L}{b}\right)^2\right) \\
u(x) &= \frac{1}{\rho_0 c} \exp\left(-\left(\frac{x - 3/8L}{b}\right)^2\right)
\end{aligned}
$$

with the center of the Gaussian distribution at $x = 3/8L$ and the width $b = \sqrt{2}/2 \cdot 10^{-1} L$. The acoustic Reynolds number is set to $Re_a = 5000$ based on the length of the domain L. In Fig. 3.7 the solution of the acoustic pulse is visualized for four time-steps ($t = [1/4, 2/4, 3/4, 4/4]T$) and for different permeabilities, ranging from $\|\boldsymbol{\chi}\|_{\max} = 2 \cdot 10^0, \ldots, 2 \cdot 10^4$ (with $T = L/c$ and the

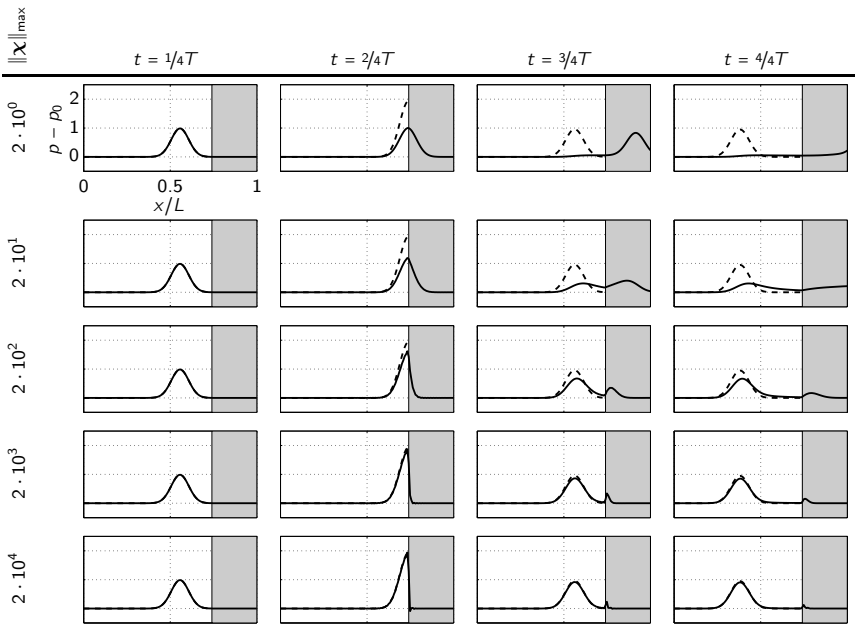

Figure 3.7: Validation case 2: Acoustic properties of a porous medium. Reflection of an acoustic wave on a porous surface depending on the permeability. Columns: Snapshots taken at four equidistant time-steps: $t = [1/4, 2/4, 3/4, 4/4]T$ with $T = L/c$ and the ambient speed of sound c. Rows: Variation of the dimensionless permeability χ ranging from $2 \leq \|\chi\|_{max} \leq 2 \cdot 10^4$. Porous wall (———); Wall boundary condition (- - - - - -). Gray area: porous domain. Amplitude of the pressure peak: $p - p_0 = 1\,[Pa]$.

ambient speed of sound c). The solid curve represents the acoustic pulse impinging on the porous material, the dashed line is the reference solution, based on the adiabatic wall boundary condition. The latter one is independent on the choice of the permeability. For both curves, the left boundary is non-reflecting and for the solid curve (including the porous material) the right boundary at $x = L$ is also non-reflecting.

In the first case, with $\|\boldsymbol{\chi}\|_{\max} = 2 \cdot 10^0$, the acoustic pulse of the solid line is entering the porous material at $t = 2/4T$ without any significant resistance. Only a little reflection is visible. Most of the acoustic pulse is transmitting into the porous medium and finally at $t = T$ leaving the domain. Hence, the reflection coefficient R is close to zero and the transmission coefficient T is

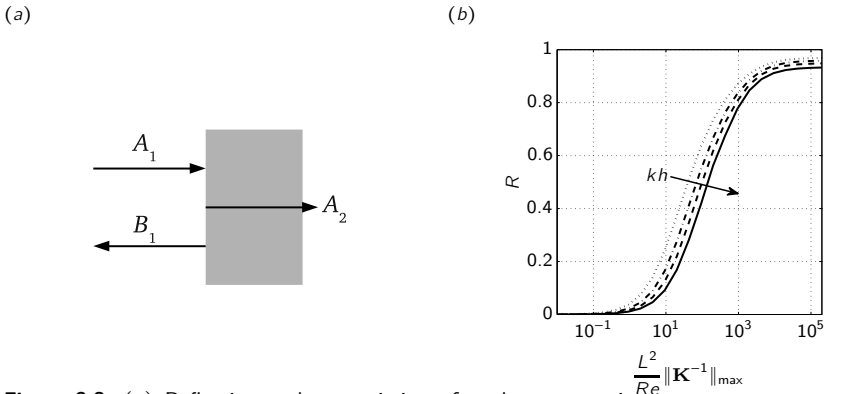

Figure 3.8: (*a*) Reflection and transmission of a planar acoustic wave on porous material. Amplitude of the impinging wave A_1, amplitude of the reflected wave B_1 and amplitude of the transmitted wave A_2. (*b*) Reflection coefficient R of Eq. (3.17a) for a porous medium over the permeability for four different wave numbers: $kh = 1/4\pi$ (———); $kh = 2/4\pi$ (- - - - - -); $kh = 3/4\pi$ (-·-·-·-·-); $kh = 4/4\pi$ (· · · · · · · ·). Only the peak values of the numerical solution of the reflected wave are considered. Phase information neglected.

close to one. Both coefficients are defined as follows:

$$R = \frac{B_1}{A_1} \tag{3.17a}$$

$$T = \frac{A_2}{A_1} \tag{3.17b}$$

and related as follows: $T = 1+R$, with the amplitude of the impinging wave A_1, the amplitude of the reflected wave B_1 and the amplitude of the transmitted wave A_2 (cf. Fig. 3.8(a) and see Ehrenfried [2004]).

A similar picture can be found for the next higher permeability with $\|\boldsymbol{\chi}\|_{\max} = 2 \cdot 10^1$, whereas the amplitude of the reflected wave is now similar to the one of the transmitted wave ($R \approx T$). In addition to that, a phase shift of the reflected wave is visible. It seems that due to the smooth surface of the porous medium, the reflected wave is first penetrating the porous medium and then reflected. Hence, the solid curve covers a larger distance and lags behind the perfectly reflected wave.

A further increase of the permeability ($\|\boldsymbol{\chi}\|_{\max} = 2 \cdot 10^2$), enhances the reflection properties of the porous medium. The amplitude of the reflected wave is larger than the transmitted wave and the phase shift is being reduced. Compared to the latter two cases, the transmitted wave is no more transported deeply into the porous medium, but damped and diffused rapidly

at the surface of the porous medium.

For the last two cases with $\|\boldsymbol{\chi}\|_{\max} = 2 \cdot 10^3$ and $\|\boldsymbol{\chi}\|_{\max} = 2 \cdot 10^4$, nearly no phase shift is visible and the amplitude of the reflected wave is close to the exact reflection. The remaining transmitted wave consists of a small but sharp pressure peak at the surface of the porous medium. It is not transported in the porous medium but as before, damped in time. For $t \to \infty$, the remaining pressure fluctuation in the porous medium will become zero. A similar result for this test case could be found by Liu & Vasilyev [2007] with a Brinkmann penalization.

The reflection properties of the porous medium can be also found in Fig. 3.8(b). Here, the reflection coefficient R is presented as a function of the dimensionless permeability χ. In addition to that, the reflection characteristics are presented for four different wave-numbers ($kh = {}^1\!/\!_{4\pi}, {}^2\!/\!_{4\pi}, {}^3\!/\!_{4\pi}, {}^4\!/\!_{4\pi}$). The trend for all wave-numbers is similar. With increasing dimensionless permeability, the reflection properties are improving. For low values of χ (comparable to void space), the reflection coefficient is close to zero. It starts to become detectable for $\chi > 10^{-1}$ and reaches $R = 0.5$ for values of $\chi \approx 10^2$. In the latter case, the half of the acoustic energy is reflected while the other half is transmitted into the porous medium. Finally, for $\chi > 10^4$ the reflection coefficient starts to converge to its maximum value which is reached at $\chi \geq 10^5$. The maximum value depends on the wave-number and is in the range of $0.95 \leq R \leq 0.98$. It does not reach $R = 1$, which corresponds to a perfect reflection, and is increasing with the wave-number.

One can see that the reflection coefficient is shifted to the low values of the permeability when reducing the wave-number. Hence, a low wave-number will be reflected more efficiently at a lower permeability χ than a high wave-number acoustic. To give an example: a wave-number of $kh = {}^3\!/\!_{4\pi}$ with $\chi = 10^2$ will be reflected with $R = 0.45$; a wave-number of $kh = {}^1\!/\!_{4\pi}$ with the same permeability will be reflected with $R = 0.58$. The dependence of the wave-number is also visible in Fig. 3.9(b).

In all studies, concerning the reflection coefficient, only the amplitudes are considered. The effect of a possible phase shift is neglected. To investigate the overall efficiency of the reflection properties, including the phase information, the difference of the perfectly reflected wave and the wave reflected on the porous surface, is measured in the L_2-norm. The results are presented in Fig. 3.9(a). One can identify a similar behavior as in panel (b), where no phase information is included, yet, the wave-number dependence is more dominant. The least error (10^{-3}) can be gained for a high permeability combined with a high wave-number. The worst scenario can be obtained for the opposite case. Here, the dependence on the wave-number has reverted com-

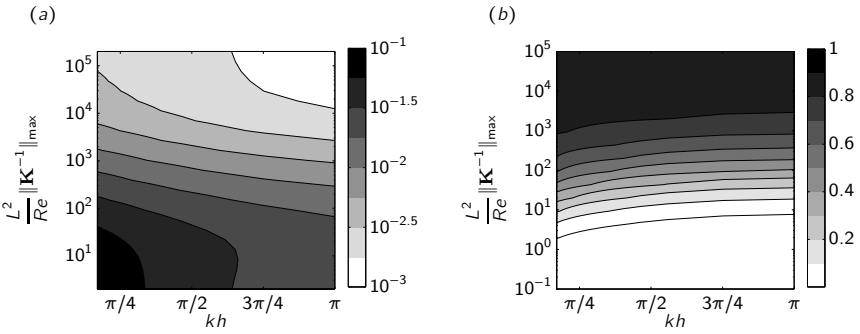

Figure 3.9: (*a*) Deviation of the reflected wave of a porous medium compared to a wall boundary condition over the permeability and wavenumber. Measured in the L_2-norm. (*b*) Reflection coefficient R of Eq. (3.17a) for a porous medium over the permeability and wavenumber. Only the peak values of the numerical solution of the reflected wave are considered. Phase information neglected. See also Fig. 3.8.

pared to the case where the reflection coefficient is considered, only which is due to the included phase information. One has to keep in mind, that a phase shift, especially in screech noise computations, can lead easily to wrong noise predictions (see the influence of an acoustic reflector on screech tones in Sec. § 1.1.2). Hence, care has to be taken, to guarantee sufficient solid properties of e. g. a jet nozzle. For the present screech noise computations, the dimensionless permeability is set to $\chi = 10^5$ inside the solid part of the nozzle.

3.2.3 Flow past a circular cylinder

To validate the porous material on a complex application the flow past a circular cylinder is investigated. This flow configuration is a standard validation test in the field of fluid mechanics. For Reynolds numbers larger than $Re_D = \rho u D/\mu \approx 50$ this flow is unstable and characterized by the well known Kármán vortex street. The flow past the cylinder separates periodically with a Strouhal number of $Sr = fD/u \approx 0.2$ (depending on the Reynolds number with the frequency f, the diameter of the cylinder D and the free stream velocity u).

Two computations are performed to validate the porous cylinder flow. First, a computation based on a Cartesian grid with an embedded porous (solid) cylinder and secondly a cylinder surrounded by a curvilinear (body

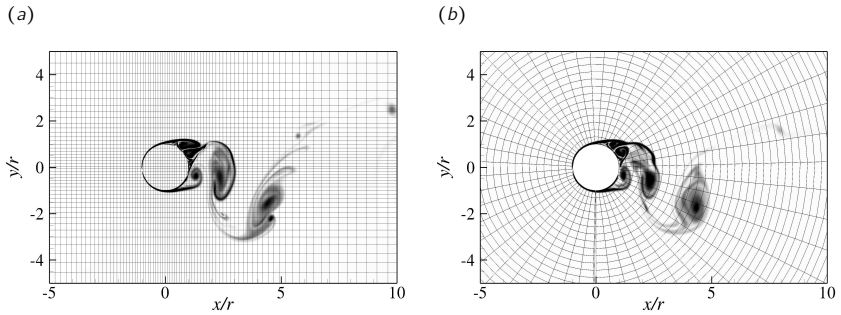

Figure 3.10: Instantaneous snapshot of the vorticity past a cylinder. (*a*) porous cylinder with Cartesian grid. (*b*) cylinder with solid boundary condition and curvilinear grid. Taken at two similar flow situations. Only every tenth grid point is shown.

fitted) grid and an adiabatic wall boundary condition. The Reynolds number is identical for both cases and set to $Re_D = 5000$ based on the free stream Mach number of $M = 0.4$. The permeability of the porous cylinder is set to $\chi = 2 \cdot 10^4$, based on an isotropic and homogeneous material. In Fig. 3.10 an instantaneous snapshot of the vorticity past the two cylinders is presented. Panel (*a*) shows the cylinder modeled by the porous material with the Cartesian grid which is stretched in the stream-wise and transverse direction to refine the grid at the boundary of the cylinder, based on Eq. (2.40) with $\tau_x = \tau_y = 5$ and $\eta_x = \eta_y = 0$. Only every tenth grid point is shown. In panel (*b*) the curvilinear grid is presented with the cylinder for a similar flow situation. Note, that this flow is turbulent and an exact comparison of instantaneous snapshots is not possible. In addition to that, the surface of the porous cylinder is rough whereas the curvilinear cylinder has a smooth surface. The roughness depends on the resolution of the Cartesian grid and adds additional turbulence in the boundary layer of the cylinder surface. This turbulence excites the unstable mode of the cylinder and is responsible for a fast transition of the laminar initial condition (based on the potential theory) to the unsteady oscillating flow. In the case of the curvilinear grid, the numerical error or an artificially added noise is necessary for the transition process and may take much longer. In the present case, noise of a relative amplitude of 10^{-12} is added to each flow variable of the initial condition to force the transition.

In Fig. 3.11 the mean Mach number for both computations is presented in a close up of the cylinder surface to illustrate the grid resolution. In this figure

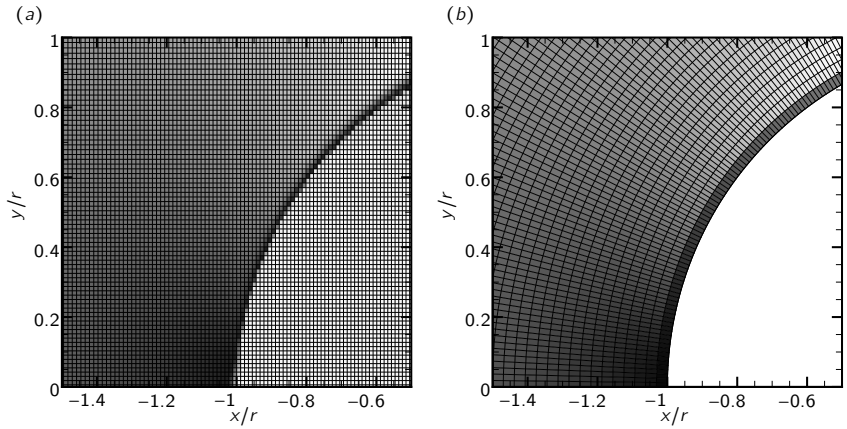

Figure 3.11: Mean Mach number in the color range of $0 < M < 0.6$ including the grid. (a) porous cylinder with Cartesian grid. (b) cylinder with solid boundary condition and curvilinear grid.

every grid point is visualized. The surface roughness of the porous cylinder is clearly visible in panel (a) whereas the smooth surface of the curvilinear cylinder is visible in panel (b). One can also identify that the boundary layer of both computations is not well resolved.

A more quantitative comparison of both computations is presented in Fig. 3.12. At six different measurement locations, the mean absolute velocity profiles along the transverse direction are presented. The measurements are taken at the stream-wise positions $x/r = -1, -0.5, 0, 0.5, 1, 1.5$ (cf. Fig. 3.13(a) for details). Each panel (a) – (f) corresponds to one measurement location with the solid line corresponding to the data of the porous cylinder and the circles to the measurements of the curvilinear cylinder. For all positions the measurement from both computations are in good agreement. Except for the measurement in the wake of the cylinder some deviations are visible. Here, the measured velocities of the porous cylinder are slightly above the ones of the curvilinear cylinder.

The oscillating flow past the cylinder is one of the characteristics of this application. Periodically detaching vortices cause an oscillating force in the transverse direction of the flow. This force can be expressed by the lift coefficient C_l and is presented in Fig. 3.13(b) for both computations. Again, both results are in good agreement concerning the amplitude and frequency. The

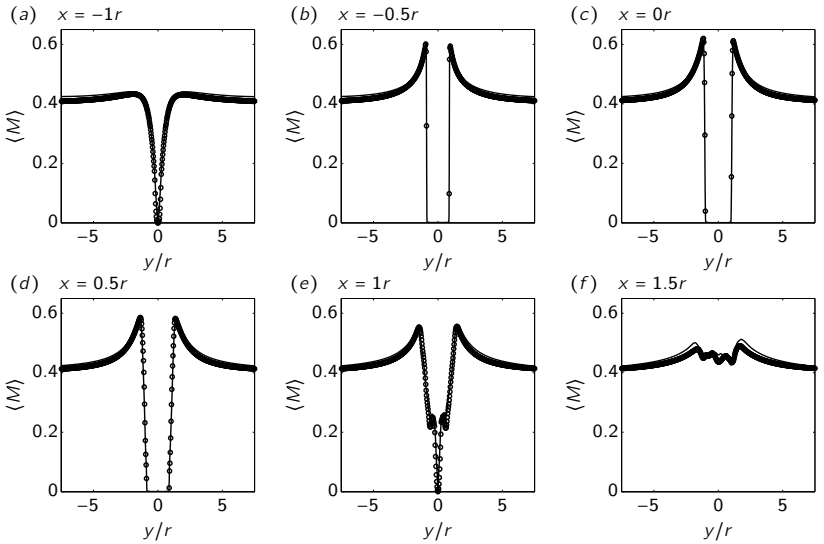

Figure 3.12: Mean absolute velocity profiles along the transverse direction for six measurement locations (x/r = −1; −0.5; 0; 0.5; 1; 1.5; also shown in Fig. 3.13(a)). Circle (∘): cylinder based on solid boundary condition with curvilinear grid. Solid Line (———): cylinder based on porous medium with Cartesian grid.

deviations of the results and the non-periodic behavior may be explained due to the turbulent (chaotic) behavior of the high Reynolds number flow.

3.3 Examples of porous flow simulations

In the following section some examples, to demonstrate the method of porous flow simulations, are given. All examples demonstrate the ability to use a porous medium as a solid body to model complex geometries. The first example is based on the subsonic flow about a Joukowsky wing with a high Reynolds number. The second case deals with the complex geometry of a fluidic device used in active control environments. The results of the porous jet nozzle can be found in Sec. § 4.

3.3.1 Porous wing

In fluid dynamics the flow past a wing profile is a standard application. In the present application the flow past a Joukowsky profile with zero angle

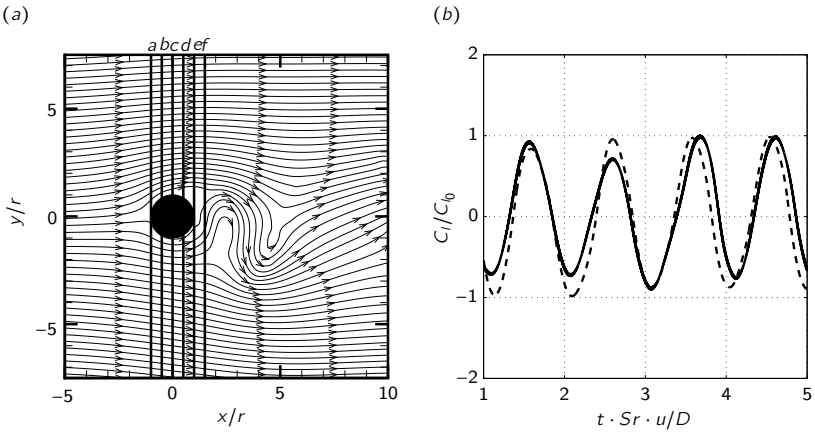

Figure 3.13: (*a*) Measurement locations (———) *a*–*f* for the mean absolute velocity profiles along the transverse direction of Fig. 3.12. Snapshot of the streamlines in the background. (*b*) Comparison of the lift coefficient C_l for the porous (———) and curvilinear cylinder (- - - - - -). $Sr = 0.2$.

of attack is presented. The geometry of the wing is based on the following conformal mapping (Joukowsky):

$$z = \xi - \frac{1}{\xi} \tag{3.18}$$

with the unit circle $\xi \in \mathbb{C}$ shifted in the complex plane with $-0.1 + 0.1i$.

The free stream Mach number is $M = 0.5$ with a Reynolds number based on the chord length L_c of $Re = 10^6$. With the homogeneously distributed and isotropic dimensionless permeability set to $\|\boldsymbol{\chi}\|_{\max} = 18490.0$, the porous wing can be represented as a solid body. The computation is based on a two-dimensional Cartesian grid stretched in the normal direction (y-direction) to refine the wall boundary layers on the wing surface (for the grid stretching see § 2.4.2). It contains 2048×1024 grid points and is solved in parallel on 256 cores. The inlet boundary is fixed and the flow variables are approximated based on the potential theory. At the outlet a sponge, similar to the one for the jet computations (see § 2.4.3.2), avoids spurious energy scattering back into the computational domain. Non-reflecting boundary conditions in the normal direction remove reflections from acoustics leaving the domain. Time- and space discretization is based on the methods presented in Sec. § 2.3.

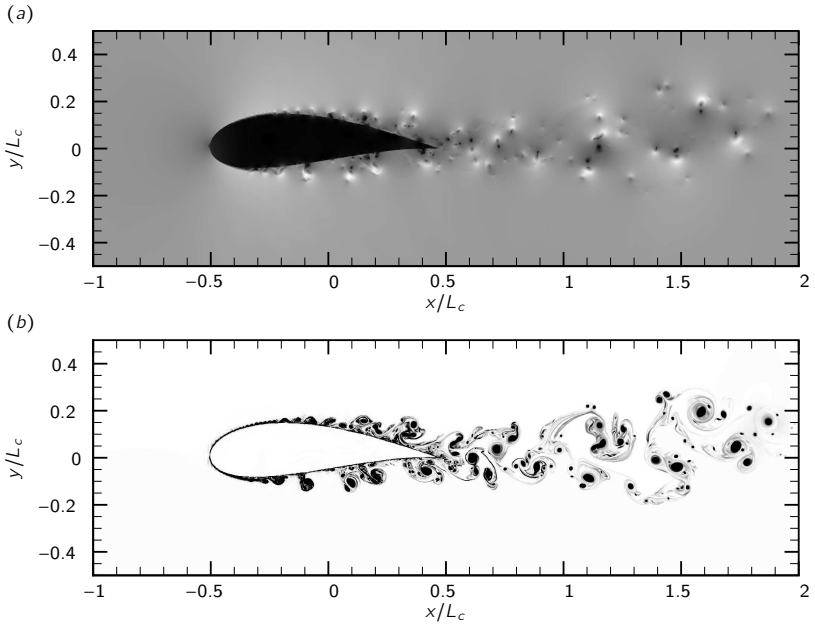

Figure 3.14: Two-dimensional simulation of a porous Joukowsky wing. Snapshots taken after 33790 time-steps. Reynolds number: $Re_{L_c} = 10^6$; free stream Mach number: $M = 0.5$; Dimensionless permeability: $\|\chi\|_{\max} = 18490$. Scaled with the chord length L_c. (a) Mach number in the range of $(0 : 0.75)$. (b) Absolute value of the z-vorticity in the range of $(0 : 2000)[1/s]$.

In Fig. 3.14 two snapshots of the flow are presented. Panel (a) visualizes the Mach number and in panel (b) the vorticity is presented. One can identify the typical vortex shedding downstream the wing with a strong separation on both sides of the wing. Due to the high Reynolds number, the flow structures become very small which is especially visible in panel (b) at the trailing edge of the wing. Although the grid resolution with its two million grid points in the two-dimensional plane is high for a state of the art computation in the field of CFD, the computation is still not resolved. Based on that Reynolds number a total of $N \sim Re^{3/2} = 10^9$ grid points would be necessary to resolve the smallest scales based on Kolmogorov's theory. Note, that Kolmogorov's theory accounts for three-dimensional turbulent flows. This flow is forced to be two-dimensional due to the two-dimensional computational domain. Hence, coherent structures, like vortices, do not break up to three-dimensional turbulence and the smallest scales may be larger than expected.

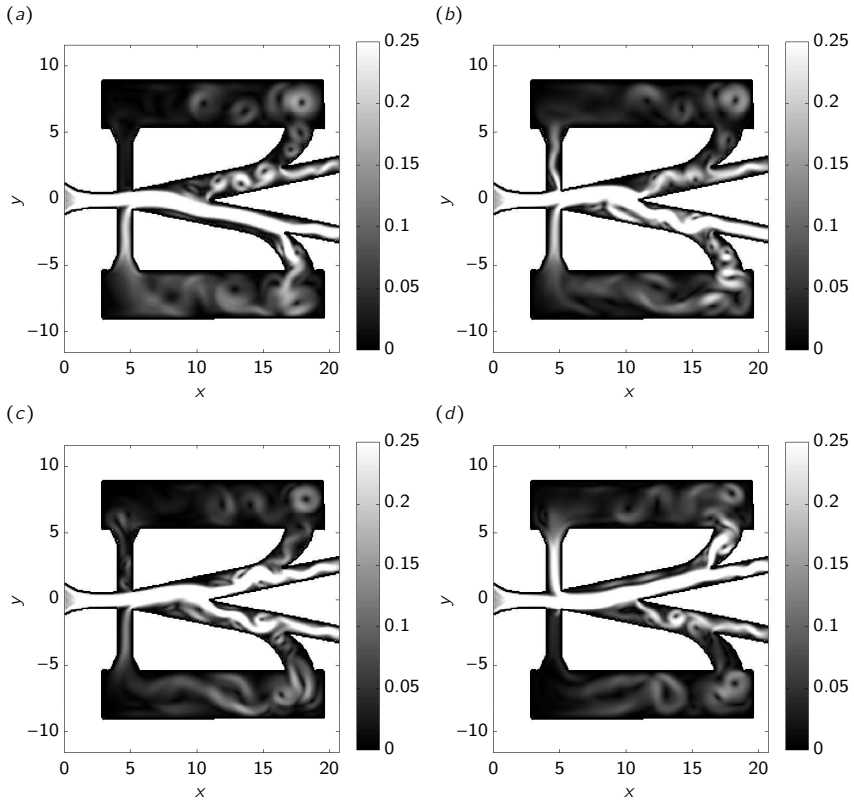

Figure 3.15: Snapshots representing the Mach number of the fluidics simulation taken at four equidistant time-steps: (*a*) $t = 8T_f$; (*b*) $t = 8.16T_f$; (*c*) $t = 8.33T_f$; (*d*) $t = 8.5T_f$. Color range $(0; 0.25)$.

This case demonstrates, that the computation of a high Reynolds number flow with a complex geometry can be performed in an efficient way, using porous media to define the solid geometry.

3.3.2 Porous fluidic

The next example is based on a fluidic oscillator to demonstrate the ability to compute the flow in complex geometries with feedback. Fluidic oscillators are feedback actuators with no moving parts. They are used as active control

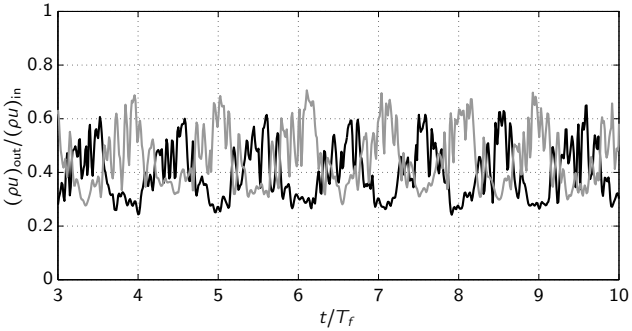

Figure 3.16: Relative mass flux at the upper and lower outlet of the fluidic of Fig. 3.15. Scaled with the mass flux at the inlet. Upper outlet (———); Lower outlet (———).

devices in a variety of technological applications due to their robustness. The oscillator investigated in this example is based on the geometry found in Cerretelli & Gharaibah [2007].

The computation is based on a two-dimensional domain with an equally spaced Cartesian grid containing 229×256 grid points. The Reynolds number based on the height h of the straight inlet channel is $Re_h = 250$ with a Mach number of $M = 0.7$. To obtain a solid wall, the dimensionless permeability is set to $\|\boldsymbol{\chi}\|_{\max} = 10^4$.

In Fig. 3.15, the Mach number of four equidistant time-steps represent a half switching cycle. In panel (a) the main mass-flux leaves the device at the lower exit. At this stage of the oscillator, a part of the mass-flux is entering the feedback chamber and redirected back to the jet at the inlet of the device. This redirected flow forces the jet to swith in the upper channel. Panel (b) shows an intermediate snapshot of the flow switching from the lower to the upper exit. Still, the main flux is leaving the device at the lower exit. In panel (c) the jet already points in the upper channel and the mass flux is divided equally over the lower and upper exit. Finally, in panel (d) the jet switched completely into the upper channel, resulting in a similar picture as in panel (a) flipped at the x-axis. From this point, the cycle continues to switch back to the lower exit. This process is repeated with a constant frequency $f_f = 1/T_f$.

In Fig. 3.16 the mass-flux of the upper an lower exit of the device is presented and scaled with the mass flux of the inlet. One can identify the π-shifted oscillating behavior measured over seven cycles.

As a conclusion of this chapter, we can see, that the presented porous and compressible Navier–Stokes equations are capable to treat both, acoustic and hydrodynamic flow problems with geometries of high complexity. These equations will be used in the following section to include a convergent nozzle in the Cartesian computational domain to investigate supersonic jet noise. The focus of the jet noise computation will lie on jet screech, which is amplified due to the reflected acoustic wave at the nozzle lip. Hence, the porous material needs to show its capability to handle both, a proper reflection characteristic and sufficient hydrodynamic properties, like an impermeable wall. In addition to this, in Sec. § 6, a porous material will be added to the nozzle exit to eliminate the feedback mechanism where high demands are made on the damping properties of the porous material. All these properties are shown to be controllable with the present porous flow equations.

4

Results of supersonic jet noise simulation

In the following chapter the results on supersonic jet noise computations are presented. It is divided in two main parts. The first part deals with planar jets whereas axisymmetric jets are investigates in the second part. In both cases the nozzle is implemented in the computational domain by means of a porous material with solid properties. No porous material is added to suppress screech tones. The results of the minimization of supersonic jet noise are presented in Sec. § 6.

The focus of the computations presented in the present chapter is to investigate screech tones and to validate the numerical method. In the first part, dealing with planar jets, a parametric study on the influence of jet Mach number to the flow physics, like emanated noise and mean values are, is performed. In the second part dealing with an axisymmetric jet, the Mach number is kept constant and the spatial resolution is modified.

Tabular 4.1 gives an overview of the main parameters, like Mach number and grid resolution, of the computations investigated. Both, the planar and the round jet are based on a Reynolds number of $Re = 5000$. In the planar case the Reynolds number is based on the jet height h and in the round case on the jet diameter D:

$$Re_D = \frac{\rho_\infty D u_j}{\mu_\infty} \tag{4.1a}$$

$$Re_h = \frac{\rho_\infty h u_j}{\mu_\infty} \tag{4.1b}$$

	M_j	p_r/p_∞	p_e/p_∞	n1 × n2 × n3	# points	Re	opt
planar	1.00	1.89	1.00	$512 \times 256 \times 64$	$8.4 \cdot 10^6$	5000	
	1.10	2.14	1.13	$512 \times 256 \times 64$	$8.4 \cdot 10^6$	5000	
	1.20	2.42	1.28	$512 \times 256 \times 64$	$8.4 \cdot 10^6$	5000	
	1.30	2.77	1.46	$512 \times 256 \times 64$	$8.4 \cdot 10^6$	5000	
	1.40	3.18	1.68	$512 \times 256 \times 64$	$8.4 \cdot 10^6$	5000	
	1.50	3.67	1.94	$512 \times 256 \times 64$	$8.4 \cdot 10^6$	5000	
	1.55	3.95	2.09	$512 \times 256 \times 64$	$8.4 \cdot 10^6$	5000	
	1.60	4.25	2.25	$512 \times 256 \times 64$	$8.4 \cdot 10^6$	5000	
	1.70	4.94	2.61	$512 \times 256 \times 64$	$8.4 \cdot 10^6$	5000	
	1.80	5.75	3.04	$512 \times 256 \times 64$	$8.4 \cdot 10^6$	5000	
	1.90	6.70	3.54	$512 \times 256 \times 64$	$8.4 \cdot 10^6$	5000	
	2.00	7.82	4.13	$512 \times 256 \times 64$	$8.4 \cdot 10^6$	5000	
round	1.55	3.95	2.09	$256 \times 128 \times 128$	$4.2 \cdot 10^6$	5000	■
	1.55	3.95	2.09	$512 \times 256 \times 256$	$33.6 \cdot 10^6$	5000	■
	1.55	3.95	2.09	$1024 \times 512 \times 512$	$268.4 \cdot 10^6$	5000	

Table 4.1: Investigated numerical simulations on planar and round supersonic jets. The two cases marked with a ■ will be optimized in Sec. § 6. p_r: reservoir pressure; p_e: nozzle exit pressure; p_∞: ambient pressure.

with the fully expanded jet velocity $u_j = M_j c_j$ and the density and viscosity based on the ambient conditions. In Tab. 4.2 an exemplary sketch of the main flow parameters of a jet with $M_j = 1.55$ are presented for four characteristic locations: in the ambient fluid, in the reservoir chamber, at the nozzle exit and in the fully expanded jet. Ambient temperature and pressure in all cases is chosen to be $T_\infty = 300$ [K] and $p_\infty = 10^5$ [Pa], respectively. Based on these conditions, the diameter or hight of the jet is $D = h = 1.66 \cdot 10^{-4}$ [m]. Prandtl number is $Pr = 0.71$ with a constant ration of specific heats $\gamma = 1.4$. In all simulations a CFL number (Courant-Friedrichs-Lewy) of CFL = 0.7 is adjusted to compute the time step. During the Krylov time integration a maximum of 15 subspaces is used.

4.1 Planar jet

The computational domain of the planar jet is periodic in the z-direction and has the dimension of $25h \times 15h \times 4h$ in the x, y and z-direction (with

Position		p	M	T	ρ	s	c	u	μ
Ambient	$(\cdot)_\infty$	$1.00 \cdot 10^5$	0	300.00	1.16	8110.19	347.19	0	$1.71 \cdot 10^5$
Reservoir	$(\cdot)_r$	$3.95 \cdot 10^5$	0	300.00	4.59	7716.04	347.19	0	$1.71 \cdot 10^5$
Nozzle exit	$(\cdot)_e$	$2.09 \cdot 10^5$	1.00	250.00	2.91	7716.04	316.94	316.94	$1.48 \cdot 10^5$
Fully exp. jet	$(\cdot)_j$	$1.00 \cdot 10^5$	1.55	202.63	1.72	7716.04	285.34	442.28	$1.24 \cdot 10^5$

Table 4.2: Showcase of the flow conditions for a $M_j = 1.55$ jet at four different characteristic locations. With the pressure p [Pa], the Mach number M [-], the temperature T [K], the density ρ [kg m^{-3}], the entropy s [m^2 K^{-1} s^{-2}], the speed of sound c [m s^{-1}], the stream-wise velocity u [m s^{-1}] and the viscosity μ [kg m^{-1} s^{-1}].

the height of the nozzle h). The convergent nozzle extends $3h$ in the computational domain (cf. Fig. 2.8(a)). With a total of $16 \times 16 = 256$ blocks, the computational domain is decomposed and solved in parallel on 256 cores.

In Fig. 4.1 a snapshot of the planar jet for the Mach number $M_j = 1.55$ is presented as an exemplary picture for this parametric study. It shows the nozzle and the magnitude of the vorticity as an iso-surface. The slice, normal to the periodic directions, visualizes the pressure fluctuations in the color-range of ±10 [kPa]. One can identify loud acoustic waves emanating from the position of the third shock cell with a distinct wavelength. These acoustic waves correspond to the screech tone and dominate the acoustic near-field with a wave length of about two shock cells. In addition to that, the flapping mode can be identified as the acoustic signal on both sides of the jet is π-shifted. The acoustic waves are emanated alternatively on each side of the jet.

Responsible for this behavior is the secondary instability of the jet which is clearly visible in the iso-surface of the vorticity. Whereas the first two shock cells seem to be very stationary and stable, the jet undergoes a strong oscillation (flapping) staring at the third shock cell. Thereby, alternating vortices are generated at each side of the jet and convected downstream. In the low vorticity region, between two consecutive vortices, the circularly shaped acoustic wave is emanating. A phenomenon also referred to as shock-leakage [see Suzuki & Lele, 2003].

At the nozzle exit, the interaction of upstream propagating acoustic waves and the hydrodynamic instabilities in the mixing-layer takes place. As we have seen already, this phenomenon can be amplified by increasing the nozzle lip thickness. The upstream propagating acoustic waves are reflected at this point and causing a strong acoustic pressure peak triggering the instabilities.

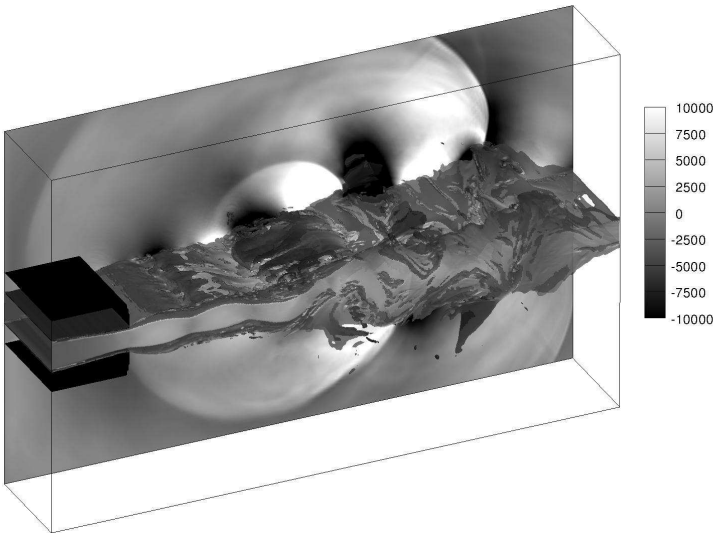

Figure 4.1: Snapshot of the planar jet showing the convergent nozzle and the iso-surface of the vorticity magnitude. Slice visualizes the pressure fluctuation in the color-range of ±10 [kPa]. Sponge at the outlet not included.

To this end a thick nozzle, with a lip as thick as the jet height is chosen. In Fig. 4.2 the dimensions of the planar nozzle are presented. The total length of the nozzle is $L_o = 3h$ with the height h of nozzle exit. At the inlet of the nozzle, the height is chosen such that the Mach number of the convergent nozzle is $M_i = 0.5$. This corresponds to a height of $D_{ii} = 1.34h$ (cf. also Eq. (1.8)). At this point, an inlet condition prescribes the pressure, the entropy and the velocities in the nozzle to match the state of under-expansion. The velocity satisfies the non-slip condition at the inlet with a sharp boundary layer thickness (one grid point). Inside the nozzle the boundary layer develops and reaches its final thickness at the nozzle exit. Pressure and entropy are distributed uniformly over the nozzle inlet. No additional forcing or turbulent energy is applied.

Shock cell spacing In Fig. 4.3 the shock cell spacing of the planar jet is presented as a function of the fully expanded Mach number. The numerical data are extracted for all investigated Mach numbers above $M_j = 1$ (cf. Tab. 4.1). For this design Mach number, the jet is ideally expanded and no shocks are

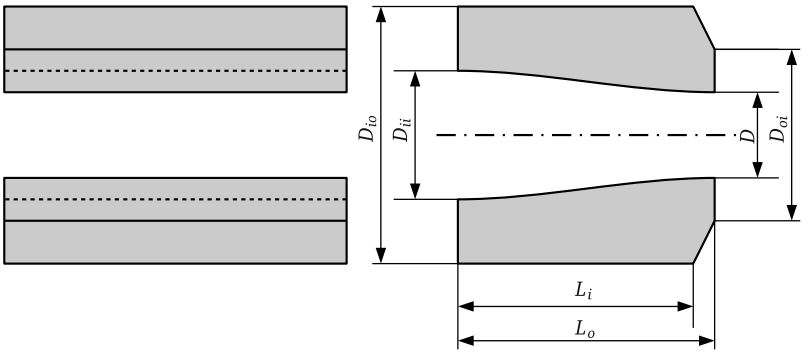

Figure 4.2: Dimensions of the planar convergent nozzle. Design Mach number $M_d = 1$; inlet Mach number $M_i = 0.5$. $D = h$, $D_{io} = 3D$, $D_{ii} = 1.34D$, $D_{oi} = 2D$, $L_i = 2.9D$, $L_o = 3D$.

present. The values above the design point correspond to the mean length of the first two shock cells and are taken from the mean pressure field of the fully developed jet. In this study, experimental, analytical and other numerical data are included to validate the result. The analytical data corresponds to a theory by Tam [1988] (solid and dashed line) whereas the dashed line stands for a nozzle aspect ratio of $b/h = 4$ and the solid line for an infinitely large aspect ratio ($b \gg h$). One can identify that the shock cell spacing of the present investigation (filled black bullets) matches well the analytical theory for a jet with aspect ratio $b/h = 4$ as in the present study, although the jet is periodic (infinitely large aspect ratio). There seems to be a relation between the domain length in the periodic direction and the aspect ratio of the jet.

Various experimental data on jets with different aspect ratios and Mach numbers confirm the analytical theory of Tam [1988] and validate the present numerical computation. In addition to that, two other numerical data are included in the figure. The first corresponds to an investigation of a jet with a nozzle modeled by a velocity profile at the inlet [Schulze et al., 2009a] and a fully expanded jet Mach number of $M_j = 1.61$. Their results match the analytical and experimental data. According to Tam [1988] an Morris et al. [1989] the shock cell spacing is related to the jet Mach number and the height of the supersonic area in the jet. The latter one strongly depends on the shear layer thickness. For a velocity profile at the inlet, the initial shear layer thickness can be adjusted to match the analytical data. Berland et al. [2007] who provide the second numerical data in this figure underestimate

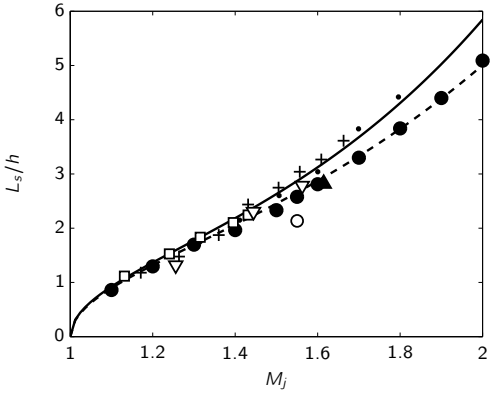

Figure 4.3: Shock cell spacing as a function of the fully expanded jet Mach number M_j for various experimental and numerical data. Experimental: +, Hammitt [1961]; □, Powell [1953b]; ▽, Raman & Rice [1994]; ◦, Panda et al. [1997]; Numerical: ○, Berland et al. [2007]; ▲, Schulze et al. [2009a] (nozzle: velocity profile); ●, current computation (porous nozzle); Theory: (———), Tam [1988] for $b \gg h$; (- - - - - -), Tam [1988] for $b/h = 4$ (as in the current computation).

the shock cell length. They explain this deviation with the initial shear layer thickness which is larger than in experimental data.

The mean velocity profile of the planar jet is shown in Fig. 4.4. Besides experimental data from Gutmark & Wygnanski [1976], Bradbury [1965] and Ramaprian & Chandrasekhara [1985] and numerical data from Berland et al. [2006] it also contains an analytical solution based on [Pope, 2000, Eq. (5.187)] which reads:

$$\frac{\bar{u}}{U_m} = \cosh^{-2}\left(\log\left(1+\sqrt{2}\right)\frac{y}{\delta_{0.5}}\right) \tag{4.2}$$

with the distance to the jet axis y and the half width of the self-similar profile $\delta_{0.5}$. The mean velocity profile of the current numerical computation is measured at $x/h = 17$. It is in good agreement to the experimental, numerical and analytical data especially in the area close to the jet axis $0 \le y/\delta_{0.5} \le 2$. At the edges of the profile the numerical solution tends more rapidly to zero as the analytical solution. This deviation is related to the "uniform turbulent viscosity" assumption used in the analytical solution which can not be applied in areas where the turbulent viscosity is diminishing [see L'vov et al., 2008, Pope, 2000].

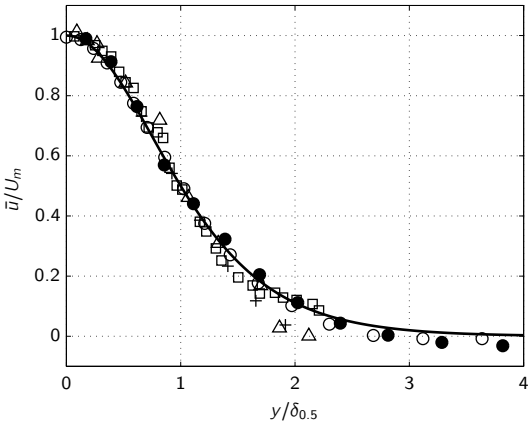

Figure 4.4: Mean velocity profile in the transverse direction of the jet for analytical data: (———), Pope [2000], experimental data: +, Gutmark & Wygnanski [1976]; □, Bradbury [1965]; △, Ramaprian & Chandrasekhara [1985]; and numerical data: ○, Berland et al. [2006]; ●, current computation with $M_j = 1.55$ measured at $x/h = 17$.

Screech frequency and amplitude According to the theory on jet screech presented in the introduction of this thesis, the screech frequency strongly depends on the shock cell spacing. Hence, the correct prediction of the shock cell spacing is of particular importance for screech computations. The correct prediction of the shock cell spacing could be shown in the last paragraph.

The screech frequency (here expressed with the Strouhal number $Sr = fh/U_j$) as a function of the fully expanded jet Mach number is presented in Fig. 4.5(b). It includes, besides the current numerical data (black filled bullet), an analytical theory by Tam [1988] (solid line), experimental data by Panda et al. [1997] and two numerical investigations. The current numerical simulation on planar jet screech for Mach numbers in the range of $1.2 \leq M_j \leq 2.0$ perfectly matches the theoretical prediction.

The acoustic signal (pressure fluctuations) is measured in the near field of the jet in a distance of $6.5h$ to the jet axis and in an angle of $\Theta = 90°$. Hence, above the nozzle exit. It is decomposed in frequency space and the dominant peak of the spectrum extracted and presented in the figure. For Mach number below $M_j = 1.2$ no screech tone could be identified in the spectrum and the corresponding data points are not included (for $M_j = M_d = 1$ no shocks and hence no screech is present). A screech tone for high Mach numbers above $M_j = 1.8$ can be identified also. Even for $M_j = 2$ a peak, occurring at the

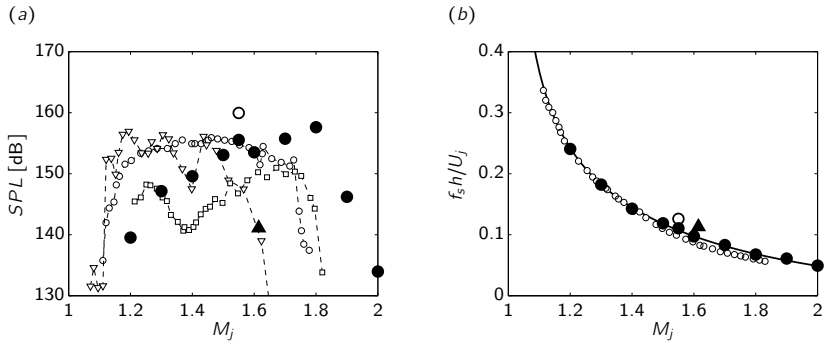

Figure 4.5: Screech amplitude and frequency of a rectangular jet versus the fully expanded jet Mach number M_j. Experimental: ◦, Panda et al. [1997]; ▫, Raman [1997b]; ▽, Raman & Rice [1994]; Numerical: ○, Berland et al. [2007]; ▲, Schulze et al. [2009a] (nozzle: velocity profile); ●, current computation (porous nozzle); Theory: (———), Tam [1988]. (*a*) Screech amplitude versus the fully expanded jet Mach number. (*b*) Dominant screech frequency as a function of the jet Mach number M_j.

estimated screech frequency, is visible in the spectrum. Yet, the amplitude of this high Mach number peak, compared to the moderate Mach number computations, is small.

In addition to the analytical theory by Tam [1988], the experimental data by Panda et al. [1997] match the theoretical estimation and validate the current numerical computation. Again, the two numerical data by Berland et al. [2007] and Schulze et al. [2009a] confirm that the correct prediction of the screech frequency is by no means trivial. As for the shock cell spacing, the numerical data of Berland et al. [2007] show deviations due to the wrong shear-layer thickness. A similar deviation can be found in the data of Schulze et al. [2009a]. It may be a result of their artificial forcing to close the screech feedback loop when modeling the presence of the nozzle.

To find an agreement of the screech amplitude between experimental data and numerical data is even more challenging. Up to now no analytical theory exists to predict the correct screech amplitude. Even between different experimental data, big discrepancies can be found. In Fig. 4.5(*a*) the screech amplitude of the detectable screech tones of the current computation is presented as a function of the fully expanded jet Mach number, including various experimental and numerical data. Between the experimental data of Panda et al. [1997] and Raman [1997b] a deviation of up to 15 dB occurs at a Mach number of $M_j = 1.4$ with a jet of the same aspect ratio ($b/h = 5$) but differ-

ent size (Raman used a two times larger nozzle than Panda et al.). Raman & Rice [1994] used a similar height of the jet as Panda et al. [1997] (7 % larger) yet with an aspect ratio of $b/h = 9.63$. At a Mach number of $M_j = 1.4$ a deviation of 10 dB is visible between the experimental data of Raman & Rice and Panda et al.. This concludes that the prediction of the screech amplitude is strongly dependent on the environmental conditions and specific nozzle geometries.

In the same figure the numerical data of the present investigation are included and marked with a black filled bullet. The amplitudes of the Mach number range $1.3 \leq M_j \leq 1.6$ lie between the experimental data of Panda et al. [1997], Raman [1997b] and Raman & Rice [1994]. They reach values from 147 dB up to 155 dB increasing with the Mach number in the range of $1.3 \leq M_j \leq 1.55$. One can identify a slight dropping in the amplitude of about 2 dB when increasing the Mach number up to a value of $M_j = 1.6$. This dropping is also visible in the experimental data by Panda et al. [1997]. Raman [1996], who investigated the same nozzle as Panda et al. [1997], could reproduce this dropping at the Mach number $M_j = 1.6$. It is noted by Raman [1996] that the screech phenomenon becomes unstable for Mach numbers above $M_j = 1.65$. This unsteadiness may be the reason for the drop in the amplitude. Furthermore, they explain the sudden cessation of screech for higher Mach numbers $M_j \geq 1.75$ due to a diminishing of the acoustic feedback and receptivity. Responsible for this phenomenon is the increased expansion of the jet boundary, the "barrel" shock (or "bottle" shock [see Crist et al., 1966]). The growth of the maximum jet boundary beyond the nozzle lip blocks the feedback. This concludes that a thicker nozzle can shift the cessation of screech to higher Mach numbers and was proved experimentally by Raman [1996]. In the experimental data shown in Fig. 4.5(a) the nozzle thickness t is about $t/h = 0.2$. With such a nozzle the screech diminishes at a Mach numbers of $M_j \geq 1.75$. Increasing the nozzle lip to $t/h = 2$ the cessation of screech can be shifted to $M_j = 1.95$ [see Raman, 1996]. Similar results on axisymmetric jets could be observed by Ponton & Seiner [1992]. They increased the nozzle lip of their axisymmetric jet from $t/D = 0.2$ to $t/D = 0.625$ and could shift the point of screech cessation from $M_j = 1.6$ up to $M_j = 1.9$.

In the present numerical investigation the nozzle lip thickness is $t/h = 1$ and the diminishing of the screech tone starts at $M_j = 1.8$ and ceases at $M_j = 2$. The maximum height of the shear layer within the first shock cell due to the barrel shock is presented in Fig. 4.6 including experimental and analytical data by Raman [1996] and Love et al. [1959], respectively. A good agreement of the current numerical data and the experimental and analytical results can be found. For a Mach number of $M_j = 1.8$, the maximum height

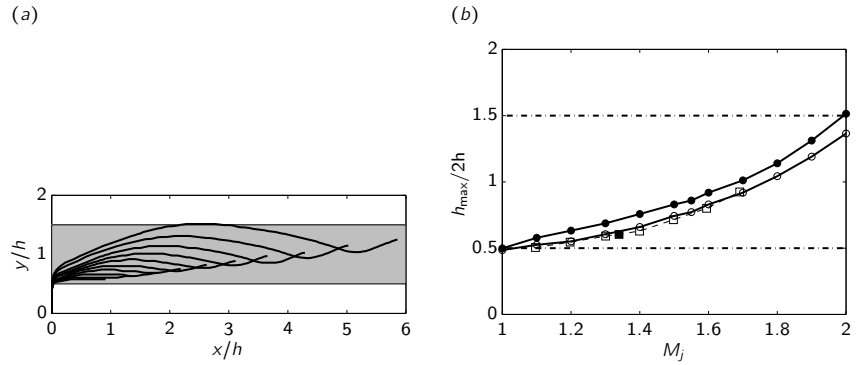

Figure 4.6: (*a*) Shape of the "barrel" shock based on the current computation for different Mach numbers. Extracted for $u > 0.1c_\infty$. Starting from $M_j = 1.1$ (innermost curve) up to $M_j = 2.0$ (outermost curve) in 0.1 steps. Gray area marks the size of the nozzle lip. (*b*) Maximum height of the expanded jet within the first shock cell. Due to the imperfectly expanded condition, the shear-layer follows the "barrel" shock. Current computation: (•) for $u > 0.1c_\infty$; (◦) for $u > 0.4c_\infty$. Experimental data: □ Raman [1996]. Analytical data: ■ Love et al. [1959].

(based on $u = 0.5c_\infty$) of the jet is about $h_{\max} = 2.0h$ which corresponds to a lip thickness of $t/h = 1$. This confirms the assumption of Raman [1996] that the barrel shock blocks the feedback loop and that one can shift the point of screech cessation by increasing the nozzle lip. In the latter case, to shift the point of screech cessation, the nozzle lip needs to be at lest as thick as the corresponding maximum height of the barrel shock (cf. Fig. 4.6).

In Fig. 4.5, two other numerical data are presented. The first (Schulze et al. [2009a]) underestimate the screech amplitude. As already mentioned, they use an artificial forcing to close the feedback loop where the gain of the forcing is chosen arbitrarily. So, a correct prediction of the screech amplitude is not possible. The second numerical data by Berland et al. [2007] slightly over-predicts the experimental data. They explain this behavior with an increased shock strength of the planar geometry compared to the rectangular geometries in the experiments.

As we could see, the present method is not only capable to predict the correct screech frequency of planar jets but also suitable to estimate a screech intensity comparable to experimental data. In the following paragraph the noise signal emanated of a supersonic jet is investigated in more detail.

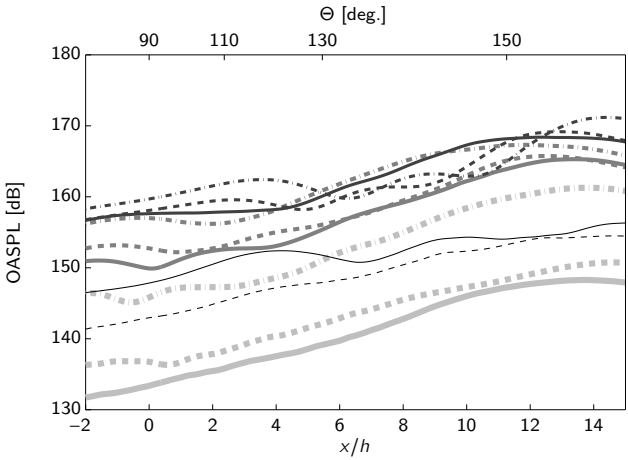

Figure 4.7: Overall sound pressure level as a function of observation location. M_j = 1.0 ( ), M_j = 1.1 ( ), M_j = 1.2 ( ), M_j = 1.3 ( ), M_j = 1.4 ( ), M_j = 1.5 ( ), M_j = 1.6 ( ), M_j = 1.7 ( ), M_j = 1.8 ( ), M_j = 1.9 ( ), M_j = 2.0 ( ) .

Noise and their spectra In Fig. 4.7 the OASPL of the planar jet as a function of the observation location (angle) is presented for all planar jets investigated. The OASPL includes all noise components of the jet and it is measured along a line parallel to the jet axis in a distance of $6.5h$. One can see that the OASPL is increasing for all jets with an increase of the observation angle (measured from the upstream direction). The maximum peak occurs in the area of $11 \leq x/h \leq 15$ which corresponds to an observation angle of about $\Theta = 150°$ and agrees well with experimental data [see amongst others Seiner et al., 1986a]. Only two curves, corresponding to $M_j = 1$ and $M_j = 2$, grow monotonically in the noise level up to the peak value. For these two Mach numbers no screech tone (for $M_j = 1.0$), or only a weak screech tone (for $M_j = 2.0$) can be detected and the noise is dominated by mixing noise in the downstream direction. As one might expect, the ideally expanded jet with $M_j = 1.0$ shows the smallest noise level in all observation directions. All higher jet Mach numbers are louder. For the imperfectly expanded Mach numbers up to a Mach number of $M_j = 1.9$ local minima can be identified. These minima occur mainly at observation angles of $90° \leq \Theta \leq 100°$. In this direction the screech tone is less dominant than in the upstream direction and hence reduces the OASPL [Seiner, 1984].

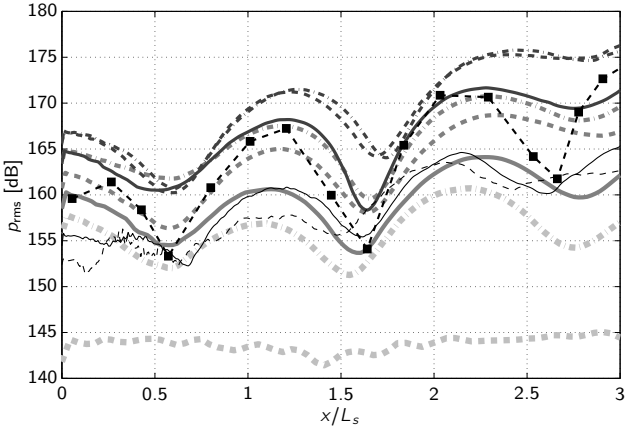

Figure 4.8: RMS pressure fluctuations just outside the jet boundary. Experimental data: ■ Panda et al. [1997] for $M_j = 1.42$; current computation (same line types used as in Fig. 4.7).

It is interesting to note that the two highest Mach numbers $M_j = 1.9$ and $M_j = 2.0$ are not the loudest jets. This correlates with the cessation of the screech tone for these high Mach numbers. The $M_j = 2.0$ jet is quieter than the $M_j = 1.9$ jet and still quieter than the low Mach number but screeching jet with $M_j = 1.2$. This fact illustrates the efficient mechanism of noise production on screeching jets. It can also be seen clearly in the jump of the sound pressure levels when increasing the Mach number from $M_j = 1.1$ (no screech detectable) to $M_j = 1.2$ (screeching jet). As in the remaining cases, the jump of the Mach number is in the order of 5 dB when switching to the next higher Mach number, it is more than 10 dB when the jet starts to "screech".

The overall loudest jet in the upstream direction can be identified with a Mach number of $M_j = 1.8$ followed by decreasing Mach number (produces also the loudest screech tone with 159 dB). In addition to that, this jet is the loudest candidate in the downstream direction. Up to 170 dB are measured at a location of $x/h = 14$. Only in a narrow band between $5 \leq x/h \leq 12$ the two slower jets ($M_j = 1.6$ and $M_j = 1.7$) are two to five dB louder.

Supersonic jet screech is due to a feedback mechanism of acoustic waves propagating upstream and being reflected at the solid nozzle lip (assuming that the nozzle lip is thick enough; cf. screech cessation due to the "barrel" shock). A planar acoustic wave which is reflected at a solid wall forms a

standing wave with nodes and antinodes (cf. § 1.1.2: "Acoustic reflector"). An antinode can be found at the nozzle lip followed by a node in the distance of one fourth of the screech wavelength λ_s. The presence of the standing wave in the acoustic near-field, close to the boundary of the jet, is an indication for the feedback loop. To visualize the standing wave, the RMS value of the pressure fluctuation is presented in Fig. 4.8. It is measured in dB with a reference pressure of $p_{\text{ref}} = 2{\cdot}10^{-5}$ [Pa] as a function of the downstream distance from the nozzle exit, scaled with the shock cell spacing. The latter one is approximated with Eq. (1.3). To avoid an interaction with the hydrodynamic pressure fluctuations of the spreading jet, the measurement is performed on line with an inclination angle of 10° with respect to the jet axis and starts in a distance of $y/h = 1$ from the centerline of the jet. The data points are interpolated if they do not match the computational grid. It has to be mentioned that a standing wave is not specific to supersonic screeching jets. Lepicovsky & Ahuja [1985] found a standing wave in the near-field of subsonic edge-tone situations [see also Raman, 1998].

One can identify clearly the standing wave characteristic in Fig. 4.8 for Mach numbers larger than $M_j = 1.1$. One can also identify that, due to the scaling with the shock cell spacing, the individual curves are aligned. This feature is again an indication that the standing wave is a important length scale for screeching jets [see Panda et al., 1997].

As there is no analytical solution for a shock cell spacing for the perfectly expanded jet with $M_j = M_d = 1.0$, the first jet shown starts at $M_j = 1.1$. The corresponding curve shows no identifiable pressure modulation with respect to a standing wave. It is nearly constant at a level of 144 dB over the whole range in the downstream direction. For this jet no screech is detectable in the measured spectrum which again is an indication that a standing wave is essential for the formation of screech tones. The first jet including a detectable screech in the spectrum has a Mach number of $M_j = 1.2$. In this case, the corresponding curve is more than 10 dB louder than in the previous case and the typical modulation for a standing wave is visible. The RMS value of the pressure fluctuation starts with an antinode at the nozzle lip followed by a node at $x/L_s = 0.5$. This pattern is repeated in the downstream direction. Jets with larger Mach number show higher levels up to peak values of more than 175 dB for the jet with $M_j = 1.8$ above the third shock cell. From this point on, the levels are decreasing again (for $M_j = 1.9$, 2.0). The standing wave pattern is still visible but with a low amplitude in the order of the $M_j = 1.2$ jet. In addition to that, an experimental data from Panda et al. [1997] for a $M_j = 1.42$ jet is included in this figure. The data is based on a round jet measured at an inclination angle of 5.7° (numerical data at 10°).

A good agreement between the numerical and the experimental data can be observed. Both the standing wave spacing and the amplitude align with the current computation.

In Fig. 4.9 the spectra of each planar jet investigated is presented. All spectra are captured at an observation angle of $\Theta = 90°$ in a distance of $y/h = 6.5$ to the jet axis. A logarithmic scaling is used for the abscissa and the frequency is expressed with the Strouhal number $Sr = f \cdot h/u_j$ in the range of $0.01 \leq Sr \leq 3$. The spectra for the screeching jets ($1.2 \leq M_j \leq 1.8$) present the typical spectrum of a supersonic jet including the screech tone. All three noise components can be identified. The mixing noise with low frequency and an amplitude in the order of 130 dB. The broadband shock-associated noise with high frequency and finally the dominant peak in the spectrum, the fundamental screech tone. In addition to that, the analytical solution [based on the theory of Tam, 1988] of the screech tone including its seven subharmonics is included in the spectra and marked with vertical dashed lines (except for $M_j = 1.0$ as $M_j = M_d$).

The first spectrum where one can observe screech is for $M_j = 1.2$. A peak occurring at the analytical estimation of the fundamental screech tone with an amplitude of 140 dB can be identified. No higher subharmonics of the fundamental screech tone are detectable. This picture is different for the next higher Mach number investigated ($M_j = 1.3$). Despite the fundamental peak at the estimated screech frequency, up to seven subharmonics can be identified with decreasing amplitude. Between two subsequent subharmonics a decrease in the noise level of roughly 3 – 4 dB is visible. This behavior is maintained up to a Mach number of $M_j = 1.8$. The next higher Mach number $M_j = 1.9$ contains a peak at the estimated screech frequency, yet with a 15 dB reduced amplitude to its preceeding case an without any detectable subharmonics. In the highest Mach number case ($M_j = 2.0$), again a peak at the estimated screech frequency is visible but hard to distinguish from the remaining shock-associated noise level. Again, this observation concludes that screech starts to cease for the present nozzle configuration at a fully expanded jet Mach number of $M_j > 1.8$. For the present nozzle configuration with a lip thickness of $t/h = 1$ this result is in good agreement to experimental data [see amongst others, Ponton & Seiner, 1992, Raman, 1996].

The low Mach number under-expanded jet with $M_j = 1.1$ does not contain any identifiable screech tones. Neither the fundamental one nor its subharmonics. However, a wide peak is visible with a maximum between $Sr = 0.5$ and $Sr = 0.6$ (the estimated screech Strouhal number is $Sr = 0.37$). One can assume that the peak in the spectrum is due to shock-associated noise. And indeed, when estimating the peak shock-associated noise based on Eq. (1.12)

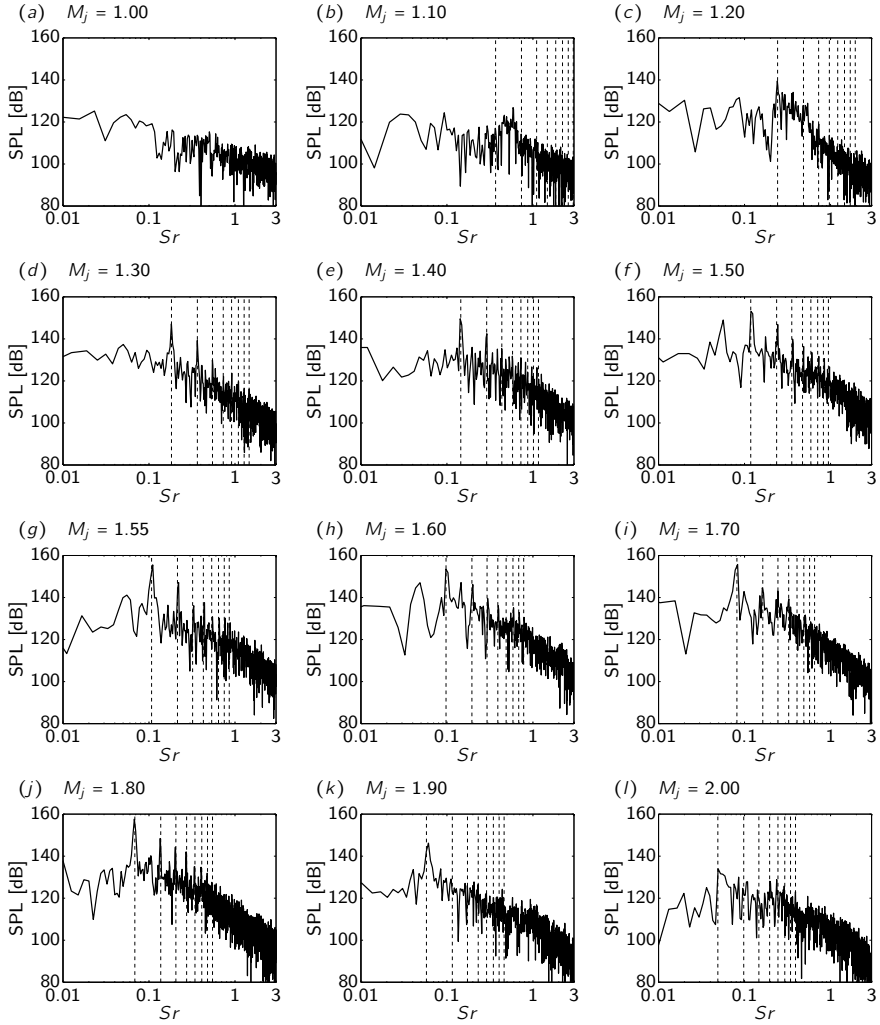

Figure 4.9: Spectra of the planar jet for different Mach numbers ($1.00 \leq M_j \leq 2.00$ corresponding to panel (*a*) to (*l*)). Vertical dashed lines represent the fundamental screech frequency including the first seven subharmonics based on the theory of Tam [1988].

one obtains a Strouhal number of $Sr_{BB} = 0.54$ which matches the measured peak. Another evidence for this peak to be related to shock associated noise is the fact that it is missing in the $M_j = 1.0$ jet. In this case, the loudest noise source is located at the lower end of the displayed spectrum and related to jet mixing noise.

All spectra are based on a FFT of the pressure fluctuations starting from the time where the screech tone is developed (cf. also Fig. 4.11). In Fig. 4.10 the signal corresponding to the spectra of Fig. 4.9 are presented. Only a small time span containing the history of the last ten computed screech cycles is shown. One can identify that the amplitude is increasing with the Mach number at least up to a value of $M_j = 1.8$ and then decreasing again. In addition to that, one can see that the screech tone is dominating the signal for the screeching jet Mach numbers. For Mach numbers in the range of $1.4 \leq M_j \leq 1.8$ the signal shows a characteristic sawtooth like shape with sharp wave fronts. This is not as clearly visible in the $M_j = 1.2$ and $M_j = 1.3$ jet.

All signals are superimposed with a noise component of high frequency corresponding th the broadband noise sources. Especially in the high Mach number jet with $M_j = 2.0$ the noise of high frequency dominates the signal. The signals of the screeching jets are indeed different to each other. Some seem to be very regular, like the one for $M_j = 1.4$ whereas other seem to be unstable, like the one for $M_j = 1.6$. However, most of them exhibit a regular pattern. This is especially visible for the $M_j = 1.5$ and $M_j = 1.8$ jet, where the shape of an individual wavefront is repeated every second screech cycle. A high amplitude wave is followed by a low amplitude wave and so on. One can also see that the peaks of the positive pressure fluctuations are larger, sharper and more noisy than their negative counterparts (see e. g. the signal for $M_j = 1.8$). This sharp and loud positive wavefront is likely due to the shock which "leaks" through the mixing layer and creates this sawtooth like structure. In Fig. 4.1 this behavior is also apparent where the acoustic pressure fluctuations create circularly shaped sharp wavefronts on each side of the jet. This observation confirms well with the results of e. g. Manning [1999] and Suzuki & Lele [2003] on shock laden mixing layers.

In Fig. 4.11 two characteristic noise signals for a jet with $M_j = 1.1$ and a jet with $M_j = 1.55$ are presented from the beginning of the numerical simulation. In the high Mach number case it is clearly visible that it takes some time to develop screech tones. The first time, the loud screech tone can be identified starts from roughly $t/T_s = 10$ (with the time for one screech cycle T_s). This initial time can be approximated using the following assumptions. During the initial condition, the flow in the jet core is based on a velocity distri-

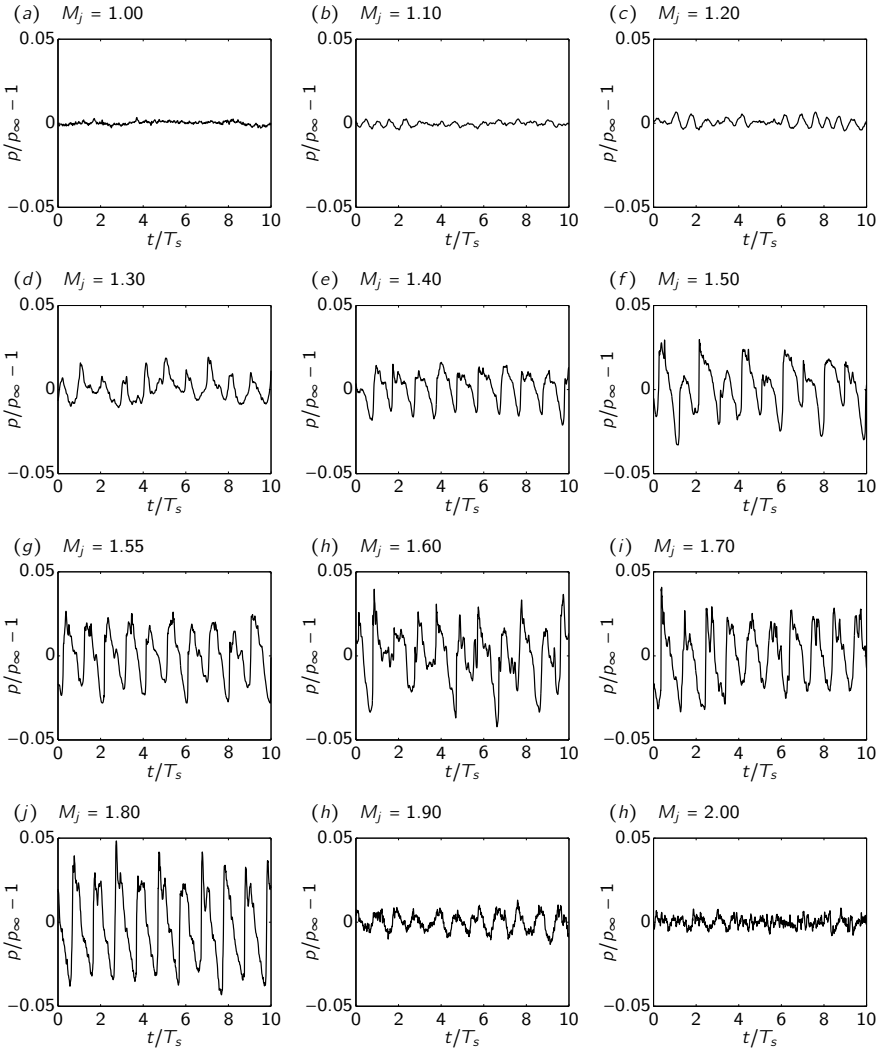

Figure 4.10: History of the pressure fluctuations containing the last ten computed screech cycles for different Mach numbers.

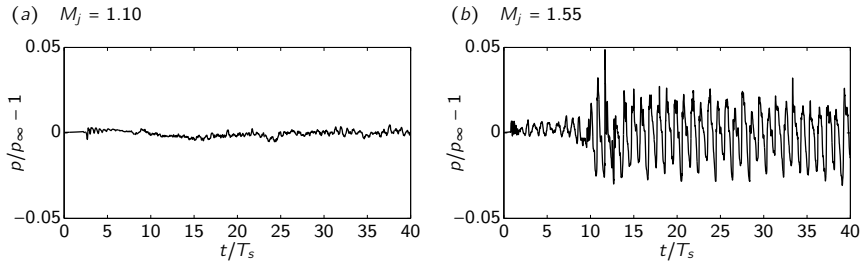

Figure 4.11: History of the pressure fluctuations captured from the beginning of the simulation. Two characteristic Mach numbers shown: (*a*) $M_j = 1.1$ and (*b*) $M_j = 1.55$.

bution typical for jet flows, like the one used in Schulze et al. [2009a] with a Mach number of $M_j = M_d = 1$. The pressure distribution is uniform and is equivalent to the ambient pressure. Hence, no shocks are present. When the simulation begins and the jet starts to expand and to adapt to the ambient pressure the characteristic shock pattern forms. It develops downstream with a velocity similar to the fully expanded Mach number. In contrast to that, the disturbances in the mixing layer are transported downstream with a convection Mach number of $M_c \approx 0.5$. Assuming that the noise source for screech tones is located at the end of the third shock cell, the first shock associated noise will emerge after $t_c = 3L_s/(M_c c)$ (with the shock spacing L_s, the ambient speed of sound c and the convective Mach number $M_c = 0.5$). This noise signal is now propagating upstream and interacting with the nozzle lip to trigger an instability. The elapsed time or the acoustic wave propagating upstream can be given by $t_a = 3L_s/c$. Now, the triggered instability is again transported downstream with M_c and interacting with the shock at $x = 3L_s$ and the feedback loop is closed for the first time. Subsequently, the emanated shock induced noise is emanated and will be detected by the microphone. In the present investigation the distance of the microphone to the noise source past the third shock cell is roughly $4L_s$, hence the elapsed time is $t_n = 4L_s/c$. Summing up all individual times, we get:

$$t = 2t_c + t_a + t_n = 19\frac{L_s}{c}.$$

For the present Mach number of $M_j = 1.55$ we can approximate the ratio of screech wavelength and shock cell spacing based on Eq. (1.3) and (1.15) and get: $\lambda_s/L_s \approx 2.30$. With this information we can estimate the total time in terms of screech cycles and get: $t = 8.26T_s$. Comparing this result with the

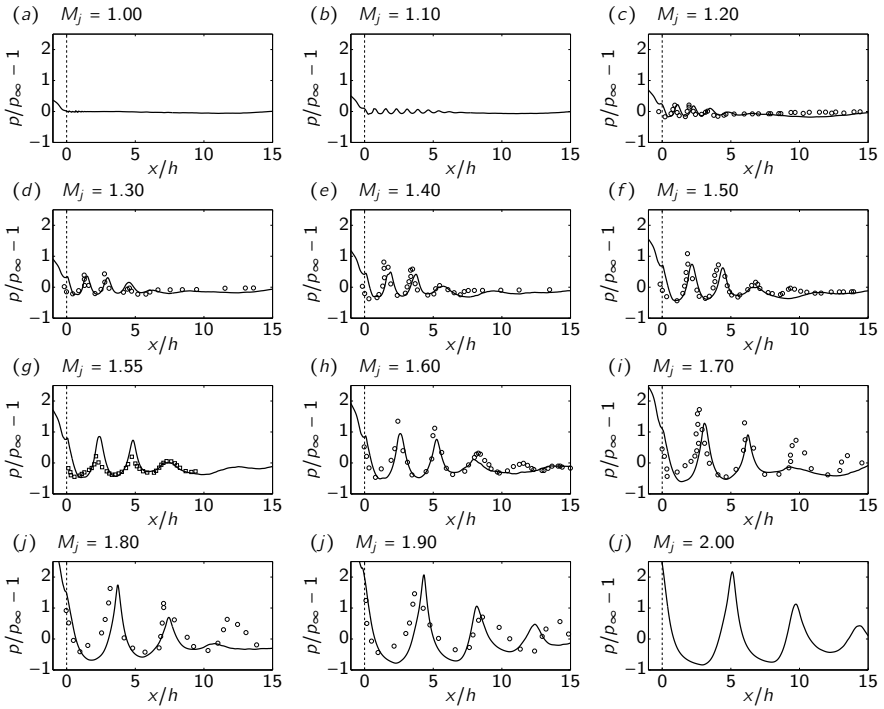

Figure 4.12: Mean pressure along the centerline of the jet for various jet Mach numbers (———). Nozzle exit at $x/h = 0$ marked with a dashed line (- - - - - -). Experimental data: □, for $M_j = 1.55$ [Raman, 1997a]; ○, for $M_j = 1.2$, 1.3, 1.4, 1.5, 1.6, 1.7, 1.8 and 1.9 [Norum, 1991].

signal of Fig. 4.11(b) where the screech tone starts at roughly $t = 10T_s$ one can conclude that the screech process, in the present numerical investigation, starts from the first time the feedback loop is closed.

Mean flow field In the following two figures, the mean values of the pressure and the stream-wise velocity are presented along the centerline of jet. The mean pressure is visualized in Fig. 4.12 for all Mach numbers investigated. Despite the numerical data, two experimental data by Raman [1997a] for the $M_j = 1.55$ jet and Norum [1991] for the remaining Mach numbers are included to validate the results. For the Mach numbers $M_j = 1.0$, 1.1 and 2.0 no experimental data are available.

For imperfectly expanded jets one can clearly identify the shock cells in the jet core with an "U"-like shape. The perfectly expanded jet does not contain any shocks in the jet core. With increasing Mach number, the nozzle exit pressure is increasing as the value of under-expansion is increasing as well (cf. Eq. (1.6)). As small part inside the nozzle (for $-1 \leq x/h \leq 0$) shows the pressure drop in the convergent nozzle as the Mach number is increasing here up to the design Mach number $M_d = 1$. Note the not the whole nozzle is visualized here. The total length of the nozzle is $x/h = 3$.

One can identify a significant difference between the screeching jets ($1.2 \leq M_j \leq 1.8$) and the non screeching jets (remaining Mach numbers). The difference is clearly visible in the number of detectable shock cells. Whereas one can count at least eight shock cells for the $M_j = 1.1$ jet, only two to three shock cells are remaining for the screeching jets. This trend is also visible for the two non screeching high Mach number jets although the presented domain is limited and not all shock cells are visible. The reason for the reduced number of shock cells for a screeching jet has been reported by many researchers and is mentioned already in the introduction of this thesis. It is related to the enhanced mixing of the screeching jet. The jet undergoes a strong oscillation (flapping or antisymmetric mode) when the screech cycle forms and this destroys the periodic shock cell structure. Hence, the reduced shock cells are an additional evidence for the screeching of a jet. In Sec. § 6 we will see that a jet with an optimized porous material (no screech) contains additional shock cells compared to a jet without porous material (screech).

The experimental data by Raman [1997a] and Norum [1991] indicate that on the one hand the shock cell spacing (which is increasing with the Mach number) is captured correctly and on the other hand that the shape of the pressure distribution along the jet axis is predicted correctly. There seems to be a difference in the amplitude of the shock cells. Whereas the data by Raman [1997a] underestimates the numerical data ($M_j = 1.55$) the data by Norum [1991] over-predicts slightly the current computation. It is also interesting to see that the number of shock cells in the experimental and numerical data is comparable. Only for the Mach number cases $M_j = 1.7$ and $M_j = 1.8$ the experimental data show an additional third and fourth shock cell which is not visible in the numerical data. Once again, this is due to the shifted cessation point of screech due to the thick nozzle lip in the present numerical investigation. The nozzle lip of the experimental data by Norum [1991] is inclined by 30° and hence less efficient to form a standing wave.

Similar to Fig. 4.12 are the data presented in Fig. 4.13. Here, the absolute velocity is shown along the centerline of the jet and scaled with the jet exit velocity u_e. One can identify first, that the velocity inside the convergent

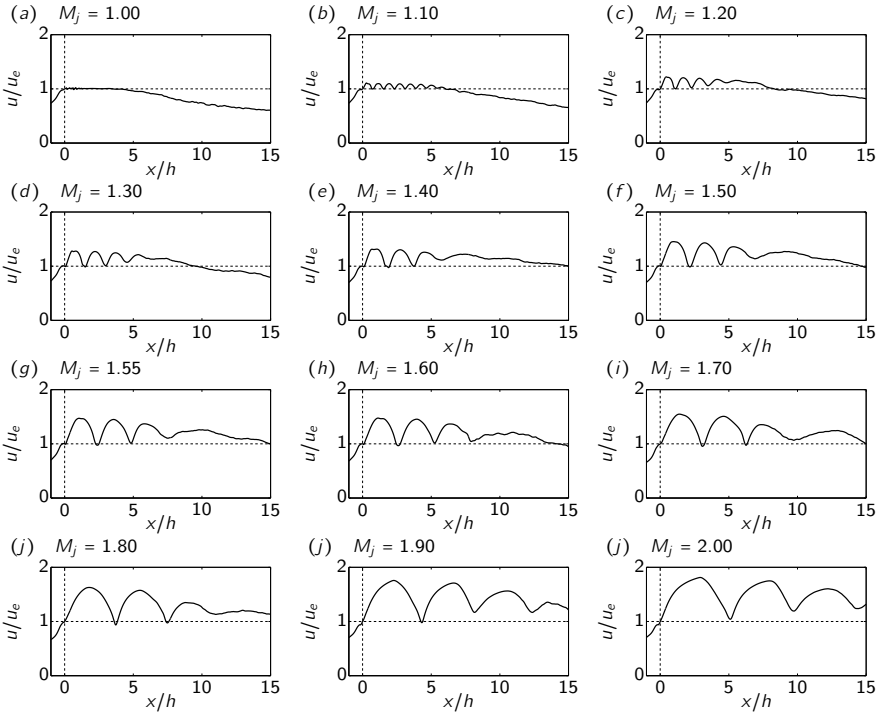

Figure 4.13: Mean absolute velocity along the centerline of the jet for various jet Mach numbers (———) scaled with the nozzle exit velocity u_e. Nozzle exit at $x/h = 0$ marked with a dashed line (- - - - - -).

nozzle is accelerated until it reaches the design Mach number $M_d = 1$. From this point on the velocity is accelerating further to match the value of underexpansion. For the ideally expanded jet ($M_j = 1$) one can identify that the potential core of the jet is about $5h$ long. After this point, the two mixing layers of each side of the jet interact and decrease the velocity in the fully developed jet to subsonic Mach numbers. The supersonic region of the $M_j = 1.1$ jet is about one jet diameter longer than the previous case ($6h$). Within the shock cells the velocity is increasing to its maximum value and then decreasing again until it reaches its minimum at the end of the shock cell. This pattern is repeated in the downstream direction until the shock cells vanish. The minimum value is the same as the jet exit velocity (here $M = 1$). Again, about eight shock cells are visible for the $M_j = 1.1$ jet and only three

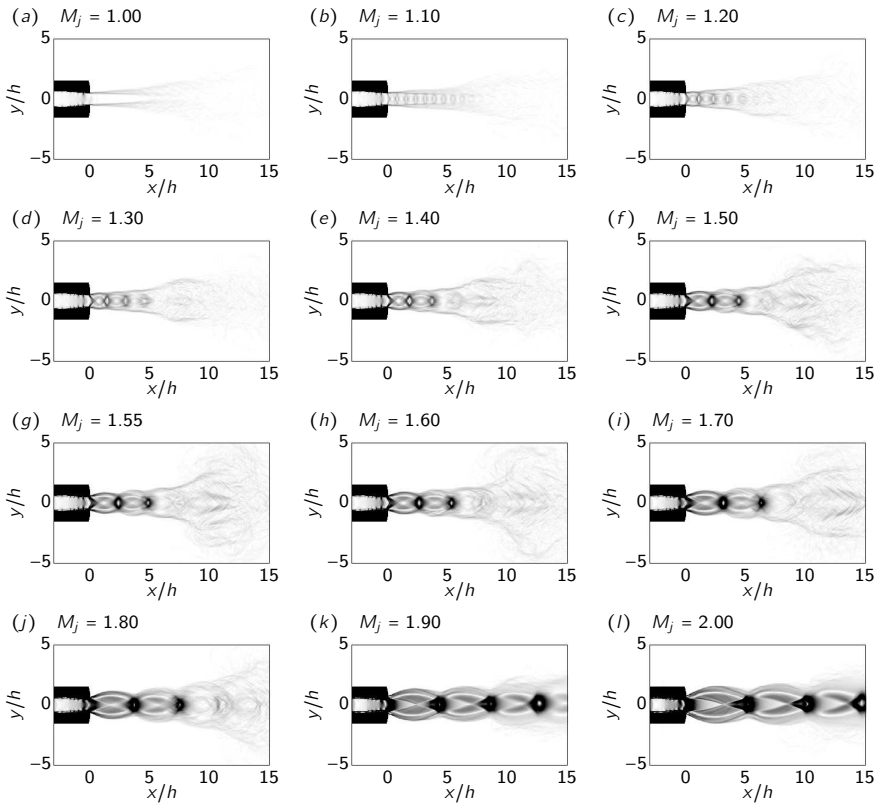

Figure 4.14: Pseudo Schlieren ($|\nabla\bar{\rho}|$) of the planar jet in the x-y-plane in the color-range of $0 \cdots 3\rho_\infty/h$. Visualization of all Mach numbers investigated ($1.0 \leq M_j \leq 2.0$) corresponding to panel ($a - l$).

to four for the screeching jets. In the latter case, the enhanced mixing due to the strong oscillations during screech blur out the regular pattern and create a uniform velocity profile which is still supersonic. As in the ideally expanded case it is decaying and finally reaching the subsonic regime (not shown for all jets).

A two-dimensional view of the mean pseudo Schlieren is given in a x-y-plane in Fig. 4.14 for all investigated Mach numbers. The visualization includes the nozzle extending from $-3 \leq x/h \leq 0$ in the domain. One can identify the complex shock cell pattern for the imperfectly expanded jets. In

the design case (M_j = 1.0, cf. panel (a)), no shocks are visible in the jet core and only the mixing layers can be identified. They are growing in the downstream direction until they finally close the potential core with a length of $x/h \approx 5$.

In the first under-expanded computation with a Mach number of M_j = 1.1 (cf. panel (b)) shock cells appear in the jet plume. Up to eight shock cells are visible with a narrow spacing of $L_s \approx 0.86h$. For the next higher Mach number (M_j = 1.2) screech occurs and the number of shock cells is reduced (4 to 5). The shape of the "barrel" shock starts to form and is just visible within the first shock cell. Due to the screech and the corresponding enhanced mixing of the jet, the jet spreads more rapidly than the two non screeching cases. The increased spreading starts past the fourth shock cell. For higher Mach numbers ($1.3 \leq M_j \leq 1.8$) the spreading starts earlier, past the third shock cell, and seems to be more intense. In addition to that, one can identify larger density gradients when increasing the Mach number due to stronger shocks. An increase of the shock cell spacing is also visible with a widening of the jet height due to the intense "barrel"-shock.

Comparing the mean pseudo Schlieren of M_j = 1.8 and M_j = 1.9 one can clearly see that in the M_j = 1.8 case the high density gradient (shock) at the end of the third shock cell is missing compared to the M_j = 1.9 jet. This again is related to the fact that the screech tone ceases for a Mach number larger than M_j = 1.8. Hence, mixing is reduced and the shock cell pattern is preserved over a wider range. This phenomenon can also be identified in panel (l) for the M_j = 2.0 jet. One can also see that the height of the "barrel"-shock in the high Mach number jet is in the order of the height of the nozzle lip (cf. also Fig. 4.6).

In Fig. 4.15 the RMS pressure fluctuations are presented in a two-dimensional x-y-plane and measured in dB ($p_{\text{ref}} = 2 \cdot 10^{-5}$ [Pa]). As in Fig. 4.8 the standing wave pattern is clearly visible for the screeching jets in the acoustic near-field of the jet close to the nozzle exit (within the first three shock cells). It is responsible for the feedback mechanism leading to the discrete screech tones. In the non screeching jets (M_j = 1.0, 1.1, 1.9 and 2.0) the standing wave is reduced or not detectable. In addition to that, one can identify loud noise levels in the upstream direction of the jet for the screeching cases. This is not visible in the non screeching jets. The acoustic near-field of the non screeching jets is dominated in the downstream direction (mainly mixing noise).

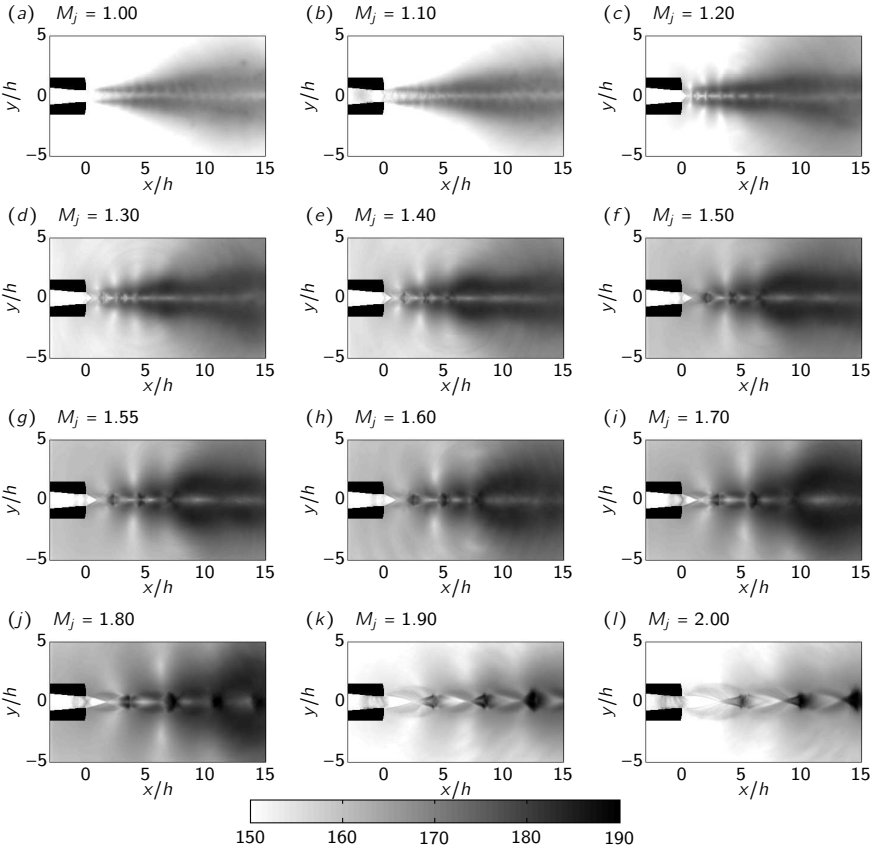

Figure 4.15: RMS pressure fluctuations in dB of the planar jet in the x-y-plane ($p_{\text{ref}} = 2 \cdot 10^{-5}$ [Pa]). Color scaling from white to black (150 - 190 dB). Visualization of all Mach numbers investigated ($1.0 \leq M_j \leq 2.0$) corresponding to panel ($a - l$).

4.2 Round jet

The physics of a round jet is different to the ones of a planar jet which we have seen in the last section. A round jet during screech undergoes oscillations with different modes depending on the Mach number, whereas the screeching planar jet is dominated by a flapping (antisymmetric) mode for all Mach numbers (besides a small symmetric range for small Mach numbers

$n1 \times n2 \times n3$	$dx_{\min}/D$	$\eta/dx_{\min}$	$n_{\text{ges}}/Re^{9/4}$	dt [s]	$Sr_{\max,\text{dt}}$	$Sr_{\max,\text{dx}}$
$256 \times 128 \times 128$	0.049	0.26	0.02	$5.28 \cdot 10^{-9}$	24.1	6.6
$512 \times 256 \times 256$	0.024	0.53	0.16	$2.63 \cdot 10^{-9}$	48.3	13.3
$1024 \times 512 \times 512$	0.012	1.06	1.28	$1.31 \cdot 10^{-9}$	96.9	26.6

Table 4.3: Time-step and grid spacing for the investigated resolution of the round nozzle. Kolmogorov scale: $\eta = (\nu^3/u_{\text{rms}}^3 L)^{1/4}$, with the approximation: $u_{\text{rms}} = 0.3c_\infty$. Maximum Strouhal number: $Sr_{\max,\text{dt}} = f_{\max,\text{dt}} D/u_j$, with $f_{\max,\text{dt}} = 1/(2dt)$; $Sr_{\max,\text{dx}} = f_{\max,\text{dx}} D/u_j$, with $f_{\max,\text{dx}} = c_\infty/(2dx)$.

[cf. Gutmark et al., 1990]). The modes of a axisymmetric jet can be either toroidal (axisymmetric), helical or flapping (see the introduction § 1.1). It has been reported by Merle [1956] that the helical mode C and the toroidal mode A2 are very stable compared to the remaining modes. Mode C can be observed in a Mach number range of $1.30 \leq M_j \leq 1.60$ and mode A2 from $1.15 \leq M_j \leq 1.25$. Panda et al. [1997] observed in an experimental investigation that the peak noise level of the C mode is more that 10 dB louder than the A2 mode.

As we will use the present flow case in section § 6 to minimize jet screech and the fact that we prefer a stable screech behavior, especially for optimization purposes, the helical mode will be investigated in the present section. To avoid an exhaustive repetition of the numerical results, some results on the axisymmetric jet will be found in comparison to the optimized jet in Sec. § 6.

The Mach number is chosen to be constant with $M_j = 1.55$ whereas the computation is performed with three different grid resolutions. Beginning with the lowest resolution of $256 \times 128 \times 128$ grid points, followed by the moderate resolution of $512 \times 256 \times 256$ points and finally the highest resolution of $1024 \times 512 \times 512$ points. To the best of the authors knowledge, the latter case with a total of 268 million grid points is the largest computation on axisymmetric supersonic jet screech ever performed.

Despite the grid resolution, all other parameters are the same for all three computations. The reservoir temperature is equal to the ambient temperature ($T_\infty = 300\text{K}$). Note, that the CFL number of all computations is CFL = 0.7. As the time-step is a function of the grid spacing and CFL number, the time-step is different in all three cases ($dt = dx_{\min}\text{CFL}/(u_j + c_\infty)$, see also Müller [1990] for a more detailed description of the computation of the time-step). A summary of the parameters, like the time-step and the grid spacing, can be found in Tab. 4.3. In addition to that, an approximation of the smallest

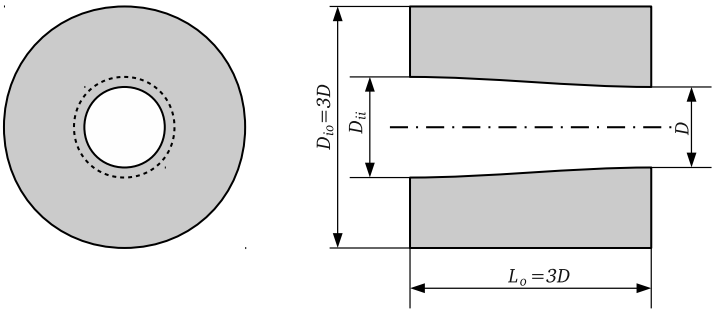

Figure 4.16: Dimensions of the round convergent nozzle. Design Mach number M_d = 1; inlet Mach number M_i = 0.5. D_{io} = 3D, D_{ii} = 1.16D, L_o = 3D.

scale, the Kolmogorov scale, can be found in the same table. It is scaled with the smallest grid spacing and is a measure for the accuracy of the grid resolution. A value of $\eta/dx_{\min}$ = 2 in combination with a spectral scheme corresponds to a DNS, as it resolves and captures the smallest scales. In the present investigation, the value ranges from 0.26 for the smallest resolution up to 1.06 for the high resolution case. The latter one is close to a DNS although there is a factor of two missing in the grid resolution and the discretization scheme is only spectral-like (see Sec. § 2.3.1). A frequently cited numerical work on jet noise by Freund [2001] shows a DNS of a high subsonic round jet (M_j = 0.9) based on a Reynolds number of Re_D = 3600. This leeds to a value of $(\eta/dx_{\min})_{\text{Freund}}$ = 1.09 which is comparable to the present computation with the high resolution (1.06). To this end, the grid of the high resolution case with $1024 \times 512 \times 512$ points, can be considered as a DNS. Yet, due to the dissipative upwind schemes, it can be regarded as a LES with a DNS-like resolution.

In contrast to the planar jet, all boundaries are non-periodic and based on non-reflecting boundary conditions including a sponge at the outlet. The convergent nozzle extends 3D inside the computational domain with the diameter of the nozzle exit D. Based on that diameter, the total size of the domain including the nozzle is $25D \times 15D \times 15D$ in the x-, y- and z-direction.

The computational domain is decomposed in all three directions and solved in parallel. For the small resolution a total of $8 \times 8 \times 8 = 512$ cores are used. Twice as many cores are used for the moderate resolution ($16 \times 8 \times 8 = 1024$) and with a further doubling of cores ($8 \times 16 \times 16 = 2048$) the high resolution case is solved.

In Fig. 4.16 the dimensions of the round nozzle are presented. Compared to the planar nozzle, the nozzle exit is straight and the inlet diameter is smaller than the inlet height of the planar nozzle. This is due to the fact that the cross-section ratio is important for the ratio of inlet to outlet Mach number. As for the planar case, the inlet Mach number is $M_i = 0.5$. Inside the nozzle the contoured part is based on a cubic spline with an inlet and outlet inclination angle of 0°.

Instantaneous flow field Snapshots of the round jet for a Mach number of $M_j = 1.55$ are presented in Fig. 4.17 and 4.18. Figure 4.17 shows a slice of the pseudo Schlieren ($|\nabla\rho|$) in the x-y-plane for all three investigated resolutions (panel (a)–(c)). All cases are captured for the same simulation time $t = 20T_s$ (with the time for one screech cycle T_s). In all cases, the turbulent structure in the mixing-layers and the shock cell structure in the jet core is visible. The shape of the shock cell structure within the first two shock cells is similar in all cases. Between the moderate and high resolution, the differences are small compared to the low and high resolution. The grid of the low resolution case is very coarse and the resulting picture looks, compared to the higher resolutions, noisy and diffuse. The difference between the moderate and high resolution is a smaller shock width for the high resolution case, which is especially visible in the compression and expansion waves within the first shock cell. In addition to that, one can see that the size of the smallest turbulent scales is decreasing for the high resolution jet.

Another difference of the moderate to high resolution jet is the increased mixing for the jet with moderate resolution. The spreading of the jet, beginning at $x/D > 6$ is more distinct for the moderate resolution as it is the case for the high resolution. As we will see later, the screech intensity for the jet with moderate resolution is about 1.2 dB louder than the jet with high resolution. The screech intensity is linked to the corresponding (helical) screech mode which is responsible for the mixing of the jet. This leads to the conclusion that the helical mode of the jet with moderate resolution is more distinct than for the high resolution jet.

In Fig. 4.18, both, the instantaneous pressure fluctuations ($p' = p - \langle p \rangle$) in the left column and the entropy in the right column are presented. The increased mixing of the jet with moderate resolution is also visible in the entropy. Note, that the entropy is a function of the temperature and the pressure. As the present investigation is based on a cold jet, where the reservoir temperature is equal to the ambient temperature ($T_r = T_\infty = 300\text{K}$), the entropy in the reservoir is different to the ambient entropy. Based on

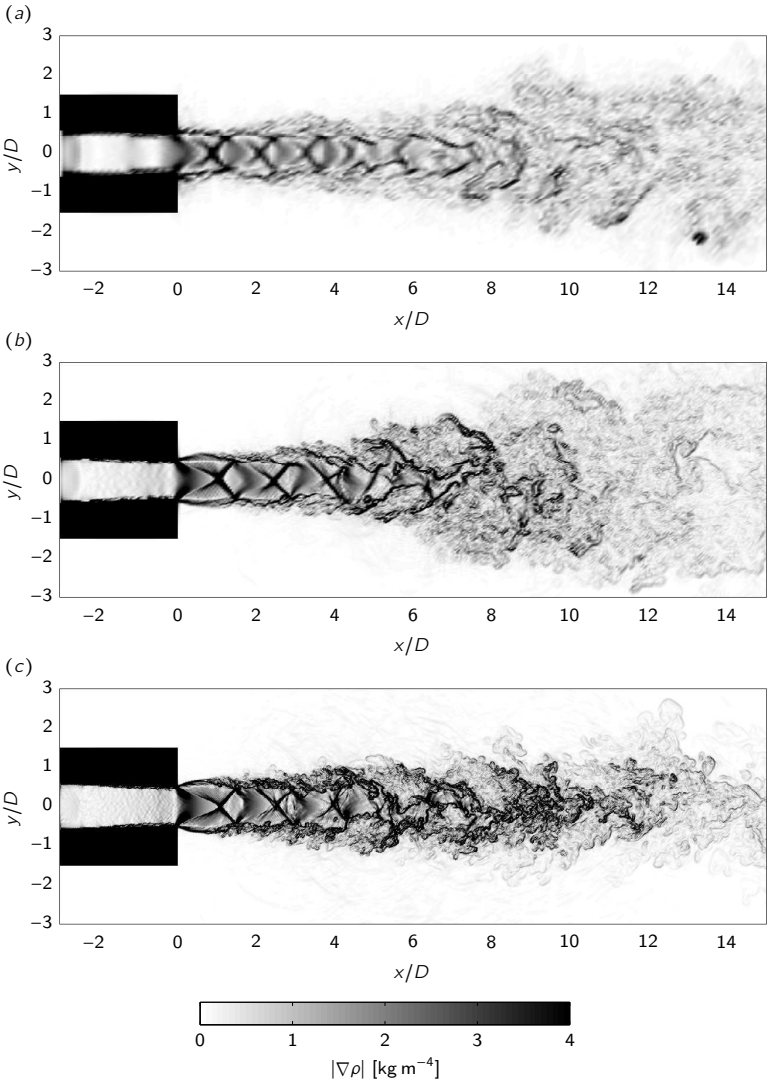

Figure 4.17: Instantaneous snapshot of the pseudo Schlieren ($|\nabla\rho|$) in the x-y-plane taken at the same physical time $t = 20T_s$ with the time for one screech cycle T_s. Three different resolutions: (a): $256 \times 128 \times 128$; ($b$): $512 \times 256 \times 256$; ($c$): $1024 \times 512 \times 512$.

Gibbs fundamental relation, in combination with the assumption of an ideal gas, a relation for the entropy as a function of the pressure and temperature can be given:

$$s(p,T) = C_p \left[\ln R + \ln T + \frac{1-\gamma}{\gamma} \ln p \right].$$

Now, as $(1-\gamma)/\gamma$ is negative for $\gamma = 1.4$, the entropy in the reservoir is below the ambient entropy. In the present case: $s_\infty = 8110.2$ $[\mathrm{m^2\,K^{-1}\,s^{-2}}]$ and $s_r = 7716.0$ $[\mathrm{m^2\,K^{-1}\,s^{-2}}]$, with $p_r/p_\infty = 3.95$ (see also Tab. 4.2). The expansion of the gas from the reservoir to the nozzle exit is an isentropic process. To this end, the entropy at the nozzle exit is equal to the reservoir entropy and hence below the ambient entropy. This circumstance is visible in the right column of Fig. 4.18, where the low entropy jet is mixing with the ambient fluid of high entropy (color scale from black to white).

In the left column of Fig. 4.18 the pressure fluctuations are presented and based on the mean pressure field $p' = p - \langle p \rangle$ in the color-range of ±2000 [Pa]. In all three cases with different resolution, the acoustic waves, corresponding to the screech tone, are visible. Especially for the moderate and high resolution distinct acoustic waves are propagating in the upstream direction of the jet. Their origin seems to be around $x = 7D$ which corresponds to $x = 5.5L_s$ (with the average shock cell spacing $L_s = 1.28D$; see next paragraph). The typical π-shift of the waves at the upper and lower side of this plane is clearly visible and is caused by the helical mode (investigated in detail later). In the high resolution case, the amplitude of the upstream propagating screech noise is slightly reduced compared to the moderate resolution. For the low resolution, the amplitudes are even smaller and the screech tone is hard to see.

Comparing all three resolutions, it becomes evident that the higher the resolution, the smaller the wavelength, especially for the broadband noise components. This additional noise, which is missing in the low and moderate resolution case will be visible in the noise spectra, discussed later. In the downstream direction, the Mach wave radiation can be see particularly for the high resolution jet although it is superimposed by the much louder screech tone. In addition to the noise, the hydrodynamic turbulent fluctuations are visible in the jet plume. For the present color-scale, the full range of the hydrodynamic fluctuations can not be visualized. They range from ±45 [kPa].

Shock cell spacing As for the planar jet, the shock cell structure is a characteristic feature of the supersonic round jet. Especially the shock cell spacing is a crucial factor for the screech frequency. Hence, the correct prediction of

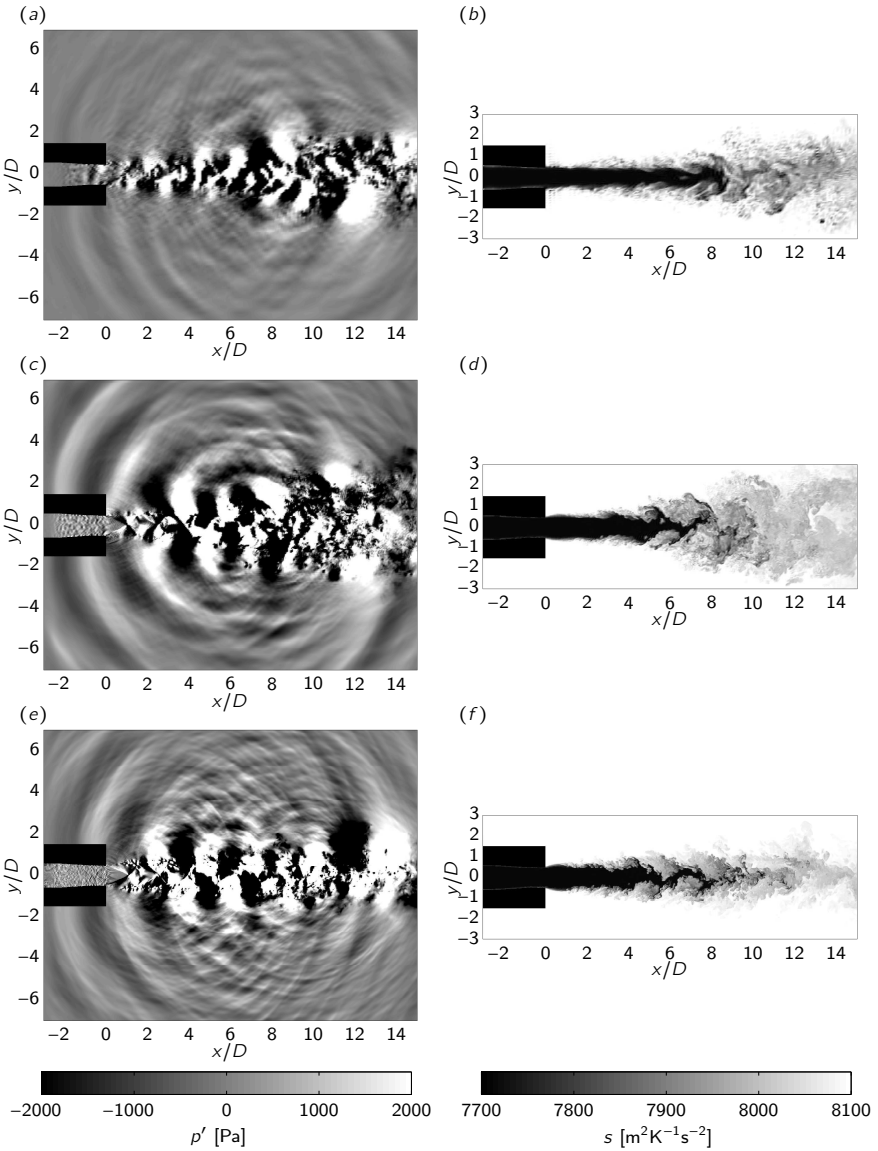

Figure 4.18: Instantaneous snapshot of the pressure fluctuations (p', left column) and the entropy (s, right column) in the x-y-plane taken at the same physical time $t = 20T_s$ with the time for one screech cycle T_s. Three different resolutions: (a, b): $256 \times 128 \times 128$; (c, d): $512 \times 256 \times 256$; (e, f): $1024 \times 512 \times 512$.

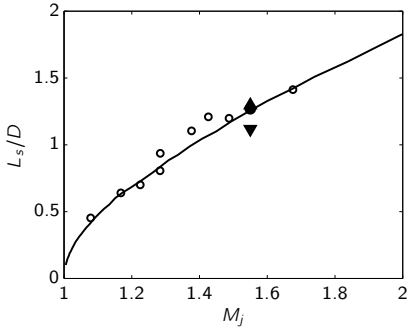

Figure 4.19: Mean shock cell spacing for the axisymmetric jet as a function of the fully expanded jet Mach number M_j. Experimental data: ○, Seiner & Norum [1980]; (———), logarithmic fit of experimental data from Seiner & Norum [1980]; Numerical: current computation ▲, $1024 \times 512 \times 512$; ●, $512 \times 256 \times 256$; ▼, $256 \times 128 \times 128$.

the shock cell spacing is important. In Fig. 4.19 the shock cell spacing of the round jet for all three investigated resolutions, is presented. In what follows, the resolutions are marked as:

Resolution	Symbol	Line style
$1024 \times 512 \times 512$	▲	———
$512 \times 256 \times 256$	●	———
$256 \times 128 \times 128$	▼	- - - - - -

if not mentioned differently. To obtain the shock cell spacing of the numerical data, the average spacing of the first five shock cells is taken, based on the mean pressure field. Besides the current numerical data, experimental data of Seiner & Norum [1980] are included for comparison. One can see that the moderate and high resolution case match each other and are in good agreement to the expected experimental data. The low resolution case, on the other hand, is slightly under predicted. Whereas the shock cell spacing for the moderate and high resolution case is $L_s = 1.28D$ and $L_s = 1.29D$, respectively, a value of only $L_s = 1.12D$ can be obtained for the low resolution case. This deviation of 12 % will have a severe influence on the screech frequency. Based on the theory of screech noise, we will expect a higher frequency due to the reduced shock cell spacing for the low resolution case. As we will see later, this feature will come true. One can see also that there is a strong deviation

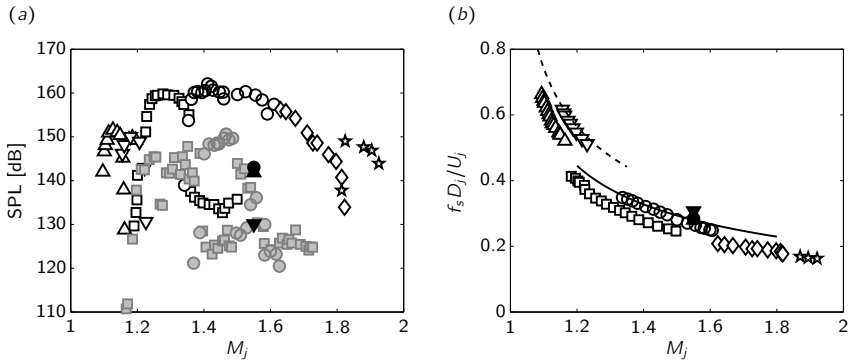

Figure 4.20: Screech amplitude and frequency of a circular jet versus the fully expanded jet Mach number M_j for different screech modes Experimental data from Panda et al. [1997]: A1 △; A2 ▽; B □; C ○; D ◇; E ☆. Experimental data from Seiner [1984]: B ■; C ●. current computation: C ▲, 1024 × 512 × 512; ●, 512 × 256 × 256; ▼, 256 × 128 × 128. (*a*) Screech amplitude versus the fully expanded jet Mach number. (*b*) Dominant screech frequency as a function of the jet Mach number M_j. Analytic solution for mode A (- - - - - -) and analytical solution for mode C (———) by Massey [1997].

in the experimental data of Seiner & Norum [1980]. A difference of 10 % to the logarithmic fit can be identified. The reason for these jumps might be explained due to the individual screech modes.

Screech frequency and amplitude As we have already seen for the planar jet, the correct prediction of the shock cell spacing is important for the correct prediction of the screech frequency. In the previous paragraph, the shock cell spacing has been presented for all three resolutions. We could see that the low resolution jet shows deviations to the experimental data by Seiner & Norum [1980]. In Fig. 4.20(*b*) the screech frequency of the three numerical investigations are presented and compared to experimental data by Panda et al. [1997] and analytical data by Massey [1997]. The screech frequency is expressed with the Strouhal number, based on the fully expanded jet values: $Sr = f_s D_j / u_j$. Note, that for the planar jet, the length-scale in the Strouhal number is based on the nozzle exit conditions (h) and not on the fully expanded jet conditions (h_j) as in the present round case (D_j). All numerical data of panel (a) and (b) are measured normal to the jet axis ($\Theta = 90°$) in a distance of $7.8D$ to the jet axis.

Both, the moderate and high resolution jet are in very good agreement to

the analytical and experimental data. For both cases, a Strouhal number of Sr = 0.2848 (moderate resolution) and Sr = 0.2803 (high resolution) can be obtained for the fundamental screech tone. Based on the analytical data by Massey [1997], a Strouhal number for the present Mach number M_j = 1.55 of Sr = 0.2801 can be predicted. Corresponding to the high resolution case, this is an error of less than 0.1 %. The deviation of the moderate resolution with respect to the analytical data is less than 1.7 %. In the case of the low resolution, the error is larger (as expected) and reaches a value of 9.8 %. Note, that the error in the correct prediction of the shock cell spacing for this case is 12 %. The previous assumption that the under predicted shock cell spacing for the low resolution jet will lead to a higher screech frequency could be confirmed. Berland et al. [2007] observe a similar phenomenon in their LES investigation on planar jet noise. They explain the reduced shock cell spacing and the corresponding increase of the fundamental screech frequency with the momentum thickness of the initial shear layers at the nozzle exit. In their simulation, the momentum thickness is larger as for experimental investigations. This leads to a reduction of the effective diameter (height) of the jet nozzle and will consequently reduce the shock cell spacing. In the present round case with the low resolution, the boundary layer is not properly resolved. This will also lead to an increase of the momentum thickness and finally increase the fundamental screech frequency [see also the experimental work by Morris et al., 1989, where this phenomenon could be documented for round jets].

In panel (a) of Fig. 4.20 the corresponding screech amplitudes are presented for all three resolutions. In addition to the present numerical data, experimental results on round jets by Panda et al. [1997] and Seiner [1984] are included for comparison. As usual for screech noise predictions, the amplitudes of the screech tone are spread over a wide range of noise levels. Differences between both experimental data of more than 20 dB for the same Mach number can be observed. Especially at the investigated Mach number M_j = 1.55, Panda et al. [1997] measures a value of 160 dB whereas the results of Seiner [1984] show a value of 135 dB. Nevertheless, the present numerical data is in the range of the experimental work of Seiner [1984]. For the high resolution a noise level of 141.8 dB is computed, for the moderate resolution a value of 143.0 dB and for the low resolution a value of 130.1 dB. The largest amplitude can be obtained for the moderate resolution, followed closely by the high resolution with 1.2 dB less amplitude and then finally with a difference of about 10 dB, by the low resolution. As we will see in the next paragraph, where the emanated noise signal is investigated in detail, the noise level of the moderate and high resolution case matches well an addi-

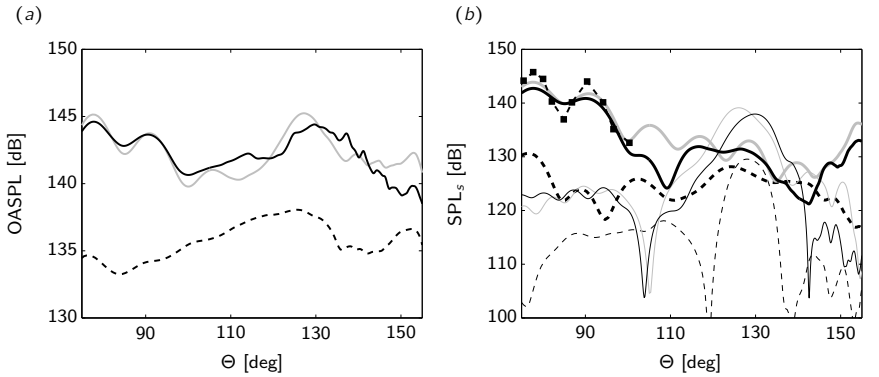

Figure 4.21: (*a*) Overall sound pressure level (OASPL) as a function of the observation direction for different resolutions. (*b*) SPL of the fundamental screech tone (thick lines) and the first subharmonic (thin lines) as a function of the observation direction for different resolutions. Experimental data (▪) adapted from Panda [1999].

tional experimental data by Panda [1999] (cf. Fig. 4.21(*b*)). In combination with the experimental data of Panda et al. [1997] in the present figure one can conclude that the amplitude of the moderate and high resolution jet matches well the experimental data, whereas the amplitude of the low resolution jet is under-predicted.

Noise and their spectra In Fig. 4.21(*a*) the overall sound pressure level of the round jet is presented for all three resolutions. It is measured along a line parallel to the jet axis at the location $y = z = 5.5$ which corresponds to a distance of $7.8D$ to the jet centerline. The high and moderate resolution are in good agreement with deviations up to 3 dB. A large deviation of about 7 dB, in peaks up to 10 dB, lies between the moderate/high resolution and the low resolution. In all directions, the noise level of the low resolution jet is smaller than the moderate/high resolution jet. Especially in the upstream direction, where the screech tone is the dominant noise source, the largest deviations are visible. At an observation angle of $\Theta = 90°$, the OASPL of the low resolution jet is 134.2 dB. For the moderate and high resolution jet, 143.7 dB and 143.6 dB, respectively. The loudest OASPL's can be observed for all three cases in the up- and downstream direction, yet with a different amplitude. In the downstream direction for the high resolution case: 144.4 dB at 129.8°; for the moderate resolution: 145.2 dB at 127.4°; for the low resolution: 138 dB

at 126.4°. Hence, a loud noise can be observed in the downstream direction at about $\Theta = 127°$. Similar noise levels can be measured in the upstream direction for the moderate and high resolution jet. At an observation angle of $\Theta = 78°$, the OASPL of the moderate and high resolution jet is 145.1 dB and 144.6 dB, respectively. In this direction, the noise level is dominated by the screech tone and is 0.5 dB louder for the moderate resolution jet.

In panel (b) the sound pressure level of the screech tone of the round jet is presented for all three resolutions. In addition to that, the first subharmonic of the screech tone is included (thin lines). To compare the results with experimental data, the SPL of the screech tone adapted from Panda [1999] is included within a small region around $\Theta = 90°$. One can identify a good agreement of the SPL of the fundamental screech tone of the moderate and high resolution jet and the experimental data. Both, amplitude and wavelength of the experimental work are in good agreement to the present numerical data. It seems that the screech amplitudes of the moderate resolution are slightly larger as the ones of the high resolution. In the downstream direction, the amplitudes start to vary and peak deviation up to 10 dB can be observed at 110° and up to 6 dB at 138°. The amplitudes of the low resolution jet are about 10 dB smaller than for the remaining two cases. Only in a small region around 140°, the low resolution jet is 4 dB louder than the high resolution jet.

All three curves of the fundamental screech tone, show the typical behavior of a standing wave with nodes and antinodes. The standing wave is responsible for the feedback mechanism of the screech generation process and is caused due to the reflected waves at the nozzle exit. It is interesting to see that the standing wave pattern of the first subharmonic of the screech tone is not as prevalent as for the fundamental screech tone. It is hardly visible in the upstream direction of the jet for the moderate and high resolution jet with half the wavelength of the fundamental standing wave. Another feature of the SPL of the first subharmonic is that it is not decreasing when measuring further downstream, as it is the case for the fundamental frequency, but shows a peak at $\Theta = 130°$. At this location the subharmonic is louder than the fundamental tone and dominates the overall spectrum, as we will see later.

Another comparison of experimental data and the present numerical work has been carried out in Fig. 4.22. Here, a well known figure of the experimental work of Panda [1999] (panel (b)) has been adapted to the present numerical data (panel (a)), where only the results of the moderate resolution are used. This figure is divided in two parts, in the top part the SPL in a two-dimensional x-y-plane is given. In the bottom part of the figure,

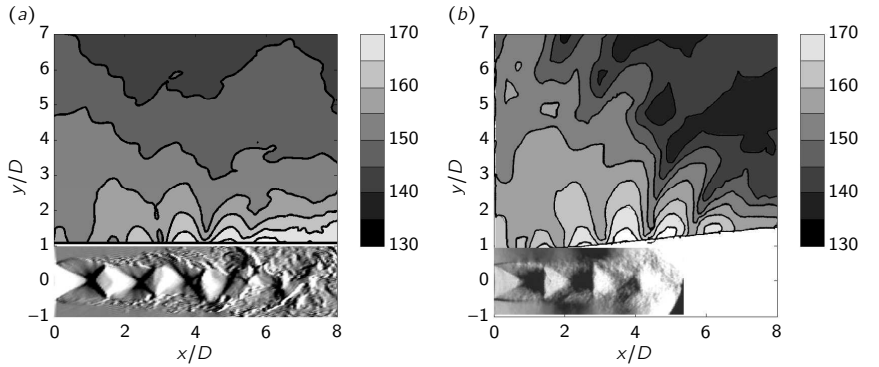

Figure 4.22: Top part: Sound pressure level in the acoustic near-field measured in dB. Bottom part: (Pseudo)-Schlieren to visualize the shock cells with arbitrary color-scale. (*a*) OASPL of the round jet based on the current numerical computation with $M_j = 1.55$. (*b*) SPL of the screech frequency of a round jet based on experimental data by Panda [1999] with $M_j = 1.42$ (axis scaled to match the shock cell spacing of a jet at $M_j = 1.55$).

the (pseudo)-Schlieren of the jet are presented. They visualize the density gradient in the stream-wise direction of the jet and highlight the shock cell structure and the turbulence in the mixing-layers. For the experiment, the Schlieren are integrated over the whole jet diameter and in the numerical data only a two-dimensional slice is shown. This fact is responsible for a difference of both visualizations although the differences are small. In addition to that, the color-scale of the Schlieren pictures are chosen arbitrarily as no information of the amplitudes for the experimental data are available.

The noise measured in the top part of both panels is based on the OASPL for the numerical data and on the screech SPL of the experimental data. This circumstance leads to deviations, especially in the downstream direction, where the screech amplitude is decreasing and the OASPL in increasing (compare also panel (*a*) and (*b*) of Fig. 4.21). Nevertheless, the deviations in the upstream direction are small and a good agreement of the experimental and the numerical data can be found. Not only the amplitudes of both cases match each other but also the spatial distribution of the noise in the acoustic near-field is in good agreement. Again, the standing wave pattern, typical for screech noise, can be identified in both cases with the characteristic lobes facing in the normal direction of the jet.

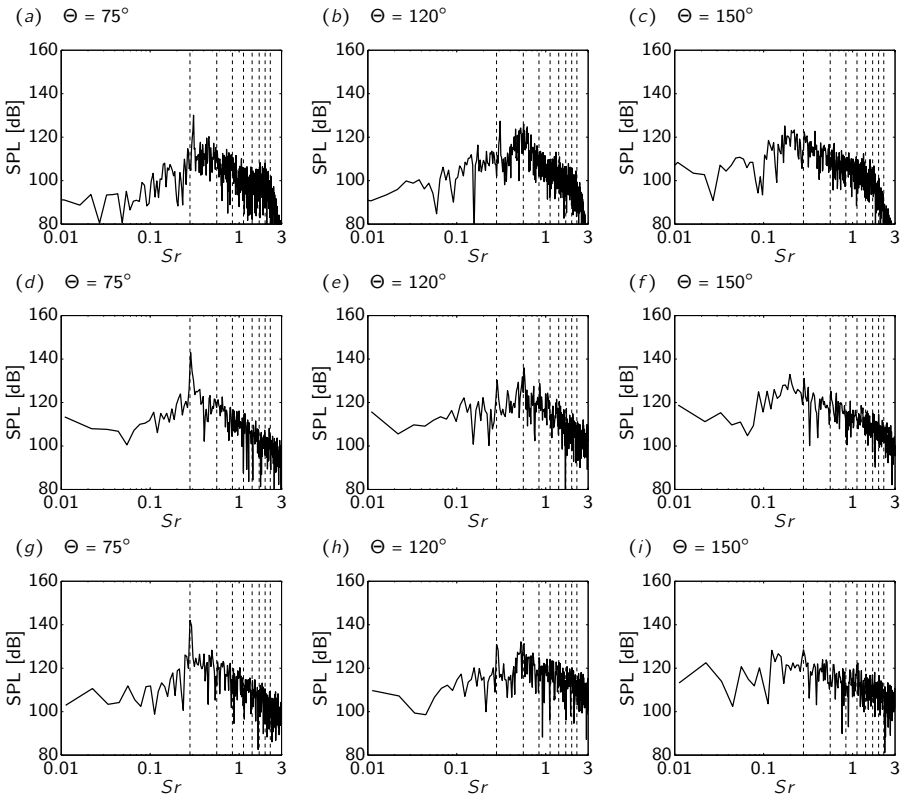

Figure 4.23: Spectra for three different observation directions for different resolutions. First row (a, b, c): low resolution; Second row (d, e, f): moderate resolution; Third row (g, h, i): high resolution.

Spectra The spectra of the noise measured at three different locations is presented in Fig. 4.23 for all three resolutions. The signals are captured in a constant distance to the jet axis at $y = z = 5.5$ and at the stream-wise positions $x = -2.1D$ ($\hat{=}\ \Theta = 75°$), $x = 4.5D$ ($\hat{=}\ \Theta = 120°$) and $x = 13.5D$ ($\hat{=}\ \Theta = 150°$). As we have seen already, the noise of the moderate and high resolution jet are similar. This is also the case for the corresponding spectra. Larger differences can be observed in comparison to the low resolution jet. In all three cases, one can identify the three sources of noise. The screech tone is clearly visible in the upstream direction ($\Theta = 75°$). In a slightly downstream

position ($\Theta = 120°$) broadband noise components and the first subharmonic of the screech tone are visible. Further downstream, at $\Theta = 150°$, mixing noise is the dominant noise source in all three cases. In addition to the numerical data, the analytical solution by Massey [1997] for the fundamental screech tone and its subharmonics is marked with a dashed line for comparison.

In the low resolution case, one can see the deviation of the screech frequency clearly in the upstream direction of panel (a) with a peak noise level of 135 dB. The computed screech frequency is slightly larger than predicted by the analytical theory. The mixing noise of low frequency (around $Sr = 0.15$) is very weak and in the order of 105 dB. For higher frequencies, the broadband noise components are visible with a peak value of 120 dB at a frequency of $Sr = 0.45$. The amplitudes of the broadband components are decreasing exponentially up to a Strouhal number of $Sr = 2$. From this point on, the amplitudes drop drastically with a steep slope. This phenomenon has no physical interpretation and is related to the low numerical resolution of this case. If we assume that we need six points to resolve one wavelength, based on the present discretization method, then the largest resolvable Strouhal number is $Sr_{\mathrm{max,6dx}} = 2.2$ (see also Tab. 4.3). This frequency is in good agreement to the point where the amplitudes start to decay with the steep slope. Hence, this phenomenon is related to the numerical method and the low resolution. Another evidence that the low resolution is responsible for the unresolved high frequencies, is the fact that for the moderate and high frequency this sudden drop is not visible (see the second and third row of Fig. 4.23).

It is well known that the screech frequency is constant and not a function of the observation direction. This fact can be confirmed for all jet resolutions, e. g. for the low resolution jet, when comparing panel (a) and (b). Here, the screech frequency is not changing when measuring in the up- or downstream direction. A different picture arises for the broadband components. They are Doppler shifted, which corresponds to an increase of the frequency with increasing observation angle in the downstream direction. This fact can be also observed in panel (a) and (b) where the peak of the broadband noise is at $Sr = 0.45$ for $\Theta = 75°$ and $Sr = 0.55$ for $\Theta = 120°$.

The screech frequency of the moderate and high resolution jet matches well the analytical theory and dominate the noise spectrum in the upstream direction (see panel (d) and (g)). As we have seen already, the screech amplitude of the moderate resolution jet is slightly higher than the high resolution case (about 0.5 dB). In the upstream direction, the amplitudes of the mixing noise are comparable in both, the moderate and high resolution jet. Nevertheless, the broadband components of the high resolution jet are

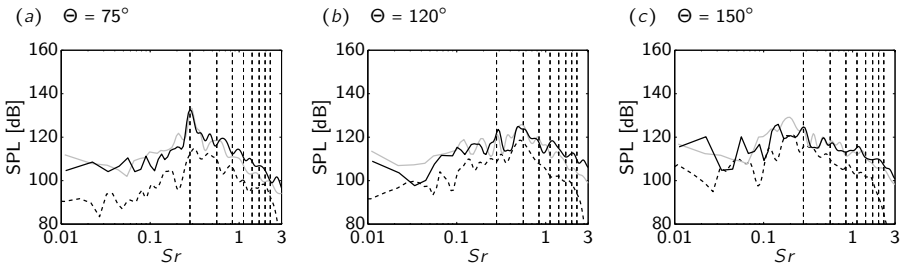

Figure 4.24: One-third octave band spectra for three different observation directions and three different resolutions.

slightly larger than for the moderate resolution case. A constant difference of about $1-2$ dB can be detected.

The differences of the individual resolutions are more evident in Fig. 4.24. In the three panels, the one-third octave band spectra are presented for the same three observation directions as in the previous Fig. 4.23. One can see that the moderate and high resolution jet is in good agreement to each other in terms of frequency and observation direction. Only in a narrow band of high frequency – the broadband shock-associated noise – the high resolution case is slightly louder (1-2 dB) than the moderate resolution. A reason for this deviation may be the reduced spatial resolution of the moderate resolution jet and the corresponding dissipation of the small wavenumber acoustics. The low resolution is for all observation directions below the two remaining resolutions with a difference of up to 10 dB (except some small exceptions).

The spectra of the previous figures are based on the acoustic pressure fluctuations measured in the acoustic near-field. In Fig. 4.25 the history of the pressure signal is presented. In the left column the signal is presented for two opposing locations of the jet. One at $y = z = -5.5$ and the other one at the opposite location at $x = 0$, $y = z = +5.5$. Both signals are measured at $\Theta = 90°$ with a distance to the jet axis of $7.8D$. For the moderate and high resolution jet one can clearly identify the π phase shift of the two signals. As we have already seen in the left column of Fig. 4.18, this is related to the helical mode of the jet. It is also a known phenomenon for the flapping mode of round and also planar jets.

In the right column, panel (b), (d) and (f), the pressure signal measured at $y = Z = 5.5$ as a function of the observation direction Θ and the time is presented. One can clearly identify the loud screech tone in the upstream

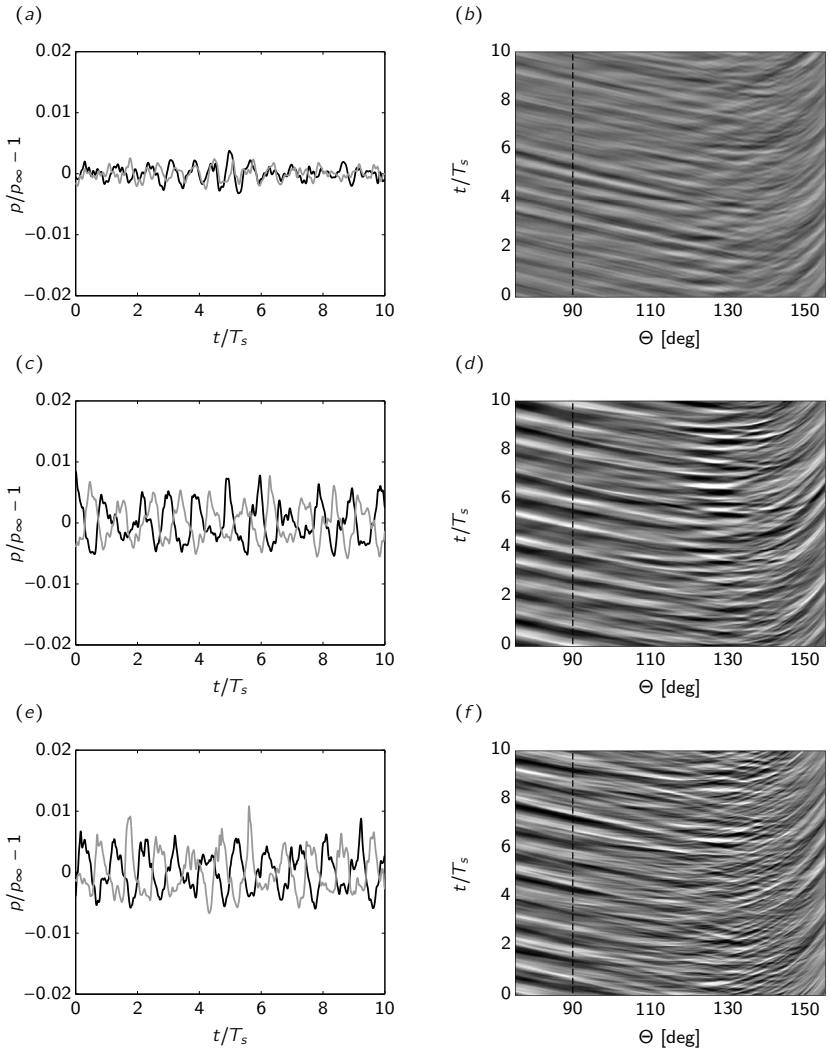

Figure 4.25: History of the pressure fluctuations containing the last ten computed screech cycles for different resolutions. Left column: signal measured at $\Theta = 90°$ with a distance to the jet axis of $7.8D$. (———) measured a $x = 0$, $y = z = -5.5$; (———) measured a $x = 0$, $y = z = +5.5$ (opposite location to the jet axis). Right column: two-dimensional view, measured at $y = z = 5.5$ along the x-direction, expressed in angles measured from the upstream direction. Dashed vertical line (- - - - - -) corresponds to the location where the pressure signal is extracted for the panels in the left column.

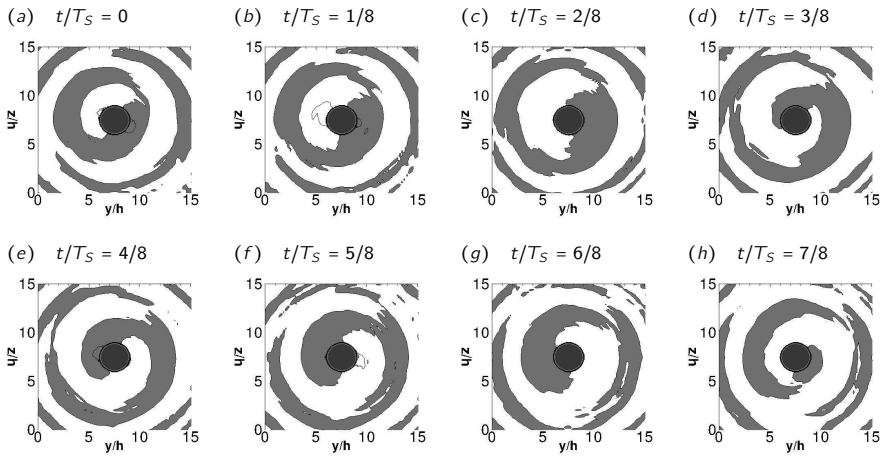

Figure 4.26: Instantaneous slice in the $y-z$-plane (normal to the stream-wise direction) captured at eight equidistantly spaced time-steps. The snapshots represent one full screech cycle (cf. helical mode in Fig. 1.15(b) and [Westley & Woolley, 1975, Fig. 9]). Contour-levels: pressure fluctuation p' in the range of 0 [Pa] (white) to 1000 [Pa] (gray). The jet is spinning clockwise around the positive x-axis; counter-clockwise in this view towards the nozzle (negative x-direction). (here: $h = D$).

direction with a constant wavelength at least for the moderate and high resolution. In an observation direction $\Theta \approx 130°$ the firs subharmonic of the screech tone can be identified. Further downstream, shock-associated noise and mixing noise dominate the acoustic signal.

Helical mode A axisymmetric screeching jet at a Mach number $M_j = 1.55$ is supposed to undergo a helical mode. To verify this behavior, the pressure fluctuations in a y-z-plane (normal to the jet axis) are presented in eight snapshots in Fig. 4.26. The snapshots are taken upstream the nozzle exit at $x/D = -2$ and are captured at eight equidistantly spaced time-steps, representing one full screech cycle (panel $(a-h)$). Pressure fluctuations are based on a two color contour-map where white stands for 0 [Pa] and gray for 1000 [Pa]. One can identify clearly the spinning (helical) mode which wraps around the nozzle (shown in a cross section in the center of each figure; outer diameter $D_{io} = 3D$). Within one screech cycle T_s, the helical mode turned once around the jet axis in the clockwise direction based on the positive x-axis. It is reported in Westley & Woolley [1975] that the helical mode rotates with

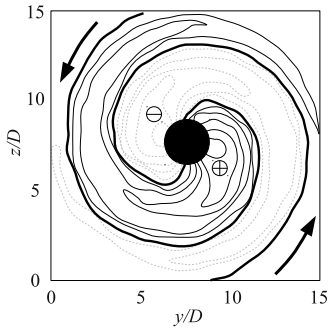

Figure 4.27: Instantaneous pressure fluctuations in the y-z-plane (normal to the stream-wise direction) adapted from experimental results of Westley & Woolley [1975]. Convergent nozzle with $M_j = 1.67$. A good agreement to Fig. 4.26(c) can be found.

the same frequency as the corresponding screech tone. This observation is in good agreement with the present numerical investigation.

To validate the shape of the pressure distribution in the plane perpendicular to the jet axis, a snapshot of the pressure fluctuations based on experimental data from Westley & Woolley [1975] are presented in Fig. 4.27. It shows a y-z-plane at $x/D = 0$ of a $M_j = 1.67$ choked jet (convergent nozzle) with contour-lines of the iso pressure (arbitrary scaling). Positive pressure fluctuations are marked with thin solid lines whereas negative pressure fluctuations are represented by gray dashed lines. The thick solid line marks the neutral line. To compare the experimental data to the current numerical investigation, the rotation direction is changed. In the original experimental data, the jet is spinning clockwise. The distribution of the experimental measured pressure fluctuations and the current numerical data are in good agreement. This is especially visible in comparison to Fig. 4.26(c) where the experimental and numerical data are in phase.

Mean flow field In the following figures, mean values of the jet are presented. In Fig. 4.28, the mean value of the pressure ($\langle p \rangle$) is presented and measured along a line parallel to the jet axis. The position of the axis is in the center of the jet for panel (a) ($r/D = 0$) and at $r/D = 0.45$ for panel (b). In the latter case, where the data are not extracted at the centerline, experimental data by Norum & Seiner [1982a] are included for comparison. The data measured at the centerline show clearly the periodically repeated shock cell

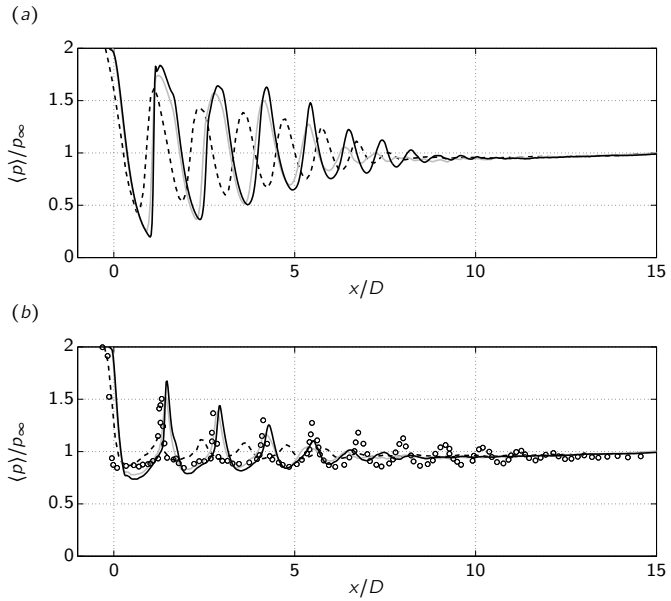

Figure 4.28: Mean pressure distribution along a line parallel to the jet axis. (a) at r/D = 0; (b) at r/D = 0.45. ○, Norum & Seiner [1982a] for M_j = 1.49 at r/D = 0.45; Numerical: current computation: (- - - - - -) 256 × 128 × 128; (———) 512 × 256 × 256; (———) 1024 × 512 × 512.

pattern. For the moderate and high resolution jet, the pressure distribution is comparable whereas the shock strength seems to be slightly larger for the high resolution jet. In addition to that, the number of detectable shock cells is larger for the high resolution jet. A total of seven shock cells are visible whereas six shock cells can be identified for the moderate resolution jet. The same number of seven shock cells can be extracted for the low resolution jet. Nevertheless, as we have seen already, the shock cell spacing and the shock strength is under-predicted. Comparing these results for the round jet with the ones of the planar jet of Sec. § 4.1 one can conclude that for the round jet about twice as many shock cells can be identified in the jet core. The planar jet with M_j = 1.55 contains only three detectable shock cells. This phenomenon might be related to the strong flapping mode of the planar jet which has a stronger impact on the shock cell structure than the helical mode of the round jet.

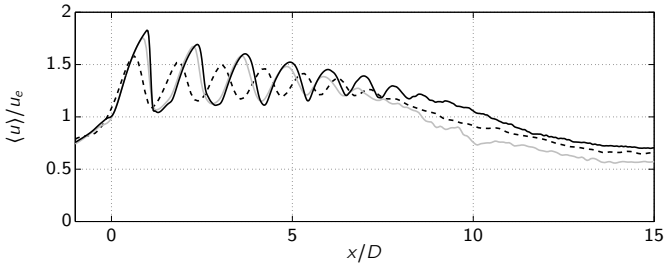

Figure 4.29: Mean stream-wise velocity distribution along the centerline of the jet. (- - - - - -) $256 \times 128 \times 128$; (———) $512 \times 256 \times 256$; (———) $1024 \times 512 \times 512$.

Panel (b) shows the pressure distribution at $r/D = 0.45$. The comparison to the experimental data shows a good agreement to the moderate and high resolution jet. Within the first four shock cells, the experimental data match well the numerical data in shape and amplitude. Further downstream, for the fifth and the following shock cells, larger deviations are visible. The shock cell structure of the experimental jet is much more extended in the downstream location as for the numerical jet. Up to ten shock cells can be detected in the experimental study whereas only seven shock cells are visible for the numerical jet. In addition to that, the shock cell spacing is decreasing more rapidly in the numerical case as in the experimental study, when measuring further downstream. Again, the amplitudes and the shock cell spacing of the low resolution jet is under-predicted.

That the low resolution shows strong discrepancies to the moderate and high resolution jet is also visible in Fig. 4.29 where the mean velocity distribution is displayed and measured along the centerline of the jet. A saw-tooth like shaped distribution is visible for the moderate and high resolution jet, with a slightly steeper slope for the high resolution jet. The velocity is scaled with the jet exit condition (here: $M_e = M_d = 1$). Hence, values above one indicate supersonic velocities and values below one mark the subsonic region. The length of the high resolution jet is slightly larger than for the moderate resolution case ($10.5D$ and $8D$, respectively). The length for the low resolution jet lies between the two larger cases ($9D$).

In the last two figures of this section, the RMS values of the stream-wise velocity and the entropy are presented and measured along the centerline of the jet. The velocity fluctuations are presented in Fig. 4.30. In addition to the present numerical data, experimental and other numerical data of subsonic jets are included for comparison. It is visible that the moderate and high

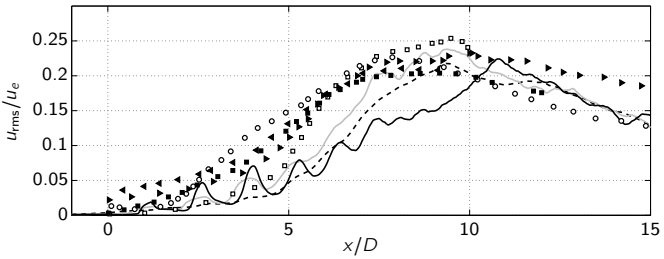

Figure 4.30: RMS stream-wise velocity distribution along the centerline of the jet. (- - - - - -) $256 \times 128 \times 128$; (———) $512 \times 256 \times 256$; (———) $1024 \times 512 \times 512$. Experimental data: ■: Raman et al. [1989]; ◀: Jordan et al. [2002]; ▶: Bridges [2006]. Numerical data: □; Bogey [2000]; ○: Cavalieri et al. [2011].

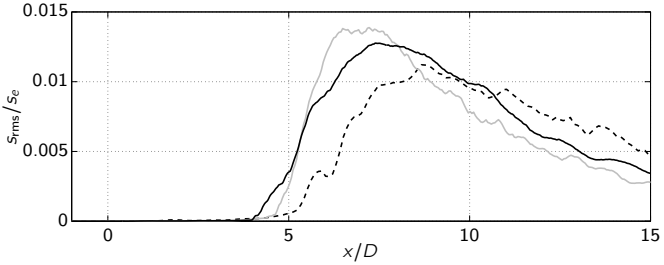

Figure 4.31: RMS fluctuation of the entropy along the centerline of the jet. (- - - - - -) $256 \times 128 \times 128$; (———) $512 \times 256 \times 256$; (———) $1024 \times 512 \times 512$.

resolution jet is modulated with the shock cell structure – a phenomenon which is missing in the subsonic experimental data. In the supersonic areas of the jet the RMS value is increasing and decreasing in the subsonic areas. The slope close to the nozzle exit of the experimental data seems to be steeper than for the numerical jet. This causes a deviation of the present numerical data to the external data in the range of $0 \leq x/D \leq 10$. Further downstream, the present numerical data match each other and are in the range of the external data.

Finally, in Fig. 4.31 the RMS value of the entropy fluctuations are presented. These values indicate the length of the potential core which is about $5D$ for the moderate and high resolution jet and about $6D$ for the low resolution case. The shape of all three resolutions is similar whereas the shape of the low resolution curve is shifted about one jet diameter downstream.

II

Minimizing supersonic jet noise

5

Optimization method

In the present application we search for the best porous material to minimize supersonic jet noise. There will be a series of porous media which will reduce jet noise and some of them might perform better than other ones. Numerical [Lai & Luo, 2008] and experimental studies [Geyer et al., 2010] show that it is by no means clear how to choose the porous medium (ϕ and $\boldsymbol{K}$) to reduce aeroacoustic noise. In some specific cases they show that a porous medium could also amplify noise.

To search for a porous medium to reduce supersonic jet noise by trail and error, especially for a numerical analysis with high performance computers, is expensive. To find the best choice may be impossible. To this end, an optimization algorithm is used to find the best porous material to minimize supersonic jet noise and in particular jet screech.

In a mathematical formulation, the minimization of a function J under nonlinear equality and inequality constraints reads:

$$\min_{x \in \Re^n} J(x) \quad \text{subject to} \begin{cases} c_i = 0 & i \in E \\ c_i \leq 0 & i \in I \end{cases} \tag{5.1}$$

where x is an n-dimensional parameter vector. E and I are a subset of equality and inequality constraints, respectively. In the present application, x is the characteristic property of the porous material.

In the field of numerical optimization, two main classes of optimization techniques can be identified: gradient based and gradient free optimization. The latter class of optimization contains e.g. genetic algorithms. These meth-

ods use a set of possible solutions (parents) and evaluate their fitness (objective function). Based on that value they choose the best candidates for a recombination and mutation to build the next generation (children). The children are now parents and the process can be repeated to build the next generation and finally to find the "fittest" individual of the population. Such algorithm have the ability to find a global minimum of a non convex function. This depends on the distribution of the individuals in the first generation. Another advantage is that they do not necessarily need to deal with continuous and differentiable functions. They can also handle integer numbers, like the optimization of the number of rotors on a propeller. For the present application, where we search for a continuously distributed material property of a porous medium with up to several million degrees of freedom, these methods are too expensive.

The second class of optimization algorithm use the gradient of the objective function to obtain the direction in which the objective function can be minimized. In a numerical analysis, the gradient can be obtained with finite differences, like

$$\nabla_{x_i} J \approx \frac{J(x_i + \delta x_i) - J(x_i)}{\delta x_i} \tag{5.2}$$

These finite differences need to be evaluated for each design variable x_i separately. One evaluation of J corresponds in the present study to one computation of the Navier–Stokes equations and is very expensive. Performing this technique for several thousand or million design variables $x \in \Re^n$ is impractical.

Within the last years a method based on adjoint equations became more and more popular in the field of fluid mechanics. With this technique it is possible to evaluate the gradient of the objective function, independently on the number of design variable, with only *one* additional computation of the adjoint equations, where the solution of the adjoint equations is about as expensive as for the direct equations. This method is particularly suitable to handle the intended multidimensional problem and will be used to optimize the porous material. In the following sections the method of adjoint based optimization is presented.

5.1 A simple example

Let us start with a very simple example to introduce the method of Lagrange multipliers (adjoint variables). Consider the following one-dimensional prob-

lem:

$$\min_{x \in \Re} \quad J(x) \quad = x^2 \tag{5.3a}$$

$$\text{subject to} \quad N(x,c) \quad = x - c = 0 \tag{5.3b}$$

In this example the objective is to minimize the function $J(x)$ subject to the equality constraint $N(x,c) = 0$ with the control c. The solution to this problem is trivial. Setting $c = 0$, the objective function $J(x)$ will reach its minimum. Although the solution to this problem is trivial it will be used in the following to introduce the concept of Lagrange multipliers.

With a new variable λ, the so called Lagrange multiplier, the corresponding Lagrange function can be defined:

$$\mathcal{L}(x,c,\lambda) = J(x) - \lambda \cdot N(x,c) \tag{5.4}$$

whereas it is equivalent whether the latter term with λ is added or subtracted. Now, if x is a stationary point of Eq. (5.3a), then there exists a λ so that (x,λ) is a stationary point of Eq. (5.4). One can reformulate the problem in finding a stationary point of $\mathcal{L}$ instead of J including all constraints in one equation. For a stationary point of a functional, all partial derivatives need to vanish and one obtains a system of equations:

$$\frac{\partial \mathcal{L}}{\partial x} = 0 = 2x - \lambda \tag{5.5a}$$

$$\frac{\partial \mathcal{L}}{\partial \lambda} = 0 = x - c \tag{5.5b}$$

$$\frac{\partial \mathcal{L}}{\partial c} = 0 = \lambda \tag{5.5c}$$

These three equations with the three unknowns x, c and λ form the optimization framework which can be solved to obtain the optimal solution. For the present system of equations, it directly follows that $c = 0$ is the optimum. Such an optimization method, where the solution can be gained within one step, is referred to as an *one-shot method*. Usually, when Eq. (5.3a) and (5.3b) are nonlinear, this approach is no more possible. To this end, an iterative gradient based method is needed. As long as the optimum is not reached, Eq. (5.5c) is the gradient of the objective function with respect to the control c. We obtain:

$$\frac{\partial J}{\partial c} = \lambda \tag{5.6}$$

The gradient is depending on the Lagrange multiplier λ and we need to solve Eq. (5.5a) to obtain an expression for the Lagrange multiplier:

$$\lambda = 2x \tag{5.7}$$

Input: initial guess c
tolerance tol
Output: optimum c
1: **while** $err > tol$ **do**
2: solve x Eq. (5.3b) (direct)
3: solve λ Eq. (5.7) (adjoint)
4: compute gradient $\frac{\partial J}{\partial c}$ Eq. (5.6)
5: update control $c^{(n+1)}$ Eq. (5.8)
6: $err = \|c^{(n+1)} - c^{(n)}\|$
7: $n \longleftarrow n + 1$
8: **end while**

Algorithm 5.1: Algorithm for a simple optimization loop.

In the following, we will call this equation "adjoint equation" and the Lagrange multiplier "adjoint variable". The reason for these names is given later.

The gradient obtained from Eq. (5.6) can be used with a simple steepest descent approach to converge to the optimum iteratively:

$$c^{(n+1)} = c^{(n)} - \alpha^{(n)} \left(\frac{\partial J}{\partial c} \right)^{(n)} \tag{5.8}$$

In Alg. 5.1, the optimization loop to obtain the minimum is presented. We start the algorithm with the initial guess of our control c and obtain the state x of the system by evaluating the direct equation (5.3b). This is followed by solving the corresponding adjoint equation (5.7) to obtain the solution of the adjoint state. Finally, the gradient (5.6), which is a function of the adjoint state, can be evaluated and with a steepest descent approach (5.8) the new control is found. This is repeated iteratively until the algorithm converged. In Fig. 5.5 the performance of the algorithm is presented with the initial guess $c = 1$ and the constant step size $\alpha = 0.1$. Panel (a) shows the objective function J in the solution space including the intermediate solutions of each iteration. One can see that the value of the objective function is decreasing and approaching to its minimum. In panel (b) the objective function and the corresponding gradient with respect to the control c is presented as a function of the iteration number. It shows that the the objective function is decreasing by nearly twenty orders of magnitude within the first 100 iterations. In the same time, the gradient decays by nearly ten orders of magnitude.

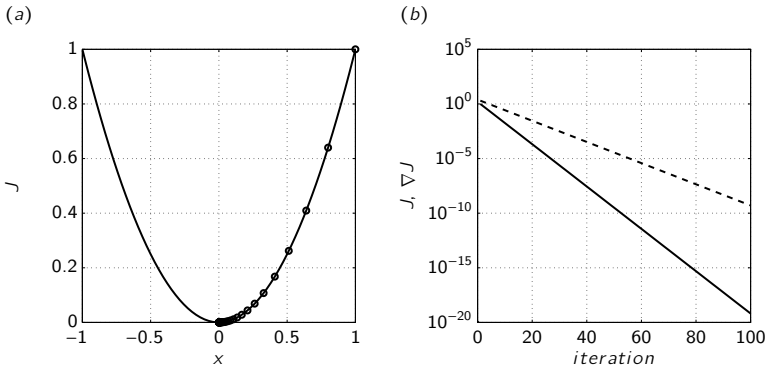

Figure 5.1: Simple example to illustrate the method of Lagrange multipliers. (*a*) Solution of the direct equation (5.3b) starting with the initial guess $c = 1$, saved for all iterations. (*b*) Convergence history for the objective function J (———) and its gradient (- - - - - -).

Above example with Lagrange multipliers can be considered from an alternative viewpoint. Let us again start with the problem formulation of Eq. (5.3). The total derivative of the objective function $J = J(x)$ (Eq. (5.3a)) with respect to the control c reads:

$$\frac{dJ}{dc} = \frac{\partial J}{\partial x}\frac{dx}{dc} \tag{5.9}$$

subject to the constraint that the sensitivity of the solution $\frac{dx}{dc}$ satisfies the direct equation:

$$\frac{\partial N}{\partial x}\frac{dx}{dc} + \frac{dN}{dc} = 0 \tag{5.10}$$

One can define the following abbreviations:

$$u := \frac{dx}{dc}; \quad A := \frac{\partial N}{\partial x}; \quad b := \frac{\partial J}{\partial x}; \quad f := -\frac{dN}{dc} \tag{5.11}$$

and end up with the following equations:

$$\frac{dJ}{dc} = b^T u = \lambda^T f \tag{5.12}$$

subject to

$$Au = f \tag{5.13}$$

under the constraint, that λ satisfies the adjoint equation:

$$A^T \lambda = b. \tag{5.14}$$

The equivalence of the last two terms in Eq. (5.12) is easily proved:

$$b^T u = (A^T \lambda)^T u = \lambda^T A u = \lambda^T f \tag{5.15}$$

with the adjoint matrix A^T (if $A \in \Re^{n \times n}$) and the corresponding adjoint variable λ. From this viewpoint, one can deduce the origin of the name *adjoint* optimization, which is not as evident when following the previous approach with Lagrange multipliers.

One of the main advantages of adjoint based optimization, compared to other gradient based optimization techniques, can be identified. The gradient of the objective function in Eq. (5.12) can be either computed by the term $b^T u$ *or* $\lambda^T f$. As f is a function of the control ($f = f(c)$), and if the dimension of the control is large, the evaluation of $b^T u = b^T A^{-1} f$, has to be performed for every single $f(c)$. To this end a system of equations has to be solved as many times as the dimension of c. In contrast to that, as $g \neq g(c)$, the evaluation of $\lambda^T f$ including the solution of the adjoint equation $\lambda = (A^T)^{-1} b$ has to be carried out only once. Especially if the dimension of the control is large and the solution of the direct equations is expensive, adjoint methods are indispensable.

In the area of fluid mechanics the dimension of the control (e. g. geometry parameters of a wing) is usually in the order of several hundred. In the present study, where the optimal spacial distribution of a porous medium is questioned, the dimension of the control can be easily in the order of several million. In addition to that, the underlying equations, to obtain the state (here u), are based on the Navier–Stokes equations. Their numerical solution is expensive and requires the use of high performance techniques.

To apply this simple example to the Navier–Stokes equations of the present investigation, the equality constraint in the Lagrange functional $N(x, c)$ has to be replaced by the Navier–Stokes equations. They constrain the solution space of the flow variables.

5.2 State of the art

Adjoint based optimization in the field of fluid mechanics is by no means new but a field of active research. The first to use adjoint based optimization was Pironneau [1974]. He derived an optimization framework to minimize the

drag of a hump on the surface of a body. At this time, he was not able to provide a numerical solution to this problem and only delivered the theoretical framework. A wide range of different research topics has followed within the next years and decades and is still ongoing. The different topics on adjoint based optimization can be classified in three main fields: shape optimization, topology optimization and active optimization. In the following, the state of the art will be addressed separately for each topic.

Shape optimization The use of adjoint equations has been pioneered by Jameson [1988, 1995]. He used several setups from two- to three-dimensional configurations based on potential equations, the Euler equations and the Navier–Stokes equations. The main focus of shape optimization is to minimize the drag of a wing while keeping or even increasing the lift. The early work of Jameson was followed by a series of researchers working on that topic up to the present date [see amongst others Asouti et al., 2008, Brezillon & Gauger, 2004, Carpentieri et al., 2007, Fazzolari et al., 2007, Giles & Pierce, 2000, 1999, Gunzburger, 2000, Kim et al., 2004, Le Moigne, 2002, Nemec & Zingg, 2001].

Some of the shape optimization applications also deal with transonic or supersonic wing configurations where shocks are present. They were investigated e. g. by Giles [2002], Giles et al. [2003], Nadarajah et al. [2001], Reuther et al. [1996]. It was reported by Giles & Pierce [2001] in an analytic one-dimensional study that the adjoint solution in the presence of shocks is incorrect and needs additional internal boundary conditions in the vicinity of the shock. The additional boundary condition arise due to the linearization of the Navier–Stokes equations when deriving the corresponding adjoints. In this step it is assumed that the solution of the equations is smooth and that a linear perturbation theory can be applied. This assumption may be violated in the presence of a shock. Especially strong shocks may be resolved in a numerical investigation by only a view grid points and a linear theory may need additional boundary conditions to predict the correct jump of the flow variables. If the shock is well resolved by the computational grid or smeared out over several grid points due to a shock capturing method, the linear theory can be applied and errors in the adjoint solution are not to be expected. The same holds true for weak and oblique shocks [see Giles et al., 2003]. In the present application on the optimization of a shock containing flow, first, no strong shocks, like a Mach disk are present, and secondly, a shock capturing scheme smears out strong gradients to obtain a smooth solution. Hence, an additional boundary condition in the vicinity of shocks is not necessary.

Shape optimization has not only been applied to lift and drag optimization but also to flow induced acoustic, like the minimization of trailing edge noise [Marsden et al., 2001, Rumpfkeil & Zingg, 2009] or the minimization of the noise of a trailing step [Cao & Stanescu, 2002]. It has also been applied to turbo-machinery noise like the minimization of fan-flow deflector noise [Xiong et al., 2010]. In another application, by Feijoo et al. [2004], an inverse acoustic scattering problem is presented to find the optimal geometry that satisfies a certain measured acoustic signal. Applications of shape optimization for an acoustic objective in combination with supersonic flows has been reported by Nadarajah et al. [2003]. They minimized the sonic boom measured at the ground surface by changing the geometry of the supersonic aircraft. A similar investigation was performed by Mohammadi [2004].

Topology optimization In the latter paragraph, the control to achieve the desired objective is to change the shape of one or several predefined geometries. This approach is limited. The optimization algorithm will neither be able to split a geometry in several geometries nor to "invent" new geometries. As a user of the shape optimization algorithm a lot of empirical information has to be provided and the solution space is restricted. In some applications, where it is neither clear how the optimal shape of the geometry should be configured nor how many obstacles should be place in the fluid flow, adjoint based topology optimization is the method of choice.

Originally, adjoint based topology optimization was used in solid state mechanics [Bendsøe, 1995, Eschenauer & Olhoff, 2001]. The first application to fluid mechanics was reported in Borrvall & Petersson [2003] with the topology optimization of fluids in Stokes flow. The main idea of any adjoint based topology optimization algorithm in fluid mechanics is based on a Darcy term in the momentum equation whose sensitivity is obtained via an adjoint computation. Hence, the Darcy term is being optimized and represents a passive control. As in topology optimization only solid materials or void space is allowed, one has to distinguish between zero permeability or a high permeability (corresponding to a solid body) based on the sensitivity map emerging from the adjoint computation. Following the early work of Borrvall & Petersson [2003], many others adapted the method like Olesen et al. [2004] for Navier–Stokes flows in micro-fluidics. Gersborg-Hansen et al. [2005] applied the method to the optimization of channel flow problems. A large scale Stokes flow problem was investigated by Aage et al. [2008]. Using a continuous adjoint formulation for the computation of topological sensitivities, ducted flows are optimized by Othmer [2008]. Recently Papoutsis-Kiachagias et al. [2011]

applied topology optimization to laminar and turbulent flows, including heat transfer.

Topology optimization is also applied to acoustic problems. Dühring et al. [2008] used it to design geometries to reduce the noise level in a certain area of a room. They applied it to the Helmholtz equations with a fluid in rest. The first to apply topology optimization to an aeroacoustic application was Schulze & Sesterhenn [2011]. They used the method to optimize the spatial distribution of a porous medium (with a variable permeability) to reduce trailing edge noise. Some of their main results are presented in Sec. § 5.5.3.

The present application on the minimization on supersonic jet noise by means of an optimized porous material can be classified as a topology optimization. Up to now, it is the first time that topology optimization with porous media is applied to supersonic jet noise. It will be discussed in detail in the remaining part of this thesis.

Active optimization Despite shape and topology optimization, which belong to the class of passive control as long as the geometry is steady in state, active control can be applied. Examples are blowing and suction, heating and cooling of a boundary or any other form of volume forcing in the domain. The first to use blowing and suction in optimal control was Joslin et al. [1995] to suppress the boundary layer instability. A similar investigation was performed by Airiau et al. [2003]. Later, Guegan et al. [2006] applied it to the optimal control in swept Hiemenz flow. Bewley et al. [2001] used blowing and suction to reduce the kinetic energy in a plane channel flow. Up to that time they performed the highest-dimensional control optimization with a total of 10^7 control variables. Based on the compressible two-dimensional Navier–Stokes equations Collis et al. [2002b] optimized two counter rotating vortices impinging on a flat plate.

Active control strategies were frequently used in aeroacoustic applications. It was first reported by Collis et al. [2002a] as they applied it to the blowing and suction of a cylinder vortex interaction and could reduce the aeroacoustic noise by 6 dB. An example based on the Euler equations and an optimal transpiration control to reduce aeroacoustic noise is reported by Collis et al. [2003].

The first application to free sher flow noise, like the one of mixing-layers or jets, is proposed by Cervino et al. [2002]. They obtained in a two-dimensional study of a $M_j = 0.5$ jet a sensitivity map to a noise signal measured in the acoustic near field. No optimization was performed in this study. They mention in Cervino & Bewley [2003] that on the one hand the actuation with

mass sources is more efficient than with heat sources and on the other hand that high frequency noise can be modified with a low frequency actuation. Wei [2004], Wei & Freund [2002] were the first to control a mixing-layer based on a thermal volume forcing in a small region in the mixing-layer. They could reduce the noise by more than 6 dB and showed that the forcing is weak and has little effect on the structures of the mixing-layer. Later, Wei & Freund [2006] showed that it is not only vortex pairing which is responsible for mixing noise, as the pairing phenomenon did not vanish for the controlled mixing-layer. Similar studies on mixing-layer noise were performed by a series of researchers, like Babucke et al. [2009], Barone [2003], Barone & Lele [2005], Kleinman & Freund [2006], Spagnoli & Airiau [2008].

Recently, Freund [2011] presented an intermediate step of the optimization of a supersonic axisymmetric jet by means of thermal actuation close to the nozzle exit (similar to the work of Wei & Freund [2006]). The Mach number of the perfectly expanded jet is $M_j = 1.3$ with a total of $2.8 \cdot 10^6$ grid points (LES, nozzle is not included). They presented the first step of the Line Search algorithm and gained a reduction of 37 % for the objective function. Their simulations are ongoing.

5.3 Objective function

In the present application on supersonic jet screech the noise is characterized by a specific structure of the frequency spectrum. It contains distinct frequency peaks with high amplitudes. In Fig. 5.2(a) a sketch of a typical spectrum of aeroacoustic jet-screech is shown, characterized by a loud and distinct peak at a specific frequency ω_{screech}. Other noise sources, such as the low-frequency mixing noise of the jet or the broadband shock noise are rather quiet by comparison.

Most recent attempts of noise reduction by iterative optimization use a quadratic objective functional where the acoustic pressure fluctuations $p'(\boldsymbol{x}, t)$ are squared and integrated over space and time. Although this approach might reduce the objective functional, it is by no means clear which frequencies of our noise source will ultimately be reduced. For example, applying the above technique could dampen the sound level at some frequencies of the spectrum, but readily amplify others. In a worst-case scenario, the dominant noise sources – the peaks in Fig. 5.2(a) – may be amplified while the other (already relatively quiet) parts in the spectrum are further reduced (cf. Fig. 5.2(b)). This may yield an overall reduced objective functional but does hardly meet the intentions. One then quickly realizes that, in order to

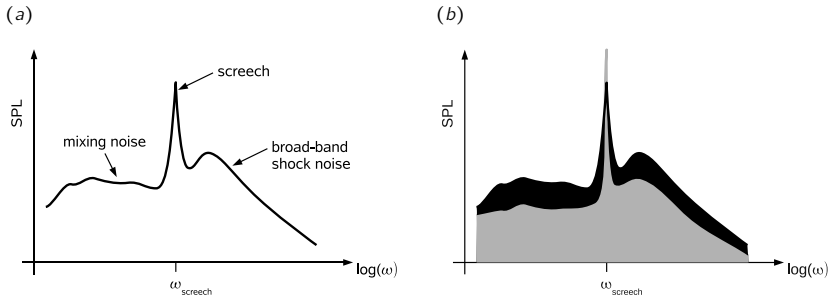

Figure 5.2: (*a*) Sketch of a typical spectrum for a supersonic jet-noise application with screech. The peak of the screech signifies the dominant noise source and can be several dB louder than all other noise sources [see Seiner, 1984]. (*b*) Sketch of a worst-case scenario for the optimization of jet screech. Black curve: without optimization. Gray curve: with optimization. Although the objective functional (shaded area under the black and gray curve, respectively) is decreasing, the dominant noise peak is even higher than before.

design effective optimization tools for targeted noise reduction, the governing objective functional has to be written in frequency space. Only then can there be a guarantee that the dominant peaks in the spectrum can be singled out and counteracted by appropriate control schemes while keeping the quiet part of the spectrum mostly unchanged.

In this section the mathematical framework for combining an iterative adjoint-based optimization technique with an objective functional formulated in frequency space is presented. It is based on the work of Schulze et al. [2011].

If the goal of an optimization is the reduction of the aeroacoustic noise levels, a commonly chosen objective functional is

$$J = \frac{1}{2} \int_{\Omega} \int_{t_0}^{t_1} (p - p_0)^2 M(\boldsymbol{x}) \, \mathrm{d}t \, \mathrm{d}\Omega, \tag{5.16}$$

with $p = p(\boldsymbol{x}, t)$ as the pressure field and p_0 denoting the mean pressure. The acoustic pressure fluctuations are then given as $p'(\boldsymbol{x}, t) = p(\boldsymbol{x}, t) - p_0(\boldsymbol{x})$. It should be noted that the mean pressure p_0 has to be chosen carefully so as to distinguish between acoustic and aerodynamic fluctuations. In the cost functional (5.16) the noise is measured in the domain Ω and recorded over a time span of $(t_1 - t_0)$. With an additional weighting function in space $M(\boldsymbol{x})$, the area where to measure the noise can be selected. Measuring only in one point (microphone), the weighting function would be the Dirac delta

($M(\boldsymbol{x}) = \delta(\boldsymbol{x}-\boldsymbol{x_m})$, where $\boldsymbol{x_m}$ is the location of the microphone). To increase numerical stability, a Dirac delta can be smoothed out by replacing it with a Gaussian distribution.

Following Parseval's theorem the energy of a signal, in our case the square of the measured noise, is the integral of the square of all its Fourier coefficients. Applied to the temporal integral in (5.16) we obtain

$$\int_{\Omega}\int_{t_0}^{t_1} (p'(\boldsymbol{x},t))^2 M(\boldsymbol{x})\,\mathrm{d}t\,\mathrm{d}\Omega = \frac{1}{2\pi}\int_{\Omega}\int_{-\infty}^{\infty} |P'(\boldsymbol{x},\omega)|^2 M(\boldsymbol{x})\,\mathrm{d}\omega\,\mathrm{d}\Omega. \tag{5.17}$$

A reduction in the objective functional J thus requires an equivalent reduction in the coefficients $|P'(\boldsymbol{x},\omega)|^2$, which corresponds to a decrease of the amplitudes in the power-spectrum. As previously mentioned, however, by following this approach it remains unclear which frequencies of the noise-spectrum are ultimately reduced. Depending on the underlying physics as well as on the applied control, it is conceivable that only a certain – maybe uninteresting – frequency-band could be minimized using the above objective functional. In the worst case, the dominant noise source may be amplified even though J is decreasing (cf. Fig. 5.2(b)).

5.3.1 Objective functional in frequency space

Given an uncontrolled noise spectrum with peaks at distinct frequencies, one can introduce an objective functional that allows not only to target certain frequencies but also to identify sharp peaks. The objective functional in the frequency domain can be written as

$$\begin{aligned} J = \quad & \underbrace{\frac{\lambda_1}{2}\int_{\Omega}\int_{\omega_l}^{\omega_u}\left\{\int_{-\infty}^{\infty} e^{-i\omega t} p'(\boldsymbol{x},t)\mathrm{d}t\right\}^2 M(\boldsymbol{x})\,\mathrm{d}\omega\,\mathrm{d}\Omega}_{J_1} \\ + \quad & \underbrace{\frac{\lambda_2}{2}\int_{\Omega}\int_{\omega_l}^{\omega_u}\left\{\frac{\partial}{\partial\omega}\int_{-\infty}^{\infty} e^{-i\omega t} p'(\boldsymbol{x},t)\mathrm{d}t\right\}^2 M(\boldsymbol{x})\,\mathrm{d}\omega\,\mathrm{d}\Omega}_{J_2} \end{aligned} \tag{5.18}$$

with λ_1 and λ_2 as user-defined weights to give more emphasis to the first or second term in the above expression and to influence the convergence of the optimization algorithm.

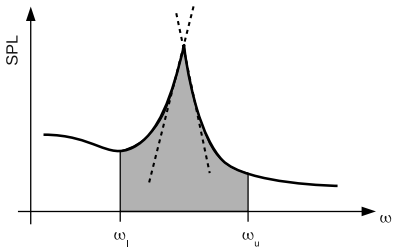

Figure 5.3: Sketch of a typical spectrum of an aeroacoustic noise source. The objective functional to be minimized consists of the gray area between ω_l and ω_u (J_1) and a term proportional to the gradient illustrated by the dashed lines (J_2).

The first term in (5.18) denoted by J_1 describes the area under the power-spectrum between a lower frequency ω_l and an upper frequency ω_u and is expressed as an integral over the square of the Fourier-coefficients of the acoustic pressure fluctuations p' between ω_l and ω_u. This area corresponds to the frequency-band over which the acoustic noise is to be minimized (cf. Fig. 5.3). Considering a high and wide peak in the frequency-band to minimize, the term J_1 might not be sufficient to accomplish this task. To specifically target sharp peaks within the frequency band $[\omega_l, \omega_u]$, a second term, denoted by J_2, is added to penalize high gradients of the power spectrum with respect to the frequency ω (indicated by the dashed lines in Fig. 5.3). After some standard manipulations, expression (5.18) can be reformulated using the common abbreviation $\mathcal{F}\{q\} = \int_{-\infty}^{\infty} q(t) e^{-i\omega t} \mathrm{d}t$ to yield

$$J = \frac{1}{2} \int_{\Omega} \int_{\omega_l}^{\omega_u} \left(\lambda_1 \left(\mathcal{F}\{p'\} \right)^2 - \lambda_2 \left(\mathcal{F}\{t \cdot p'\} \right)^2 \right) M(\boldsymbol{x}) \, \mathrm{d}\omega \, \mathrm{d}\Omega \tag{5.19}$$

where the derivative with respect to ω in frequency-space (in term J_2) transforms into a multiplication by $-t$ in the time-domain. For the present investigation, the weights are chosen as $\lambda_1/\lambda_2 = 10$. A detailed summary of the parameters for a modified version of the objective function (5.20) is given in Tab. 5.1 on page 168.

With expression (5.18) it is now possible to define an objective functional that focuses on the reduction of a certain frequency band. Nevertheless, the remaining frequencies outside the frequency band are not accounted for. It is conceivable that the peak in the spectrum moves outside the frequency-

band	$\lambda_{1,k}$	$\lambda_{2,k}$	$\omega_{l,k}$	$\omega_{u,k}$
$k = 1$	1	0.1	0	$0.95\,\omega_s$
$k = 2$	10	1	$0.95\,\omega_s$	$1.05\,\omega_s$
$k = 3$	1	0.1	$1.05\,\omega_s$	∞

Table 5.1: Parameters of the objective function (5.20) to minimize supersonic jet noise. Screech frequency: ω_s. The first band $k = 1$ accounts for mixing noise, the second band $k = 2$ for the screech tone and the third band for shock-associated noise.

band $[\omega_l, \omega_u]$ during the optimization process, therefore causing a substantial drop in the objective functional. Consider, for example, the present application of screech reduction. Changing the effective jet diameter by adding a porous material inside the nozzle, would reduce the shock cell spacing and consequently increase the screech frequency. If the screech frequency moves outside the upper limit ω_u, the objective function will be reduced but it would certainly not solve the intended problem.

Different strategies are possible to address this issue. If our objective is simply the reduction of noise with emphasis on a certain frequency, one could add a second objective functional of the form (5.18) where the integration is performed over all frequencies outside the dominant frequency, i.e. $\omega \in]0, \omega_l[\cup]\omega_u, \infty[$. By means of appropriate weights for the two expressions one could focus on the frequency-band $[\omega_l, \omega_u]$. In a general case this approach reads for N distinct frequency bands:

$$J = \frac{1}{2} \sum_{k=0}^{N} \int_{\Omega} \int_{\omega_{l,k}}^{\omega_{u,k}} \left(\lambda_{1,k} \left(\mathcal{F}\{p'\} \right)^2 - \lambda_{2,k} \left(\mathcal{F}\{t \cdot p'\} \right)^2 \right) M_k(\boldsymbol{x}) \, \mathrm{d}\omega \, \mathrm{d}\Omega \qquad (5.20)$$

Now, the different weights and frequency bands define the noise sources to be minimized. In addition to that, the position where to minimize the noise ($M_k(x)$) can be different for each frequency band. In the present application on supersonic jet noise, the objective function as defined in Eq. (5.20) is used to minimize jet screech. The parameters are summarized in Tab. 5.1. With this set of parameters, the effect of the screech frequency is weighted ten times stronger than the remaining frequencies (mixing noise and broadband shock-associated noise). One could also account for the subharmonics of the screech tone by adding additional frequency bands with $\omega = n \cdot \omega_s$ ($n = 2, 3, 4, ...$).

Nevertheless, the subharmonics are linked to the fundamental screech tone and a reduction of the screech tone will also reduce its subharmonics. To this end, only the fundamental screech frequency ω_s is accounted for.

An alternative strategy is based on keeping the uncontrolled frequencies unchanged. In the present application this corresponds to a reduction of screech noise while keeping the amplitudes of the mixing noise and the shock-associated noise on a constant level. From an environmental point of view, this strategy is not desirable as the optimization may not be as efficient as the reduction of all frequencies. Nevertheless, this approach can be of particular interest if our goal is not only the minimization of noise in particular frequency bands but also the discovery and understanding of noise generation mechanisms by specific acoustic sources. In other words, by keeping all uncontrolled frequencies unchanged and simultaneously reducing only the dominant peak within a given frequency band, one can extract the mechanism responsible for this specific peak in the spectrum. Mathematically, we introduce non-negative terms that penalize any changes in the noise spectrum from the uncontrolled spectrum for frequencies outside the target interval $[\omega_l, \omega_u]$. For this strategy, the uncontrolled spectrum has to be determined and stored. We obtain

$$P = P_1 + P_2 \tag{5.21a}$$

$$P_1 = \frac{1}{2} \int_{\Omega} \int_{-\infty}^{\omega_l} \left(\mathcal{F}\{p'\} - \mathcal{F}\{p'_0\}\right)^2 M(\boldsymbol{x}) \, \mathrm{d}\omega \, \mathrm{d}\Omega \tag{5.21b}$$

$$P_2 = \frac{1}{2} \int_{\Omega} \int_{\omega_u}^{\infty} \left(\mathcal{F}\{p'\} - \mathcal{F}\{p'_0\}\right)^2 M(\boldsymbol{x}) \, \mathrm{d}\omega \, \mathrm{d}\Omega \tag{5.21c}$$

with the controlled acoustic pressure fluctuations denoted by p' and the uncontrolled fluctuations by p'_0. The term P_1 penalizes changes in the spectrum below the target frequency-band, i.e, $\omega \in [-\infty, \omega_l[$; the term P_2 ensures minimal changes of the spectrum in the frequency-band $\omega \in]\omega_u, \infty[$.

In the present investigation, the additional penalty term is not included in the minimization of jet screech, as the focus also lies on the reduction of the remaining noise sources. Nevertheless, this term can be used for future investigations, to focus on the individual noise sources.

In addition to the two penalty terms P_1 and P_2 an additional penalty term is usually added in control theory. This additional penalty term has the

following form:

$$P_3 = \frac{\beta}{2} \int_{\Omega} \int_{t_0}^{t_1} \|\boldsymbol{K}\|_2^2 \, \mathrm{d}t \, \mathrm{d}\Omega \tag{5.22}$$

where $\boldsymbol{K} = \boldsymbol{K}(x)$ stands for the control variable, and β represents a user-specified parameter that measures the cost of the control. Small values of β will cause the control to be expended generously, while large values of β will result in more parsimonious levels of control. In the present application, the control is passive and no energy in the classical meaning is wasted when the control is large. In other words, a large control in the present investigation stands for a solid body, whereas a small control is equal to void space. As we have seen in the previous chapters, on the derivation of the porous flow equations, a solid porous material can be responsible for numerical instabilities. These instabilities can justify the additional penalty term to limit the stiffness of the system of equations. Nevertheless, the choice of the user-defined parameter β is by no means trivial. If the gain is too strong, it can lead to a poor convergence and if it is too weak, it can lead to the already mentioned numerical instabilities. To this end, the additional penalty term is not included in the present investigation. Rather, the control is simply limited to an upper pre-defined limit which guarantees numerical stability and sufficient solid properties. In the present application, the upper limit is $\chi_{\max} = 2 \cdot 10^5$.

5.4 Optimization framework

With the objective function J (5.20) of the previous section, we can now define the optimization framework. The goal of the present investigation is to apply optimization methods to fluid-mechanical/aeroacoustical problem described or modeled by nonlinear partial differential equations. The optimization algorithm then drives the objective functional, given above, toward a minimum while observing that the final solution has to satisfy the governing equations, boundary and initial conditions. The latter set of equations thus represents a constraint on the minimization problem, and the constrained optimization problem can be recast into an unconstrained problem by adding the constraints via Lagrange multipliers. We obtain the Lagrange functional $\mathcal{L}$ as follows,

$$\mathcal{L} = J - \langle \mathcal{N}(\boldsymbol{q}, \boldsymbol{K}), \boldsymbol{q}^\star \rangle - [H(\boldsymbol{q}), \boldsymbol{h}^\star] - (G(\boldsymbol{q}), \boldsymbol{g}^\star) \,. \tag{5.23}$$

The objective functional is given by (5.20). $\mathcal{N}(\boldsymbol{q}, \boldsymbol{K}) = 0$ is a symbolic way of stating the governing equations for the state variable $\boldsymbol{q}$ and control $\boldsymbol{K}$, given

by the compressible Navier-Stokes equations. In a similar symbolic form, the boundary conditions and initial conditions can be formulated as $H(\boldsymbol{q}) = 0$ and $G(\boldsymbol{q}) = 0$, respectively. We note that the governing equations, boundary and initial conditions are added to the objective functional and penalty terms by the Lagrange multipliers $\boldsymbol{q}^\star, \boldsymbol{h}^\star$ and $\boldsymbol{g}^\star$. Since the constraints have to be satisfied locally, the Lagrange multipliers are fields, and the three different scalar products in (5.23) are thus given as

$$\langle p, q \rangle = \int_{t_0}^{t_1} \int_{\Omega} p(\boldsymbol{x}, t)^H q(\boldsymbol{x}, t) \, \mathrm{d}\Omega \mathrm{d}t \tag{5.24a}$$

$$(p, q) = \int_{\Omega} p(\boldsymbol{x})^H q(\boldsymbol{x}) \, \mathrm{d}\Omega \tag{5.24b}$$

$$[p, q] = \int_{t_0}^{t_1} p(t)^H q(t) \, \mathrm{d}t \tag{5.24c}$$

with the superscript ^{H} denoting the complex conjugate transpose for vector valued variables and simply the complex conjugate for scalar variables. For real valued problems, as in the present application, the conjugate transpose turns simply into a transpose with the superscript ^{T}. The variables $\boldsymbol{q}^\star, \boldsymbol{h}^\star$ and $\boldsymbol{g}^\star$ are the adjoint variables which enforce, respectively, the governing equations, the boundary conditions and the initial conditions. In what follows, adjoint variables will be indicated by the superscript *. A detailed and recent review of adjoint optimization using a Lagrange functional can be found in Bewley [2001].

The Lagrange functional depends on the independent variables $\boldsymbol{q}(\boldsymbol{x}, t)$, $\boldsymbol{q}^\star(\boldsymbol{x}, t)$, $\boldsymbol{h}^\star(t)$, $\boldsymbol{g}^\star(\boldsymbol{x})$, $\boldsymbol{K}(\boldsymbol{x}, t)$, and a minimum (or stationary point) of $\mathcal{L}$ requires the first variations with respect to all independent variables to vanish. Equating the first variation of the Lagrange functional with respect to $\boldsymbol{q}$, $\boldsymbol{q}^\star$,$\boldsymbol{h}^\star$, $\boldsymbol{g}^\star$ and $\boldsymbol{K}$ to zero yields a system of equations that can be solved iteratively to determine the minimum of the objective functional.

This system of equations, in general form, can be written as

$$\frac{\partial \mathcal{L}}{\partial \boldsymbol{q}^\star}\delta\boldsymbol{q}^\star = 0 \;\rightarrow\; \mathcal{N}(\boldsymbol{q},\boldsymbol{K}) = 0 \qquad \text{direct equation} \tag{5.25a}$$

$$\frac{\partial \mathcal{L}}{\partial \boldsymbol{h}^\star}\delta\boldsymbol{h}^\star = 0 \;\rightarrow\; H(\boldsymbol{q}) = 0 \qquad \text{direct boundary conditions} \tag{5.25b}$$

$$\frac{\partial \mathcal{L}}{\partial \boldsymbol{g}^\star}\delta\boldsymbol{g}^\star = 0 \;\rightarrow\; G(\boldsymbol{q}) = 0 \qquad \text{direct initial conditions} \tag{5.25c}$$

$$\frac{\partial \mathcal{L}}{\partial \boldsymbol{q}}\delta\boldsymbol{q} \;\; = 0 \;\rightarrow\; \mathcal{N}^\star(\boldsymbol{q}^\star,\boldsymbol{q},\boldsymbol{K}) = 0 \qquad \text{adjoint equation and its boundary conditions} \tag{5.25d}$$

$$\frac{\partial \mathcal{L}}{\partial \boldsymbol{K}}\delta\boldsymbol{K} = 0 \;\rightarrow\; \nabla_{\boldsymbol{K}} J \qquad \text{gradient} \tag{5.25e}$$

This set of equations can be used in an optimization loop to iteratively optimize the control parameter. In Fig. 5.4 the basic optimization framework is presented including the necessary equations. Starting with an initial guess of the control parameter, e. g. $\boldsymbol{K} = 0$, the direct equations are solved forward in time to obtain the state $\boldsymbol{q}$ based on which the objective functional J can be computed. With an adjoint terminal condition $\boldsymbol{q}^\star(T)$, depending on the objective functional, the adjoint equations need to be solved backwards in time. Due to the nonlinearity of the direct equations, the adjoint equations need the direct state $\boldsymbol{q}$ of the forward computation. Hence, $\boldsymbol{q}$ has to be saved throughout one optimization loop. Finally obtaining the adjoint state $\boldsymbol{q}^\star$, the gradient of the objective functional can be evaluated and the control parameter can be updated.

For a more detailed statement of the system of equations, specific information about the governing equations, boundary and initial conditions, and the objective functional have to be provided. In the next sections, we will demonstrate the above optimization framework by deriving a set of governing equations for iteratively optimizing the frequency output of the nonlinear Navier–Stokes equations.

Discrete vs. continuous approach The variation of the objective function with respect to the independent parameters corresponds to a linearization, followed by an integration by parts. This linearization and the integration by parts can be performed in two ways: discrete or continuous. In the latter case, the nonlinear PDEs are first linearized and then, during the integration by parts, the corresponding adjoint equations can be found. Finally, these equations can be discretized to solve them numerically. In the discrete case,

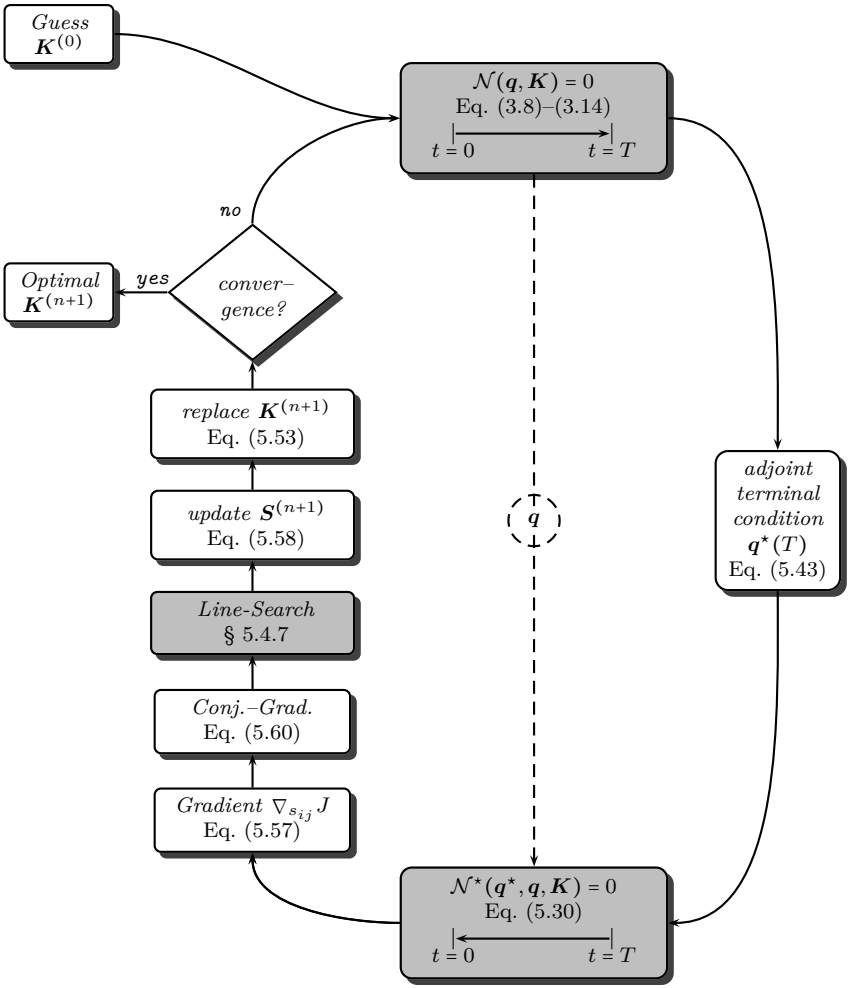

Figure 5.4: Iterative optimization loop for the nonlinear Navier–Stokes equations. Beginning with an initial guess $\boldsymbol{K}^{(0)}$ of the desired control, the direct equation $\mathcal{N}(\boldsymbol{q}, \boldsymbol{K})$ is solved forward in time. With an adjoint terminal condition the adjoint equation $\mathcal{N}^\star(\boldsymbol{q}^\star, \boldsymbol{K}, \boldsymbol{q})$ is solved backwards in time, using the direct state $\boldsymbol{q}$. Followed by a series of gradient evaluations, the new control state $\boldsymbol{K}^{(n+1)}$ is found. This loop is repeated iteratively n times until the algorithm shows convergence.

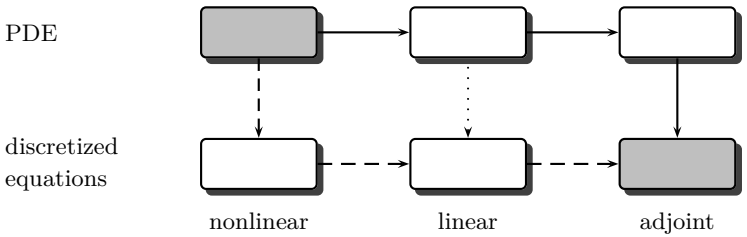

Figure 5.5: Different ways of the discretization of adjoint equations [see e. g. Giles & Pierce, 2000].

the nonlinear PDEs are first discretized, then linearized and based on that, the corresponding adjoint equations can be found. In Fig. 5.5 these two basic concepts are presented. There is even an intermediate step, where one first linearizes the equations and then discretizes the linear equations to finally obtain the discrete adjoints. Nevertheless, this intermediate approach is not common.

In the discrete approach, the discretized equations need to be differentiated. This step is usually performed automatically with so called "automatic differentiation" (AD) software like ADIFOR [see Bischof et al., 1992]. These tools use an existing code and derive the first derivative of all dependent variables. The new code can be used to obtain the discretized adjoint solution.

In the continuous approach, the equations need to be linearized and discretized by hand, which can be, especially for compressible codes, challenging. Which approach is the best choice, is hard to answer and remains, following Giles & Pierce [2000], a matter of personal taste. Giles & Pierce [2000] states some advantages of the two methods, which will be summarized and completed in Tab. 5.2.

Obviously, both approaches show advantages, which may be a reason to favor one of both methods. In the present investigation, we will follow the continuous approach. The main reason to prefer this approach instead of the discrete one, which is nowadays widely used, is the fact that the physical significance of the adjoint variables and especially the influence of the frequency based objective functional is much clearer. In addition to that, we will see in the following sections, especially in Sec. § 5.4.8 and § 5.4.9, that the main advantages of a discrete code, like the exact gradient and the same eigenvalues of both operators, can be also gained in good approximation for a continuous approach when carefully deriving and implementing the adjoint

Discrete approach	Continuous approach
The exact gradient of the objective function is obtained. This ensures the fully convergence of the optimization algorithm.	Physical significance of adjoint variables, boundary conditions and adjoint forcing is much clearer.
Derivation of the discrete adjoints can be performed with AD tools. Hence, it can be straightforward. The same eigenvalues of the direct and adjoint operator can be obtained.	The adjoint code is simpler and needs less memory. It can be optimized easier.
The code is numerically more stable than the continuous approach.	It is easier to include additional terms, like the Darcy term, without creating a completely new code as in the discrete case.

Table 5.2: Advantages of the discrete and continuous approach to obtain the discretized adjoint equations based on Giles & Pierce [2000].

equations. The continuous approach has also the advantage that the influence of the additional Darcy term on the adjoint equations is clearer and that its implementation in an existing adjoint code is straightforward. Nevertheless, a disadvantage of the continuous approach remains: the poor numerical stability. In the present investigation, a new method has been developed to stabilize the continuous adjoint code without affecting the solution of the gradient. It is presented in Sec. § 5.4.8 and shows that the disadvantage of the poor numerical stability of a continuous code can be efficiently eliminated without loosing the computational performance.

5.4.1 Application to the compressible porous Navier–Stokes equations

To apply the optimization algorithm to the present case, the Navier–Stokes equations, the objective functional and the initial and boundary conditions need to be included in the Lagrange functional of Eq. (5.23). The optimization framework can be obtained by evaluating the first variation with respect to all independent variables of the Lagrange functional. Trivial solutions

arise for the variation with respect to the adjoint variables, $\boldsymbol{q}^\star$, $\boldsymbol{h}^\star$ and $\boldsymbol{g}^\star$, corresponding to Eq. (5.25a), (5.25b) and (5.25c). As a result, one obtains the direct equation and the boundary and initial conditions. These relations are already present and nothing else has to be done at this step. More effort has to be exerted to determine the equations stemming from the first variations with respect to the direct state $\boldsymbol{q}$ and the control $\boldsymbol{K}$, corresponding to Eq. (5.25d) and (5.25e). The first variation of the Lagrange functional with respect to the control yields an expression for the gradient. Its derivation is presented in Sec. § 5.4.3. The first variation of the Lagrange functional with respect to the direct state yields an evolution equation for the adjoint state and the corresponding boundary conditions. It reads:

$$\frac{\partial \mathcal{L}}{\partial \boldsymbol{q}}\delta\boldsymbol{q} = \underbrace{\frac{\partial J}{\partial \boldsymbol{q}}\delta\boldsymbol{q}}_{①} + \underbrace{\left(\frac{\partial G}{\partial \boldsymbol{q}}\delta\boldsymbol{q}, \boldsymbol{g}^\star\right)}_{②} - \underbrace{\left[\frac{\partial H}{\partial \boldsymbol{q}}\delta\boldsymbol{q}, \boldsymbol{h}^\star\right]}_{③} - \underbrace{\left\langle\frac{\partial \mathcal{N}}{\partial \boldsymbol{q}}\delta\boldsymbol{q}, \boldsymbol{q}^\star\right\rangle}_{④} = 0 \tag{5.26}$$

Each term of Eq. (5.26) can be treated separately. The first term ①, the variation of the objective function, yields a source term for the adjoint equations. It forces the adjoint state, while it is integrated backwards in time. Its derivation is presented in Sec. § 5.4.1.3. The second ② and the third term ③ will result in the adjoint boundary and terminal condition. They are summarized in Sec. § 5.4.2. Finally, the fourth term ④ yields an expression for the unforced adjoint Navier–Stokes equations. The variation of the individual terms corresponds to a linearization, followed by an integration by parts. Hence, the variation of the fourth term can be accomplished in two steps. First, by linearizing the direct nonlinear equation and, secondly, by integrating the linearized equation by parts. These two steps are presented for the nonlinear compressible Navier–Stokes equations in the following section.

5.4.1.1 Adjoint Navier–Stokes equations

In a common notation, the Navier–Stokes equations cover the conservation of mass, momentum and energy. Nevertheless, the basic formulation of these three equations is not closed. Additional information on the specific properties of the fluid needs to be included to close the system of equations. Three additional algebraic equations for the density, the temperature and the viscosity are necessary (see Sec. § 3.1). Hence, a total of eight coupled equations are necessary to define the closed system. In the present three-dimensional application they can be included in one state vector: $\boldsymbol{q} = [p\ u\ v\ w\ s\ \rho\ T\ \mu]^T$.

When we derive the adjoint equations, we need to transpose the whole closed system including the three algebraic equations. To this end, in the

following linearization and the subsequent integration by parts, the dimension of the system is always eight.

Without simplifications, like, e.g., a constant viscosity ($\mu = const.$) or setting $\Phi = 0$ which is a commonplace [see e. g. Cervino et al., 2002, Collis et al., 2002b, Spagnoli & Airiau, 2008, Wei & Freund, 2006], the linearized compressible and porous Navier–Stokes equations can be written in matrix formulation. With the variation of the state vector components $\boldsymbol{\delta q} = [\delta p \ \delta u \ \delta v \ \delta w \ \delta s \ \delta\rho \ \delta T \ \delta\mu]^T$, we have

$$\boldsymbol{B}\frac{\partial \boldsymbol{\delta q}}{\partial t} + \boldsymbol{A_k}\frac{\partial \boldsymbol{\delta q}}{\partial x_k} + \boldsymbol{D_{ij}}\frac{\partial^2 \boldsymbol{\delta q}}{\partial x_i \partial x_j} + \boldsymbol{C}\boldsymbol{\delta q} = 0 \tag{5.27}$$

The matrices can be found in the appendix in Sec. § B on page 261.

Based on the linearized matrix formulation, we give an expression for the term in the tilted brackets. With the scalar product of Eq. (5.24a) we get:

$$\left\langle \frac{\partial \mathcal{N}(\boldsymbol{q}, \boldsymbol{K})}{\partial \boldsymbol{q}} \delta \boldsymbol{q}, \boldsymbol{q}^\star \right\rangle = \int_{t_0}^{t_1}\int_{\Omega} \frac{\partial \delta \boldsymbol{q}^T}{\partial t}\boldsymbol{B}^T\boldsymbol{q}^\star + \frac{\partial \delta \boldsymbol{q}^T}{\partial x_k}\boldsymbol{A}_{\boldsymbol{k}}^T\boldsymbol{q}^\star + \frac{\partial^2 \delta \boldsymbol{q}^T}{\partial x_i \partial x_j}\boldsymbol{D}_{\boldsymbol{ij}}^T\boldsymbol{q}^\star + \delta\boldsymbol{q}^T\boldsymbol{C}^T\boldsymbol{q}^\star \,\mathrm{d}\Omega\mathrm{d}t \tag{5.28}$$

The dimension of the adjoint state $\boldsymbol{q}^\star$ is consequently the same as for the direct state $\boldsymbol{q}$ and it can be given as $\boldsymbol{q}^\star = [p^\star \ u^\star \ v^\star \ w^\star \ s^\star \ \rho^\star \ T^\star \ \mu^\star]^T$ with the adjoint pressure, the adjoint velocities, the adjoint entropy, the adjoint density, the adjoint temperature and the adjoint viscosity.

After integration by parts and the fact, that the variation $\delta\boldsymbol{q}^T$ is arbitrary, the unforced adjoint equations read:

$$-\frac{\partial}{\partial t}\left(\boldsymbol{B}^T\boldsymbol{q}^\star\right) - \frac{\partial}{\partial x_k}\left(\boldsymbol{A}_{\boldsymbol{k}}^T\boldsymbol{q}^\star\right) + \frac{\partial^2}{\partial x_i \partial x_j}\left(\boldsymbol{D}_{\boldsymbol{ij}}^T\boldsymbol{q}^\star\right) + \boldsymbol{C}^T\boldsymbol{q}^\star = 0. \tag{5.29}$$

Due to the integration by parts, the signs of the first partial derivatives change while they keep unchanged for the second derivatives and the source term. The negative sign of the temporal derivative forces us to integrate the adjoint equations backwards in time to guarantee a numerically stable solution. During the integration by parts, the additional boundary conditions define the adjoint boundary and initial conditions. They will be addressed separately in Sec. § 5.4.2. Despite the boundary conditions, the adjoint Navier–Stokes

equations are not complete, yet. The first variation of the objective function with respect to the direct state will contribute as a forcing/source term to the equations and drive the solution backwards in time. The specific role of the frequency based objective function will be discussed separately in Sec. § 5.4.1.3.

Above matrix formulation can be expanded in separate equations leading to a set of adjoint PDEs. A total of eight equations will arise as the dimension of the square matrices in Eq. (5.29) is eight. Five PDEs, one for the adjoint pressure, three for each adjoint velocity component and one for the adjoint entropy. The additional three algebraic equations, the adjoint density, adjoint temperature and adjoint viscosity close the system of equations. The five PDEs read:

$$\frac{\partial p^\star}{\partial t} = -u_i \frac{\partial p^\star}{\partial x_i} - \frac{1}{\rho}\frac{\partial {u_i}^\star}{\partial x_i} + \Theta_e^p + \Theta_f^p + \Theta_p^p \tag{5.30a}$$

$$\frac{\partial {u_i}^\star}{\partial t} = -u_j \frac{\partial {u_i}^\star}{\partial x_j} - \gamma p \frac{\partial p^\star}{\partial x_i} + \Theta_e^{u_i} + \Theta_f^{u_i} + \Theta_p^{u_i} \tag{5.30b}$$

$$\frac{\partial s^\star}{\partial t} = -u_i \frac{\partial s^\star}{\partial x_i} + \frac{p}{C_v}\left(\frac{\partial p^\star}{\partial t} + u_i \frac{\partial p^\star}{\partial x_i}\right) + \Theta_e^s + \Theta_f^s + \Theta_p^s \tag{5.30c}$$

The abbreviation for the adjoint sources can be split into three contributions, an Euler part without friction Θ_e^α, a friction-dependent part Θ_f^α and a part arising from the porous terms Θ_p^α, where α can be one of p, u_i or s. Depending on the application, some source terms might be omitted, e. g. the term related to the porous Navier–Stokes equations (Θ_p^α) when no porous material is concidered.

The explicit form of the adjoint source terms is given as follows:

Friction independent adjoint sources

$$\Theta_e^p := -\left((1-\gamma)\frac{\partial u_j}{\partial x_j} + \frac{1}{C_v}\left(\frac{\partial s}{\partial t} + u_j \frac{\partial s}{\partial x_j}\right)\right) p^\star + \left(\frac{1}{\rho^2}\frac{\partial \rho}{\partial x_j}\right) {u_j}^\star$$

$$\Theta_e^{u_i} := -\left((\gamma-1)\frac{\partial p}{\partial x_i} + \frac{p}{C_v}\frac{\partial s}{\partial x_i}\right) p^\star - \frac{\partial u_j}{\partial x_j} {u_i}^\star + \frac{\partial u_j}{\partial x_i} {u_j}^\star + \frac{\partial s}{\partial x_i} s^\star$$

$$\Theta_e^s := \frac{1}{C_v}\left(\frac{\partial p}{\partial t} + \frac{\partial (p u_j)}{\partial x_j}\right) p^\star - \frac{\partial u_j}{\partial x_j} s^\star$$

Friction dependent adjoint sources

$$
\begin{aligned}
\Theta_f^p &:= -\frac{1}{c^2}\rho^\star - \frac{1}{\rho R}T^\star \\
\Theta_f^{u_i} &:= 2\frac{\partial}{\partial x_j}\left(\frac{\tau_{ij}{}^\star}{\rho}\right) - \frac{\partial^2}{\partial x_j^2}\left(\frac{\mu}{\varrho}u_i{}^\star\right) - \frac{\partial^2}{\partial x_i \partial x_j}\left(\frac{1}{3}\frac{\mu}{\varrho}u_j{}^\star\right) + 2\frac{\partial}{\partial x_j}\left(\frac{\tau_{ij}}{\rho T}s^\star\right) \\
\Theta_f^s &:= \frac{p}{c^2 C_v}\rho^\star
\end{aligned}
$$

with the further abbreviations

$$
\begin{aligned}
\tau_{ij}{}^\star &:= 2\left(s_{ij}{}^\star - \frac{1}{3}s_{kk}{}^\star\delta_{ij}\right) \\
s_{ij}{}^\star &:= \frac{1}{2}\left(\frac{\partial \mu}{\partial x_i}u_j{}^\star + \frac{\partial \mu}{\partial x_j}u_i{}^\star\right).
\end{aligned}
$$

Porous dependent adjoint sources

$$
\begin{aligned}
\Theta_p^p &:= 0 \\
\Theta_p^{u_i} &:= \frac{\mu}{\rho\phi}\left(K^{-1}\right)_{ij}u_j{}^\star - 2\frac{\mu}{\rho\phi T}\left(K^{-1}\right)_{ij}u_j s^\star \\
&\quad -\left(\frac{R}{\phi}\frac{\partial \phi}{\partial x_i} + 2\frac{\mu}{\rho\phi T}\left(K^{-1}\right)_{ij}u_j\right)s^\star \\
\Theta_p^s &:= 0
\end{aligned}
$$

Three additional algebraic equations, the adjoint density, temperature and viscosity need to be introduced to close the system of adjoint equations (also obtained by Eq. (5.28)). For the sake of clearness, the porous terms are discussed in an extra term $(\cdot)_p$. We obtain the following expressions:

Adjoint density

$$
\begin{aligned}
\rho^\star &= -\frac{1}{\rho^2}\left(-\frac{\partial p}{\partial x_i} + \frac{\partial \tau_{ij}}{\partial x_j}\right)u_i{}^\star \\
&\quad -\frac{1}{\rho^2 T}\left(\frac{\partial}{\partial x_j}\left(\lambda\frac{\partial T}{\partial x_j}\right) + \Phi\right)s^\star - \frac{T}{\rho}T^\star + \rho_p{}^\star \qquad (5.31) \\
\rho_p{}^\star &:= \frac{\mu}{\rho^2\phi}\left(K^{-1}\right)_{ij}u_j u_i{}^\star - \frac{\mu}{\rho^2\phi T}\left(K^{-1}\right)_{ij}u_i u_j s^\star
\end{aligned}
$$

Adjoint temperature

$$\begin{aligned} T^\star &= \frac{\partial}{\partial x_k}\left(-\frac{1}{\rho T}\frac{\partial \lambda}{\partial x_k}s^\star\right) - \frac{1}{\rho T^2}\left(\frac{\partial}{\partial x_j}\left(\lambda\frac{\partial T}{\partial x_j}\right)+\Phi\right)s^\star \\ &\quad -\frac{\partial^2}{\partial x_j^2}\left(-\frac{\lambda}{\rho T}s^\star\right)+\frac{d\mu(T)}{dT}\mu^\star + {T_p}^\star \\ {T_p}^\star &:= -\frac{\mu}{\rho\phi T^2}\left(K^{-1}\right)_{ij}u_i u_j s^\star \end{aligned} \tag{5.32}$$

Adjoint viscosity

$$\begin{aligned} \mu^\star &= \frac{\partial}{\partial x_i}\left(-\frac{\tau_{ij}}{\mu\rho}{u_j}^\star\right)+\frac{\partial}{\partial x_i}\left(-\frac{C_p}{Pr\rho T}\frac{\partial T}{\partial x_i}s^\star\right) \\ &\quad +\frac{1}{\rho}\left(\frac{\partial}{\partial x_j}\left(\frac{\tau_{ij}}{\mu}\right){u_i}^\star\right) \\ &\quad +\left(\frac{C_p}{Pr\rho T}\frac{\partial^2 T}{\partial x_j^2}+\frac{\Phi}{\rho T\mu}\right)s^\star + {\mu_p}^\star \\ {\mu_p}^\star &:= -\frac{1}{\rho\phi}\left(K^{-1}\right)_{ij}u_j{u_i}^\star + \frac{1}{\rho\phi T}\left(K^{-1}\right)_{ij}u_i u_j s^\star \end{aligned} \tag{5.33}$$

Now, one can see that the adjoint equations are a function of the direct state $\boldsymbol{q}$. Therefore, the direct state has to be saved throughout the forward computation. Remarks on that topic are given later. Due to the linearization and the subsequent integration by parts a large number of source terms arise which makes the implementation a challenging task. This fact is the reason why it is a commonplace to use simplifications during the linearization, like setting $\mu = const.$ or $\Phi = 0$. Nevertheless, these simplifications will result in a wrong gradient. Its impact on the gradient and finally on the solution of the optimum is not clear and hence will not be used in the present investigation.

Despite the challenging implementation of the large number of source terms, they can lead to a bad condition of the overall system and finally lead to numerical instabilities. A method to deal with these numerical issues is presented in Sec. § 5.4.8.1.

5.4.1.2 Characteristic formulation

The direct Navier–Stokes equations are written in a characteristic formulation of Sesterhenn [2000]. In a continuous adjoint approach it is important to

use the same numerical method for the direct and for the adjoint computation. To this end, the adjoint Navier–Stokes equations are also decomposed into characteristic waves. A detailed derivation is given in the appendix in Sec. § C.

In three-dimensional space, the adjoint Navier–Stoles equations including porous media can be written in a characteristic formulation:

$$\begin{aligned}
\frac{\partial p^\star}{\partial t} &= -\frac{1}{2\rho c}\left(\left(X^{+\star}+X^{-\star}\right)+\left(Y^{+\star}+Y^{-\star}\right)+\left(Z^{+\star}+Z^{-\star}\right)\right) \\
&\quad +\Theta_e^p+\Theta_f^p+\Theta_p^p && \text{(5.34a)}\\
\frac{\partial u^\star}{\partial t} &= \frac{1}{2}\left(X^{+\star}-X^{-\star}\right)+Y^{u\star}+Z^{u\star}+\Theta_e^u+\Theta_f^u+\Theta_p^u && \text{(5.34b)}\\
\frac{\partial v^\star}{\partial t} &= X^{v\star}+\frac{1}{2}\left(Y^{+\star}-Y^{-\star}\right)+Z^{v\star}+\Theta_e^v+\Theta_f^v+\Theta_p^v && \text{(5.34c)}\\
\frac{\partial w^\star}{\partial t} &= X^{w\star}+Y^{w\star}+\frac{1}{2}\left(Z^{+\star}-Z^{-\star}\right)+\Theta_e^w+\Theta_f^w+\Theta_p^w && \text{(5.34d)}\\
\frac{\partial s^\star}{\partial t} &= X^{s\star}+Y^{s\star}+Z^{s\star}+\frac{p}{C_v}\frac{\partial p^\star}{\partial t}+\Theta_e^s+\Theta_f^s+\Theta_p^s && \text{(5.34e)}
\end{aligned}$$

with the following abbreviation:

$$X^{v\star} := -u\frac{\partial v^\star}{\partial x} \quad \text{(5.35a)} \qquad X^{w\star} := -u\frac{\partial w^\star}{\partial x} \quad \text{(5.36a)}$$

$$Y^{u\star} := -v\frac{\partial u^\star}{\partial y} \quad \text{(5.35b)} \qquad Y^{w\star} := -u\frac{\partial w^\star}{\partial y} \quad \text{(5.36b)}$$

$$Z^{u\star} := -w\frac{\partial u^\star}{\partial z} \quad \text{(5.35c)} \qquad Z^{v\star} := -u\frac{\partial v^\star}{\partial z} \quad \text{(5.36c)}$$

$$\begin{aligned}
X^{\pm\star} &:= (-u\pm c)\left(-\rho c\frac{\partial p^\star}{\partial x}\pm\frac{\partial u^\star}{\partial x}\right) && \text{(5.37a)}\\
Y^{\pm\star} &:= (-v\pm c)\left(-\rho c\frac{\partial p^\star}{\partial y}\pm\frac{\partial v^\star}{\partial y}\right) && \text{(5.37b)}\\
Z^{\pm\star} &:= (-w\pm c)\left(-\rho c\frac{\partial p^\star}{\partial z}\pm\frac{\partial w^\star}{\partial z}\right) && \text{(5.37c)}
\end{aligned}$$

$$X^{s\star} := u\left(\frac{p}{C_v}\frac{\partial p^\star}{\partial x} - \frac{\partial s^\star}{\partial x}\right) \tag{5.38a}$$

$$Y^{s\star} := v\left(\frac{p}{C_v}\frac{\partial p^\star}{\partial y} - \frac{\partial s^\star}{\partial y}\right) \tag{5.38b}$$

$$Z^{s\star} := w\left(\frac{p}{C_v}\frac{\partial p^\star}{\partial z} - \frac{\partial s^\star}{\partial z}\right) \tag{5.38c}$$

In the same way as for the direct Navier–Stokes equations the adjoint Navier–Stokes equations can be derived for curvilinear grids. They are presented in the appendix in Sec. § C.

5.4.1.3 Adjoint forcing

As mentioned already, the adjoint Navier–Stokes equations are not complete, yet. The forcing term, which accounts for the specific structure of the objective functional is missing. Its origin lies in the first variation of the objective functional with respect to the direct state. It is the first term ① of Eq. (5.26). Due to the uncommon frequency based structure, its derivation and interpretation is discussed in detail in the following. The corresponding term reads:

$$\frac{\partial J(\boldsymbol{q})}{\partial \boldsymbol{q}}\delta\boldsymbol{q} = \int_\Omega\int_{\omega_l}^{\omega_u}\Big(\lambda_1\mathcal{F}\{p'\}\mathcal{F}\{\delta p'\} - \lambda_2\mathcal{F}\{tp'\}\mathcal{F}\{t\delta p'\}\Big)M(x)\,\mathrm{d}\omega\,\mathrm{d}\Omega$$

We need to factor the variation of the state out of above equation. To this end we include the definition of the Fourier transform in a next step and get for the right hand side:

$$\int_\Omega\int_{\omega_l}^{\omega_u}\left(\lambda_1\mathcal{F}\{p'\}\int_{-\infty}^{\infty}e^{-i\omega t}\delta p'\,\mathrm{d}t - \lambda_2\mathcal{F}\{tp'\}\int_{-\infty}^{\infty}e^{-i\omega t}t\delta p'\,\mathrm{d}t\right)M(x)\,\mathrm{d}\omega\,\mathrm{d}\Omega$$

Now, the order of the integration can be changed and if we assume that the state and its variation is only existing during the simulation time $t \in [t_0, t_1]$ and zero elsewhere, we can define the following transformation:

$$\int_{-\infty}^{\infty}p'\,\mathrm{d}t = \int_{t_0}^{t_1}p'\,\mathrm{d}t, \qquad \text{if} \quad p'(t) = \begin{cases} 0, & t < t_0 \\ p', & t_0 \le t \le t_1 \\ 0, & t > t_1 \end{cases}.$$

Finally, after some rearrangement we get:

$$\int_{\Omega}\int_{t_0}^{t_1}\int_{\omega_l}^{\omega_u} \left(\lambda_1 \mathcal{F}\{p'\} e^{-i\omega t}\delta p' - \lambda_2 \mathcal{F}\{tp'\} e^{-i\omega t} t\delta p'\right) M(x)\,\mathrm{d}\omega\,\mathrm{d}t\,\mathrm{d}\Omega.$$

To clarify the meaning of this term, an abbreviation can be defined and included in the relation above. We get:

$$\int_{\Omega}\int_{t_0}^{t_1} \left(\lambda_1 \mathcal{F}^{-1}\left\{\mathcal{F}\{p'\}\Big|_{\omega_l}^{\omega_u}\right\} - \lambda_2 \mathcal{F}^{-1}\left\{\mathcal{F}\{tp'\}\Big|_{\omega_l}^{\omega_u}\right\} t\right) M(x)\delta p'\,\mathrm{d}t\,\mathrm{d}\Omega. \quad (5.39)$$

with the definition of the abbreviation:

$$\mathcal{F}^{-1}\left\{\mathcal{F}\{p'\}\Big|_{\omega_l}^{\omega_u}\right\} = \int_{\omega_l}^{\omega_u} \mathcal{F}\{p'\} e^{-i\omega t}\,\mathrm{d}\omega = \int_{-\infty}^{\infty} \mathcal{F}\{p'\}\cdot T(\omega) e^{-i\omega t}\,\mathrm{d}\omega \quad (5.40)$$

Now, this introduced abbreviation is nothing else as a filter with the filter function $T(\omega)$ and the inverse Fourier transform $\mathcal{F}^{-1}$. The shape of the filter function is a top-hat filter with:

$$T(\omega) = \begin{cases} 0, & \omega < \omega_l \\ 1, & \omega_l \le \omega \le \omega_u \\ 0, & \omega > \omega_u \end{cases} \quad (5.41)$$

It can be regarded as a band-pass filter for the quantity p' (here the pressure). Equation (5.40) and Eq. (5.28) can be added, as both terms appear in the variation of the Lagrange function with respect to the state and both terms are integrands of the same double integral. To this end, the forcing of the adjoint Navier–Stokes equations can be written as:

$$\sum_{k=0}^{N} \left(\lambda_{1,k} \mathcal{F}^{-1}\left\{\mathcal{F}\{p'\}\Big|_{\omega_{l,k}}^{\omega_{u,k}}\right\} - \lambda_{2,k} \mathcal{F}^{-1}\left\{\mathcal{F}\{tp'\}\Big|_{\omega_{l,k}}^{\omega_{u,k}}\right\} t\right) M(x) \quad (5.42)$$

It is a source term, acting on the right hand side of the adjoint pressure equation (5.30a). It is forcing the equation with the band-passed pressure signal. The latter one is measured during the forward computation and applied backwards in time with the spatial distribution $M(x)$. With the introduction of the sum in the forcing of the right hand side, we can account for N distinct bands with different frequency ranges $\omega_{l,k} \le \omega \le \omega_{u,k}$ and individual weights $\lambda_{1,k}$ and $\lambda_{2,k}$, corresponding to the objective function (5.20).

5.4.2 Adjoint boundary- and terminal-condition

The boundary conditions can be derived by carefully evaluating the two parts marked with a ② and ③ of the first variation of the Lagrange functional with respect to the direct state (5.26). In addition to that, additional terms arise as a result of the integration by parts of the remaining terms. These terms can be combined and form the adjoint boundary conditions in space and the adjoint initial (terminal) condition in time.

5.4.2.1 Adjoint terminal condition

In the adjoint case, the terminal condition at $t = T$ is the initial condition, as the adjoint equations are solved backwards in time. The specific character of the adjoint terminal condition depends on the definition of the objective function J. It can be either zero or reach any other state, depending on J. If J is, e. g. an integral over the whole simulation time $t \in [0, T]$, then the terminal condition will be zero. If the objective function is defined only at the terminal condition, like in cases where the objective is the minimization of the terminal kinetic energy, then the terminal condition will reach some state unequal to zero. These relations can be easily proven with a simple example.

In the present case, the objective function is an integral in time and its influence on the adjoint equation is a source term rather than a terminal condition. To this end, the terminal condition for the adjoint computation is zero:

$$\boldsymbol{q}^{\star}(x, T) = \mathbf{0}. \tag{5.43}$$

with the adjoint state $\boldsymbol{q}^{\star}$ at the terminal time.

Several numerical boundary conditions are implemented to treat the aeroacoustic application properly. Each boundary condition for the direct computation needs a corresponding adjoint boundary condition. In the following, three boundary conditions are presented: the adjoint sponge in Sec. § 5.4.2.2, a non-reflecting boundary in Sec. § 5.4.2.3 and an adiabatic wall boundary in Sec. § 5.4.2.4.

5.4.2.2 Sponge boundary condition

An easy but efficient way of implementing a boundary condition in the direct and adjoint case, is a sponge (see Sec. § 2.4.3.2). This boundary condition is a linear source term and can be implemented in a similar way as for the

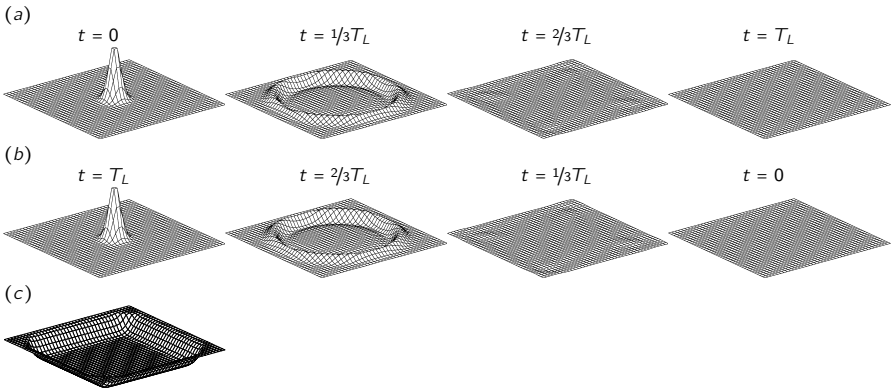

Figure 5.6: Two–dimensional test of the sponge boundary conditions for the direct (a) and the adjoin case (b). Each with the same initial condition. Pressure peak in the direct case and adjoint pressure peak in the adjoint case with the same amplitude. The adjoint solution is running backwards in time. Acoustic waves leaving the domain in both cases with negligible reflections. Solved on a Cartesian mesh with 40×40 points. Solution is self–adjoint (linear acoustic propagation). (c) Spatial distribution of the sponge based on Eq. (2.42) on all four boundaries ($L_{sp} = 0.1L$, $C_{sp} = 0.05L$, L: length of the quadratic domain). Values at the domain boundary $\sigma = 1$. In the center of the domain $\sigma = 0$. Time for an acoustic wave to propagate through the domain $T_L = L/c$ (c: speed of sound).

direct Navier–Stokes equations (see Eq. (2.41) and the references Meliga et al. [2010], Spagnoli & Airiau [2008], Wei [2004]). Due to the linearization of the direct equations and the fact that $\boldsymbol{q_0}$ is constant, the adjoint sponge looks simply:

$$\frac{\partial \boldsymbol{q}^\star}{\partial t} = \mathcal{N}^\star(\boldsymbol{q}^\star, \boldsymbol{q}) + \tau_{\mathrm{sp}}\sigma(\boldsymbol{x})\boldsymbol{q}^\star \tag{5.44}$$

Compared to its direct counterpart, the adjoint reference solution is zero and the sponge has a sign facing in the opposite direction to ensure its damping properties and numerical stability. The sponge-function $\sigma(\boldsymbol{x})$ has the same shape for the direct and adjoint case (see Eq. (2.42) and Fig. 2.12). The same holds true for the sponge amplitude τ_{sp}.

In Fig. 5.6 a two-dimensional acoustic example to test the boundary condition is presented. In this validation case a Gaussian pressure peak is integrated in time on a Cartesian domain with 40×40 points. For the forward case (a), at the time $t = 0$, the pressure peak is in the center of the domain. As there is no base flow, the occurring acoustic wave is propagating concen-

tric in the domain and finally leaving the domain boundaries. At the final time–step shown ($t = T_L$), all acoustics left the domain without significant reflections at the boundaries (time-span of an acoustic propagating through the domain: $T_L = L/c$ with the length of the quadratic domain L and the ambient speed of sound c). The spatial distribution of the sponge function σ is visualized in sub–figure (c) and based on Eq. (2.42) acting on all four boundaries.

In sub–figure (b), the corresponding adjoint pressure $p^\star$ is presented. To compare the direct and adjoint case, the same Gaussian fluctuation is used as initial condition. As the adjoint equations are integrated backwards in time, its initial condition starts at $t = T_L$. One can see, that the solution of the adjoint pressure is identical to one of the direct pressure. The only difference is the reversed time axis $t_{\text{adjoint}} = T_L - t_{\text{direct}}$. This behavior is not surprising, since the propagation of acoustic waves is a linear phenomenon and the sponge is a linear source term. For this strictly acoustic case, most of the terms in the Navier–Stokes equations cancel out and the remaining equation is of the type of a wave equation which is self-adjoint. According to that, the direct and adjoint solution need to match each other. Again, no spurious reflections at the domain boundaries are visible.

The kinetic energy (only $\boldsymbol{u}^2$) and the corresponding adjoint kinetic energy ($\boldsymbol{u}^{\star 2}$) are presented in Fig. 5.7(a) as a function of the time. The energy is scaled with the maximum energy in the domain and the time is scaled with the time-span of an acoustic propagating through the domain $T_L = L/c$. To compare both, the direct and adjoint computation, the time axis of the adjoint computation is reversed. One can see that most of the kinetic energy (four orders of magnitude) is leaving the domain at $t/T_L = 1$ when all acoustics past the domain boundaries. The reflected acoustics are leaving the domain within the next time-span $1 \leq t/T_L \leq 2$ and reduce the energy in the domain for further three magnitudes to a total of seven orders of magnitude. At this point ($t/T_L \geq 2$) a small deviation of the direct and adjoint solution is visible. It seems that in the adjoint computation a larger amount of kinetic energy stays in the domain as it is the case for the direct computation. This additional energy is not related to inefficient adjoint boundary conditions and the corresponding spurious acoustic reflections but can be reduced to a small adjoint entropy spot ($s^\star$) in the center of the domain. This entropy spot is created during the first time-steps of the adjoint computation and decays only very slowly. Based on the coupled adjoint equations the entropy spot is responsible for adjoint velocity components $u^\star$ and $v^\star$ which contribute to the kinetic energy. This slowly decaying energy contribution is also visible in panel (b) which corresponds to the non-reflecting boundary condition. Here,

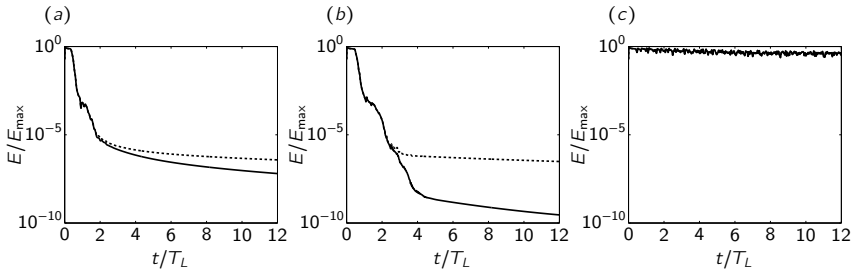

Figure 5.7: Kinetic energy as a function of the computational time in the two-dimensional domain with three different boundary conditions. (a) sponge boundary condition; (b) non-reflecting boundary condition; (c) adiabatic wall boundary condition. Energy scaled with the maximum energy. Time scaled with the time-span of an acoustic propagating through the domain ($T_L = L/c$ with the length of the quadratic domain L and the ambient speed of sound c). Direct computation (———); adjoint computation (- - - - - -) with reversed time axis.

the adjoint kinetic energy converges to the same value ($\sim 10^{-7}$) for $t/T_L = 12$.

5.4.2.3 Non-reflecting boundary condition

In the acoustic far-field, non-reflecting boundary conditions aid in reducing acoustic reflections. As the direct and adjoint code are based on the characteristic formulation, the realization of a non-reflecting boundary is achieved by simply setting the incoming wave to zero. For the adjoint boundaries this reads:

$$\Xi_{\pm}^{k\star} = 0 \tag{5.45}$$

for the boundary in the k–direction and the definition of the wave in Eq. (C.7a). A subscript "+" corresponds to an acoustic wave in the positive k-direction and a "−" to a wave in the negative k–direction. An analogous formulation exists for the forward version of the code.

In Fig. 5.8 the same case as in Fig. 5.6 is presented, however with the non-reflecting boundary conditions. In both solutions the acoustic waves are leaving the domain without visible spurious reflections at the boundaries. Again, this example is self–adjoint. So both, the direct and adjoint solution need to match each other.

As for the sponge boundary condition, the kinetic energy (only $\boldsymbol{u}^2$) and the corresponding adjoint kinetic energy ($\boldsymbol{u}^{\star 2}$) are presented in Fig. 5.7(b) as a function of the time. The shape of the two curves for the direct and adjoint computation are similar to the one of the sponge boundary condition (panel

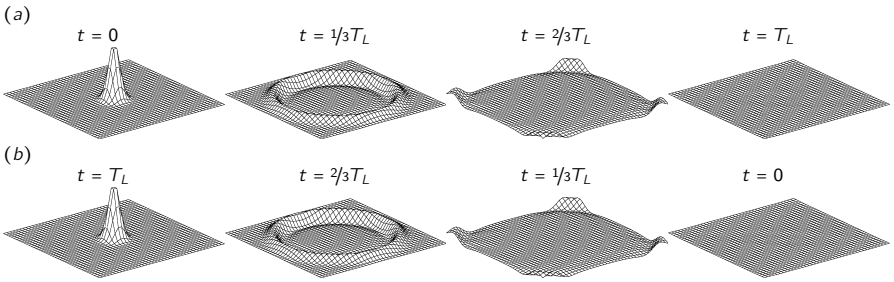

Figure 5.8: Two–dimensional test of the non–reflecting boundary conditions for the direct (a) and the adjoint case (b). Each with the same initial condition. Pressure peak in the direct case and adjoint pressure peak in the adjoint case with the same amplitude. The adjoint solution is running backwards in time. Acoustic waves leaving the domain in both cases with negligible reflections. Solved on a Cartesian mesh with 40×40 points. Solution is self–adjoint (linear acoustic propagation). Time for an acoustic wave to propagate through the domain $T_L = L/c$ (L: length of the domain; c: speed of sound).

(a)). For the non-reflecting BC the kinetic energy of the direct computation is reduced for eight orders of magnitude within $0 \leq t/T_L \leq 4$. Comparing the results to the sponge boundary condition one can conclude that these boundary condition show improved non-reflecting properties. In the adjoint case the same amount of acoustic energy remains in the domain as for the sponge boundary condition and is related to the entropy spot mentioned earlier.

5.4.2.4 Adiabatic wall boundary condition

In the present application on supersonic jet noise no solid wall boundary conditions are present. Nevertheless, for the sake of completeness and as these boundary conditions are used for a validation case, the adjoint boundary conditions for a solid wall with adiabatic properties will be presented. We will see that the present adjoint implementation with an explicit formulation of the adjoint temperature is particularly suited to deal with adiabatic conditions. The non-slip condition of a wall sets the time derivative of the velocity components to zero. This approach is valid for non moving walls and appropriate chosen initial conditions ($u_w = 0$). Setting the boundary condition

$$G(u_w) = \frac{\partial u}{\partial t} = 0 \tag{5.46}$$

in the Lagrangian one obtains an analogous condition for the corresponding adjoint boundary condition, namely:

$$\left.\frac{\partial u^\star}{\partial t}\right|_w = 0 \tag{5.47}$$

for a wall at X_p and X_m, respectively. With this information and after some rearrangement of the adjoint equations one can obtain a formulation for the unknown waves at the boundaries:

- Wall at X_m

$$\begin{aligned}
X_w^{+\star} &= X_w^{-\star} - 2Y_w^{u\star} - 2Z_w^{u\star} - 2\left(\Theta_{ew}^u + \Theta_{fw}^u + \Theta_{pw}^u\right)\\
X_w^{v\star} &= \frac{1}{2}(Y_w^{+\star} - Y_w^{-\star}) + Z_w^{v\star} - \Theta_{ew}^v - \Theta_{fw}^v - \Theta_{pw}^v\\
X_w^{w\star} &= \frac{1}{2}(Z_w^{+\star} - Z_w^{-\star}) + Y_w^{w\star} - \Theta_{ew}^w - \Theta_{fw}^w - \Theta_{pw}^w
\end{aligned}$$

- Wall at X_p

$$\begin{aligned}
X_w^{-\star} &= -X_w^{+\star} + 2Y_w^{u\star} + 2Z_w^{u\star} + 2\left(\Theta_{ew}^u + \Theta_{fw}^u + \Theta_{pw}^u\right)\\
X_w^{v\star} &= \frac{1}{2}(Y_w^{+\star} - Y_w^{-\star}) + Z_w^{v\star} - \Theta_{ew}^v - \Theta_{fw}^v - \Theta_{pw}^v\\
X_w^{w\star} &= \frac{1}{2}(Z_w^{+\star} - Z_w^{-\star}) + Y_w^{w\star} - \Theta_{ew}^w - \Theta_{fw}^w - \Theta_{pw}^w
\end{aligned}$$

Walls at the remaining two dimensions (y and z) can be applied in a similar way.

Adiabatic Wall For an adiabatic wall the temperature fluxes are zero:

$$\frac{\partial T}{\partial n} = 0 \tag{5.48}$$

where n is the wall normal direction. Including this boundary condition in the Lagrangian formulation one obtains the simple condition for the adjoint temperature:

$$T_w{}^\star = 0 \tag{5.49}$$

As we can see, the Neumann boundary condition for the direct case switched to a Dirichlet boundary condition for the adjoint case. This is a typical behavior for adjoint boundary condition. The implementation of this boundary condition is, due to the use of the additional adjoint variable $T^\star$, straightforward. In Fig. 5.9 the same case as in Fig. 5.6 is presented, however with the

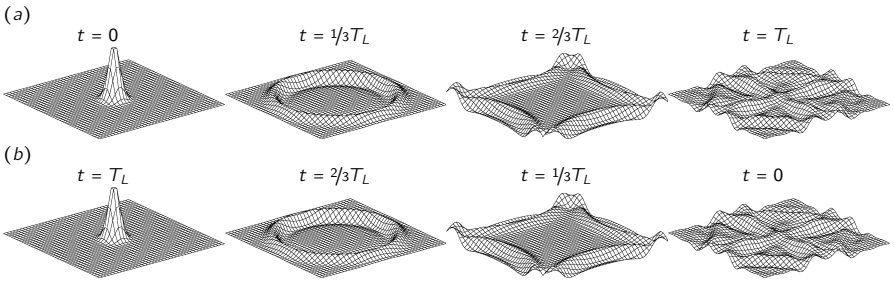

Figure 5.9: Two–dimensional test of the adiabatic wall boundary conditions for the direct (a) and the adjoin case (b). Each with the same initial condition. Pressure peak in the direct case and adjoint pressure peak in the adjoint case with the same amplitude. The adjoint solution is running backwards in time. Acoustic waves are reflected at the domain boundaries in both cases. Solved on a Cartesian mesh with 40×40 points. Solution is self–adjoint (linear acoustic propagation). Time for an acoustic wave to propagate through the domain $T_L = L/c$ (L: length of the domain; c: speed of sound).

adiabatic wall boundary conditions. In both solutions the acoustic waves are reflected at the boundaries. Again, this example is self-adjoint. So both, the direct and adjoint solution need to match each other.

As for the sponge and non-reflecting boundary condition, the kinetic energy (only $\boldsymbol{u}^2$) and the corresponding adjoint kinetic energy ($\boldsymbol{u}^{\star 2}$) are presented in Fig. 5.7(c) as a function of the time. Here the acoustic waves are reflected at the boundaries and are trapped in the domain. Hence, the kinetic energy should stay constant despite physical and numerical diffusion. The physical diffusion is depending on the Reynolds number. In the present application a Reynolds number of $Re = 1000$, based on the speed of sound and the diameter of the Gaussian initial condition, is chosen. The shape of the two curves for the direct and adjoint computation math each other.

5.4.3 Gradient

One of the main advantages of adjoint based optimization is the possibility to obtain a multidimensional gradient in an efficient way. In the present application the control is the space dependent permeability. In order to optimize the permeability of a porous material the gradient of the objective functional with respect to the permeability needs to be evaluated. The gradient can be found by computing the first derivative of the Lagrange functional with respect to the permeability (optimality condition, Eq. (5.25e)). As the per-

meability is a symmetric tensor $\boldsymbol{K} = \kappa_{ij}$, the gradient has to be derived for each element of the tensor κ_{ij} separately. We get:

$$\nabla_{\kappa_{ij}} \mathcal{L} = -\left\langle \nabla_{\kappa_{ij}} \mathcal{N}(\boldsymbol{q}, \boldsymbol{K}), \boldsymbol{q}^\star \right\rangle . \tag{5.50}$$

The gradient of the Lagrangian simply reduces to the gradient of the objective functional [see e. g. Guegan et al., 2006], and we get:

$$\nabla_{\kappa_{ij}} J = -\left\langle \nabla_{\kappa_{ij}} \mathcal{N}(\boldsymbol{q}, \boldsymbol{K}), \boldsymbol{q}^\star \right\rangle . \tag{5.51}$$

Finally, after replacing $\mathcal{N}(\boldsymbol{q}, \boldsymbol{K})$ by the porous Navier–Stokes equations of Sec. § 3.1 one obtains the gradient of the objective functional with respect to the permeability:

$$\nabla_{\kappa_{ij}} J = -\left[\frac{\mu}{\rho} u_j, u_i{}^\star \right] + \left[\frac{\mu}{\rho T} u_i u_j, s^\star \right], \tag{5.52}$$

with the scalar product defined in Eq. (5.24c) to obtain a space dependent gradient. Hence, both terms on the right hand side of Eq. (5.52) are integrated in time which corresponds to a time average. The first term is the scalar product of the direct and adjoint velocity components. It arises from the adjoint momentum equations. The second term is a scalar product of the direct kinetic energy and the adjoint entropy. It has its origin in the adjoint energy equation.

As we will see in the next section, we can not use this gradient directly but need to transform it to account for an inequality constraint.

5.4.4 Treating inequality constraints

In the present study, the control is the permeability of the porous material. This value can be positive or zero, only. A negative value of $\boldsymbol{K}$ would accelerate the fluid in the porous material which has no physical meaning. Besides that, positive eigenvalues would arise and cause numerical instabilities for the time integration method. Thereby, the inequality condition ($\boldsymbol{K} \geq \boldsymbol{0}$) has to be treated in a special way. One possibility is to use a projected gradient method like for non–negative matrix factorization [see Lin, 2007]. This technique truncates the gradient to satisfy the constraint, which is easy to implement with the tradeoff of bad convergence. Another common approach, to treat inequality conditions properly, is to apply the optimization problem to the Sequential Quadratic Programming (SQP). This technique interpolates the objective function with a quadratic polynomial and linearizes the

constraints. In addition to that is uses the second derivative of the objective function (Hessenberg matrix; usually approximated) in a Newton like optimization method. For a small number of optimization parameters this method is very efficient and, due to the variety of available implementations (MatLab[1], NLPQLP[2], and many others), straightforward to use. Anyway, as the approximation of the Hessenberg matrix is expensive, the method becomes impractical if the problem is too large as in the present application [see Schittkowski, 2010].

A different approach is to transform the inequality condition into an equality condition by introducing a so called *slack variable* $\boldsymbol{S} = (s_{ij})$ [see e. g. Boyd & Vandenberghe, 2004], satisfying the following relation:

$$\boldsymbol{K} = (\boldsymbol{\kappa}_{ij}) = (\boldsymbol{s}_{ij}^2). \tag{5.53}$$

Note, that $\boldsymbol{S}^2 = (\boldsymbol{s}_{ij})^2 \neq (\boldsymbol{s}_{ij}^2)$. The square in Eq. (5.53) is an element-wise multiplication. In the following we will use the Hadamard product to notate the element-wise product of two matrices: $(\boldsymbol{s}_{ij}^2) = \boldsymbol{S} \circ \boldsymbol{S}$. In addition to that the permeability is space dependent and each element of the tensor is a vector.

Now, since $\boldsymbol{S} \circ \boldsymbol{S}$ is positive only, the inequality constraint can be rewritten to an equality constraint: $\boldsymbol{K} - \boldsymbol{S} \circ \boldsymbol{S} = 0$. By introducing an additional Lagrange multiplier $\boldsymbol{S}^\star$, this equality constraint can be added to the Lagrange functional of Eq. (5.23), with the following scalar product:

$$\left\langle \boldsymbol{\kappa}_{ij} - \boldsymbol{s}_{ij}^2, \boldsymbol{s}_{ij}{}^\star \right\rangle$$

The aim of the optimization task has now changed in finding the optimal slack variable $\boldsymbol{S}$ instead of the optimal control $\boldsymbol{K}$. So, $\boldsymbol{K}$ is replaced by $\boldsymbol{S} \circ \boldsymbol{S}$ and the gradient with respect to $\boldsymbol{S}$ has to be evaluated. Within the optimization process, the slack variable is updated as in Eq. (5.58) and then replaced by Eq. (5.53). The gradient $\nabla_{\boldsymbol{s}_{ij}} J$ is obtained by the first variation of the Lagrange functional with respect to the slack variable and reads:

$$\nabla_{\boldsymbol{s}_{ij}} \mathcal{L} = -\left\langle 2\boldsymbol{s}_{ij}, \boldsymbol{s}_{\boldsymbol{ij}}{}^\star \right\rangle. \tag{5.54}$$

In an optimal point, the variation of the Lagrange functional has to vanish and we obtain for the gradient:

$$\nabla_{\boldsymbol{s}_{ij}} J = -\left\langle 2\boldsymbol{s}_{ij}, \boldsymbol{s}_{\boldsymbol{ij}}{}^\star \right\rangle. \tag{5.55}$$

[1] `http://www.mathworks.com`
[2] `http://www.ai7.uni-bayreuth.de/nlpqlp.htm`

Including the variation of the Lagrange functional with respect to the control $\boldsymbol{K}$ in Eq. (5.55) and the relation that

$$\frac{dJ}{d\boldsymbol{s_{ij}}} = \frac{\partial J}{\partial \boldsymbol{\kappa_{ij}}} \frac{d\boldsymbol{\kappa_{ij}}}{d\boldsymbol{s_{ij}}},$$

the gradient with respect to the slack variable reads:

$$\nabla_{\boldsymbol{s}_{ij}} J = -\left\langle 2\boldsymbol{s}_{ij} \nabla_{\boldsymbol{\kappa}_{ij}} \mathcal{N}(\boldsymbol{q}, \boldsymbol{K}), \boldsymbol{q}^{\star} \right\rangle. \tag{5.56}$$

With the gradient with respect to the permeability as defined in Eq. (5.52), we get:

$$\nabla_{s_{ij}} J = -2\left[\frac{\mu}{\rho} s_{ij} u_j, u_i{}^{\star}\right] + 2\left[\frac{\mu}{\rho T} s_{ij} u_i u_j, s^{\star}\right]. \tag{5.57}$$

This gradient is used, within the optimization loop (Fig. 5.4), to compute the optimal distribution of porous media to minimize the objective function. Given that $\boldsymbol{K} = (\boldsymbol{\kappa}_{ij})$ and $\boldsymbol{S} = (\boldsymbol{s}_{ij})$ are tensors, the gradient itself is a tensor and has to be evaluated pointwise. Each of the six elements of the symmetric tensor are in addition to that fields in space. Consequently, the number of parameters to control can be easily in the order of 10^6.

Note, that the method of slack variables is equivalent to replacing $\boldsymbol{K} = \boldsymbol{S} \circ \boldsymbol{S}$ in the porous Navier–Stokes equations and then optimizing for $\boldsymbol{S}$.

5.4.5 Steepest descent

The gradient of the objective function with respect to the control (here the slack variable due to the inequality constraint of the previous section) can be used in a simple steepest descent algorithm to compute a new set of control variables in an iterative way. We have

$$\boldsymbol{S}^{(n+1)} = \boldsymbol{S}^{(n)} - \alpha^{(n)} \left(\nabla_{s_{ij}} J\right)^{(n)}. \tag{5.58}$$

The gradient is defined in Eq. (5.57) and is itself a tensor. The positive and scalar valued step-size $\alpha^{(n)}$ has to be chosen carefully to avoid numerical instabilities and to guarantee an efficient convergence. How to choose a proper step-size is outlined in Sec. § 5.4.7.

However, to improve the convergence properties and the robustness of the optimization algorithm, a conjugate gradient (CG) algorithm is applied. In the following section the implemented CG methods are presented an validated on a test function.

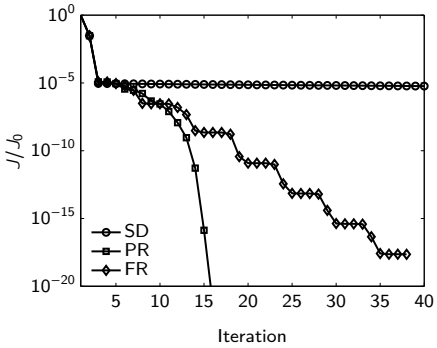

Figure 5.10: Convergence rate of three different optimization directions (SD: Steepest descent, PR: Polak–Ribière, FR: Fletcher–Reeves). Objective function: Rosenbrock-Valley Eq. (5.59).

5.4.6 Conjugate gradient

The method of steepest descent can lead to a very slow convergence rate, especially for objective functions with a long, flat and narrow valley. An example of a two-dimensional function with such properties is the *Rosenbrock–Valley*

$$J(x, y) = 100(y - x^2)^2 + (x - 1)^2 \tag{5.59}$$

This function is often used to test the performance of optimization algorithms and will be used here as well. Three different methods are implemented:

- Steepest-Descent (SD)
- Conjugate Gradient – Polak–Ribière (PR)
- Conjugate Gradient – Fletcher–Reeves (FR)

Conjugate gradient methods use the direction not only of the current step but a linear combination of all previous directions. With these information one can construct a more *straight* way down the valley.

A prototype of each CG method is outlined in Alg. 5.2. The difference in the methods lies in the computation of the new search direction $h^{(n)}$ in step 3. In the simplest case – the steepest descent – the new direction $h^{(n)}$ is the negative gradient:

$$h^{(n)} = -g^{(n)}$$

Conjugate gradient methods compute $h^{(n)}$ as follows:

$$h^{(n)} = g^{(n)} + \gamma^{(n)} h^{(n-1)} \tag{5.60}$$

Input: initial guess $x^{(0)}$
tolerance tol
Output: optimum $x^{(n)}$
1: **while** $err > tol$ **do**
2: $g^{(n)} = -\nabla J^{(n)}$ (gradient)
3: $h^{(n)} = g^{(n)} + \gamma^{(n)} h^{(n-1)}$ (conjugate gradient based on PR or FR)
4: $\alpha^{(n)}$ (optimal step-size, see § 5.4.7)
5: $\boldsymbol{K}^{(n+1)} = \boldsymbol{K}^{(n)} + \alpha^{(n)} h^{(n)}$ (update control)
6: $err = \|x^{(n+1)} - x^{(n)}\|$
7: $n \longleftarrow n + 1$
8: **end while**

Algorithm 5.2: Algorithm for a simple CG loop.

with Fletcher–Reeves [see Polak, 1997, Alg. 42]:

$$\gamma^{(n)} = \frac{(g^{(n)}, g^{(n)})}{(g^{(n-1)}, g^{(n-1)})} \tag{5.61}$$

or Polak–Ribière [see Polak, 1997, Alg. 51]:

$$\gamma^{(n)} = \frac{(g^{(n)} - g^{(n-1)}, g^{(n)})}{(g^{(n-1)}, g^{(n-1)})}. \tag{5.62}$$

In Fig. 5.10 the convergence history of all three implemented methods is presented. One can see that the convergence of the steepest descent is very slow compared to the conjugate gradient methods. A better convergence can be identified for the Fletcher–Reeves method which decays the objective function 20 orders of magnitude in 40 iterations. The best results can be gained with the Polak–Ribière method. A decay of 20 orders of magnitude can be gained in only 16 iterations. To this end, in what follows, the method of Polak–Ribière will be used to compute conjugate gradients.

In Fig. 5.11 the optimization history is shown for the steepest descent (a and b) and Polak–Ribière method (c and d). One can see that the steepest descent method is jumping from one side of the flat valley to the other one (cf. panel b) and thus causing a very slow convergence rate. Even after 200 iteration the solution is far away (tolerance 10^{-6}) from reaching the optimum. On the other hand the Polak–Ribière method is taking the *direct* way (cf. panel d) and reaching the optimality-condition ($(x_{i+1} - x_i)/x_{i+1} < \varepsilon_{mashine}$) after only 16 Iterations.

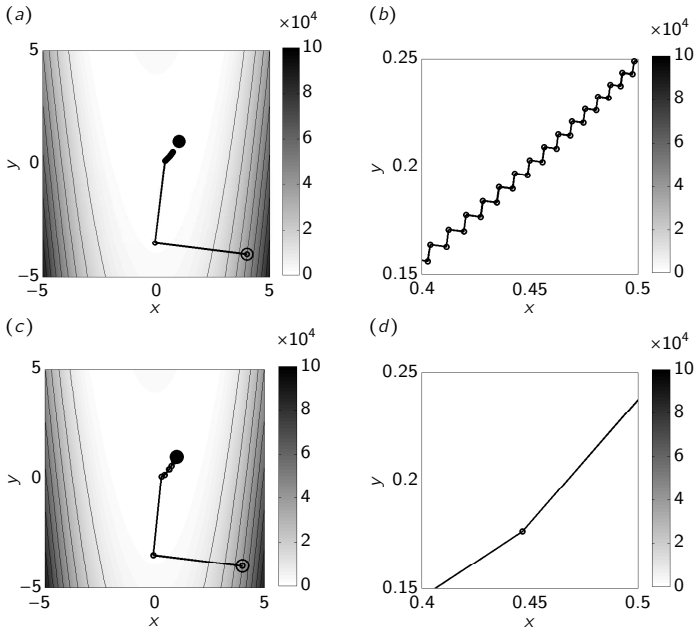

Figure 5.11: Optimization history for SD (steepest descent (*a*) and zoom (*b*)) and PR (Polak–Ribière (*c*) and zoom (*d*)). Test-function: Rosenbrock-Valley Eq. (5.59). Initial guess $x = 4$, $y = -4$ (○). Analytical minimum at $x = y = 1$ (●). The method of steepest-descent is jumping from one side of the flat valley to the other one and thus converging very slow, cf. (*b*).

5.4.7 Line search

Once the optimization direction is obtained, either by steepest descent or conjugate gradients, the step-size (how far one has to go in the desired direction) has to be determined. Algorithm determining the (optimal) step-size are referred to as *line search* methods. These methods are again some kind of optimization algorithm and can be computational expensive. The idea is to find the optimal step-size which minimizes:

$$\Phi(\alpha^{(n)}) = J(\boldsymbol{S}^{(n)} + \alpha^{(n)} h^{(n)}); \qquad \alpha^{(n)} \in \mathbb{R}_+$$

Different approaches exist in minimizing $\Phi(\alpha^{(n)})$ exactly by solving $\Phi'(\alpha^{(n)}) = 0$ or loosely by asking for a sufficient decrease of Φ. As the exact computation of the optimal step-size is often too expensive, loosely methods are used instead. The latter ones can be performed in several ways, e. g.

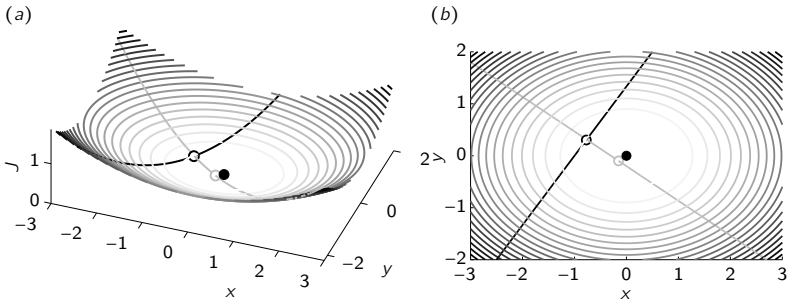

Figure 5.12: Quadratic objective function ($J = (x^2 + 2y^2)/10$) for two optimization parameters (x and y). Along the black line (——— ; first search direction; steepest descent or conjugate gradient) a local minimum (○) has to be found (quadratic line–search algorithm). From this point on, a new search direction (———) is computed and the optimization algorithm is repeated iteratively until it is converged to the global minimum (●).

by using the Wolfes condition [Wolfe, 1969] (a generalization of the Armijo method [Armijo, 1966]) or by assuming a quadratic shape of the objective function. As methods based on the Wolfes condition can be still expensive (more than five function evaluations) the latter method based on a quadratic approximation will be applied.

In this case a quadratic shape of the objective functional is assumed and a quadratic line-search algorithm is implemented to estimate the step-size $\alpha^{(n)}$. Three evaluations of the objective functional in the $h^{(n)}$-direction are performed at each optimization iteration ($J([0,1,2]^T\alpha^{(n)})$). In fact, only two new evaluations of J are necessary since the evaluation for $J([0]^T\alpha^{(n)})$ is already available. With these three function values a quadratic polynomial can be defined. The abscissa to its analytic minimum is the optimal value $\alpha^{(n)}$ (cf. Fig. 5.12).

This line-search algorithm is only valid for a quadratic shape of the objective functional. In a variety of applications the objective functional is quadratic as in the present application of noise reduction (p'^2). If the underlying equations are linear then the objective function with respect to the control will stay quadratic. In the nonlinear case, a quadratic objective function may be mapped on some unknown nonlinear state and the assumption of a quadratic shape may be a poor approximation. In the present investigation, the equations are nonlinear (Navier–Stokes). Nevertheless, the present numerical investigations show that it seems a good and above all efficient approximation even for these nonlinear equations.

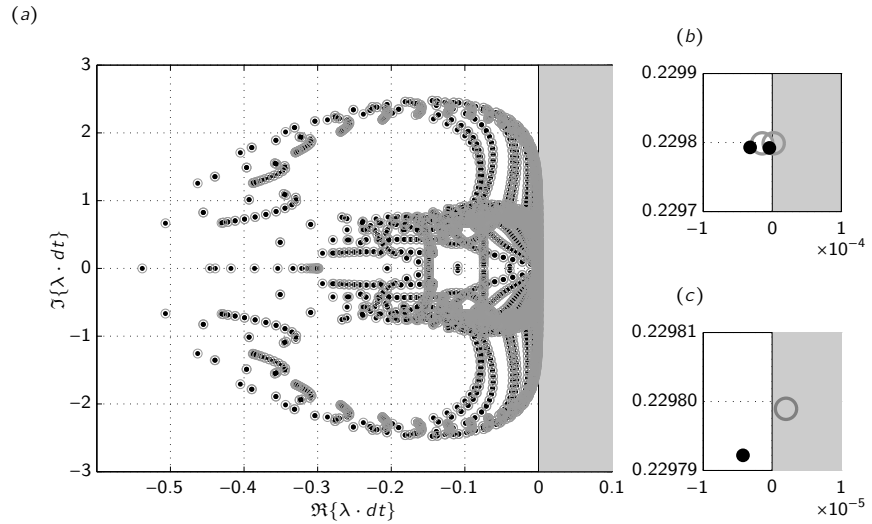

Figure 5.13: (*a*) Instantaneous eigenvalues λ of the direct (•) and adjoint (◦) evolution operator for the case of the trailing edge, taken at $t = 0$ (initial condition). Extracted with a Krylov subspace technique (full Hessenberg matrix, Schulze et al. [2009a]) for a small 64×32 domain. Scaled with the time–step dt, based on a CFL number of $CFL = 1$. Eigenvalues of the adjoint operator should be flipped on the imaginary axis (negative transpose discrete matrix). As dt is negative for the adjoint case, both eigenvalues coincide. Porosity in the advection dominated regime (cf. Fig. 3.3). Magnified view in (*b*) and (*c*).

5.4.8 Numerical issues

In the following section some numerical peculiarities of adjoint based optimization algorithms and implementational issues are summarized.

5.4.8.1 Numerical stability

In some specific cases, the present numerical experiments show, especially in areas with strong gradients in the flow field, numerical instabilities in the adjoint solution. To study this phenomenon, the eigenvalues of the direct and adjoint evolution operator are investigated.

In Fig. 5.13 the eigenvalues of the direct and adjoint evolution operator are presented. They are extracted with a Krylov subspace technique (full Hessenberg matrix, Schulze et al. [2009a]) for a small 64×32 domain based on a two-dimensional jet flow. A total number of 8192 eigenvalues are extracted.

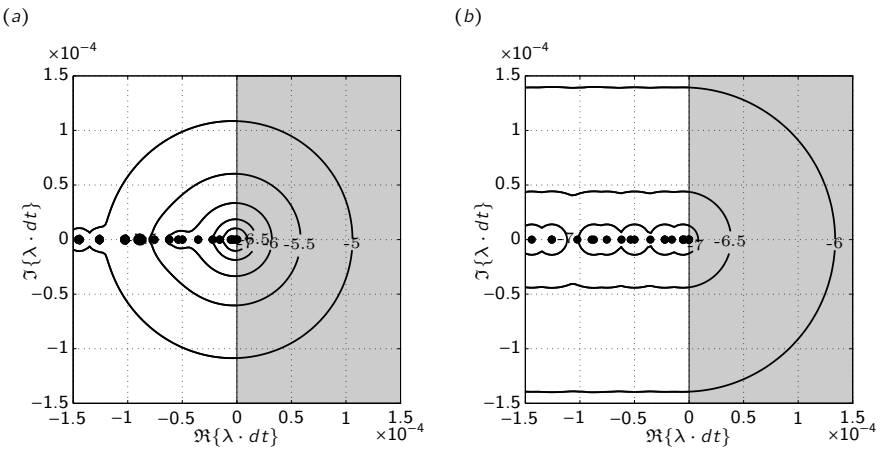

Figure 5.14: Solid curves represent boundaries of the ϵ-pseudospectra in a magnified visualization around the center of the spectrum. Contour lines in $\log_{10}$ scaling ranging from $\epsilon = 10^{-7}$ (innermost curve), $\epsilon = 10^{-6.5}, \ldots, \epsilon = 10^{-5}$. Bold points represent eigenvalues. Scaled with the time–step dt, based on a CFL number of $CFL = 1$. (a) Spectrum of the evolution operator of the direct case. (b) Spectrum of the evolution operator of the adjoint case.

As in the discrete case, the adjoint operator is the negative transpose of the discrete direct operator, the eigenvalues of the adjoint operator are simply flipped on the imaginary axis (opposite sign of the real part). To compare the direct and adjoint case, both eigenvalues are scaled with the corresponding time–step. For the direct one dt and $-dt$ for the adjoint one. Eigenvalues of the direct operator are marked with a black bullet (•) and eigenvalues of the adjoint operator with a gray circle (○). One can see in the big picture (a), that the adjoint eigenvalues match the direct ones, which should be exactly the case for a discrete adjoint approach. Following a continuous approach, as it is carried out in the present work, the eigenvalues do not necessary need to match each other. This strongly depends on the discretization of both operators. According to this, such an analysis, together with the validation of the gradient (see Sec. § 5.4.9), is a good proof for the correct implementation of the adjoint equations.

To extract some more details, a magnified visualization of two characteristic eigenvalues is presented in panel (b) and with an even stronger magnification in panel (c). The scale of panel (b) is four orders of magnitude smaller than the one of the panel (a) and five orders for panel (c). One can identify slight

deviations of the eigenvalues of the adjoint operator compared to the direct one. In particular, one adjoint eigenvalue is moving in the unstable half–plane (positive real part). Such an instability grows exponentially for linear equations, as for the adjoint equations. To avoid this numerical instability, the spectrum of the adjoint operator is shifted in the stable half–plane. To this end, the real valued amplitude of the most unstable eigenvalue $\Re\{\lambda\}_{\max}$ – which can be detected with a power iteration – is used to shift the spectrum. In a matrix formulation this reads:

$$\dot{\boldsymbol{q}}^\star = (\boldsymbol{N}^\star - \Re\{\lambda\}_{\max}\boldsymbol{I})\,\boldsymbol{q}^\star, \tag{5.63}$$

with the discrete adjoint Navier–Stokes operator $\boldsymbol{N}^\star$, the adjoint state $\boldsymbol{q}^\star$ and an identity matrix $\boldsymbol{I}$. Note that in the present study, the adjoint operator $\boldsymbol{N}^\star$ is accessed in a matrix free implementation. In the present applications on supersonic jet noise, the largest detectable unstable eigenvalue of the adjoint operator is less than $\Re\{\lambda\}_{\max} \cdot dt = 10^{-5}$ (cf. also Fig. 5.13(c)).

The numerical inaccuracy of the eigenvalues of the adjoint operator can be explained with its high nonnormality. Compared to the direct operator, the condition number of the adjoint operator is four orders of magnitude larger. In Fig. 5.14 the boundaries of the ϵ-pseudospectra [see Trefethen, 2005] are visualized in a magnified sketch. Panel (a) is based on the direct operator, whereas panel (b) is based on the adjoint operator. Solid curves represent boundaries of the ϵ-pseudospectra in $\log_{10}$ scaling, ranging from $\epsilon = 10^{-7}$ (innermost curve), to $\epsilon = 10^{-5}$ in $\Delta\epsilon = 10^{0.5}$ steps. The fact that the contour lines of the adjoint operator are less concentric than the ones of the direct operator and about one order of magnitude further away form the center of the spectrum, shows that these eigenvalues are extremely sensitive to perturbations. A small perturbation due to a discretization error in the adjoint operator will cause an increased numerical error and can be responsible for numerical instabilities.

By adding a shift only to the adjoint operator and not in the same way to the direct operator, the gradient of the objective function with respect to the control will change. As we will see in Sec. § 5.4.9, the error of the gradient due to the applied shift is in the same order as without shift (10^{-5}) and from an engineering point of view insignificant.

5.4.8.2 Implementation

The adjoint equations are implemented in the same way as the direct equations and solved on the same computational domain and grid. In the adjoint case, the flow direction is reversed and the fluctuations are leaving the domain

at the inlet. Hence, the role of the in- and outlet changed. To this end, it may be necessary to add a sponge boundary condition at the inlet (now outlet) of the domain. In the present application, with supersonic jet noise, the co-flow of the jet is at rest and the only fluid entering the domain is through the jet nozzle. During the adjoint computation the fluctuations are transported backwards through the jet plume inside the nozzle and are finally leaving the domain. To avoid spurious reflections at this point, a small sponge, which is existing only inside the nozzle and extends $0.5D$ in the domain, is added. Note, that the nozzle extends $3D$ into the domain and the small additional sponge has no effect on the gradient evaluation.

Another difference lies in the time integration which is now performed backwards in time (with a negative time-step). Furthermore, the adjoint equations are linear equations and hence the linearization during the Krylov time integration (cf. Sec. § 2.3.2), which is necessary for the direct and nonlinear Navier–Stokes equations, can be omitted.

During the adjoint computation, the direct state has to be provided and hence needs to be saved throughout the computation. The additional time used for I/O strongly depends on the used architecture. It can vary from 0 % (not measurable) up to 400 % of the computational time. The latter extreme can occur when the I/O-load of the computer is high combined with a small I/O-bandwidth. During the present investigations on the optimization with adjoint based methods, the average additional time used for I/O is less than 10 %. In addition to the increased computational time used for writing and reading of the direct solution, the required space needs to be available. Considering a three-dimensional optimization problem with $256 \times 128 \times 128$ grid points and an optimization window of 5000 time-steps (here corresponding to 65 screech cycles) a total of $[(256{\cdot}128{\cdot}128){\cdot}5000{\cdot}7]{\cdot}8\text{byte} \approx$ 1TB needs to be saved. This estimate takes into account that one needs to save seven variables, the five primitive variables (p, u, v, w, s) and the two time derivatives $\frac{\partial p}{\partial t}$ and $\frac{\partial s}{\partial t}$. Furthermore, each variable is saved in double precision and allocates 64bit = 8byte of the available hard disk space. The state of the art High Performance Computers are equipped with a temporary storage space of about 1PB = 1024TB, so the temporal space needed for the adjoint computation is in the order of one per mill of the available storage and hence is to be of no consequence.

When the available storage or the I/O-bandwidth is limited, methods for data compression can be used. Possible approaches are storing not every point in space and time but e. g. every second and reconstructing the data by means of interpolation as applied in Wei [2004] and many others. Due to the interpolation, this kind of data compression is lossy and hence will affect

the accuracy of the gradient and finally of the optimized solution.

A lossless method and widely used technique to reduce the storage space and I/O traffic is called *checkpointing*. Here, the computation of the adjoint code is split and is done part-by-part from restart points called checkpoints [see e. g. Charpentier, 2001]. The position of the checkpoints can be optimized to achieve a logarithmic behavior with respect to storage and re-computation based on e. g. the algorithm of Griewank [1992] when the number of time-steps is known a priori. A dynamically algorithm when the number of time-steps is not known is given by Wang et al. [2009].

5.4.9 Validation

A procedure to validate the adjoint based optimization framework is to compare the gradient of the objective function obtained by the adjoint approach with the one obtained by a finite difference approach. Finite differences yield a numerical approximation of the exact gradient based on the order of the differentiation. For a first order forward finite difference, the approximation of the gradient reads:

$$\nabla_{\boldsymbol{K}} J \approx \frac{J(\boldsymbol{K} + \delta\boldsymbol{K}) - J(\boldsymbol{K})}{\delta\boldsymbol{K}} \tag{5.64}$$

For the present validation case, the gradient is based on a one-dimensional implementation of the porous Navier–Stokes equations and its adjoints. The gradient is space dependent and evaluated at each discrete position in the one-dimensional space. Here, 128 discrete points are used. Using the finite difference approach of Eq. (5.64), a total of 128+1 evaluations are necessary to compute the space dependent gradient. In the adjoint case, only one forward (direct) and one backward (adjoint) computation is necessary.

As the inequality constraint $\boldsymbol{K} \geq 0$ can not be included in the gradient formulation of the finite difference approach, only the gradient with respect to the control $\boldsymbol{K}$ is considered (Eq. (5.52)). For a specific nonlinear example, the finite difference based gradient and the adjoint based gradient are presented in Fig. 5.15(a). Their relative difference is visualized in Fig. 5.15(b). Both figures show a very good agreement between the two gradients. The relative error is in the order of 10^{-5} which is a very good result for continuous adjoint implementations.

Influence of the shift on the gradient In the following the influence of the shift, as presented in Sec. § 5.4.8.1, on the gradient is considered. The value of the shift depends on the most unstable eigenvalue λ of the adjoint operator

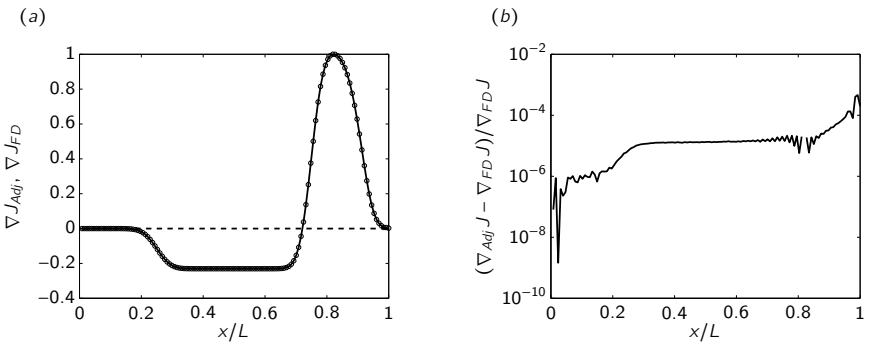

Figure 5.15: Validation of the gradient. Comparison of finite difference based gradient and adjoint based gradient. Based on a specific case for the compressible and porous Navier–Stokes equations and its corresponding adjoints. (*a*) Adjoint based gradient (———); finite difference based gradient (∘); difference of both gradients (- - - - - -). (*b*) Relative deviation of the finite difference based gradient and the adjoint based gradient in logarithmic scaling.

($\Re\{-\lambda\}_{\max}$, consider the negative sign due to the reverse time integration of the adjoint equations). This value can be extracted with a power iteration of the adjoint operator. As the adjoint operator is depending on the direct state (nonlinear Navier–Stokes equations) the most unstable eigenvalue changes in every time-step. A power iteration in each time-step is inefficient and would reduce the total performance of the implemented optimization scheme drastically. Instead, a default value, which showed to be a good compromise between a sufficient numerical stability and caused error of the gradient, is used. In the present study a value of $\Re\{\lambda_{\max}\}dt = 10^{-5}$ is implemented. This value is larger than the most unstable eigenvalue detected in the adjoint operator and therefore guarantees numerical stability (see also Fig. 5.13(*c*) for the location of the unstable adjoint eigenvalue with a real part of $\Re\{\lambda\}dt = 0.2 \cdot 10^{-5}$).

Figure 5.16 shows the error of the adjoint based gradient to the finite difference based gradient ($\|(\nabla_{Adj} J - \nabla_{FD} J)/\nabla_{FD} J\|_2$) as a function of the shift value. It shows that the influence of the shift parameter for values smaller than $\lambda_{\text{shift}}dt = 10^{-5}$ – as used in the present study – is insignificant. To this end the method of shifting the adjoint operator with a value of $\lambda_{\text{shift}}dt = 10^{-5}$ as described in § 5.4.8.1 is increasing the numerical stability of the adjoint solution without affecting the solution of the of the optimization algorithm.

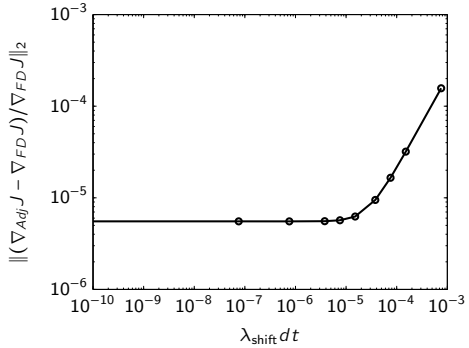

Figure 5.16: Error of the adjoint based gradient to the finite difference based gradient ($\|(\nabla_{Adj}J - \nabla_{FD}J)/\nabla_{FD}J\|_2$) as a function of the shift value.

5.5 Examples

In the following sections some applications for validation purposes are given. All cases are strictly two-dimensional. The following cases are studied:

5.5.1 Navier–Stokes equations:
noise cancellation in frequency space to test the formulation of the frequency based objective function

5.5.2 Porous Navier–Stokes equations:
optimization of a porous wall to minimize the reflected acoustic wave to test the performance of the optimization with porous media on a simple example

5.5.3 Porous Navier–Stokes equations:
minimization trailing edge noise to test the performance of the optimization with porous media on a complex and nonlinear aeroacoustic example

5.5.1 Anti noise with Navier-Stokes (freq. space)

A widely used application to test the optimization scheme is given by the noise cancellation problem using the compressible Navier-Stokes equations [see e. g. Wei, 2004]. In this application, the compressible Navier-Stokes equations are solved in a two-dimensional domain with the objective functional defined in frequency space as shown in (5.18) and based on the work of Schulze

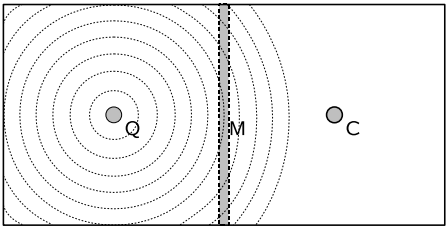

Figure 5.17: Setup for noise-canceling problem based on the compressible Navier–Stokes equations solved in a two-dimensional domain. At the location (Q) a noise source produces a signal with an artificial and fixed spectrum. At the location (C) a second noise source is positioned with a controllable signal. At the location (M) we attempt to reduce a given frequency-band of the noise by destructive interference (anti-noise, Ffowcs Williams [1984]) of the two signals.

et al. [2011]. An approach based on destructive interference or anti-noise will be employed [see Ffowcs Williams, 1984]. The basic setup is presented in Fig. 5.17. At the location Q ($x_Q = 0.5L$ and $y_Q = 0.5L$; L: height of the domain; length of the domain: $2L$) a source produces an acoustic signal with an artificial and fixed spectrum. This signal is propagating through the domain and passing the measurement location M at $x_M = L$. The objective of this test is to reduce the noise along this line. To this end, a second noise source C is located at $x_C = 1.5L$ and $y_C = 0.5L$ with a controllable signal to eliminate the noise at the measurement location.

The computational domain is discretized by an equidistantly spaced grid of 128×64 points in the x- and y-coordinate directions. The four boundaries of the domain are padded by a sponge layer which simulates non-reflecting boundary conditions. Both, the direct and adjoint Navier–Stokes equation are discretized with the methods discribed in Sec. § 2.3 and for this case, the porous related parts of the equations are omitted ($\chi = 0$).

To put the optimization procedure and the control of user-defined frequency bands to a stringent test, the source at the location Q is emitting an acoustic signal with an artificially generated spectrum that models the main components of jet-noise — including screech (see, e.g., the spectrum in Fig. 5.2(a)). Such a spectrum can be created by an envelope function, with a similar shape of that in Fig. 5.2(a), multiplied by white noise in frequency space and then transformed back into the time domain. In this input spectrum three distinct noise sources are included with different frequencies and amplitudes. The objective of the present exercise is to reduce the screech noise component independently from the other noise sources.

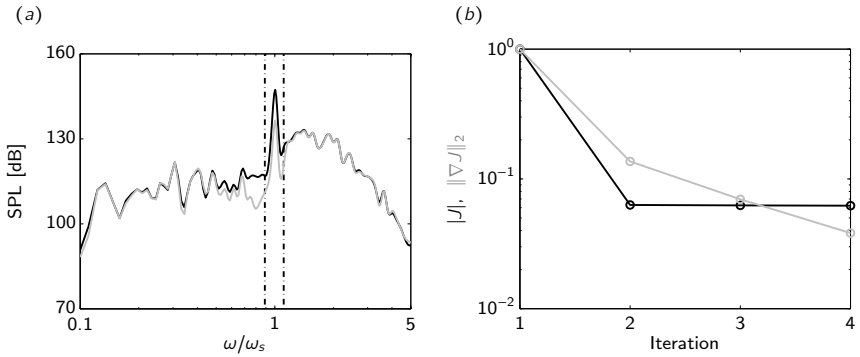

Figure 5.18: (*a*) Spectrum of the uncontrolled (———) and controlled (———) case. The area between the two dashed lines (-·-·-·-) marks the frequencies to be reduced. (*b*) Ojective function versus the optimization loops (———). Gradient of the objective function with respect to the control (———).

5.5.1.1 Control of screech noise

For the control of screech noise only a narrow frequency band is singled out from the spectrum (between the dashed lines in Fig. 5.18(a)) and included in the objective functional. The uncontrolled spectrum is displayed in black in Fig. 5.18(a) and is overlayed by the controlled spectrum in gray. A marked reduction of about 10 dB in the screech frequency can be observed; the spectrum outside of the frequency band is rather unaffected by the control. The two panels in the first row of Fig. 5.19 visualize pressure fluctuations for the uncontrolled and controlled case (in panels a, b). The snapshots are taken at a simulation time $t = 0.75T$; the colormap covers the range of $[-2000, 2000]$ [Pa]. Noise is emitted from the control location such that screech (measured at the black line) is optimally diminished. In panel (*c*) the OASPL of the controlled case is presented. One can see that the noise at the measurement location has been minimized. Nevertheless, for this case only the screech component is investigated and the OASPL covers all frequancies. To this end, the overall noise level at the measurement location is not zero.

The adjoint pressure fluctuations (Fig. 5.19(d)) give an indication of the sensitivity of the objective functional to pressure forcing. It is interesting to note that the adjoint pressure fluctuations propagate from the location where the cost functional is evaluated (the area of the black line) toward the control point; at the control point, they give information about how to modify the

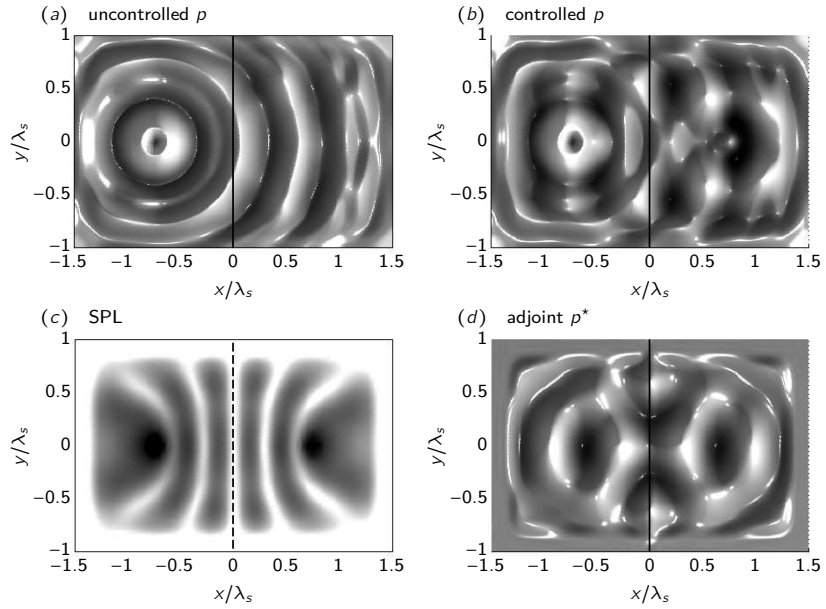

Figure 5.19: Reduction of screech noise by adjoint-based iterative optimization. (a) Pressure fluctuations at $t = 0.75T$ for the uncontrolled case. (b) Pressure fluctuations at $t = 0.75T$ for the controlled case. The objective functional is evaluated at the vertical black line (———). (c) OASPL in the domain. The objective functional is evaluated at the vertical dased line (- - - - - -). (d) Adjoint pressure fluctuations at $t = 0.75T$; color-range $[-10^{-3}, 10^{-3}]$.

pressure forcing during the previous iteration such that a reduction in our objective functional is accomplished during the next iteration.

The history of the objective functional is presented in Fig. 5.18(b). Within the first iteration the objective function decays by more than one order of magnitude. In the following iterations, no improvement of the noise reduction can be gained. The corresponding gradient is presended in the same figure (gray curve). After four iterations the gradient has been reduced by more than one order of magnitude.

5.5.1.2 Control of all frequencies

As a second test of the present optimization scheme, all frequencies are included in the objective functional and attempt to reduce the energy indiscriminately over the entire spectrum. In Fig. 5.20(a) the spectrum of the

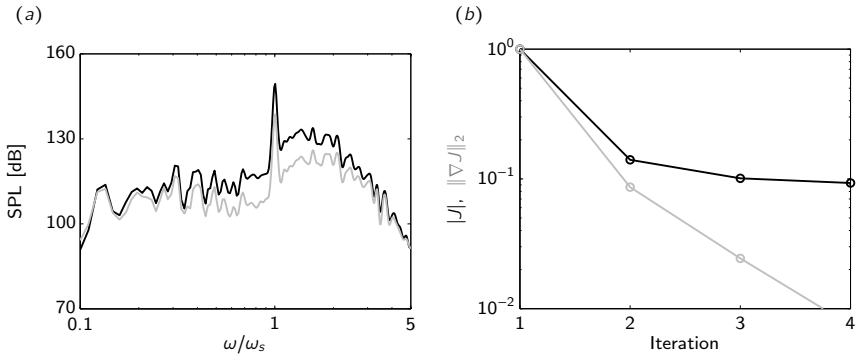

Figure 5.20: (a) Spectrum of the uncontrolled (———) and controlled (———) case. All frequencies will be reduced. (b) Ojective function versus the optimization loops (———). Gradient of the objective function with respect to the control (———).

uncontrolled (black curve) and the controlled (gray curve) case are presented. One can see, compared to the previous case, that not only the screech tone is reduced, but also frequencies in the neighborhood of the screech tone. The amount of the reduction in the neighborhood of the screech tone is in the order of 10 dB. This value could be also gained in the previous case where the focus is the reduction of the screech tone only. This shows, that the presented method is not only able to reduce noise of specific frequency bands but also reduces the noise bands with a high efficiency.

In the pressure fields of Fig. 5.21(a, b)) definite similarities to the case where we targeted screech noise (Fig. 5.19(a, b)) are evident. As before, this can be attributed to the dominance of the energy in the screech frequency which overwhelms other noise sources. This also holds true for the corresponding adjoint pressure fluctuation in panel (d) and the OASPL level in panel (c). Only slight differences to the screech elimination case are visible.

In Fig. 5.20(b) the performance of the optimization algorithm is presented. The objective function is being reduced by one order of magnitude within the first four iterations. In the same time, the corresponding gradient is reduced by more than two orders of magnitude.

The present test case shows that the implementation of a frequency based objective functional is capable to reduce specific frequency bands of a noise signal. This approach will be used in the application on supersonic jet noise to focus on the screech component during the optimization process.

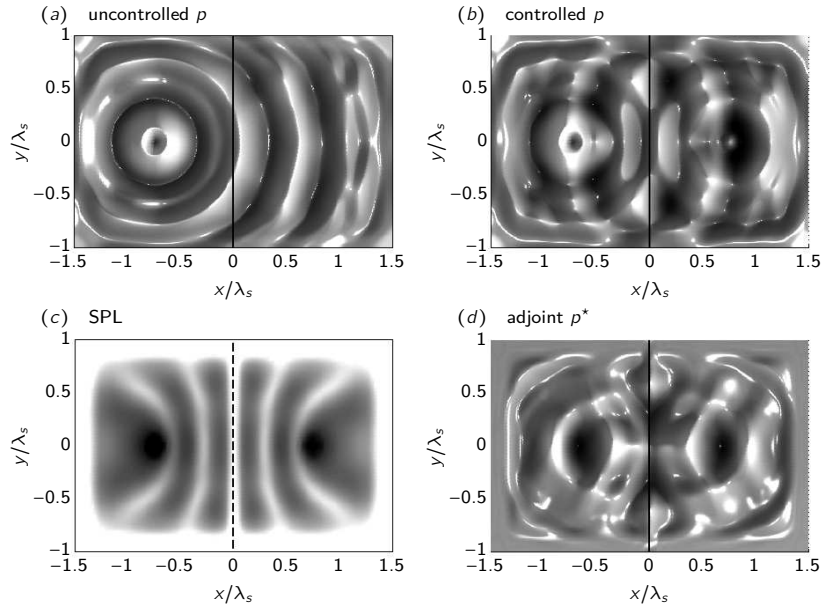

Figure 5.21: Reduction of all frequencies by adjoint-based iterative optimization. (a) Pressure fluctuations at $t = 0.75T$ for the uncontrolled case. (b) Pressure fluctuations at $t = 0.75T$ for the controlled case. The objective functional is evaluated at the vertical black line (———). (c) OASPL in the domain. The objective functional is evaluated at the vertical dased line (- - - - - -). (d) Adjoint pressure fluctuations at $t = 0.75T$; color-range $[-10^{-3}, 10^{-3}]$.

5.5.2 Porous wall

In the following, the application to the optimization of a porous material is investigated. This two-dimensional case is based on a quadratic computational domain with an adiabatic wall at Y_m and non-reflecting boundary conditions at the three remaining boundaries. The flow in the domain is at rest and only disturbed with a small pressure peak during the initial condition ($t = 0$) with an amplitude of one Pascal and a Gaussian distribution in space. Based on the edge length L of the domain, the disturbance is located at $x = 0.25L$ and $y = 0.5L$. At the opposite side of the domain, at $x = 0.75L$ and $y = 0.5L$ a microphone is located, weighted with the same Gaussian distribution as the pressure peak of the initial condition. In Fig. 5.22 a sketch of the computational domain is given with the location of the pressure peak and the location of the microphone, marked with F and M, respectively.

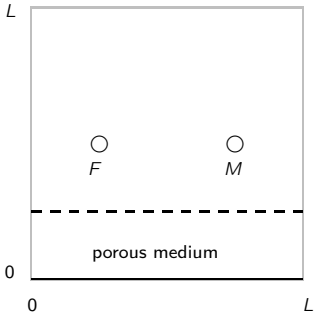

Figure 5.22: Sketch of the two-dimensional computational domain of the case with a porous wall. Adiabatic wall at Y_m (———); Non-reflecting boundary conditions otherwise (———); area between adiabatic wall and dashed line (- - - - - -) can be filled with porous material. Circle (∘) at F indicates the location of the initial pressure disturbance ($x_F = 0.25L$, $y_F = 0.5L$). Circle (∘) at M indicates the location of the microphone (measurement location, $x_M = 0.75L$, $y_M = 0.5L$). Edge length of the domain: L.

As there is no base-flow the disturbance of the pressure peak will cause an acoustic wave propagating concentric through the domain. It will leave the domain at the non-reflecting boundaries and will be reflected at the adiabatic wall located at the lower side of the domain. Finally, after a certain period of time, the reflected wave will also leave the domain passing the three non-reflecting boundaries. Within this time span the microphone detects the passing of two acoustic waves. First, the non reflected acoustic of the concentric wave and shortly after the reflected wave of the wall boundary.

The objective of the present test case is to minimize the noise measured at the microphone by means of a spatially optimized porous medium. This medium can be placed by the optimization algorithm only in a layer on top of the wall with a thickness of $0.25L$. It will influence mainly the reflected wave and will not be able to eliminate the passing of the first acoustic wave. The results of the spatially optimized porous medium will be compared to an uniformly distributed porous medium.

The porous Navier–Stokes equations and its corresponding adjoints are solved on an equidistantly spaced grid with 64×64 points. Based on a CFL number of CFL = 1 a total of 100 time steps are integrated forwards and backwards in time. This corresponds to a time span of $T = 1.5T_L$ with $T_L = L/c$, the time for an acoustic wave propagating once through the computational domain (c, ambient speed of sound). The Reynolds number, based on the length of the domain and the ambient speed of sound, is $Re_L = 1000$.

As initial condition, a Gaussian distribution of the pressure fluctuation is chosen with the following shape:

$$\sigma_F(x) = \exp\left(-\left(\frac{x - x_F}{\delta}\right)^2 - \left(\frac{y - y_F}{\delta}\right)^2\right)$$

and finally:

$$p'(x, t = 0) = \alpha_p \sigma_F(x) + p_0$$

with the width of the peak $\delta = 0.04L$, the ambient pressure $p_0 = 10^5$Pa and the amplitude of the fluctuation $\alpha_p = 1$Pa. The microphone (measurement location) has the same shape as above equation only located at x_M and y_M instead of F. With this weighting function, the objective function can be given:

$$J = \int_\Omega \int_0^T \sigma_M(\boldsymbol{x}) p'^2(\boldsymbol{x}, t)\, \mathrm{d}t\, \mathrm{d}\boldsymbol{x}$$

Note, that in the present application no frequency dependent objective function is used, hence all frequencies detected by the microphone will be minimized. The corresponding terminal condition or adjoint initial condition has to be zero ($\boldsymbol{q}^\star(T) = 0$) and the adjoints are forced at the location M with the pressure signal captured by the microphone during the forward computation.

In Fig. 5.23(a) the objective function is presented as a function of the optimization iterations. A total of 30 iterations are performed (corresponds to a tolerance of 10^{-4}). One can see that during the first optimization iteration most of the objective function can be reduced (more than 20 %). In the remaining iterations, the objective function decreases for further 3 % to its final value of 77.4 % of its initial value J_0. Again, the objective function is chosen such that it can not become zero as the first acoustic wave will always pass the microphone and the integration time covers the whole computational time ($0 \le t \le T$). In panel (b) of the same figure, the time history of the signal measured in the center of the microphone (x_M and y_M) is presented. Both, the optimized case (gray curves) and the case without porous material (black curve) are presented, whereas two curves are shown for the optimized case. One after the first iteration (gray dashed line) and one after 30 iterations (gray solid line). The non optimized case (black curve) clearly shows the two acoustic waves passing the microphone. First, the direct wave at $t \approx 0.5T_L$ and shortly after at $t \approx 1.2T_L$ the reflected wave. In the optimized case,

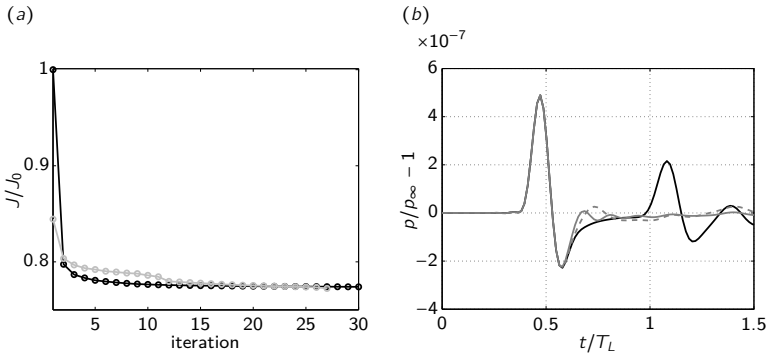

Figure 5.23: (*a*) Objective function over the optimization iterations. (—o—) initial guess: void space. (—o—) initial guess: sinusoidal distribution. (*b*) Time history of the pressure fluctuations in the center of the measurement area ($x = 0.75L$; $y = 0.5L$). No optimization (———); Optimization after one iteration (- - - - - -); Optimization after 30 iterations (———).

both, after one and 30 iterations, the reflected wave is nearly eliminated with a better performance for the case after 30 iterations (gray solid line). The main difference of the converged result after 30 iterations to the first iteration can bee seen at $t \approx 0.7T_L$ when the first acoustic passes the microphone. It is especially apparent that the converged result shows less overshoots and reaches the baseline ($p' = 0$) faster than the result after one iteration. The reason for this behaviour becomes more evident when we look at the optimized porous medium in the following.

The spatial distribution of the optimized porous material is presented in Fig. 5.24. Panel (*a*) shows the result after one optimization iteration and panel (*b*) the converged result after 30 iterations. Both optimization results are similar but differ mainly in the amplitude. Visualized is the dimensionless permeability χ in the color-range of $0 \leq \chi \leq 87$ whereas a dark value corresponds to a rather solid body and a light area to void space. In the converged result the largest permeability is outside the color-range at $\chi_{\max} = 2700$. Comparing this high value to the validation cases of Sec. § 3.2 it is evident, that the optimization algorithm created both, solid bodies (black areas) and a porous medium (gray areas). The largest detectable permeability in panel (*b*) corresponds to the sharply bounded thin bar ranging from $0.4 \leq x/L \leq 0.6$ and $y = 0.25L$. The porous material underneath this bar shows a parabolic shape repeated in a regular pattern. Directly at the wall the permeability vanishes,

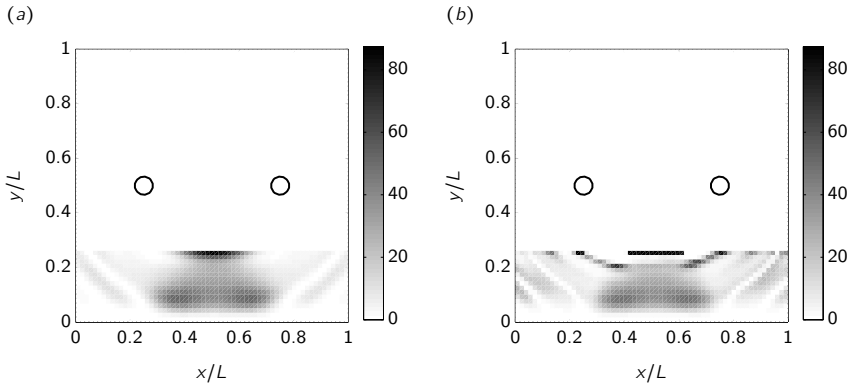

Figure 5.24: Optimized porous material in the lower quarter of the computational domain presented in the dimensionless variable χ. (a) Result after one optimization iteration. The maximum value $\chi_{\max}$ corresponds to the largest color-range ($\chi_{\max}$ = 87) (b) Result after 30 optimization iterations. The maximum value $\chi_{\max}$ is outside the presented color-range ($\chi_{\max}$ = 2700).

which is no surprise since the gradient is a scalar product of the direct and adjoint velocities which are both zero at the wall (no slip condition).

In Fig. 5.25($a.3, b.3, c.3, d.3$) the effect of the spatially distributed optimal porous material with its solid bar and the porous medium distributed underneath becomes more obvious. Presented are four snapshots of the pressure fluctuation in the domain including the porous material (indicated by the solid contour lines). The snapshots are taken at the non equidistantly spaced time-steps $t/T_L = [0.29, 0.59, 0.75, 1.20]$. In the first snapshot ($a.3$) the acoustic wave is entering the porous material and hits the left corner of the solid thin bar. The subsequent panel ($b.3$) shows the acoustic wave being reflected at the solid bar and following the first acoustic wave. By means of this reflected acoustic wave, which is following the first wave in short distance, the optimization algorithm achieved the goal to raise the pressure drop in the wake of the first acoustic wave as fast as possible (cf. Fig. 5.23(b) at $0.6 \leq t/T_L \leq 0.7$). At the next time step captured ($c.3$) one can see that this reflected wave is passing above the microphone with only little overlapping. Finally, in the last panel ($d.3$) at $t/T_L = 1.20$ most of the acoustic waves left the domain.

To compare the optimized result with the uncontrolled case, the pressure fluctuations without porous material are presented for the same time steps in Fig. 5.25($a.1, b.1, c.1, d.1$). One can clearly identify the reflected acoustic

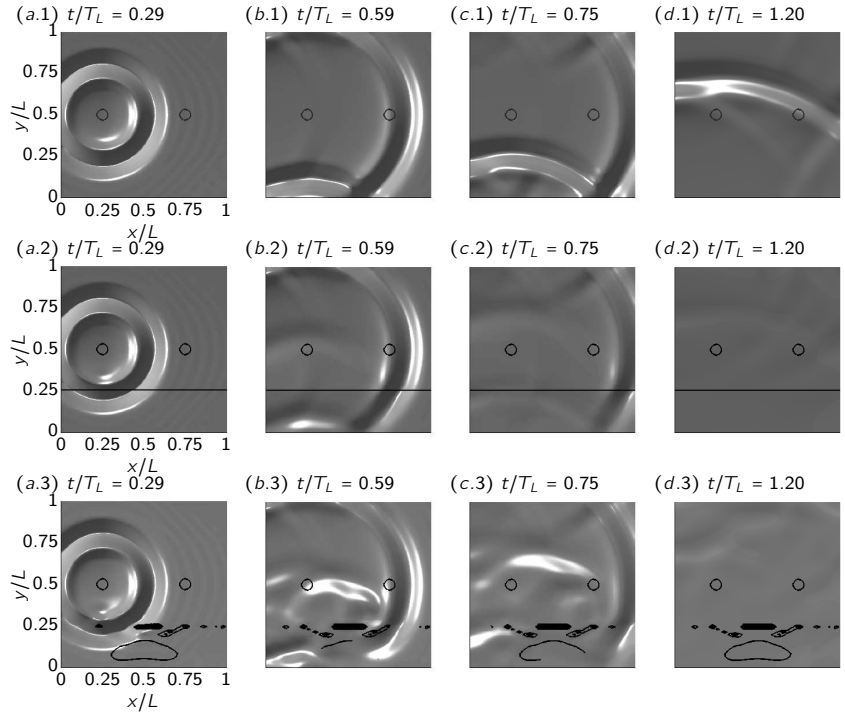

Figure 5.25: Four snapshots of the propagation of the acoustic wave in the quadratic computational domain with an adiabatic wall at Y_m and non-reflecting boundary conditions otherwise. Top figures (?.1) without porous material (no optimization). Figures in the middle row with uniformly distributed porous material with χ_{min}. Figures in the last row with optimized porous material (after 30 iterations). All snapshots taken at four (non equidistant) time-steps: $t/T_L = [0.29, 0.59, 0.75, 1.20]$. Contours of the porous medium marked with a black solid line (———). Initial pressure peak and measurement location marked with a circle (∘).

wave at the adiabatic wall and the passing of two waves in panel $(b.1)$ and $(d.1)$, the direct and reflected one, respectively.

How does a homogeneously distributed porous material perform? To answer this question, a homogeneously distributed porous material is placed in the lower quarter of the computational domain and the objective function is evaluated for different values of the permeability. The result is presented in Fig. 5.26(a). It shows the objective function as a function of the dimensionless permeability χ (solid line with circles). The curve is decreasing

monotonically until it reaches a minimum point at $\chi_{\min} = 10.7$ with a value of $J/J_0 = 0.7926$. From this point on the objective function is increasing again and reaches $J/J_0 = 1.1232$ at the end of the investigated range of permeabilities ($0 \leq \chi \leq 3 \cdot 10^4$). The global minimum of the investigated range of permeabilities is at $\chi_{\min} = 10.7$, which corresponds to the optimum of a homogeneously distributed porous material to minimize the noise at the location of the microphone. In addition to that, the optimal result obtained by the adjoint based optimization algorithm is presented in the same figure and marked with a dashed line at $J/J_0 = 0.7740$. One can see that the value of the dashed line lies below the minimum of the homogeneously distributed porous material (a decrease of nearly 2 %). Hence, the result of the adjoint based optimization algorithm is better (as expected) than the one of homogeneously distributed porous material. The spatially distribution of the porous material of the adjoint based optimization algorithm apparently plays an important role.

In panel (b) of Fig. 5.26 the time history of the pressure fluctuations are presented as already done in Fig. 5.23(b) with the difference that in this figure the global minimum of the uniformly distributed porous medium is presented and marked with a gray dashed line. The two remaining curves represent the non optimized case (black curve) and the optimized case with adjoint methods (gray solid line, after 30 iterations). In this figure the importance of the solid thin bar to the optimized porous material becomes apparent as it raises the pressure drop in the wake of the first acoustic wave faster than in the case of the homogeneously distributed porous material.

For the sake of completeness the four snapshots of the pressure fluctuations of the homogeneously distributed porous material with the minimal value of $\chi_{\min} = 10.7$ is presented in Fig. 5.25$(a.2, b.2, c.2, d.2)$. The homogeneous distribution damps the acoustic wave during its way through the porous material and minimizes the amplitude of the wave being reflected at the adiabatic wall. During the penetration of the wave in the porous material a part of its energy is reflected back into the computational domain. This part is contributing to the noise detected at the microphone (peak at $t = 0.75T_L$). In Fig. 5.27 the homogeneously distributed porous medium is presented with the same color-range as in Fig. 5.24 for comparison.

Is it a global minimum? Gradient based optimization algorithms find local minima, only. The chance to find the global minimum of the objective function depends on the shape of the objective function itself and the choice of the initial guess. Especially when optimizing a porous material one can

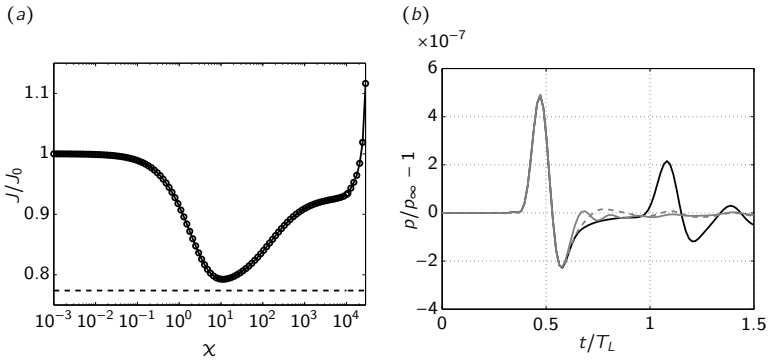

Figure 5.26: (*a*) Objective function over the dimensionless permeability χ of a uniformly distributed porous medium in the lower quarter of the computational domain (——o——). The local minimum is at $\chi_{min} = 10.7$ with a value of $J/J_0 = 0.7926$. The dashed line (- - - - - -) corresponds to the minimum obtained by the adjoint optimization algorithm with a value of $J/J_0 = 0.7740$. As the permeability varies in this case, no specific value for χ can be given. (*b*) Time history of the pressure fluctuations in the center of the measurement area ($x = 0.75L$; $y = 0.5L$). No optimization (———); Global minimum of the uniformly distributed porous medium ($\chi_{min} = 10.7$) (- - - - - -); Adjoint based optimization after 30 iterations (———).

think of an infinitely large number of different porous material with the same fluid-mechanical properties and hence the same value of the objective function. Considering e. g. the spatial distribution of a porous material inside a cylinder surrounded by solid material will make, from a fluid-mechanical point of view, no difference to an overall solid cylinder. Generally spoken, in areas where the velocity components are zero, the present optimization algorithm can not control the porous medium (see also the definition of the gradient which is depending on the velocity). In these areas the solution of the spatial distribution of the porous material is arbitrary and may lead to an infinitely large number of optimal solutions. This fact makes the localization of the global minimum an even more challenging task.

To test this property, the same optimization case is performed, yet starting with a different initial guess. In the previous case the initial guess is simply void space (no porous material). Now, as initial guess a regular pattern based on a sinusoidal distribution is chosen and reads:

$$\chi = 10.7\left(\sin\left(\frac{4\pi x}{L}\right)\sin\left(\frac{4\pi y}{L}\right)\right)^2$$

This initial distribution is presented in Fig. 5.28(*a*). The maximum value

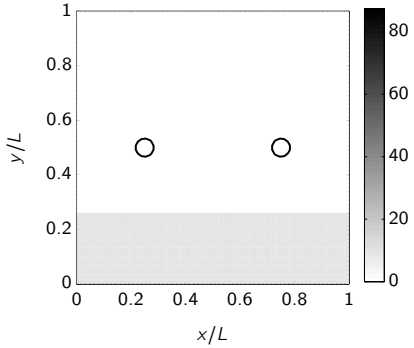

Figure 5.27: Optimal homogeneously distributed porous material in the lower quarter of the computational domain presented in the dimensionless variable χ. To compare it with the adjoint cased optimization, the same color-range as in Fig. 5.24 is chosen. Optimal permeability: $\chi_{\text{min}} = 10.7$ (cf. also Fig. 5.26(a)).

($\chi_{\max} = 10.7$) is taken from the previous study with a homogeneously distributed porous medium as it showed to be the optimal value. The converged optimal solution can be gained after 27 optimization iterations (with a tolerance of 10^{-4}) and reaches the same optimal value as in the previous study. In the history of the objective function (presented in Fig. 5.23(a), gray curve) one can identify that the initial guess is a better choice as simply void space since the value of the first iteration starts at $J/J_0 = 0.84$, with the value of the objective function J_0 based on the void space initial guess. In addition to that, the final optimal value after 27 iteration reaches the same value as the one of the void space initial guess. Now, one could postulate that both optimizations found the same optimal solution and hence ended up in the same local minimum which now could be a global one. In fact, when comparing both optimal solutions in Fig. 5.24(b) (void initial guess) and Fig. 5.28(b) (sinusoidal initial guess) one can identify differences. Still the main features are present, like the thin solid bar and the parabolic shaped porous medium underneath it. A main difference is the missing porous medium directly below the solid thin bar (gray area at $x = 0.5L$, $y = 0.1L$). Nevertheless, this area is covered by the thin bar and surrounded by porous medium. To this end, no fluid (acoustic waves) can penetrate this area from outside and, from a fluid-mechanical point of view, does not play a role for the optimization objective.

To conclude the results of this test case we can see that the optimization with a spatially distributed porous medium is capable to minimize acous-

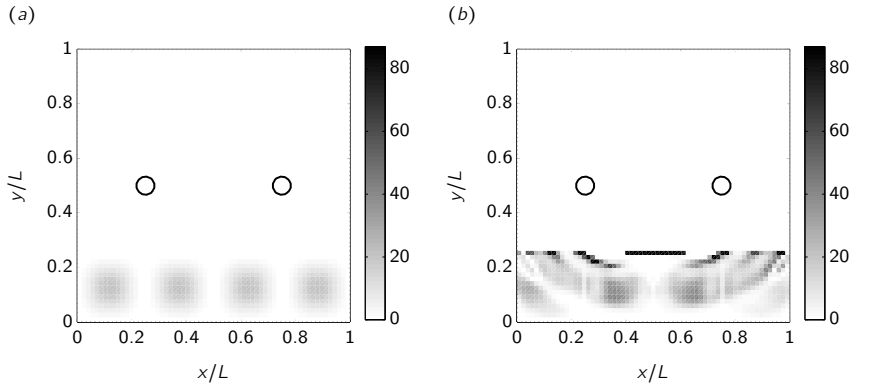

Figure 5.28: Optimized porous material in the lower quarter of the computational domain presented in the dimensionless variable χ. (*a*) Initial guess with a sinusoidal distribution. Maximum permeability χ_{max} = 10.7. (*b*) Result after 27 optimization iterations (converged result with tol. 10^{-4}). The maximum value χ_{max} is outside the presented color-range (χ_{max} = 1887).

tic noise. Moreover, it performes better than a homogeneously distributed porous material. However, the optimal solution might look different based on the initial guess but can show the same fluid-mechanical properties.

5.5.3 Trailing edge noise

The previous test case is a purely acoustic application. In the present test case, we will now demonstrate the potential of such an iterative adjoint–based optimization algorithm by identifying the optimal distribution of porous media to reduce flow induced trailing edge noise. For the present setup the domain is discretized on a Cartesian grid with 512×256 points stretched in the normal direction. To increase the performance, the code (forward and backward) is parallelized with the Message Passing Interface (MPI) using 16 cores for the current setup. The results are based on Schulze & Sesterhenn [2011] where additional information can be found.

5.5.3.1 Flow parameter

The Reynolds number is based on the mean velocity in the acoustic far-field u_0 and the height of the trailing edge h.

$$Re = \frac{\rho_0 u_0 h}{\mu_0}$$

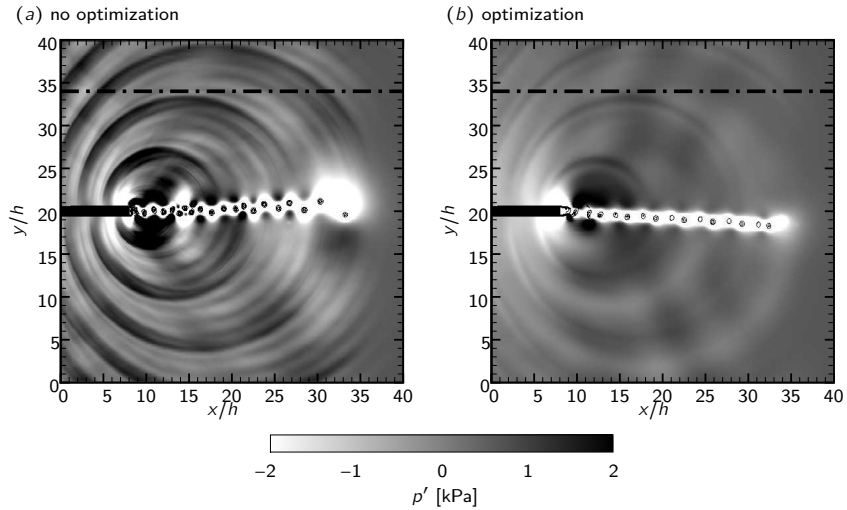

Figure 5.29: Pressure distribution of the uncontrolled (a) and controlled (b) case. Color-range: $p' = \pm 2000$ [Pa]. (———) iso-countour of the abolute vorticity. Objective function (noise) is measured along dash dotted line (-·-·-·-).

For the present application, a Reynolds number of $Re = 10^4$ is adjusted with a subsonic Mach number in the far field of $M = 0.5$. Ambient pressure and temperature are set to $p_0 = 10^5$ [Pa] and $T_0 = 300$ [K], respectively.

5.5.3.2 Optimized porous medium

In Fig. 5.29 the pressure fluctuations of the uncontrolled (a) and controlled case (b) are visualized in a color-plot together with the iso-lines of the normal vorticity. Both snapshots are taken at the final time-step at $t = T$ with the same colormap covering a range of ±2 [kPa].

In the uncontrolled case one can see loud acoustic waves emerging from the origin of the trailing edge and scattering in the far-field. This noise is directed mainly in the upstream direction, while being shifted from the base-flow. In the wake of the trailing edge periodically detaching vortical structures are visible. The relative distance of two vortex cores, measured close to the trailing edge, is approximately the height of the trailing edge h.

Along the dashed-dotted line, the noise is measured and being minimized. The optimized case, presented in Fig. 5.29(b), shows a reduced fluctuating pressure, not only along the line where to minimize the noise, but also in the

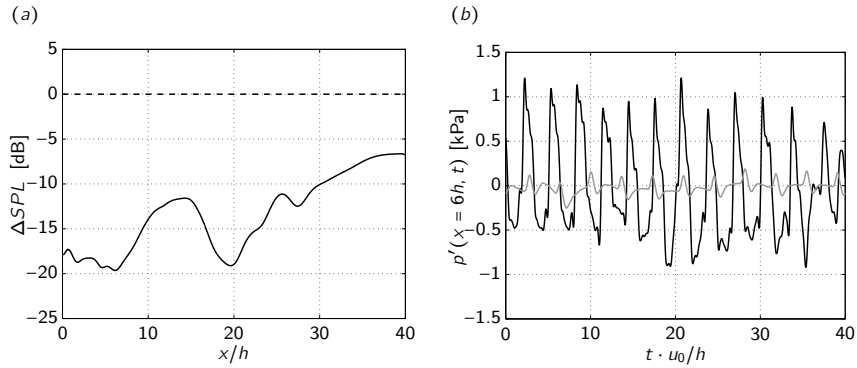

Figure 5.30: (a) Noise reduction measured along the control-line, compared to the uncontrolled case. Up to 19 dB reduction possible in the upstream direction ($x \approx 6h$). (b) Pressure fluctuation p' measured at the position $x = 6h$ in the control–line. Uncontrolled case (———); Controlled case (———).

whole domain. Some low amplitude acoustic waves are still visible, especially in the transverse direction. In the wake of the trailing edge one can see a distinct difference in the controlled and uncontrolled case. The wake is tilted slightly in the negative y-direction, away from the line where to measure the noise. Besides that, the detached vortices loosed in intensity and their relative distance has doubled compared to the uncontrolled case.

The performance of the optimal control is presented in Fig. 5.30(a). Here, the difference of the measured sound pressure level (SPL) of the controlled case to the uncontrolled case is outlined as a function of the measurement location. Negative values represent a noise reduction. One can see that the noise is being reduced along the entire measurement section. A local reduction of almost 20 dB is reached in the upstream direction ($x \approx 6h$). In the normal direction, where some acoustics are visible in Fig. 5.29 ($x \approx 15h$), the noise reduction is still 12 dB. Further downstream, especially in the area where the sponge is acting ($x > 34h$), the noise reduction is less than 10 dB.

In Fig. 5.30(b) the reduction of the pressure fluctuation is visualized as a function of the time. The fluctuations are measured in the control line at the position $x = 6h$, where the noise reduction is most efficient (cf. Fig. 5.30(a)). Visualized is the uncontrolled case with a black curve and the controlled case with a gray curve. For the uncontrolled case one can see a periodic fluctuation with amplitudes of up to ±1 [kPa] with a dominant frequency and additional higher frequencies with lower amplitude. In the controlled

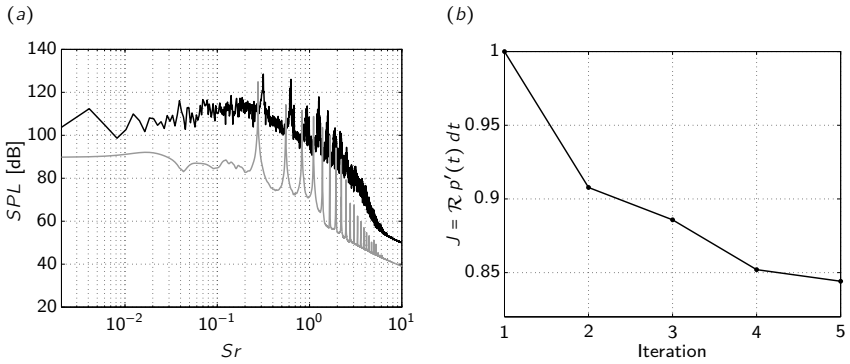

Figure 5.31: (a) Sound pressure distribution (SPL) along the control-line depending on the frequency. Uncontrolled case: black curve; Controlled case: gray curve. $Sr = fh/u_0$. (b) Objective function (Eq. (5.16)) depending on the number of iterations normed with $J(1)$. The algorithm obtained a converged result in only five iterations.

case the fluctuations are reduced by the order of one and seem to have less broadband components as the uncontrolled case.

This effect can be also seen in Fig. 5.31(a) where the sound pressure level is visualized as a function of the frequency. Following Parceval's theorem, the total energy of a signal is the integral in frequency space of its Fourier coefficients. This corresponds to the area below the curves in the power spectrum. In Fig. 5.31(a) both, the uncontrolled (black curve) and the controlled case (gray curve) is presented. One can identify a reduction of the total energy. Anyway, for some frequencies, especially for the first dominant harmonic, the noise reduction is only 3 dB. Additionally, the peaks of the first harmonic and its sub-harmonics are shifted slightly to lower frequencies.

To get an impression of the spatial distribution of the porous material, the permeability is visualized in Fig. 5.32. It represents the dimensionless permeability χ in the color-range of $0 \leq \chi \leq 1000$. In panel (a) one can identify a part with a high value of the dimensionless permeability close to the trailing edge. This part can be treated as an additional solid extention to the trailing edge with the shape of a quarter of a circle. In between the shape of the trailing edge and the added solid structure, a tiny embedded cavity (white area) is visible. As no fluid can neither enter nor leave this closed system, it can be interpreted as a solid body. Again, the reason for the appearance of such a cavity lies in the way the optimization algorithm is evaluating the gradient. It is the scalar product of the direct and adjoint

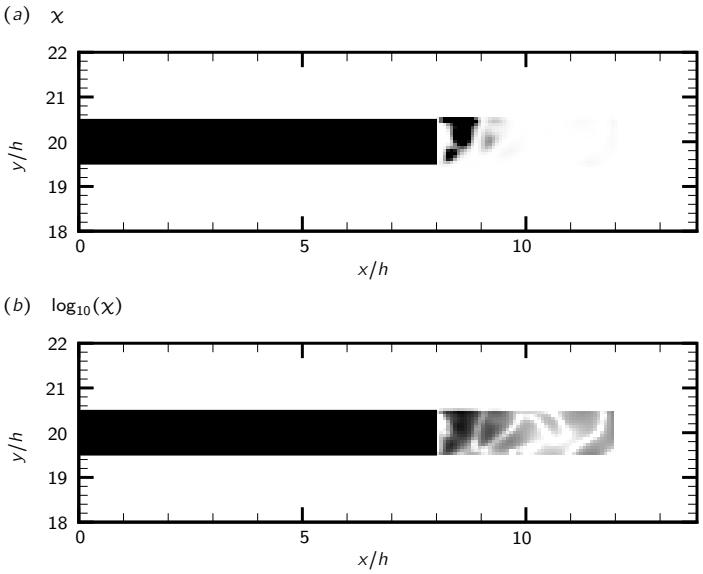

Figure 5.32: Optimal distribution of porous media. (*a*) Dimensionless permeability χ. Dark values denote solid parts, light areas void space. (*b*) Dimensionless permeability in logarithmic scaling to display the vast range of scales in the optimal porous medium.

velocities. If one of each is zero, the gradient will be zero and no porous medium can be created. This particularly occurs in areas where already some porous medium is available. During the optimization process the porous medium is "growing" and the gradient can not reach areas inside a porous medium. Hence, cavities can be the consequence.

Further downstream, the porous medium is hardly visible in this color-range. It turns out that the optimization algorithm creates a porous medium with a vast range of scales in the permeability. To visualize the spatial distribution of all scales in one figure, a logarithmic scaling of the dimensionless permeability is used in panel (*b*). Two areas can be identified. First, the solid part close to the trailing edge and secondly a porous part with a complex structure of elongated pores and channels running through it. From this sketch, a highly anisotropic behavior of the optimal porous medium is recognized.

For completeness, Fig. 5.31(*b*) displays the convergence behavior of the optimization algorithm. Visualized is the objective function (5.16) depending

on the number of iterations. The algorithm shows convergence in only five iterations. This test case is the first to apply the optimization of a porous material to an aeroacoustic application. It can be showed that the present optimization algorithm is capable treat these problems. In the following chapter. This method is applied to reduce the noise of a supersonic jet with the focus on jet screech.

6

Results of the minimization of supersonic jet noise with porous media

In the following section the potential of adjoint-based optimization to reduce supersonic jet noise will be demonstrated. The control objective is to optimize a porous material at the nozzle exit to minimize the noise of the jet in a predescribed location of the computational domain. From a physical point of view, the porous material at the nozzle exit is supposed to influence the receptivity at the nozzle lip to eliminate the feedback loop, responsible for screech tones. To this end the dominant noise source in a supersonic jet will be eliminated.

It has been shown by a series of researchers, who investigated supersonic jet noise experimentally that a porous material can reduce the screech tone (already mentioned Sec. § 1.1.2). Harper-Bourne & Fisher [1973] added a porous material at the surface of an acoustic reflector to act as a sound absorbing material and showed that the screech tone could be reduced. A recent investigation on this topic is reported by Khan et al. [2008]. They added a porous reflector at the nozzle exit (similar as in the present investigation) and showed that the screech tone could be reduced by more than 6 dB. However, their data also show that on the one hand the screech tone is not completely eliminated and on the other hand that the OASPL of the jet is nearly one dB louder *with* the porous reflector than without. Especially the broadband shock associated noise and the mixing noise is louder with porous material than without (cf. Fig. 6.1). The correct choice of the porous material to

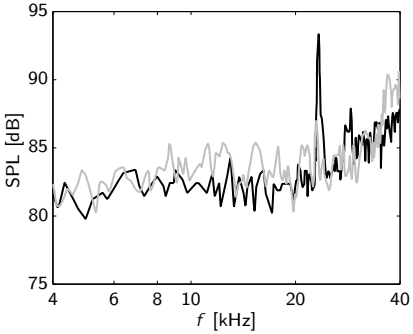

Figure 6.1: Experimental result by Khan et al. [2008]. Screech reduction of a round jet with $M_j = 1.25$ by a porous reflector at the nozzle exit ($D = 10$ [mm], measured at $\Theta = 90°$). (———): no porous reflector; (———): with porous reflector. Screech tone reduced by more than 6 dB with porous reflector. Mixing and broadband noise increased with porous reflector.

not only reduce screech but also reduce supersonic jet noise in general, is obviously by no means clear. To this end, we will use the adjoint-based optimization algorithm of Sec. § 5.4.1 to optimize a porous material at the nozzle exit to reduce supersonic jet noise with the focus on screech tones.

As we have seen in Sec. § 3 a porous material can be modeled by the porosity and permeability. Both parameters are in general functions of space and time. So, we can model a porous material with a non homogeneous material distribution in space and also time. The latter one would represent a moving material. From an manufacturing point of view, a moving porous material (which is usually based on rigid materials like polyurethane or metal foams) is hard to fabricate. Adding a moving material to reduce noise would also create an active control device. In the present investigation we want to focus on passive devices as they are much easier to handle in real world environments. To this end, the time dependency of the material properties we will neglected in the present optimization study. The remaining degrees of freedom are the spacial distribution of the permeability and the porosity. Usually both parameters are linked. So, changing for instance the porosity of the material will also change the permeability. For the universal porous material investigated in the present study, no correlation between permeability and porosity is available. Hence, for simplicity, the only controllable parameter in the present investigation will be the space dependant permeability. The porosity is supposed to be constant and is set to $\phi(\boldsymbol{x}, t) = 1$.

The remaining question is where to allow the optimization algorithm to place a porous material. As, the permeability is a source term of the compressible Navier–Stokes equations and valid in the whole computational domain, the optimization algorithm has the freedom to place the porous material anywhere. This freedom usually creates some kind of trivial solutions. One of such trivial solutions to reduce supersonic jet noise would be to place a porous material with solid properties inside the nozzle. Hence, the flow inside and outside the nozzle would stagnate and supersonic jet noise would be eliminated completely. This is obviously the global minimum but not the solution we search for. Another trivial solution could be a porous material placed in between the noise source and the microphone. This again would reduce the measured noise, but not solve the intended problem. There are two possibilities to avoid these trivial solutions. The first is to add a penalty term to the objective function which penalizes the optimization algorithm when for example the mass flow inside the nozzle is reduced. This approach can exclude only the trivial solution where the penalty term is sensitive to, like the mass flow inside the nozzle. Therefore, for each trivial solution, one penalty term has to be found and needs to be added to the objective function. This approach can be very time consuming, since the possible trivial solutions are not always previously known, especially if the flow is complex. The second possibility to avoid trivial solutions is to limit the domain where the optimization algorithm can place a porous material. This approach is used in the present investigation. In doing so, the domain is chosen such that it does not intersect the mean-flow of the jet. Only acoustic properties of the porous material will be investigated.

In Fig. 6.2 a sketch of the nozzle, including the domain where the porous material can be optimized, is presented. The nozzle is identical to the round nozzle of Sec. § 4.2 except that a porous domain is added at the nozzle exit. This additional porous material has a thickness of $0.5D$ in the streamwise direction and covers the whole nozzle lip (same nozzle lip thickness of $t/D = 1$). To avoid an interaction with the outwards tilted mixing-layers due to the "barrel"-shock, the porous material is inclined by 45°. Compared to the whole nozzle, this additional porous part is small and it has no direct contact to the mean flow. But as we will see later it has a strong effect not only on the acoustics of the jet but also on its mean flow.

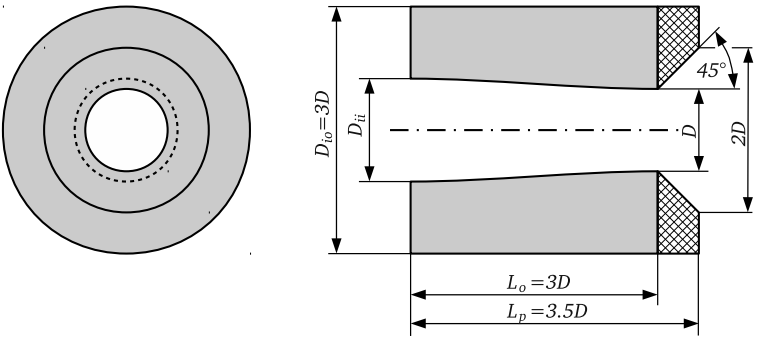

Figure 6.2: Dimensions of the round convergent nozzle with the domain where porous material can be placed (shaded area). Design Mach number M_d = 1; inlet Mach number M_i = 0.5. D_{ii} = 1.16D (cf. Fig. 4.16).

6.1 Adjoint solution

Adjoint based optimization, as implemented in the present investigation, is an iterative algorithm and has to be repeated until it falls below some predefined error bound. Within each iteration first the direct equations and subsequently the corresponding adjoint equations need to be solved forward and backwards in time, respectively. Both simulations run within the same time window. The width of this window (the simulation time) can be chosen arbitrarily. There is no general rule how to define the correct (optimal) simulation time. In the present investigation, where the gradient is an integral over the total simulation time, the simulation time should be large enough to obtain a converged result. As one optimization loop is expensive and the complete history of the forward computation has to be saved, a tradeoff between simulation time and computational resources has to be found.

In the present investigation this tradeoff looks as follows: First the adjoint based optimization is performed on the coarse grid only ($256 \times 128 \times 128$). The optimized porous material obtained by this investigation is then applied to the higher resolution ($512 \times 256 \times 256$) by means of a three-dimensional interpolation. As we will see later, both, the high and low resolution optimized case show similar properties, which justifies this approach. From a computational point of view, it is much cheaper to perform the adjoint optimization on the coarse grid. On the one hand, the computation itself is about eight times faster (assuming that the same number of cores is used for the paral-

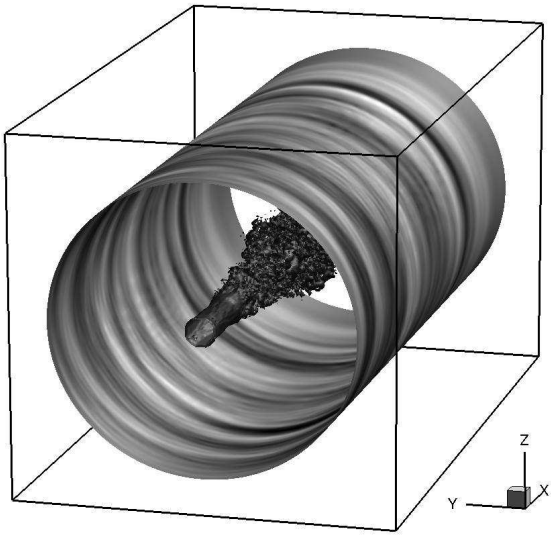

Figure 6.3: Location of the objective function to measure the noise of the round supersonic jet. Cylindrical surface: objective function flooded by instantaneous pressure fluctuations. Jet in the center of the domain visualized by iso surface of the vorticity magnitude. Arbitrary color-scaling. Box limits the size of the computational domain.

lelization). One the other hand, the snapshots to save on disc are eight times smaller. And finally, due to the two times larger time-step of the coarse grid, the physical process develops and converges faster. Still, one iteration loop on the coarse grid is expensive. For the present investigation, a total of 5000 time-steps are used for the width of the time window. This corresponds to a total of about 66 screech cycles. For a complete optimization loop, including one forward computation, one backward computation and the subsequent line-search, a wall-clock time of 48h is used. This corresponds to 24 576 COREh, as this case is solved in parallel with 512 cores. A total of 1.06TB are saved throughout the computation ($(256 \times 128 \times 128) \times 7 \times 5000 \times 8$byte, with 7 variables to store (5 flow variables plus 2 time derivatives) and 64 bit = 8 byte for each entry in double precision). To increase the performance of the optimization loop and to avoid any spurious disturbances of the initial condition, the optimization loop starts from a computation where the screech tone is already fully established ($t = 20T_s$, with the time for one screech cycle T_s).

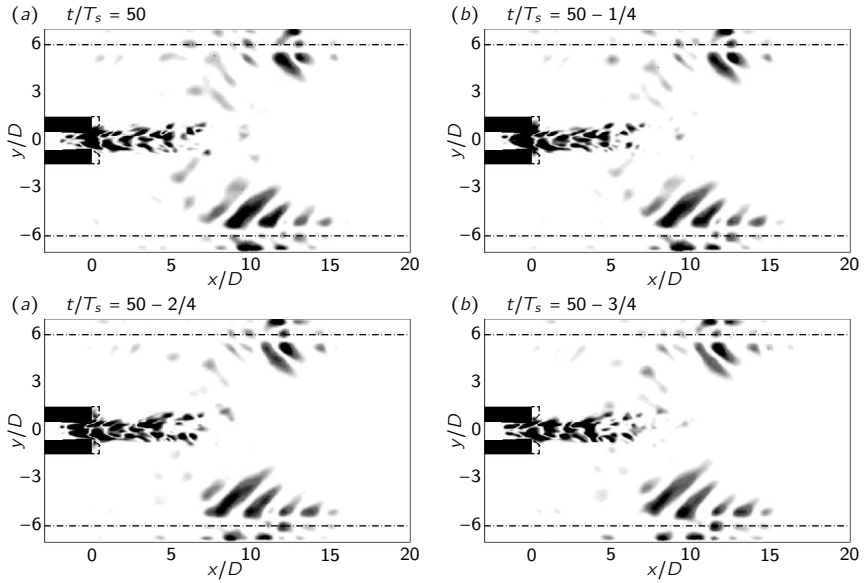

Figure 6.4: Solution of the absolute adjoint pressure fluctuation $|p^\star|$ in a two-dimensional x-y-plane in the range of [0 1000] (from white to black). Four subsequent time-steps ($a - d$).

The objective function measures the noise in a distance of $6D$ to the jet axis on a cylindrical surface. This distribution is also used to force the adjoint computation. To avoid numerical instabilities, the surface is smoothed with a Gaussian distribution and finally reads:

$$\sigma(x, y) = \exp\left(-\left(\frac{\sqrt{y^2 + z^2} - r_m}{\delta_m}\right)^2\right) \tag{6.1}$$

with the distance to the jet axis $r_m = 6D$ and the width of the Gaussian distribution $\delta_m = 0.2D$. In Fig. 6.3 the position of the surface is visualized, flooded by instantaneous pressure fluctuations and including the vorticity of the jet.

The adjoint solution is presented in Fig. 6.4 for four subsequent time-steps in a two-dimensional slice in the x-y-plane. Visualized is the absolute value of the adjoint pressure fluctuation $|p^\star|$ in the range of [0 1000] (from white to black). In the adjoint case, the simulation is running backwards in time. The first snapshot is taken at $t/T_s = 50$ (panel (a)) which corresponds to

75 % of the total computation time $t = 66T_s$. Hence, at this point the adjoint computation is running since $t = 16T_s$ (25 % of T). In the top and bottom of each panel, the dash dotted lines mark the area, where the objective function is evaluated (cf. Eq. (6.1)). In this area, the adjoint equations are forced (here the equation of the adjoint pressure) with the noise measured during the direct computation. One can identify clearly the noise corresponding to the Mach wave radiation which is dominant in the area of $x/D = 10$. During the backwards running adjoint computation, these disturbances are transported backwards towards their source location (the jet). In this area (the acoustic near-field) the direct solution is mainly at rest and the adjoint disturbances are transported with the speed of sound. In addition to that, most of the source terms of the adjoint equations are zero and the adjoint equations behave like a wave equation.

Once the disturbances reach the area of the jet, the adjoint source terms can no more be neglected and they start to amplify the disturbances. With the instantaneous velocity of the jet (supersonic in the jet core), the adjoint pressure fluctuations are convected towards the nozzle and are finally sucked up by the nozzle. Inside the nozzle the fluctuations are damped due to the additional sponge. Some of the fluctuations in the mixing-layers of the jet hit during their way towards the nozzle the nozzle lip and are deflected in the radial direction. These deflected fluctuations are passing the area where the porous material can be placed and are responsible for the shape of the gradient. The area where the gradient is evaluated is marked by a dashed line at the nozzle exit in each panel. In the first time-step shown (a) nearly no adjoint fluctuation is visible in the porous area. This picture is different in the next time-step shown (b). Here, the upper part of the porous area and the half of the lower part contains nonzero adjoint contribution. The same holds true for the subsequent time-step (c) although the amplitude is decaying. Finally in the last time-step shown (d) the fluctuations are no more present. This phenomenon is repeated throughout the adjoint simulation and suggests that the frequency of the screech tone is dominating this region.

The adjoint solution also tells us where the placing of a porous material is most sensitive to influence supersonic jet noise. This is obviously the case inside the jet core and also inside the nozzle. Hence, placing the porous material inside the nozzle and thus choking the flow would obviously influence the noise. It would lead to one of the trivial solutions mentioned earlier. The other dominant location is around the measurement lines. Placing a porous material in this area would also reduce the noise since the porous material acts as a sound absorbing device and reduces the noise. Finally and not to neglect are the fluctuations inside the porous areas close to the nozzle lips,

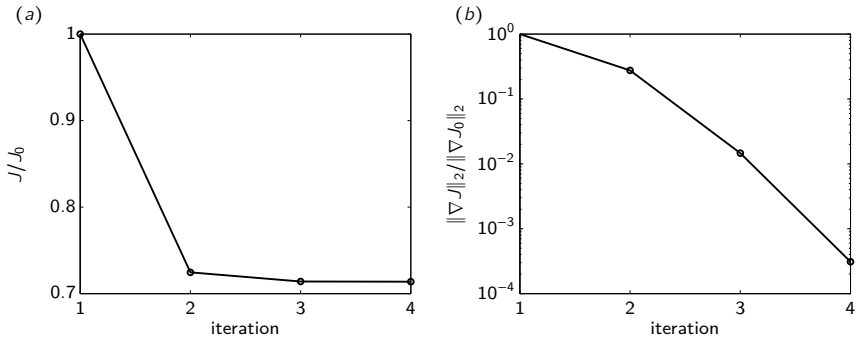

Figure 6.5: (*a*) Objective function as a function of the optimization loops. (*b*) Gradient of the objective function with respect to the control.

hence in the areas where we want to place a porous material. In this case the adjoints tell us that is efficient to place a porous material at the nozzle lip. If one would not know the physical phenomenon responsible for screech in advance, like the feedback loop and the receptivity at the nozzle lip, this would be a helpful hint to understand the underlying physical processes. To this end adjoints can not only be understood as a simple black box optimization algorithm but also as a tool to investigate the flow physics.

In Fig. 6.5(*a*) the objective function of the optimization is presented. Within the first loop, the objective function decreased by 27.54 %. In the two subsequent iterations, the decrease is slower and reaches finally 28.62 % after the fourth loop. In panel (*b*) the 2-norm of the corresponding gradient is presented. With in the first four loops it drops by more than three orders of magnitude ($\|\nabla J\|_2/\|\nabla J_0\|_2 = 3.1 \cdot 10^{-4}$). The optimization stops when it reaches a tolerance of 10^{-3}.

6.2 Optimized nozzle

The optimized porous nozzle is presented in Fig. 6.6, 6.7 and 6.8. A three-dimensional view is shown in Fig. 6.6 with the iso-surface of the permeability (taken at $\chi = 10$). One can identify a complex three-dimensional structure of pores. In parts they are coherent and in parts they are free floating.

Several two-dimensional slices in the y-z-plane of the porous material are presented in Fig. 6.7. They show the porous material at six different x-

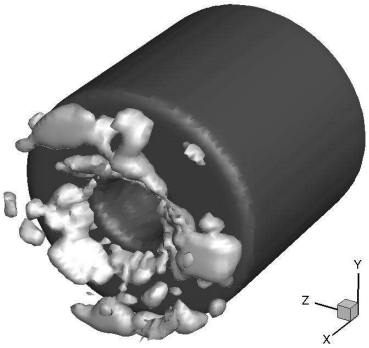

Figure 6.6: Nozzle with optimized porous material. Dark gray: iso-surface of the solid part of the nozzle. Light gray: iso-surface of the optimized porous material (at $\chi = 10$).

locations. The first slice is taken slightly above the nozzle lip ($x/D = 0.05$, panel (a)). Most of the porous material in this plane is located around the nozzle exit. It has solid behavior (black color-range) and covers the whole nozzle area in one coherent ring. The outer parts of the nozzle lip are void space, only. In a further distance to the nozzle lip ($x/D = 0.1$, panel (b)) more porous material appears on the outer regions of the nozzle lip. This trend is repeated in the subsequent slices (panel $(d-f)$). In these panels one can identify large and small coherent areas with high permeability (black). The permeability of these black areas is outside the color-range and reaches values up to $\chi = 2000$. It can be treated as a solid body.

The smallest identifiable solid obstacles are about $0.1D$ in diameter whereas the largest obstacles are around $1.5D$. In Fig. 6.8 several slices in the x-Φ-plane are given. They are taken at constant radial positions (from $r/D = 0.5$ to $r/D = 1.5$ in 0.1 steps) and unwounded in a plane view. The abscissa s measures circumferential distance ($s = 2r\pi$, from $0 \le \Phi \le 2\pi$) whereas $s = 0$ is at $y/D = 0$ and $z = r$ (cf. Fig. 6.7). Positive s values measure in the clockwise and negative values in the counterclockwise direction. Especially for locations close to the nozzle exit ($0.5 \le r/D \le 0.8$) small solid obstacles ($0.1D - 0.3D$) are visible. Further outside ($0.8 < r/D \le 1.5$) the size of the obstacles becomes larger (up to $1.5D$). One can also see that the solid parts in the outer regions of the nozzle have no contact to the solid nozzle surface at $x/D = 0$. From a manufacturing point of view, this feature is hard to realize.

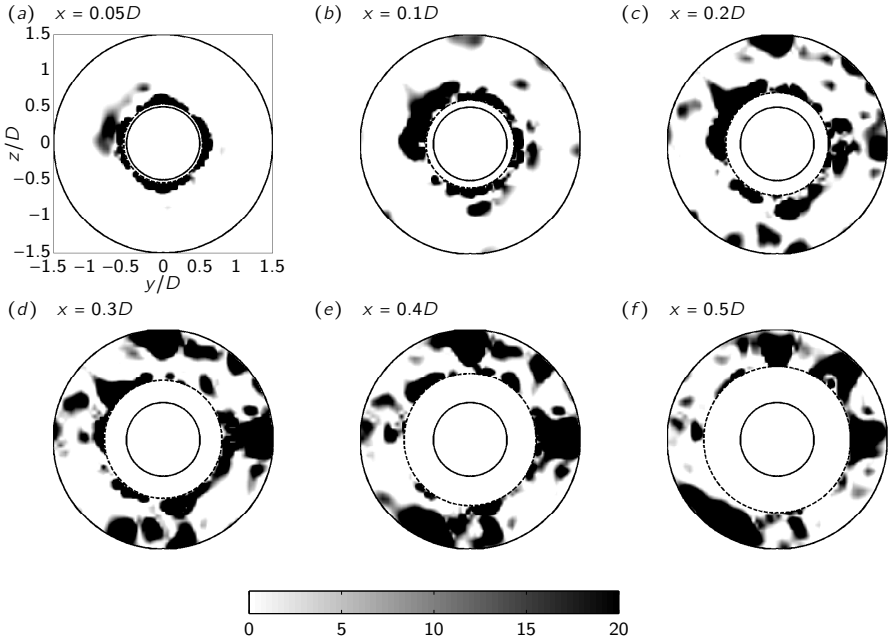

Figure 6.7: Slice through the optimized porous material in the y-z-plane at six different x-locations: x/D = 0.05, 0.1, 0.2, 0.3, 0.4 and 0.5 from panel (a – f). Color-range from $0 \leq \chi \leq 20$. Inner concentric solid line: diameter of the nozzle; between outer concentric solid line and dashed line: porous material.

6.3 Noise reduction

In the previous sections we have seen the performance of the optimization algorithm. The objective function could be reduced by more than 28 %. We will now investigate how the noise signal changes by adding the optimized porous nozzle. To this end, the nozzle with and without porous material will be compared. Both, the results of the low resolution ($256 \times 128 \times 128$) and the higher resolution ($512 \times 256 \times 256$) will be presented. Again, the adjoint based optimization is performed for the low resolution, only. To adapt the results to the high resolution, the parameter of the porous material are interpolated from the coarse to the fine grid (three-dimensional cubic Lagrange interpolation in barycentric formulation).

The main result of the optimized porous material can be seen when we

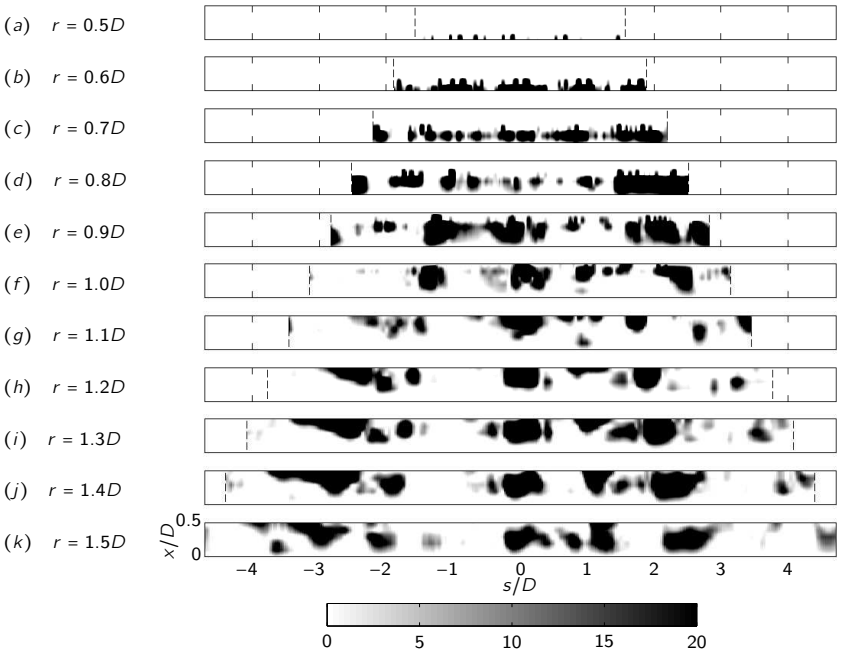

Figure 6.8: Slice through the optimized porous material in a x-Φ-plane at eleven different r-locations: from $r/D = 0.5$ to $r/D = 1.5$ in 0.1 steps. s measures the circumferential distance ($s = 2r\pi$, from $0 \leq \Phi \leq 2\pi$) where $s/D = 0$ is at $y/D = 0$.

compare the spectra of the nozzle with and without porous material. In Fig. 6.9 the acoustic spectra of the jet measured at three different locations are presented for the low and high resolution. The three panels on the left side ((a), (c) and (e)) stand for the low resolution and the remaining panels in the right column ((b), (d) and (f)) for the high resolution. From the top row to the bottom row of the panels, the observation angle is increasing. Staring from an upstream position ($\Theta = 75°$) in panel (a) and (b), followed by two downstream position ($\Theta = 135°$) in panel (c) and (d) and further downstream ($\Theta = 150°$) in panel (e) and (f). The screech tone is visible mainly in the upstream position ($\Theta = 75°$). In both cases, the low and high resolution, the screech tone could be eliminated with the optimized porous material. In the low resolution case, a drop from 130 dB down to 117 dB is measured which corresponds to a screech noise reduction of 13 dB (10 %). In the high resolution case, a drop from 143 dB to 125 dB can be identified.

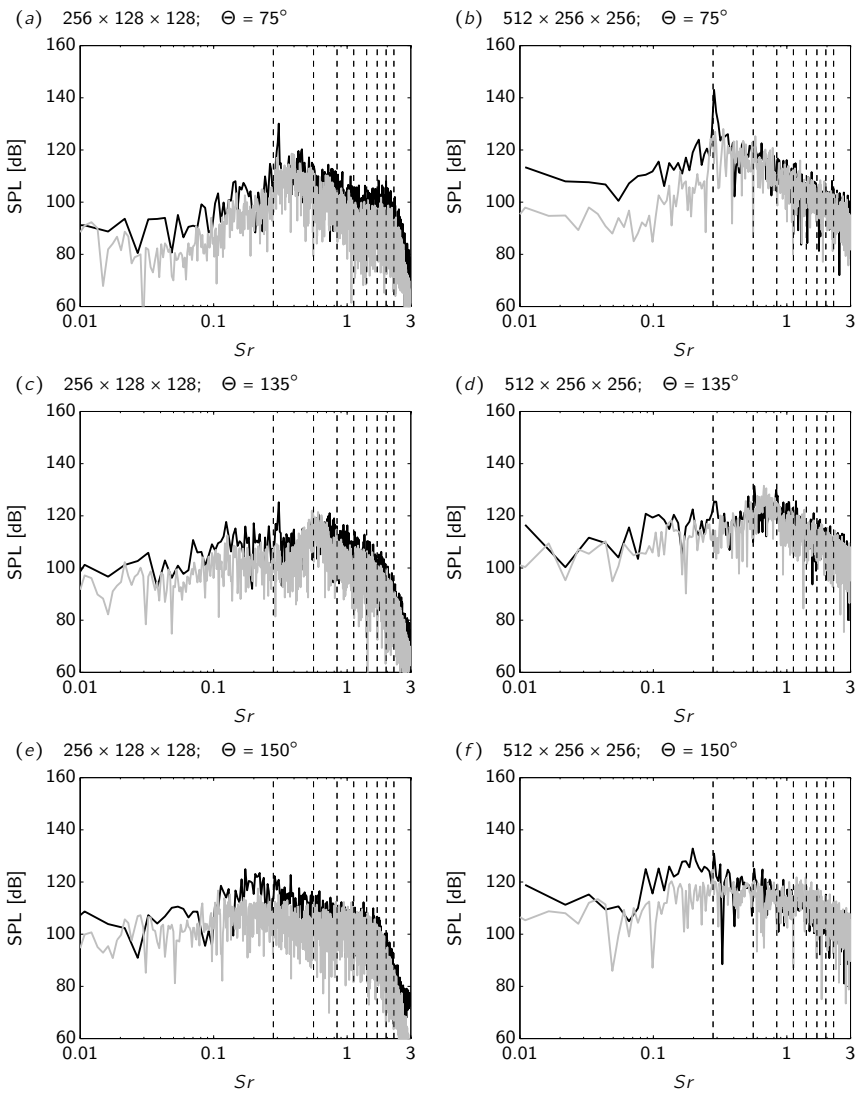

Figure 6.9: Spectra of the axisymmetric jet for two different spatial resolutions and three different observation angles Θ with respect to the upstream direction. Comparison of the optimized porosity (———) and without porous material (———). Vertical dashed lines represent the fundamental screech frequency including the first seven subharmonics based on the theory of Massey [1997].

This corresponds to a noise reduction of 18 dB of the screech tone (12.6 %). Compared to the experimental data of Khan et al. [2008], who obtained a reduction of 6 dB (6.4 %), this numerical result is quite impressive.

In addition to the screech tone, the mixing noise could also be reduced. This is especially visible in the high resolution case (b). For Strouhal numbers in the range of $0.01 \leq Sr \leq 0.3$ the amplitude of the mixing noise is reduced by up to 20 dB. This trend is also visible in the low resolution case but less dominant (up 10 dB mixing noise reduction). The reduction of mixing noise for the optimized jet can be explained with the screech tone cancellation. Once the jet is screeching it undergoes strong oscillations (here the helical mode). These oscillations increase the mixing of the jet and emanate mixing noise. In the optimized case, the helical mode is suppressed and the mixing is reduced. This will also reduce the mixing noise.

The reduction of the broadband noise component in the upstream direction is only visible for the low resolution case (a). A reduction of up to 5 dB can be identified. This trend is not visible in the high resolution case where both, the nozzle with and without porous material show the same shock-associated noise characteristics.

In supersonic jet noise the screech tone is emanated mainly in the upstream direction. Hence, in a downstream position ($\Theta = 135°$), the amplitude of the screech tone is reduced even for the nozzle without porous medium. In the low resolution case (c), the screech tone of the un-optimized nozzle is still visible with an amplitude of 125.2 dB and drops to an amplitude of 104.6 dB with porous medium. A peak of the broadband noise component is visible at the first subharmonic of the screech tone ($Sr_2 = 0.56$). At this specific frequency, the optimized nozzle is louder (1.5 dB) than the solid nozzle. This increased broadband noise level is also responsible for a louder OASPL of the controlled jet (cf. Fig. 6.10(a)). At the higher resolution (d) the behavior is similar. In addition to the fundamental screech frequency of the solid nozzle one can identify the first two subharmonics with amplitudes of 125.4 dB, 131.4 dB and 130.0 dB, respectively. All of witch are suppressed for the optimized nozzle (110.0 dB (12 %), 122.4 dB (7 %) and 119.8 dB (8 %)). As for the low resolution, the optimized nozzle is louder for this observation angle ($\Theta = 135°$). A peak of the broadband noise is visible in the signal of the porous nozzle. This peak is about 5 dB louder than the noise of the solid nozzle at the same frequency (cf. Fig. 6.10(b)).

Further downstream at an observation angle of $\Theta = 150°$ again, both the low and high resolution jets show the same characteristics. In both cases the mixing noise components are reduced whereas the broadband components of high frequency are unaffected due to the control. The reduction of mixing

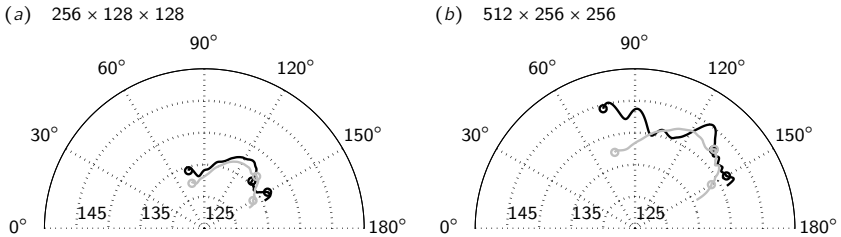

Figure 6.10: OASPL as a function of the observation angle with respect to the upstream direction. No optimization (———); optimized porous material (———). Circles (∘) mark the positions where the spectra of Fig. 6.9 are captured.

noise at a Strouhal number of $Sr \approx 0.2$ is in both cases around 10 dB.

In Fig. 6.10 the OASPL as a function of the observation angle is presented. Although the low and high resolution case predict different OASPL's the trend is similar. The largest reduction can be identified in the upstream and downstream direction. In the low resolution case (a) the OASPL drops from 134.39 dB to 132.35 dB in the upstream direction ($\Theta = 75°$). This corresponds to a reduction of 2.04 dB. A similar reduction can be reached in the downstream direction ($\Theta = 150°$). Here the OASPL drops from 136.42 dB to 133.79 dB (a reduction of 2.63 dB). In an observation angle of $\Theta = 135°$ the OASPL with optimized nozzle is louder than with solid nozzle (plus 1.04 dB). Compared to the corresponding spectrum in Fig. 6.9(c), the broadband shock-associated noise component is responsible for the increase of the OASPL in this direction. An explanation for this phenomenon may be the increased number of shock cells in the optimized case due to the suppressed helical mode (see the comparison of mean flow fields in Sec. § 6.4). The additional shocks cells emanate shock associated noise and may increase the SPL of the broadband noise components. This is the tradeoff between screech noise reduction and the corresponding suppression of the helical mode.

A similar picture of the OASPL can be found for the high resolution case (Fig. 6.10(b)). In the upstream direction, a reduction of 7.06 dB can be observed, which corresponds to a drop from 144.40 dB to 137.34 dB. Less efficient is the reduction in the downstream direction. At an observation angle of $\Theta = 150°$ the OASPL drops from 141.50 dB to 138.78 dB which corresponds to a reduction of 2.72 dB. As for the low resolution case, in an intermediate observation direction ($\Theta = 135°$) the OASPL of the optimized nozzle is louder. An increase of 0.15 dB can be measured (from 142.38 dB to

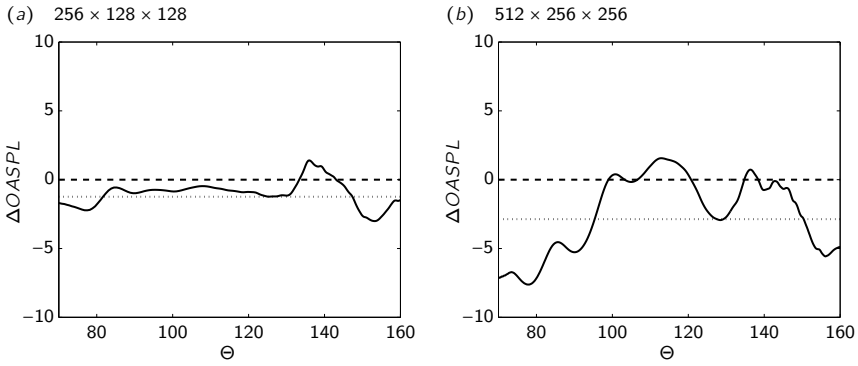

Figure 6.11: Reduction of the OASPL as a function of the observation angle with respect to the upstream direction. Reduction due to the optimized nozzle (———). Mean reduction averaged over all observation angles (· · · · · · · ·).

142.53 dB). Again, the increased OASPL has its origin in the shock associated noise components (cf. Fig. 6.9(d)) and may be explained due to the suppressed helical mode.

The reduction of the OASPL as a function of the observation angle is more clearly visible in Fig. 6.11 where the difference of the noise level of the controlled an uncontrolled nozzle are presented. Positive values indicate an increase of the OASPL due to the optimized nozzle and negative values a reduction. In addition to that, a dotted line measures the mean reduction averaged over all observation angles (in the range from $75° \leq \Theta \leq 160°$). The average reduction for the low resolution case is 1.24 dB. In the high resolution

res.		min $\Theta<90°$	min $\Theta>90°$	min $75°\leq\Theta\leq160°$	max $75°\leq\Theta\leq160°$	mean $75°\leq\Theta\leq160°$
low	ΔOASPL	-2.26	-3.01	-3.01	1.40	-1.24
	Θ	76.81°	153.10°	153.10°	135.74°	[.]
high	ΔOASPL	-7.62	-5.57	-7.62	1.56	-2.87
	Θ	77.47°	156.15°	77.47°	112.45°	[.]

Table 6.1: Reduction of the OASPL in different observation directions. Local and global minima and maxima with the corresponding directions presented. Negative differences represent a noise reduction. Positive values a noise amplification.

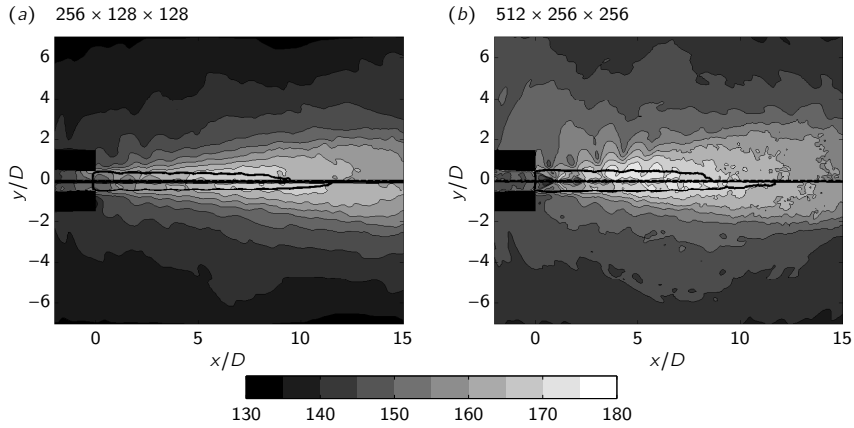

Figure 6.12: OASPL in a two-dimensional x-y plane. Figure is split in two parts, separated by dashed line; Top half: no optimization (solid nozzle); Bottom half: optimized nozzle (porous). Solid line: $M = 1$.

case, the average reduction measures 2.87 dB.

A summary over the local minima and maxima of the noise reduction can be found in Tab. 6.1. In both, the low and high resolution case, the minima in the up- and downstream direction are measured at similar observation angles (upstream: $\Theta \approx 77°$; downstream: $\Theta \approx 155°$). In the low resolution case, the global minimum can be found in the downstream direction whereas in the high resolution case, the global minimum is in the upstream direction.

In Fig. 6.12 the OASPL is presented in the two-dimensional x-y plane. The figure is split in two parts. In the top half the uncontrolled case is presented with the solid nozzle. In the bottom half, the solution of the optimized porous nozzle is presented. The main differences can be seen in the high resolution case (b). Especially in the upstream direction of the uncontrolled case, strong acoustic pressure fluctuations are visible. These loud areas, where the screech tone is dominant, are minimized in the controlled case (bottom half of panel (b)).

In the acoustic near field of the uncontrolled jet, pressure fluctuations in the shape of lobes are visible. They represent the standing wave pattern, responsible for the screech feedback closure. These lobes are still visible in the controlled jet but with reduced amplitude. Especially at the nozzle lip exit, where the standing wave forms an anti-node, the pressure fluctuations are hardy visible in the controlled case. In addition to that, a solid line

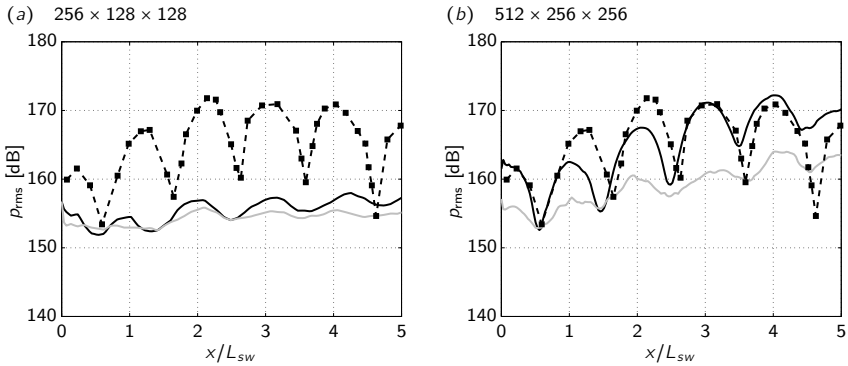

Figure 6.13: OASPL along a measurement line slightly above the shear-layer. No optimization (———); Optimization (———); Experimental data: ■ from Panda et al. [1997] for a $M_j = 1.51$ axisymmetric jet. Scaled with the standing wave spacing L_{sw}.

represents the iso-contour of the mean velocity for $M = 1$. Inside this line, the flow is supersonic and subsonic elsewhere. The extension of the supersonic area of the controlled jet is about two shock cells longer in the downstream direction than the one of the uncontrolled jet. Again, the reason for this is the suppressed screech mode (helical) in the controlled case (see next section). The differences of the OASPL in this two-dimensional view is hardly visible for the low resolution jet (a).

To get a deeper insight in the differences of the standing wave pattern for the controlled and uncontrolled case, the RMS pressure fluctuations (OASPL) are measured along the shear layer boundary. To avoid an interaction with the turbulent hydrodynamic pressure fluctuations, the data of Fig. 6.13 is extracted from a line parallel to the growing shear layer with an inclination angle of 5.7° (same as in Panda et al. [1997]). In the high resolution case (b) one can clearly identify the standing wave pattern of the uncontrolled case. The numerical data matches quite well the experimental data of Panda et al. [1997] for a $M_j = 1.51$ axisymmetric jet. In the controlled case (gray line), the standing wave pattern is drastically reduced. A difference of more than 10 dB to the uncontrolled jet can be observed at the locations of the anti-nodes. At the nodes of the standing wave (here at $x/L_{sw} = 0.5, 1.5, 2.5, \ldots$) the pressure fluctuation of the controlled and uncontrolled jet coincide only within the first wavelength ($0 \leq x/L_{sw} \leq 2$). Further downstream, the noise level at the nodes of the controlled jet is reduced (about 5 dB at $x = 5.5L_{sw}$).

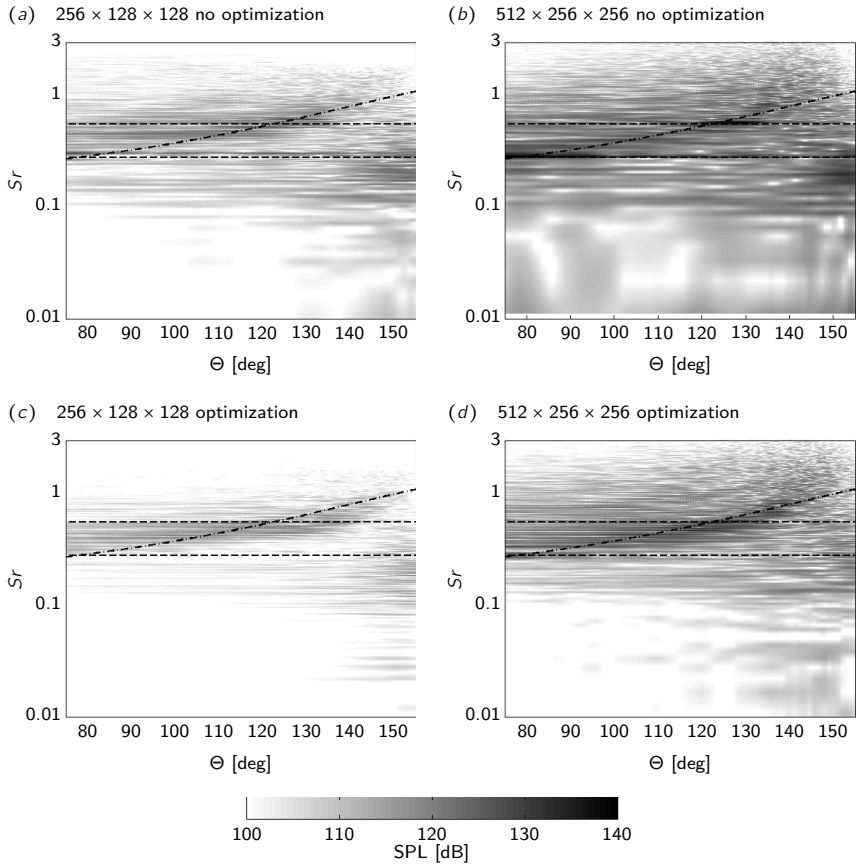

Figure 6.14: Colormap of the SPL as a function of the observation angle Θ with respect to the upstream direction and the Strouhal number Sr. Dashed lines (- - - - - -) correspond to the fundamental screech frequency and its first subharmonic based on the theory of Massey [1997]. Dash dotted line (-·-·-·-·-) corresponds to the central frequency of shock associated noise based on the theory of Tam [1987] with $M_c = 0.5$ (cf. also Eq. (1.12)).

The reduced standing wave pattern for the controlled jet is a good evidence for an efficient suppression of the screech generation mechanism. This trend is also visible in the low resolution case (a) yet with a reduced amplitude and strong discrepancies to the experimental data.

The spectra of the controlled an uncontrolled jet are presented in Fig. 6.9

for three different observation locations. A similar picture can be found in Fig. 6.14 yet in a two-dimensional color plot including a wide range of observation directions. The x-axis covers the observation angle whereas the y-axis is a function of the frequency. In the right column the high resolution case is presented with the uncontrolled jet in panel (b) and the controlled jet in panel (d). One can clearly identify the fundamental screech frequency and its first subharmonic in the uncontrolled spectra (b). To validate the screech frequency, a dashed line marks the theoretical screech frequency as predicted by Massey [1997]. A good comparison between the numerical and analytical data is visible. In this view one can see that the fundamental screech tone is dominant in the upstream direction up to an observation angle of $\Theta = 100°$. In this upstream range, the first subharmonic screech tone is not visible. It starts to appear in the downstream direction for observation angles in the range of $115° \leq \Theta \leq 135°$. This is the range, where the predicted peak shock-associated noise level crosses the first subharmonic screech frequency. Shock-associated noise is affected by a Doppler shift by which the peak noise level is shifted to higher frequencies when measuring further downstream. This effect is indicated by a dash dotted line and based on the theory of Tam [1987] with a convective Mach number of $M_c = 0.5$ (cf. also Eq. (1.12)). That the peak value of the shock-associated noise is following the theoretical prediction is especially visible in the controlled case (d). Here, the broadband shock-associated noise seems to be the dominant noise source within the investigated observation directions. In addition to that, one can see that the mixing noise of low frequency is drastically reduced, especially in the upstream direction and, of course that all discrete screech tones are missing in the spectrum. All these effects can also be identified in the low resolution case (a and c) but with a reduced amplitude.

In Fig. 6.15 the history of the pressure fluctuations as a function of time and observation angle is presented. The time axis is scaled with the fundamental screech frequency based on the theory of Massey [1997] and starting from an arbitrary point at the end of the simulation. In the high resolution case, the harmonic fluctuations due to the screech tone are clearly visible in the upstream direction (b). Further downstream ($\Theta \approx 135°$), the amplitude of the screech induced pressure fluctuations are decreasing and the broadband components of the shock-associated noise become the dominant noise source. In the controlled case (d), the amplitudes in the upstream direction are drastically reduced and the harmonic pattern is missing. The upstream direction is now governed by broadband noise components related to shock-associated noise. Also in the far downstream direction, the amplitudes of the pressure fluctuations are reduced and seem to exhibit more broadband characteristics

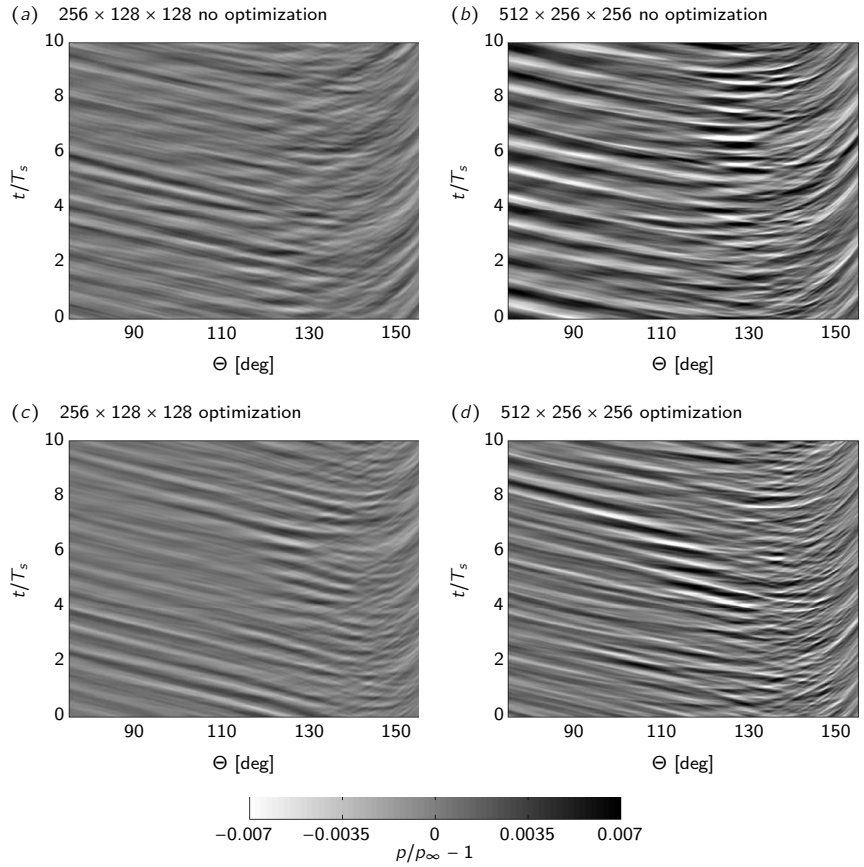

Figure 6.15: History of the pressure fluctuations as a function of time and observation angle with respect to the upstream direction. Time scaled with the fundament screech frequency based on the theory of Massey [1997] and starting from an arbitrary point at the end of the simulation.

than in the uncontrolled jet. Again, these effects are also visible in the low resolution case, but with reduced amplitude.

In the following section we will focus on the influence of the optimized nozzle to the flow field. Some of these effects were already mentioned in the present section.

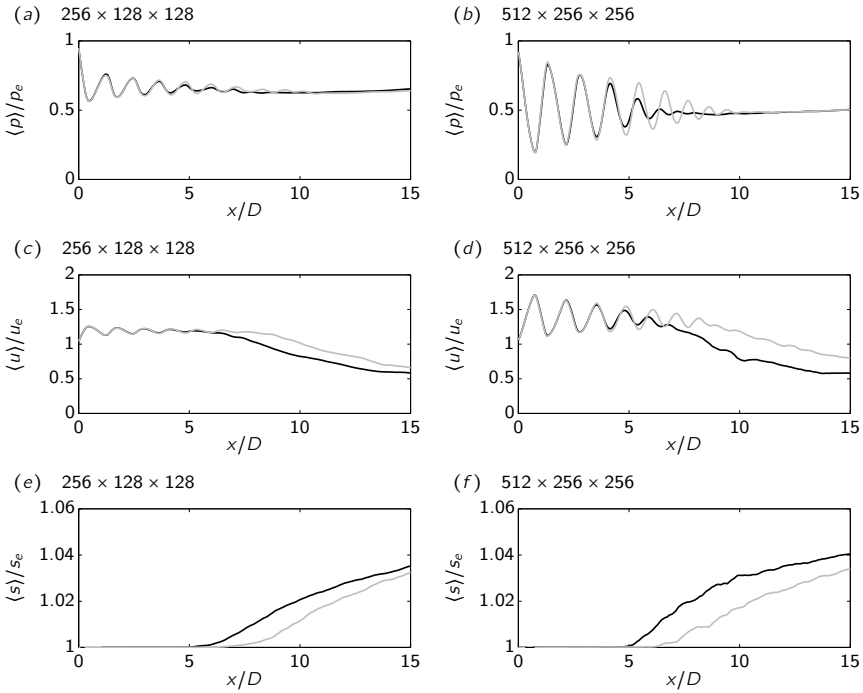

Figure 6.16: Mean values of the pressure (a) and (b), the stream-wise velocity u (c) and (d) and the entropy (e) and (f) along the centerline of the jet. No optimization (———); optimized porous material (———).

6.4 Influence on the flow field

Suppressing the screech tone of a supersonic jet has a fundamental effect on the flow characteristics of the jet. During screech, the jet undergoes strong oscillations, like the helical mode as in the present investigation. These oscillations are responsible for an enhanced mixing of the jet. The screech source location and the point, where the jet starts to undergo strong oscillations, are linked and located between the third to fifth shock cell. From this point on, the potential core of the screeching jet is reduced drastically compared to a jet with screech suppression. These effects can be clearly seen in the mean flow fields of the jet.

In Fig. 6.16 the mean values of the pressure p, the stream-wise velocity u

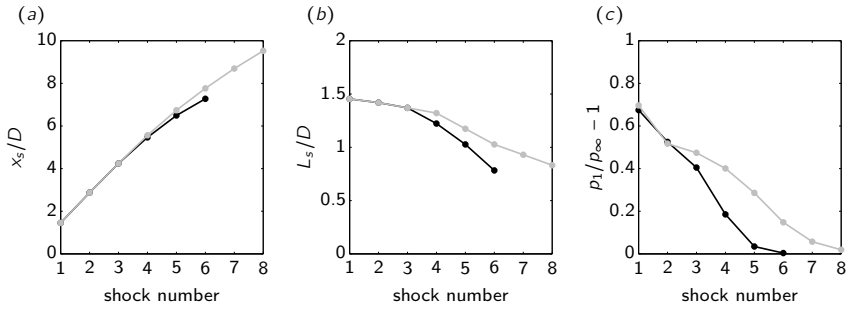

Figure 6.17: Characteristics of the shock cells for the high resolution case ($512 \times 256 \times 256$). No optimization (———); optimized porous material (———). (a) Position of the shock cell. (b) Length of the shock cell. (c) Strength of the shock cell (p_1 is the pressure upstream the shock).

and the entropy s are presented along the centerline of the jet. The values of the optimized nozzle with porous media (gray curve) are compared to the solid nozzle without optimization (black curve). Both, the low and high resolution case are presented whereas the high resolution case is presented in the right column. Each of the values are scaled with its nozzle exit conditions and the abscissa is scaled with the nozzle diameter. In panel (b) the mean pressure is visualized. One can clearly see the shock cell pattern in the jet core for both, the solid and the porous nozzle. Within the first three shock cells ($0 \leq x/D \leq 4.14$), the pressure distribution of the controlled and the uncontrolled jet are matching each other up to slight deviation. Further downstream, beginning with the third shock cell, deviations between both jets become visible. The shock cell pattern of the screeching jet (no porous medium) starts to dissappear and can no more be detected past the sixth shock cell (around $x = 7.2D$). In the optimized case, a lager number of shock cells is preserved. Up to eight shock cells can be detected in the jet plume. In addition to that, the shock cell spacing past the third shock cell is larger for the optimized case.

This is also visible in Fig. 6.17(a) and (b), where the location of the shock and the shock cell length is presented as a function of the shock cell number. One can see that the position of the shock cell for the optimized jet is shifted further downstream than for the screeching jet. In panel (b) the shock cell length of each shock cell is presented. In both cases the shock cell length is decreasing with the shock cell number. For the screeching jet, the shock cell length starts to decrease more rapidly beginning with the third shock cell.

In panel (c) the shock cell strength is presented as a function of the shock number. It measures the pressure ratio between the pressure upstream the shock and the ambient pressure. The shock strength is decreasing monotonically with the downstream direction. A deviation between the screeching and the optimized jet is already visible in the third shock cell. Here, the shock amplitude of the screeching jet is reduced by 15 % compared to the optimized jet. The shock strength drops to zero in the sixth chock cell for the screeching jet and in the eighth shock cell for the optimized jet.

The shock cells are also visible in the velocity. In Fig. 6.16(d) the mean stream-wise velocity u is presented. The velocity is scaled with the nozzle exit velocity which is for the present convergent nozzle $M_d = 1$. Hence, values larger than one mark the supersonic regime. It is clearly visible that the supersonic region of the screeching jet is smaller than for the optimized jet. In the screeching case the supersonic region ends at $x = 8.5D$ and for the optimized jet at $x = 12.0D$. The slope of the decay of the velocity in the subsonic region is comparable for both jets. Finally, in panel (f) of the same figure, the mean value of the entropy is presented. The sudden increase of the entropy marks the end of the potential core, where the surrounding mixing layers merge. Again, the length of the potential core of the screeching jet is smaller than the one of the controlled jet. For the screeching jet, the length of the potential core is $x = 5D$ and for the optimized jet $x = 6.3D$.

In the left column of 6.16 the corresponding mean values for the low resolution case are presented. The optimized and the non optimized jet show the same behavior as in the high resolution case, yet with different amplitudes. The shock cell pattern is less dominant as in the high resolution case.

In Fig. 6.18 the RMS values of the pressure, the stream-wise velocity u and the entropy s are presented along the centerline of the jet. Again, strong deviations between the screeching jet and the optimized jet can be seen. In panel (b), the pressure fluctuations are presented. In both cases, the values are modulated with the shock cell pattern which is decaying faster past the third shock cell for the screeching jet than for the optimized jet. In panel (d) the RMS velocity fluctuations are presented. They measure the turbulent fluctuations in the jet. In addition to the two current numerical results, other numerical (Bogey [2000], Cavalieri et al. [2011]) and experimental data (Bridges [2006], Jordan et al. [2002], Raman et al. [1989]) are included for validation purposes (all based on subsonic axisymmetric jets). One can see, that the RMS values of the screeching jet are in good agreement to the numerical and experimental data. In the optimized case, the RMS value of the velocity is under predicted in the range of $5 \leq x/D \leq 10$. Further downstream, the current computation of the optimized nozzle matches again the external

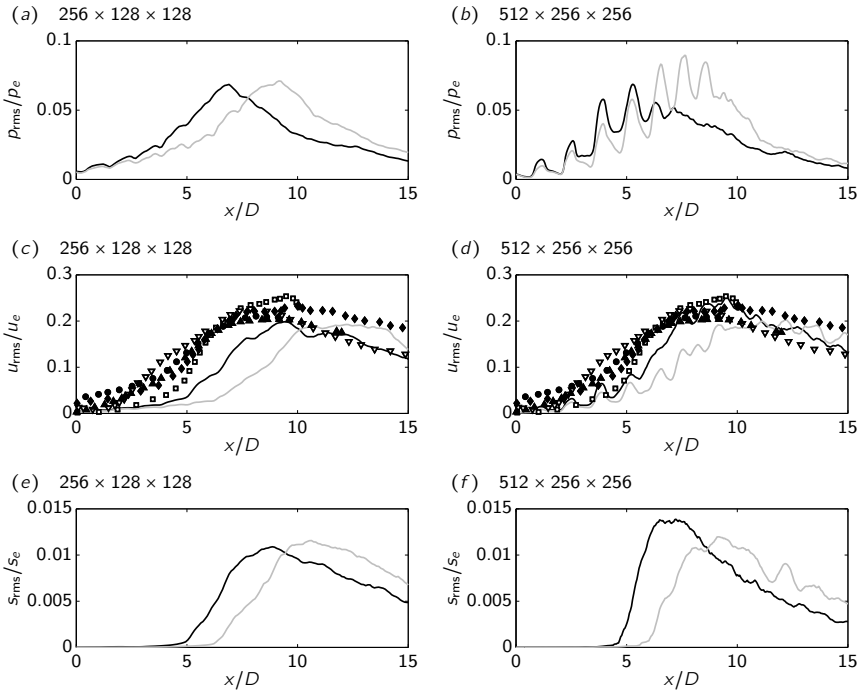

Figure 6.18: RMS values of the pressure fluctuations (*a*) and (*b*), the stream-wise velocity fluctuations u' (*c*) and (*d*) and the entropy fluctuations (*e*) and (*f*) along the centerline of the jet. No optimization (———); optimized porous material (———). For (*c*) and (*d*): Experimental data: ▲: Raman et al. [1989]; ●: Jordan et al. [2002]; ◆: Bridges [2006]. Numerical data: □; Bogey [2000]; ▽: Cavalieri et al. [2011].

data. The delayed increase of the turbulence values of the optimized jet is due to the suppression of the helical mode. In panel (f) the entropy fluctuations are presented. As for the mean value of the entropy in Fig. 6.16(f), the RMS value can be used to estimate the length of the potential core. The core length of the optimized jet is about $2D$ longer than the one of the screeching jet.

The RMS values of the low resolution case behave in a similar way as the high resolution case. Their amplitudes are in general smaller than for the high resolution jet.

In Fig. 6.19 the RMS value of the Lighthill sources ($\frac{\partial^2}{\partial x_i \partial x_j} T_{ij}$) are com-

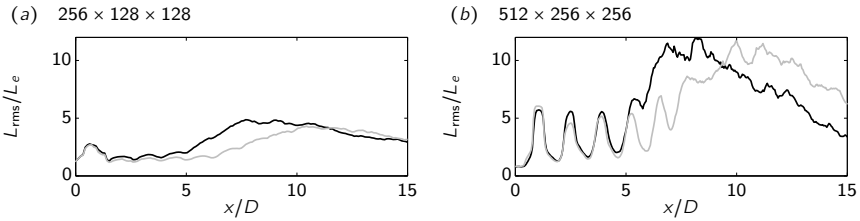

Figure 6.19: RMS value of the fluctuations of the Lighthill source term along the centerline of the jet. No optimization (———); optimized porous material (———).

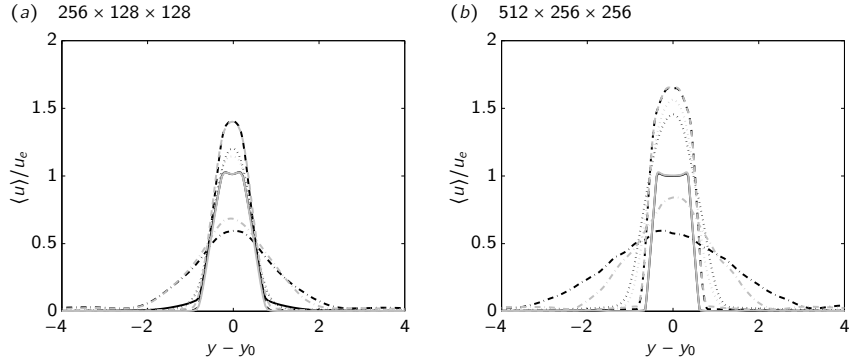

Figure 6.20: Mean velocity profiles of the jet measures at four different locations in the downstream direction. Black curve: no optimization; Gray curve: optimized porous material: Measurement location: $x = 0$ (———), $x = 0.6D$ (- - - - - -), $x = 5D$ (· · · · · · · ·), $x = 14D$ (-·-·-·-·-).

pared. They are measured along the centerline of the jet and give an indication of the location and strength of the acoustic source. In the high resolution case in panel (b) one can clearly identify that the location of the acoustic source for the optimized jet is shifted to the downstream direction (about $2D$ further downstream). The peak source amplitudes of both, the screeching and the optimized jet are in the same range. The same effects can be observed for the low resolution case (a), but with a reduced amplitude.

The differences between the optimized and screeching jet are also visible in the transverse y-direction. In Fig. 6.20 the mean velocity profiles are compared and measured at four different downstream directions ($x/D = 0$, 0.6, 5 and 14). At the first two measurement locations, at the nozzle exit

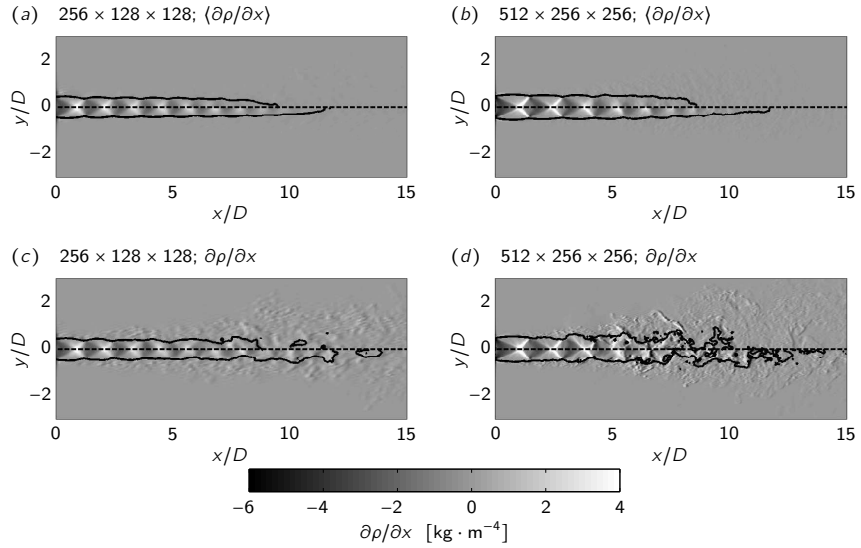

Figure 6.21: Pseudo-Schlieren in the x-direction of a two-dimensional slice. Slice divided in two parts separated by dashed line (- - - - - -). Top part: no optimization; Lower part: optimized porous material. Solid Line (———): $M = 1$.

($x/D = 0$) and slightly downstream ($x/D = 0.6$) the shape and amplitude of the optimized and screeching jet match each other. Further downstream, at $x/D = 5$ and $x/D = 14$, distinct deviations between both jets become visible. In the screeching case, the amplitudes of the velocity profiles are reduced and the width of the profile is increased compared to the optimized case. The increased mixing of the screeching jet with its helical mode is responsible for the early widening of the velocity profile. This effect is especially visible at $x/D = 14$ for the high resolution case (b). Again, the same trend is visible in the low resolution case (a) but less clearly.

Finally, to summarize the effects of the optimized porous media on the flow field of the jet, two-dimensional slices of the jet are presented in Fig. 6.21. Visualized are the pseudo-Schlieren in the x-direction ($\partial\rho/\partial x$) of the averaged ((a) and (b)) and the instantaneous flow field ((c) and (d)) for both, the low and high resolution. Each panel is divided in two parts. The top half of the figure shows the non optimized (screeching) jet whereas the lower part shows the optimized case. In addition to the pseudo-Schlieren, a solid line marks the sonic region ($M = 1$). Inside this line the flow is supersonic and

subsonic elsewhere. Past the nozzle exit, one can see that the sonic line follows the shape of the barrel shock (visible in the time averaged panels). This pattern is repeated in the downstream direction at least for the first three shock cells. In the time averaged panels, the sonic line marks the main difference in the flow field: the reduced potential core of the screeching jet. As we have already seen in a previous figure, the supersonic region of the screeching jet ends an $x = 8.5D$ whereas it is extended up to $x = 12D$ for the optimized jet (suppressed helical mode). One can also identify a larger number of shock cells in the jet core for the optimized jet (8 instead of 6). In the instantaneous view of the high resolution case (d) it is visible that the screeching jet is spreading faster than the controlled jet. Due to the increased mixing, caused by the helical mode, turbulent fluctuations are visible further apart from the centerline of the jet as in the controlled case.

In the last figure of this section in Fig. 6.22 the instantaneous pressure fluctuations are presented for the optimized and screeching jet. This figure highlights the instantaneous acoustic field of the jet. As the previous figure, it is devided in two parts. The top half shows the jet without optimization (screeching jet) and the bottom half with optimized porous material (screech suppression). One can clearly see that the screech tone is minimized in the optimized case, especially in the high resolution case of panel (b). In the upstream direction the frequency of the screech tone is reduced and governed by shock-associated noise. The dminant frequency of the shock-associated noise in the upstream direction is equal to the screech frequency (at lest for $\Theta = 0$). Hence, the wavelength of the screech tone can still be identified in the controlled case, yet with a reduced amplitude and superimposed by broadband components. Again, the effect can be also identified for the low resolution jet in panel (a) with a reduced amplidtude.

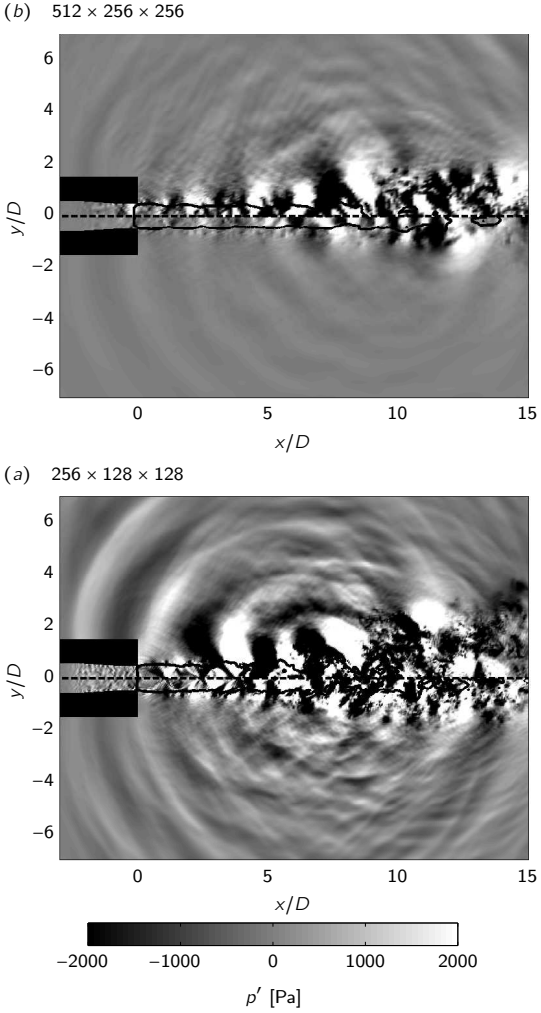

Figure 6.22: Pressure fluctuation of a two-dimensional slice. Slice divided in two parts separated by dashed line (- - - - - -). Top part: no optimization; Lower part: optimized porous material. Solid Line (———): $M = 1$.

7

Conclusion and Outlook

Supersonic jet flows and their emanated noise are governed by complex physical phenomena. On the one hand, the periodic shock cell pattern in the jet core, the shock–diamonds, and on the other hand, the propagation of the aeroacoustic noise including the complex geometry of the jet nozzle, to close the screech feedback loop, make high demands on the numerical method. To this end, a high order scheme, to solve the compressible Navier–Stokes equation is implemented in the present investigation together with a high spatial resolution. Up to now, the present work represents the largest computation on axisymmetric supersonic jet noise ever performed. In addition to this, the compressible Navier–Stokes equations were extended by a porous medium to include both, a solid body of arbitrarily complexity and a porous material to control the fluid flow.

The implemented numerical method shows the ability to solve the intended problem with high accuracy. A perfect agreement of the computed aeroacoustic noise to experimental and analytical data can be shown. Especially the computed frequency and amplitude of the screech tone, which is excited by a series of coupled physical phenomena, can be captured with high precision. It could be confirmed that the cessation of screech is a reason of the reduced receptivity due to the "barrel"-shock as proposed by Raman [1996]. In addition to that, the presence of the helical screech mode, which is the dominant mode of a $M_j = 1.55$ jet, could be identified.

Not only the acoustic properties matched the theoretical prediction but also the noise generating supersonic jet flow. Shock cell spacing and amplitude

and the number of shock cells computed by the numerical method are in good agreement to experimental observations. Statistical data concerning the turbulent Reynolds stresses and pressure fluctuations found in the literature could be reproduced by the present work. The results show that the method presented in this thesis is not only capable to compute aeroacoustic noise including complex geometries with high accuracy but also in a efficient way.

In the second part of the thesis a novel method is derived to obtain an optimized porous material to minimize supersonic jet noise. The method is based on the adjoints of the porous and compressible Navier–Stokes equations which are derived in a continuous manner without any further simplifications. Evaluating the direct and adjoint equations subsequently, one can obtain the gradient information of the objective function with respect to the control. In the present study, the control is the space dependent permeability of the porous medium and the objective is to reduce supersonic jet noise with the focus on jet screech. Repeating the evaluation of the gradient followed by an update of the control in an iterative loop, the optimal control (porous medium) can be obtained. Only three optimization loops were necessary to reduce the gradient by three orders of magnitude. As a result, a complex three-dimensional structure of a porous medium is created and placed at the nozzle exit. It acts as a sound absorbing material to influence the receptivity at the nozzle lip and finally to eliminate the screech sustaining feedback loop. A reduction of up to 20 dB of the screech tone could be observed which corresponds to a complete elimination of this tone from the measured spectrum. In addition to that, mixing and broadband noise could be reduced as well in the up- and downstream direction. Especially in the downstream direction, the mixing noise is drastically reduced. The reason for this lies in the elimination of the screech tone and the corresponding elimination of the helical mode. The latter one is responsible for an increased mixing of the jet including mixing noise. Hence, its suppression leads to a reduction of the mixing noise which is emanated mainly in the downstream direction. Only in a small area slightly tilted in the downstream direction, broadband shock associated noise of the controlled jet is louder than of the one without porous medium. Again, this phenomenon can be explained with the suppression of the helical mode. As the elimination of the screech mode sustains the periodic shock cell pattern in the downstream direction of the jet, additional sources for shock-associated noise are created. Outside this narrow observation sector, an overall noise reduction of almost 3 dB can be observed. The present method confirms the theoretical background on supersonic jet screech, especially the role of the feedback loop.

The work on adjoint based control with porous media, as presented in this

thesis, is the first to apply it to an aeroacoustic problem and can be considered as a "proof-of-concept". An impressive performance of the optimization algorithm could be shown, where the intended problem could be solved with comparable little computational effort.

The remaining question of the present investigation is, how to obtain a "real" porous material from the optimized permeability. There is no direct link between permeability and existing porous material. Even if the relation between permeability and the design of the material would be known, it may be a challenging manufacturing process. Especially if solid obstacles would not be connected to each other and hover in the material matrix. Hence, a post-processing of the optimized permeability, to obtain a real world material is necessary, and more work has to be carried out to interprete the meaning of the optimized permeability with respect to its producibility.

Once a real porous material is found, its performance to eliminate screech could be validated by an experimental setup. The supersonic jets investigated in the present thesis are based on a Reynolds number of $Re_D = 5000$. Assuming air under standard conditions for the fluid flow, the diameter of the jet would be in the order of a human hair (0.1mm). For an experimental investigation including a porous material of this size, the diameter of the jet will be too small. Hence, a computation based on a higher Reynolds number in the order of $Re \approx 100\,000$ will be necessary. To resolve the small scales, a total of about 10 billion grid points will be necessary. This is not a restriction for the next generation high performance computers with a peak performance of several PetaFlop/s (10.3PetaFlop/s, as of Nov. 2011, "K computer"). Based on that Reynolds number, a comparison to experimental setups of jets with a diameter of several centimeters will be possible.

The novel method of adjoint based optimization, in combination with porous media, are a promising and efficient method to minimize supersonic jet noise. Beyond the aeroacoustic field, this type of flow optimization may find application in a variety of disciplines and configurations where the optimization of any objective by means of a modification of the geometry and/or material is desired.

A

Compressible Navier–Stokes equations

In the following, the compressible Navier–Stokes equations are given in a characteristic formulation based on non Cartesian coordinates. In the present investigation, all derivatives are computed in the computational domain with respect to the contravariant basis vectors ξ, η and ζ. If the grid is time dependent, an additional time variable τ will arise. The physical variables are described in the x, y and z domain with the time t. To compute a derivative in the physical domain, a grid transformation has to be applied. The contravariant basis vectors are dependent on the physical domain:

$$\begin{aligned} \xi &= \xi(x,y,z,t) \\ \eta &= \eta(x,y,z,t) \\ \zeta &= \zeta(x,y,z,t) \\ \tau &= \tau(t) \end{aligned}$$

A derivative with respect to the physical space has to follow the chain rule:

$$\begin{aligned} \frac{\partial}{\partial x_i} &= \frac{\partial \xi}{\partial x_i}\frac{\partial}{\partial \xi} + \frac{\partial \eta}{\partial x_i}\frac{\partial}{\partial \eta} + \frac{\partial \zeta}{\partial x_i}\frac{\partial}{\partial \zeta} \\ &= \frac{\partial \xi^l}{\partial x_i}\frac{\partial}{\partial \xi^l} \\ &= \xi^l_{,i}\frac{\partial}{\partial \xi^l} \end{aligned}$$

with the shorthand $\xi^l_{,i} := \frac{\partial \xi^l}{\partial x_i}$.

Transformed direct Navier–Stokes equations The direct Navier–Stokes equations can be rewritten for curvilinear grids:

$$\left(\frac{\partial p}{\partial t} + u_i \xi^l_{,i} \frac{\partial p}{\partial \xi^l}\right) + \gamma p \xi^l_{,i} \frac{\partial u_i}{\partial \xi^l} = \frac{p}{C_v}\left(\frac{\partial s}{\partial t} + u_i \xi^l_{,i} \frac{\partial s}{\partial \xi^l}\right) \tag{A.1}$$

$$\left(\frac{\partial u_i}{\partial t} + u_j \xi^l_{,i} \frac{\partial u_i}{\partial \xi^l}\right) + \frac{1}{\rho} \xi^l_{,i} \frac{\partial p}{\partial \xi^l} = \frac{1}{\rho} \xi^l_{,j} \frac{\partial \tau_{ij}}{\partial \xi^l} \tag{A.2}$$

$$\left(\frac{\partial s}{\partial t} + u_i \xi^l_{,i} \frac{\partial s}{\partial \xi^l}\right) = \frac{1}{\rho T}\left(-\xi^l_{,i} \frac{\partial}{\partial \xi^l}(-\lambda \xi^l_{,i} \frac{\partial T}{\partial \xi^l}) + \Phi\right) \tag{A.3}$$

Introducing the contravariant velocity components $u^l = \xi^l_{,i} u_i$ and the abbreviation $g^{lm} := \xi^l_{,i} \xi^m_{,i}$, the Navier–Stokes equations can be rewritten for curvilinear grids. A detailed derivation of these equations can be found in Sesterhenn [2000].

$$\frac{\partial p}{\partial t} = -\sum_{k=1}^{3} \frac{\rho c}{2}\left(\Xi^k_+ + \Xi^k_-\right) + \frac{p}{C_v}\left(\frac{\partial s}{\partial t} + \sum_{k=1}^{3} \Xi^k_s\right) \tag{A.4a}$$

$$\begin{aligned}\frac{\partial u^1}{\partial t} = &-\frac{\sqrt{g^{11}}}{2}\left(\Xi^1_+ - \Xi^1_-\right) - \Xi^2_1 - \Xi^3_1 - \frac{\xi^1_{,l}\xi^2_{,l}}{2\sqrt{g^{22}}}\left(\Xi^2_+ - \Xi^2_-\right) \\ &-\frac{\xi^1_{,l}\xi^3_{,l}}{2\sqrt{g^{33}}}\left(\Xi^3_+ - \Xi^3_-\right) + \frac{\xi^1_{,i}\xi^l_{,j}}{\rho}\frac{\partial \tau_{ij}}{\partial \xi^l}\end{aligned} \tag{A.4b}$$

$$\begin{aligned}\frac{\partial u^2}{\partial t} = &-\Xi^1_2 - \frac{\sqrt{g^{22}}}{2}\left(\Xi^2_+ - \Xi^2_-\right) - \Xi^3_2 - \frac{\xi^2_{,l}\xi^1_{,l}}{2\sqrt{g^{11}}}\left(\Xi^2_+ - \Xi^2_-\right) \\ &-\frac{\xi^2_{,l}\xi^3_{,l}}{2\sqrt{g^{33}}}\left(\Xi^3_+ - \Xi^3_-\right) + \frac{\xi^2_{,i}\xi^l_{,j}}{\rho}\frac{\partial \tau_{ij}}{\partial \xi^l}\end{aligned} \tag{A.4c}$$

$$\begin{aligned}\frac{\partial u^3}{\partial t} = &-\Xi^1_3 - \Xi^2_3 - \frac{\sqrt{g^{33}}}{2}\left(\Xi^3_+ - \Xi^3_-\right) - \frac{\xi^3_{,l}\xi^1_{,l}}{2\sqrt{g^{11}}}\left(\Xi^1_+ - \Xi^1_-\right) \\ &-\frac{\xi^3_{,l}\xi^2_{,l}}{2\sqrt{g^{22}}}\left(\Xi^2_+ - \Xi^2_-\right) + \frac{\xi^3_{,i}\xi^l_{,j}}{\rho}\frac{\partial \tau_{ij}}{\partial \xi^l}\end{aligned} \tag{A.4d}$$

$$\frac{\partial s}{\partial t} = -\left(\Xi^1_s + \Xi^2_s + \Xi^3_s\right) + \frac{1}{\rho T}\left(-\xi^l_{,i}\frac{\partial}{\partial \xi^l}\left(-\lambda \xi^l_{,i}\frac{\partial T}{\partial \xi^l}\right) + \Phi\right) \tag{A.4e}$$

with the following abbreviations:

$$\Xi_{\pm}^{k} := \left(u^{(k)} \pm c\sqrt{g^{(kk)}}\right)\left(\frac{1}{\rho c}\frac{\partial p}{\partial \xi^{(k)}} \pm \frac{\xi_{,i}^{(k)}}{\sqrt{g^{(kk)}}}\frac{\partial u_i}{\partial \xi^{(k)}}\right) \tag{A.5}$$

$$\Xi_{s}^{k} := u^{(k)}\frac{\partial s}{\partial \xi^{(k)}} \tag{A.6}$$

$$\Xi_{l}^{k} := u^{(k)}\left(\xi_{,i}^{l}\frac{\partial u_i}{\partial \xi^{(k)}} - \frac{\xi_{,m}^{k}\xi^{l,m}}{g^{(kk)}}\xi_{,i}^{k}\frac{\partial u_i}{\partial \xi^{(k)}}\right) \tag{A.7}$$

B

Linearized Navier–Stokes equations

Based on the nonlinear, porous and compressible Navier–Stokes equations of Sec. § 3.1, the linearized Navier–Stokes equations can be written in matrix formulation. To obtain the adjoints of the direct equations, we need to include all information to close the system of equations. Hence, besides the five partial differential equations, three additional algebraic equations to close system need to be included. To this end, the dimension of the system is eight with the following state vector of the fluctuations:

$$\boldsymbol{\delta q} = (\delta p, \delta u, \delta v, \delta w, \delta s, \delta \rho, \delta T, \delta \mu)^T .$$

The first five entries correspond to the five PDE's of the Navier–Stokes equations for the pressure δp, the three velocity components δu, δv, δw and the entropy δs. The latter three entries correspond to the fluctuations of the density $\delta \rho$, the temperature δT and the viscosity $\delta \mu$. Note, that the viscosity is only a function of the temperature (see Sutherland's law of Eq. (2.6)) and its variational formulation can be given as:

$$\delta \mu = \frac{\mathrm{d}\mu(T)}{\mathrm{d}T} \delta T$$

Finally, the linearized, porous and compressible Navier–Stokes equations can be written as:

$$\boldsymbol{B} \frac{\partial \boldsymbol{\delta q}}{\partial t} + \boldsymbol{A_k} \frac{\partial \boldsymbol{\delta q}}{\partial x_k} + \boldsymbol{D_{ij}} \frac{\partial^2 \boldsymbol{\delta q}}{\partial x_i \partial x_j} + \boldsymbol{C} \boldsymbol{\delta q} = 0 \tag{B.1}$$

with the matrices:

$$
\boldsymbol{A_1} = \begin{bmatrix}
u & \gamma p & 0 & 0 & -\frac{pu}{C_v} & 0 & 0 & 0 \\
\frac{1}{\rho} & u - \frac{4}{3}\frac{\frac{\partial \mu}{\partial x}}{\rho} & -\frac{\frac{\partial \mu}{\partial y}}{\rho} & -\frac{\frac{\partial \mu}{\partial z}}{\rho} & 0 & 0 & 0 & -\frac{\tau_{11}}{\mu\rho} \\
0 & \frac{2}{3}\frac{\frac{\partial \mu}{\partial y}}{\rho} & u - \frac{\frac{\partial \mu}{\partial x}}{\rho} & 0 & 0 & 0 & 0 & -\frac{\tau_{12}}{\mu\rho} \\
0 & \frac{2}{3}\frac{\frac{\partial \mu}{\partial z}}{\rho} & 0 & u - \frac{\frac{\partial \mu}{\partial x}}{\rho} & 0 & 0 & 0 & -\frac{\tau_{13}}{\mu\rho} \\
0 & -2\frac{\tau_{11}}{\rho T} & -2\frac{\tau_{12}}{\rho T} & -2\frac{\tau_{13}}{\rho T} & u & 0 & -\frac{\frac{\partial \lambda}{\partial x}}{\rho T} & -\frac{C_p \frac{\partial T}{\partial x}}{\rho T \,\mathrm{Pr}} \\
0 & 0 & 0 & 0 & 0 & 0 & 0 & 0 \\
0 & 0 & 0 & 0 & 0 & 0 & 0 & 0 \\
0 & 0 & 0 & 0 & 0 & 0 & 0 & 0
\end{bmatrix}
$$

$$
\boldsymbol{A_2} = \begin{bmatrix}
v & 0 & \gamma p & 0 & -\frac{pv}{C_v} & 0 & 0 & 0 \\
0 & v - \frac{\frac{\partial \mu}{\partial y}}{\rho} & \frac{2}{3}\frac{\frac{\partial \mu}{\partial x}}{\rho} & 0 & 0 & 0 & 0 & -\frac{\tau_{12}}{\mu\rho} \\
\frac{1}{\rho} & -\frac{\frac{\partial \mu}{\partial x}}{\rho} & v - \frac{4}{3}\frac{\frac{\partial \mu}{\partial y}}{\rho} & -\frac{\frac{\partial \mu}{\partial z}}{\rho} & 0 & 0 & 0 & -\frac{\tau_{22}}{\mu\rho} \\
0 & 0 & \frac{2}{3}\frac{\frac{\partial \mu}{\partial z}}{\rho} & v - \frac{\frac{\partial \mu}{\partial y}}{\rho} & 0 & 0 & 0 & -\frac{\tau_{23}}{\mu\rho} \\
0 & -2\frac{\tau_{12}}{\rho T} & -2\frac{\tau_{22}}{\rho T} & -2\frac{\tau_{23}}{\rho T} & v & 0 & -\frac{\frac{\partial \lambda}{\partial y}}{\rho T} & -\frac{C_p \frac{\partial T}{\partial y}}{\rho T \,\mathrm{Pr}} \\
0 & 0 & 0 & 0 & 0 & 0 & 0 & 0 \\
0 & 0 & 0 & 0 & 0 & 0 & 0 & 0 \\
0 & 0 & 0 & 0 & 0 & 0 & 0 & 0
\end{bmatrix}
$$

$$
\boldsymbol{A_3} = \begin{bmatrix}
w & 0 & 0 & \gamma p & -\dfrac{pw}{C_v} & 0 & 0 & 0 \\
0 & w - \dfrac{\frac{\partial \mu}{\partial z}}{\rho} & 0 & \dfrac{2}{3}\dfrac{\frac{\partial \mu}{\partial x}}{\rho} & 0 & 0 & 0 & -\dfrac{\tau_{13}}{\mu\rho} \\
0 & 0 & w - \dfrac{\frac{\partial \mu}{\partial z}}{\rho} & \dfrac{2}{3}\dfrac{\frac{\partial \mu}{\partial y}}{\rho} & 0 & 0 & 0 & -\dfrac{\tau_{23}}{\mu\rho} \\
\dfrac{1}{\rho} & -\dfrac{\frac{\partial \mu}{\partial x}}{\rho} & -\dfrac{\frac{\partial \mu}{\partial y}}{\rho} & w - \dfrac{4}{3}\dfrac{\frac{\partial \mu}{\partial z}}{\rho} & 0 & 0 & 0 & -\dfrac{\tau_{33}}{\mu\rho} \\
0 & -2\dfrac{\tau_{13}}{\rho T} & -2\dfrac{\tau_{23}}{\rho T} & -2\dfrac{\tau_{33}}{\rho T} & w & 0 & -\dfrac{\frac{\partial \lambda}{\partial z}}{\rho T} & -\dfrac{C_p \frac{\partial T}{\partial z}}{\rho T \,\mathrm{Pr}} \\
0 & 0 & 0 & 0 & 0 & 0 & 0 & 0 \\
0 & 0 & 0 & 0 & 0 & 0 & 0 & 0 \\
0 & 0 & 0 & 0 & 0 & 0 & 0 & 0
\end{bmatrix}
$$

$$
\mathbf{C} = \begin{bmatrix}
\gamma\frac{\partial u_j}{\partial x_j} - \frac{\frac{\partial s}{\partial t} + u_j\frac{\partial s}{\partial x_j}}{C_v} & \frac{\partial p}{\partial x} - \frac{p\frac{\partial s}{\partial x}}{C_v} & \frac{\partial p}{\partial y} - \frac{p\frac{\partial s}{\partial y}}{C_v} & \frac{\partial p}{\partial z} - \frac{p\frac{\partial s}{\partial z}}{C_v} & 0 \\
0 & \frac{\partial u}{\partial x} + \frac{\mu}{\rho\phi}\left(K^{-1}\right)_{11} & \frac{\partial u}{\partial y} + \frac{\mu}{\rho\phi}\left(K^{-1}\right)_{12} & \frac{\partial u}{\partial z} + \frac{\mu}{\rho\phi}\left(K^{-1}\right)_{13} & 0 \\
0 & \frac{\partial v}{\partial x} + \frac{\mu}{\rho\phi}\left(K^{-1}\right)_{21} & \frac{\partial v}{\partial y} + \frac{\mu}{\rho\phi}\left(K^{-1}\right)_{22} & \frac{\partial v}{\partial z} + \frac{\mu}{\rho\phi}\left(K^{-1}\right)_{32} & 0 \\
0 & \frac{\partial w}{\partial x} + \frac{\mu}{\rho\phi}\left(K^{-1}\right)_{31} & \frac{\partial w}{\partial y} + \frac{\mu}{\rho\phi}\left(K^{-1}\right)_{32} & \frac{\partial w}{\partial z} + \frac{\mu}{\rho\phi}\left(K^{-1}\right)_{33} & 0 \\
0 & \frac{\partial s}{\partial x} - 2\frac{\mu}{\rho\phi T}\left(K^{-1}\right)_{1j}u_j & \frac{\partial s}{\partial y} - 2\frac{\mu}{\rho\phi T}\left(K^{-1}\right)_{2j}u_j & \frac{\partial s}{\partial z} - 2\frac{\mu}{\rho\phi T}\left(K^{-1}\right)_{3j}u_j & 0 \\
-\frac{1}{c^2} & 0 & 0 & 0 & \frac{p}{c^2 C_v} \\
-\frac{1}{\rho R} & 0 & 0 & 0 & 0 \\
0 & 0 & 0 & 0 & 0
\end{bmatrix}
$$

$$
\begin{bmatrix}
0 & 0 & 0 \\
-\frac{\frac{\partial}{\partial x}p}{\rho^2} + \frac{\frac{\partial \tau_{1j}}{\partial x_j}}{\rho^2} - \frac{\mu}{\rho^2\phi}\left(K^{-1}\right)_{1j}u_j & 0 & -\frac{1}{\rho}\left(\frac{\partial}{\partial x_j}\left(\frac{\tau_{1j}}{\mu}\right)\right) + \frac{1}{\rho\phi}\left(K^{-1}\right)_{1j}u_j \\
-\frac{\frac{\partial}{\partial y}p}{\rho^2} + \frac{\frac{\partial \tau_{2j}}{\partial x_j}}{\rho^2} - \frac{\mu}{\rho^2\phi}\left(K^{-1}\right)_{2j}u_j & 0 & -\frac{1}{\rho}\left(\frac{\partial}{\partial x_j}\left(\frac{\tau_{2j}}{\mu}\right)\right) + \frac{1}{\rho\phi}\left(K^{-1}\right)_{2j}u_j \\
-\frac{\frac{\partial}{\partial z}p}{\rho^2} + \frac{\frac{\partial \tau_{3j}}{\partial x_j}}{\rho^2} - \frac{\mu}{\rho^2\phi}\left(K^{-1}\right)_{3j}u_j & 0 & -\frac{1}{\rho}\left(\frac{\partial}{\partial x_j}\left(\frac{\tau_{3j}}{\mu}\right)\right) + \frac{1}{\rho\phi}\left(K^{-1}\right)_{3j}u_j \\
\frac{\frac{\partial}{\partial x_j}\left(\lambda\frac{\partial T}{\partial x_j}\right) + \Phi}{(\rho)^2 T} + \frac{\mu}{\rho^2\phi T}\left(K^{-1}\right)_{ij}u_i u_j & \frac{\frac{\partial}{\partial x_j}\left(\lambda\frac{\partial T}{\partial x_j}\right) + \Phi}{\rho\,(T)^2} + \frac{\mu}{\rho\phi T^2}\left(K^{-1}\right)_{ij}u_i u_j & -\frac{C_p\left(\frac{\partial^2 T}{\partial x_j^2}\right)}{\mathrm{Pr}\;\rho T} - \frac{\Phi}{\rho T\mu} - \frac{1}{\rho\phi T}\left(K^{-1}\right)_{ij}u_i u_j \\
\frac{1}{T} & 0 & 0 \\
\frac{\rho}{T} & 1 & 0 \\
0 & -\frac{d}{dT}\mu(T) & 1
\end{bmatrix}
$$

$$\boldsymbol{D_{11}} = \begin{bmatrix} 0 & 0 & 0 & 0 & 0\,0 & 0 & 0 \\ 0 & -\frac{4}{3}\frac{\mu}{\rho} & 0 & 0 & 0\,0 & 0 & 0 \\ 0 & 0 & -\frac{\mu}{\rho} & 0 & 0\,0 & 0 & 0 \\ 0 & 0 & 0 & -\frac{\mu}{\rho} & 0\,0 & 0 & 0 \\ 0 & 0 & 0 & 0 & 0\,0 & -\frac{\lambda}{\rho T} & 0 \\ 0 & 0 & 0 & 0 & 0\,0 & 0 & 0 \\ 0 & 0 & 0 & 0 & 0\,0 & 0 & 0 \\ 0 & 0 & 0 & 0 & 0\,0 & 0 & 0 \end{bmatrix} \quad \boldsymbol{D_{22}} = \begin{bmatrix} 0 & 0 & 0 & 0 & 0\,0 & 0 & 0 \\ 0 & -\frac{\mu}{\rho} & 0 & 0 & 0\,0 & 0 & 0 \\ 0 & 0 & -\frac{4}{3}\frac{\mu}{\rho} & 0 & 0\,0 & 0 & 0 \\ 0 & 0 & 0 & -\frac{\mu}{\rho} & 0\,0 & 0 & 0 \\ 0 & 0 & 0 & 0 & 0\,0 & -\frac{\lambda}{\rho T} & 0 \\ 0 & 0 & 0 & 0 & 0\,0 & 0 & 0 \\ 0 & 0 & 0 & 0 & 0\,0 & 0 & 0 \\ 0 & 0 & 0 & 0 & 0\,0 & 0 & 0 \end{bmatrix}$$

$$\boldsymbol{D_{33}} = \begin{bmatrix} 0 & 0 & 0 & 0 & 0\,0 & 0 & 0 \\ 0 & -\frac{\mu}{\rho} & 0 & 0 & 0\,0 & 0 & 0 \\ 0 & 0 & -\frac{\mu}{\rho} & 0 & 0\,0 & 0 & 0 \\ 0 & 0 & 0 & -\frac{4}{3}\frac{\mu}{\rho} & 0\,0 & 0 & 0 \\ 0 & 0 & 0 & 0 & 0\,0 & -\frac{\lambda}{\rho T} & 0 \\ 0 & 0 & 0 & 0 & 0\,0 & 0 & 0 \\ 0 & 0 & 0 & 0 & 0\,0 & 0 & 0 \\ 0 & 0 & 0 & 0 & 0\,0 & 0 & 0 \end{bmatrix} \quad \boldsymbol{D_{12}} = \begin{bmatrix} 0 & 0 & 0 & 0\,0\,0\,0\,0 \\ 0 & 0 & -\frac{1}{3}\frac{\mu}{\rho} & 0\,0\,0\,0\,0 \\ 0 & -\frac{1}{3}\frac{\mu}{\rho} & 0 & 0\,0\,0\,0\,0 \\ 0 & 0 & 0 & 0\,0\,0\,0\,0 \\ 0 & 0 & 0 & 0\,0\,0\,0\,0 \\ 0 & 0 & 0 & 0\,0\,0\,0\,0 \\ 0 & 0 & 0 & 0\,0\,0\,0\,0 \\ 0 & 0 & 0 & 0\,0\,0\,0\,0 \end{bmatrix}$$

$$\boldsymbol{D_{13}} = \begin{bmatrix} 0 & 0 & 0 & 0 & 0\,0\,0\,0 \\ 0 & 0 & 0 & -\frac{1}{3}\frac{\mu}{\rho} & 0\,0\,0\,0 \\ 0 & 0 & 0 & 0 & 0\,0\,0\,0 \\ 0 & -\frac{1}{3}\frac{\mu}{\rho} & 0 & 0 & 0\,0\,0\,0 \\ 0 & 0 & 0 & 0 & 0\,0\,0\,0 \\ 0 & 0 & 0 & 0 & 0\,0\,0\,0 \\ 0 & 0 & 0 & 0 & 0\,0\,0\,0 \\ 0 & 0 & 0 & 0 & 0\,0\,0\,0 \end{bmatrix} \quad \boldsymbol{D_{23}} = \begin{bmatrix} 0\,0 & 0 & 0 & 0\,0\,0\,0 \\ 0\,0 & 0 & 0 & 0\,0\,0\,0 \\ 0\,0 & 0 & -\frac{1}{3}\frac{\mu}{\rho} & 0\,0\,0\,0 \\ 0\,0 & -\frac{1}{3}\frac{\mu}{\rho} & 0 & 0\,0\,0\,0 \\ 0\,0 & 0 & 0 & 0\,0\,0\,0 \\ 0\,0 & 0 & 0 & 0\,0\,0\,0 \\ 0\,0 & 0 & 0 & 0\,0\,0\,0 \\ 0\,0 & 0 & 0 & 0\,0\,0\,0 \end{bmatrix}$$

$$\boldsymbol{D_{31}} = \boldsymbol{D_{13}}; \qquad \boldsymbol{D_{32}} = \boldsymbol{D_{23}}; \qquad \boldsymbol{D_{21}} = \boldsymbol{D_{12}}$$

C

Compressible adjoint Navier–Stokes equations

The direct Navier–Stokes equations are written in a characteristic formulation of Sesterhenn [2000]. In a continuous adjoint approach it is important to use the same numerical method for the direct as for the adjoint computation. To this end, the adjoint Navier–Stokes equations are also decomposed into characteristic waves. First, the scalar product of

$$\boldsymbol{\alpha}^T \left(-\mathbf{B}^T \frac{\partial \mathbf{q}^\star}{\partial t} - \mathbf{A_k}^T \frac{\partial \mathbf{q}^\star}{\partial x_k} \right) = 0 \tag{C.1}$$

is calculated with $\boldsymbol{\alpha}^T = (\alpha_1,\ \alpha_2,\ \alpha_3,\ \alpha_4,\ \alpha_5)$, where, to simplify matters, only the variations in x are considered and written in the form:

$$\begin{aligned}
&\left(-\alpha_1 + \alpha_5 \frac{p}{C_v}\right) \frac{\partial p^\star}{\partial t} && +\left(-\alpha_2 \gamma p - \alpha_1 u + \alpha_5 \frac{p}{C_v} u\right) && \frac{\partial p^\star}{\partial x} + \\
&-\alpha_2 \frac{\partial u^\star}{\partial t} && +\left(-\alpha_2 u - \frac{\alpha_1}{\rho}\right) && \frac{\partial u^\star}{\partial x} + \\
&-\alpha_3 \frac{\partial v^\star}{\partial t} && +\left(-\alpha_3 u\right) && \frac{\partial v^\star}{\partial x} + \\
&-\alpha_4 \frac{\partial w^\star}{\partial t} && +\left(-\alpha_4 u\right) && \frac{\partial w^\star}{\partial x} + \\
&-\alpha_5 \frac{\partial s^\star}{\partial t} && +\left(-\alpha_5 u\right) && \frac{\partial s^\star}{\partial x} = 0
\end{aligned}$$

As for a characteristic, the time and space variables are in the same relation, we get:

$$\begin{aligned}\lambda &= \frac{\left(-\alpha_2\gamma p - \alpha_1 u + \alpha_5 \frac{p}{C_v} u\right)}{-\alpha_1} = \frac{\left(-\alpha_2 u - \frac{\alpha_1}{\rho}\right)}{-\alpha_2} = \frac{(-\alpha_3 u)}{-\alpha_3} \\ &= \frac{(-\alpha_4 u)}{-\alpha_4} = \frac{(-\alpha_5 u)}{-\alpha_5}\end{aligned} \tag{C.2}$$

The eigenvalues of $-\boldsymbol{A}_{\mathbf{1}}^T$ are:

$$\operatorname{eig}(-\mathbf{A_1}^T) = \begin{bmatrix} -u + \frac{\sqrt{\rho\gamma p}}{\rho} \\ -u - \frac{\sqrt{\rho\gamma p}}{\rho} \\ -u \\ -u \\ -u \end{bmatrix} = \begin{bmatrix} -u + c \\ -u - c \\ -u \\ -u \\ -u \end{bmatrix}$$

So we get $\lambda_{1,2,3} = -u$, $\lambda_4 = -u + c$ and $\lambda_5 = -u - c$ for which we need to discuss the cases separately to obtain the corresponding eigenvectors. In this discussion we consider the following system of equations:

$$\left(-\alpha_1 + \alpha_5 \frac{p}{C_v}\right)\lambda - \alpha_2\gamma p - \alpha_1 u + \alpha_5 \frac{p}{C_v} u = 0 \tag{C.3a}$$

$$-\alpha_2\lambda - \alpha_2 u - \frac{\alpha_1}{\rho} = 0 \tag{C.3b}$$

$$-\alpha_3\lambda - \alpha_3 u = 0 \tag{C.3c}$$

$$-\alpha_4\lambda - \alpha_4 u = 0 \tag{C.3d}$$

$$-\alpha_5\lambda - \alpha_5 u = 0 \tag{C.3e}$$

Case $\lambda_{1,2,3} = u$ For this case the system of equations is rank deficient, so we can choose the last three parameters α_3, α_4 and α_5 free.

- Our first try is $\boldsymbol{\alpha}^T = (\alpha_1,\ \alpha_2,\ 1,\ 0,\ 0)$ and the solution of the system is $\alpha_1 = \alpha_2 = 0$. The only remaining equation is:

  $$-\frac{\partial v^\star}{\partial t} - u\frac{\partial v^\star}{\partial x} = 0$$

  We use the following abbreviation:

  $$X^{v^\star} := -u\frac{\partial v^\star}{\partial x}$$

- Our second try is $\boldsymbol{\alpha}^T = (\alpha_1,\ \alpha_2,\ 0,\ 1,\ 0)$ and the solution of the system is $\alpha_1 = \alpha_2 = 0$. The only remaining equation is:

$$-\frac{\partial w^\star}{\partial t} - u\frac{\partial w^\star}{\partial x} = 0$$

We use the following abbreviation:

$$X^{w\star} := -u\frac{\partial w^\star}{\partial x}$$

- Our last try is $\boldsymbol{\alpha}^T = (\alpha_1,\ \alpha_2,\ 0,\ 0,\ 1)$ and the solution of the system is $\alpha_1 = \alpha_2 = 0$. The only remaining equation is:

$$\left(\frac{p}{C_v}\frac{\partial p^\star}{\partial t} - \frac{\partial s^\star}{\partial t}\right) + u\left(\frac{p}{C_v}\frac{\partial p^\star}{\partial x} - \frac{\partial s^\star}{\partial x}\right) = 0$$

We use the following abbreviation:

$$X^{s\star} := u\left(\frac{p}{C_v}\frac{\partial p^\star}{\partial x} - \frac{\partial s^\star}{\partial x}\right)$$

Case $\lambda_{4,5} = -u \pm c$ For the last two eigenfunctions we choose $\alpha_1 = \sqrt{\gamma p \rho} = \rho c$

- Our first try is $\boldsymbol{\alpha}^T = (\rho c,\ \alpha_2,\ \alpha_3,\ \alpha_4,\ \alpha_5)$ and the solution of the system is $\alpha_2 = \pm 1$, $\alpha_{3,4,5} = 0$. The two remaining equations are:

$$\left(-\rho c\frac{\partial p^\star}{\partial t} \pm \frac{\partial u^\star}{\partial t}\right) - (-u \pm c)\left(-\rho c\frac{\partial p^\star}{\partial x} \pm \frac{\partial u^\star}{\partial x}\right) = 0$$

We use the following abbreviation for the adjoint wave:

$$X^{\pm\star} := (-u \pm c)\left(-\rho c\frac{\partial p^\star}{\partial x} \pm \frac{\partial u^\star}{\partial x}\right) \tag{C.4}$$

Transformed adjoint Navier–Stokes equations In the same way as for the direct Navier–Stokes equations the adjoint Navier–Stokes equations can be derived for curvilinear grids (cf. § A). Again, beginning with the replacement of the derivation in physical space by derivations in the computational domain, we get:

$$\frac{\partial p^\star}{\partial t} = -u_i\xi^l_{,i}\frac{\partial p}{\partial \xi^l} - \frac{1}{\rho}\xi^l_{,i}\frac{\partial {u_i}^\star}{\partial \xi^l} + \Theta^p_e + \Theta^p_f + \Theta^p_p \tag{C.5a}$$

$$\frac{\partial {u_i}^\star}{\partial t} = -u_j\xi^l_{,j}\frac{\partial {u_i}^\star}{\partial \xi^l} - \gamma p\xi^l_{,i}\frac{\partial p^\star}{\partial \xi^l} + \Theta^{u_i}_e + \Theta^{u_i}_f + \Theta^{u_i}_p \tag{C.5b}$$

$$\frac{\partial s^\star}{\partial t} = -u_i\xi^l_{,i}\frac{\partial s}{\partial \xi^l} + \frac{p}{C_v}\left(\frac{\partial p^\star}{\partial t} + u_i\xi^l_{,i}\frac{\partial p^\star}{\partial \xi^l}\right) + \Theta^s_e + \Theta^s_f + \Theta^s_p \tag{C.5c}$$

Finally, after some math in the same manner as for the direct Navier–Stokes equations the adjoint Navier–Stokes equations can be written in characteristic waves for curvilinear grids.

$$\frac{\partial p^\star}{\partial t} = -\sum_{k=1}^{3} \frac{1}{2\rho c}\left(\Xi_+^{k\,\star} + \Xi_-^{k\,\star}\right) + \Theta_e^p + \Theta_f^p + \Theta_p^p \tag{C.6a}$$

$$\begin{aligned}\frac{\partial u^{1\star}}{\partial t} &= \frac{\sqrt{g^{11}}}{2}\left(\Xi_+^{1\,\star} - \Xi_-^{1\,\star}\right) + \Xi_1^{2\,\star} + \Xi_1^{3\,\star} + \frac{\xi^1_{,l}\xi^2_{,l}}{2\sqrt{g^{22}}}\left(\Xi_+^{2\,\star} - \Xi_-^{2\,\star}\right) \\ &\quad + \frac{\xi^1_{,l}\xi^3_{,l}}{2\sqrt{g^{33}}}\left(\Xi_+^{3\,\star} - \Xi_-^{3\,\star}\right) + \xi^1_{,i}\left(\Theta_e^{u_i} + \Theta_f^{u_i} + \Theta_p^{u_i}\right)\end{aligned} \tag{C.6b}$$

$$\begin{aligned}\frac{\partial u^{2\star}}{\partial t} &= \Xi_2^{1\,\star} + \frac{\sqrt{g^{22}}}{2}\left(\Xi_+^{2\,\star} - \Xi_-^{2\,\star}\right) + \Xi_2^{3\,\star} + \frac{\xi^2_{,l}\xi^1_{,l}}{2\sqrt{g^{11}}}\left(\Xi_+^{2\,\star} - \Xi_-^{2\,\star}\right) \\ &\quad + \frac{\xi^2_{,l}\xi^3_{,l}}{2\sqrt{g^{33}}}\left(\Xi_+^{3\,\star} - \Xi_-^{3\,\star}\right) + \xi^2_{,i}\left(\Theta_e^{u_i} + \Theta_f^{u_i} + \Theta_p^{u_i}\right)\end{aligned} \tag{C.6c}$$

$$\begin{aligned}\frac{\partial u^{3\star}}{\partial t} &= \Xi_3^{1\,\star} + \Xi_3^{2\,\star} + \frac{\sqrt{g^{33}}}{2}\left(\Xi_+^{3\,\star} - \Xi_-^{3\,\star}\right) + \frac{\xi^3_{,l}\xi^1_{,l}}{2\sqrt{g^{11}}}\left(\Xi_+^{1\,\star} - \Xi_-^{1\,\star}\right) \\ &\quad + \frac{\xi^3_{,l}\xi^2_{,l}}{2\sqrt{g^{22}}}\left(\Xi_+^{2\,\star} - \Xi_-^{2\,\star}\right) + \xi^3_{,i}\left(\Theta_e^{u_i} + \Theta_f^{u_i} + \Theta_p^{u_i}\right)\end{aligned} \tag{C.6d}$$

$$\frac{\partial s^\star}{\partial t} = \left(\Xi_s^{1\,\star} + \Xi_s^{2\,\star} + \Xi_s^{3\,\star}\right) + \frac{p}{C_v}\frac{\partial p^\star}{\partial t} + \left(\Theta_e^s + \Theta_f^s + \Theta_p^s\right) \tag{C.6e}$$

and the abbreviation for the adjoint characteristic waves for curvilinear grids

$$\Xi_\pm^{k\,\star} := \left(-u^{(k)} \pm c\sqrt{g^{(kk)}}\right)\left(-\rho c\frac{\partial p^\star}{\partial \xi^{(k)}} \pm \frac{\xi^{(k)}_{,i}}{\sqrt{g^{(kk)}}}\frac{\partial u_i{}^\star}{\partial \xi^{(k)}}\right) \tag{C.7a}$$

$$\Xi_s^{k\,\star} := u^{(k)}\left(\frac{p}{C_v}\frac{\partial p^\star}{\partial \xi^{(k)}} - \frac{\partial s^\star}{\partial \xi^{(k)}}\right) \tag{C.7b}$$

$$\Xi_l^{k\,\star} := -u^{(k)}\left(\xi^l_{,i}\frac{\partial u_i{}^\star}{\partial \xi^{(k)}} - \frac{\xi^k_{,m}\xi^l_{,m}}{g^{(kk)}}\xi^k_{,i}\frac{\partial u_i{}^\star}{\partial \xi^{(k)}}\right) \tag{C.7c}$$

Bibliography

Aage, N., Poulsen, T., Gersborg-Hansen, A., & Sigmund, O. (2008). Topology optimization of large scale stokes flow problems. *Structural and Multidisciplinary Optimization*, 35, 175–180.

Adams, N. A. & Shariff, K. (1996). A high-resolution hybrid compact-eno scheme for shock-turbulence interaction problems. *J. Comput. Phys.*, 127(1), 27–51.

Airiau, C., Bottaro, A., Walther, S., & Legendre, D. (2003). A methodology for optimal laminar flow control: Application to the damping of tollmien schlichting waves in a boundary layer. *Phys. Fluids*, 15(5), 1131–1145.

Al-Qadi, I. & Scott, J. (2003). High-order three-dimensional numerical simulation of a supersonic rectangualr jet. In *9th AIAA/CEAS Aeroacoustics Conference and Exhibit*, number 2003-3238: AIAA.

Al-Qadi, I. M. A. & Scott, J. N. (2001). Simulations of unsteady behavior in under-expanded supersonic rectangular jets. In *AIAA/CEAS Aeroacoustics Conference and Exhibit*, number 2001-2119: AIAA.

Alkislar, M. B., Krothapalli, A., & Lourenco, L. M. (2003). Structure of a screeching rectangular jet: a stereoscopic particle image velocimetry study. *J. Fluid Mech.*, 489, 121–154.

Anderson, D., Tannehill, J., & Pletcher, R. (1984). *Computational fluid mechanics and heat transfer*. Hemisphere Publishing, New York, NY.

Angot, P., Bruneau, C.-H., & Fabrie, P. (1999). A penalization method to take into account obstacles in incompressible viscous flows. *Numerische Mathematik*, 81, 497–520. 10.1007/s002110050401.

Armijo, L. (1966). Minimization of functions having lipschitz continuous first partial derivatives. *Pacific J. Math.*, 16(1), 1–3.

Arquis, E. & Caltagirone, J. (1984). Sur les conditions hydrodynamiques au voisinage d'une interface milieu fluide-milieu poreux: application á la convection naturelle. *C.R. Acad. Sci. Paris II*, 299, 1–4.

Asouti, V. G., Zymaris, A. S., Papadimitriou, D. I., & Giannakoglou, K. C. (2008). Continuous and discrete adjoint approaches for aerodynamic shape optimization with low mach number preconditioning. *Int. J. Numer. Methods Fluids*, 57(10), 1485–1504.

Babucke, A., Spagnoli, B., Airiau, C., Kloker, M., & Rist, U. (2009). Mechanisms and active control of jet-induced noise. In C. Brun, D. Juve, M. Manhart, & C.-D. Munz (Eds.), *Numerical Simulation of Turbulent Flows and Noise Generation*, volume 104 of *Notes on Numerical Fluid Mechanics and Multidisciplinary Design* (pp. 75–98). Springer Berlin / Heidelberg.

Barone, M. F. (2003). *Receptivity of compressible mixing layers.* PhD thesis, Stanford University.

Barone, M. F. & Lele, S. (2005). Receptivity of the compressible mixing layer. *J. Fluid Mech.*, 540, 301–335.

Baur, C., Bontoux, P., Kornhaas, M., Minguez, M., Pasquetti, R., Schäfer, M., Serre, E., & Séverac, E. (2009). High-order methods for large-eddy simulation in complex geometries. In C. Brun, D. Juvé, M. Manhart, & C.-D. Munz (Eds.), *Numerical Simulation of Turbulent Flows and Noise Generation*, volume 104 of *Notes on Numerical Fluid Mechanics and Multidisciplinary Design* (pp. 309–334). Springer Berlin / Heidelberg. 10.1007/978-3-540-89956-3.

Bear, J. (1972). *Dynamics of fluids in porous media.* Environmental science series. New York: American Elsevier. 0-444-00114-X.

Bendsøe, M. (1995). *Optimization of structural topology, shape, and material*, volume 414. Springer Berlin.

Berland, J., Bogey, C., & Bailly, C. (2006). Large eddy simulation of screech tone generation in a planar underexpanded jet. In *12th AIAA/CEAS Aeroacoustics Conference (27th AIAA Aeroacoustics Conference)*, number 2006-2496: AIAA.

Berland, J., Bogey, C., & Bailly, C. (2007). Numerical study of screech generation in a planar supersonic jet. *Phys. Fluids*, 19(7), 075105.

Bewley, T. R. (2001). Flow Control: New Challenges for a New Renaissance. *Pro. Aerospace Sci.*, 37(1), 21–58.

Bewley, T. R., Moin, P., & Temam, R. (2001). Dns-based predictive control of turbulence: an optimal benchmark for feedback algorithms. *J. Fluid Mech.*, 447, 179–225.

Bischof, C., Carle, A., Corliss, G., Griewank, A., & Hovland, P. (1992). Adifor-generating derivative codes from fortran programs. *Sci. Program.*, 1, 11–29.

Bodony, D., Ryu, J., Ray, P., & Lele, S. (2006). Investigating broadband shock-associated noise of axisymmetric jets using large-eddy simulation. In *12th AIAA/CEAS Aeroacoustics Conference (27th AIAA Aeroacoustics Conference)*, number 2006-2495: AIAA.

Bodony, D. J. & Lele, S. K. (2005). On using large-eddy simulation for the prediction of noise from cold and heated turbulent jets. *Phys. Fluids*, 17(8), 085103–1–20.

Bogey, C. (2000). *Calcul direct du bruit aérodynamique et validation de modéles acoustiques hybrides.* PhD thesis, Ecole Central de Lyon.

Bogey, C. & Bailly, C. (2005). Decrease of the effective reynolds number with eddy-viscosity subgrid modeling. *AIAA J.*, 43(2), 437–439.

Bogey, C. & Bailly, C. (2009). Turbulence and energy budget in a self-preserving round jet: direct evaluation using large eddy simulation. *J. Fluid Mech.*, 627, 129–160.

Bogey, C. & Bailly, C. (2010). Influence of nozzle-exit boundary-layer conditions on the flow and acoustic fields of initially laminar jets. *J. Fluid Mech.*, 663, 507–538.

Bogey, C., de Cacqueray, N., & Bailly, C. (2009). A shock-capturing methodology based on adaptative spatial filtering for high-order non-linear computations. *J. Comput. Phys.*, 228(5), 1447–1465.

Borrvall, T. & Petersson, J. (2003). Topology optimization of fluids in stokes flow. *Int. J. Numer. Methods Fluids*, 41(1), 77–107.

Boyd, S. & Vandenberghe, L. (2004). *Convex optimization*. Cambridge Univ Pr.

Bradbury, L. J. S. (1965). The structure of a self-preserving turbulent plane jet. *J. Fluid Mech.*, 23(1), 31–64.

Brezillon, J. & Gauger, N. (2004). 2d and 3d aerodynamic shape optimisation using the adjoint approach. *Aerosp. Sci. Technol.*, 8(8), 715–727.

Bridges, J. (2006). Effect of heat on space-time correlations in jets. In *12th AIAA/CEAS Aeroacoustics Conference*, number 2006-2534: AIAA.

Brinkman, H. (1949). A calculation of the viscous force exerted by a flowing fluid on a dense swarm of particles. *Appl. Sci. Res.*, 1, 27–34. 10.1007/BF02120313.

Bruneau, C.-H. & Mortazavi, I. (2008). Numerical modelling and passive flow control using porous media. *Comput. Fluids*, 37(5), 488–498. Special Issue Dedicated to Professor M.M. Hafez on the Occasion of his 60th Birthday - Special Issue Dedicated to Professor M.M. Hafez on the Occasion of his 60th Birthday.

Caliari, M. & Ostermann, A. (2009). Implementation of exponential rosenbrock-type integrators. *Appl. Numer. Math.*, 59, 568–581.

Cao, Y. & Stanescu, D. (2002). Shape optimization for noise radiation problems. *Computers and Mathematics with Applications*, 44(12), 1527–1537.

Carbou, G. (2008). Brinkmann model and double penalization method for the flow around a porous thin layer. *J. Math. Fluid Mech.*, 10, 126–158. 10.1007/s00021-006-0221-y.

Carpentieri, G., Koren, B., & van Tooren, M. (2007). Adjoint-based aerodynamic shape optimization on unstructured meshes. *J. Comput. Phys.*, 224(1), 267–287.

Cavalieri, A. V., Daviller, G., Comte, P., Jordan, P., Tadmor, G., & Gervais, Y. (2011). Using large eddy simulation to explore sound-source mechanisms in jets. *J. Sound Vib.*, 330(17), 4098–4113.

Cerretelli, C. & Gharaibah, E. (2007). An experimental and numerical investigation on fluidic oscillators for flow control. In *37th AIAA Fluid Dynamics Conference and Exhibit*, number 2007-3854 (pp. 1–9).

Cervino, L. I. & Bewley, T. R. (2003). Adjoint analysis and control opportunities in a 2d jet. In *Proceedings of the 42nd IEEE Conference on Decision and Control*.

Cervino, L. I., Bewley, T. R., Freund, J. B., & Lele, S. K. (2002). Perturbation and adjoint analyses of flow-acoustic interactions in an unsteady 2d jet. In *CTR*, Proc. Summer Program (pp. 27–40).

Charpentier, I. (2001). Checkpointing schemes for adjoint codes: Application to the meteorological model meso-nh. *SIAM J. Sci. Comput.*, 22(6), 2135–2151.

Chen, R. H., Saadani, S. B., & Chew, L. P. (2002). Effect of nozzle size on screech noise elimination from swirling underexpanded jets. *J. Sound Vib.*, 252(1), 178–186.

Clement, S. & Rathakrishnan, E. (2006). Characteristics of sonic jets with tabs. *Shock Waves*, 15, 219–227. 10.1007/s00193-006-0017-2.

Collis, S. S., Ghayour, K., & Heinkenschloss, M. (2002a). Optimal control of aeroacoustic noise generated by cylinder vortex interaction. *Int. J. Aeroacoustics*, 1(2), 97–114.

Collis, S. S., Ghayour, K., & Heinkenschloss, M. (2003). Optimal transpiration boundary control for aeroacoustics. *AIAA J.*, 41(7), 1257–1270.

Collis, S. S., Ghayour, K., Heinkenschloss, M., Ulbrich, M., & Ulbrich, S. (2002b). Optimal control of unsteady compressible viscous flows. *Int. J. Numer. Methods Fluids*, 40(11), 1401–1429.

Colonius, T. & Lele, S. K. (2004). Computational aeroacoustics: progress on nonlinear problems of sound generation. *Pro. Aerosp. Sci.*, 40(6), 345–416.

Cook, A. W. & Cabot, W. H. (2005). Hyperviscosity for shock-turbulence interactions. *J. Comput. Phys.*, 203(2), 379–385.

Crighton, D. G. (1986). The taylor internal structure of weak shock waves. *J. Fluid Mech.*, 173, 625–642.

Crist, S., Shermann, P. M., & Glass, D. R. (1966). Study of the highly underexpanded sonic jet. *AIAA J.*, 4(1), 68–71.

Darcy, H. (1856). *Les fontaines publiques de la ville de Dijon*. Paris: Victor Dalmont.

Davies, M. G. & Oldfield, D. E. S. (1962a). Tones from a choked axisymmetric jet. I. Cell structure, eddy velocity and source locations. *Acustica*, 12(4), 257–266.

Davies, M. G. & Oldfield, D. E. S. (1962b). Tones from a choked axisymmetric jet. II. The self exited loop and mode of oscillation. *Acustica*, 12(4), 267–277.

de Cacqueray, N. (2010). *Méthodes numériques pour les écoulements supersoniques avec application au calcul du bruit rayonné par un jet sur-détendu*. PhD thesis, Ecole Central de Lyon.

de Cacqueray, N., Bogey, C., & Bailly, C. (2011). Investigation of a high-mach-number overexpanded jet using large-eddy simulation. *AIAA J.*, 49(10), 2171–2182.

De Wiest, R. J. (1969). *Flow through porous media*. Acad. Pr.

Dühring, M. B., Jensen, J. S., & Sigmund, O. (2008). Acoustic design by topology optimization. *J. Sound Vib.*, 317(3-5), 557–575.

Ehrenfried, K. (2004). *Strömungsakustik, Skript zur Vorlesung*. Mensch & Buch Verlag, Berlin.

Eidson, T. M. & Erlebacher, G. (1995). Implementation of a fully balanced periodic tridiagonal solver on a parallel distributed memory architecture. *Concurrency: Practice and Experience*, 7(4), 273–302.

Eschenauer, H. A. & Olhoff, N. (2001). Topology optimization of continuum structures: A review. *Applied Mechanics Reviews*, 54(4), 331–390.

Fazzolari, A., Gauger, N. R., & Brezillon, J. (2007). Efficient aerodynamic shape optimization in mdo context. *J. Comput. Appl. Math.*, 203(2), 548–560.

Feijoo, G. R., Oberai, A. A., & Pinsky, P. M. (2004). An application of shape optimization in the solution of inverse acoustic scattering problems. *Inverse Problems*, 20(1), 199.

Ffowcs Williams, J. E. (1963). The noise from turbulence convected at high speed. *Philos. Trans. R. Soc. London, Ser. A, Math. Phys. Sci.*, 255(1061), 469–503.

Ffowcs Williams, J. E. (1984). Anti–Sound. *Proc. R. Soc. London, Ser. A, Math. Phys. Sci.*, 395, 63–88.

Foysi, H. (2005). *Transport passiver Skalare in wandgebundener und isotroper kompressibler Turbulenz*. PhD thesis, Technical university Munich.

Freund, J. B. (2001). Noise sources in a low-reynolds-number turbulent jet at mach 0.9. *J. Fluid Mech.*, 438, 277–305.

Freund, J. B. (2011). Adjoint-based optimization for understanding and suppressing jet noise. *J. Sound Vib.*, 330(17), 4114–4122.

Freund, J. B., Lele, S. K., & Moin, P. (2000). Direct simulation of a mach 1.92 jet and its sound field. *AIAA Journal*, 38(11), 2023–2031.

Fujimatsu, N. & Misu, I. (2005). Numerical investigation of sound generation in supersonic jet screech. In *43rd AIAA Aerospace Sciences Meeting and Exhibit*, number 2005-796: AIAA.

Fulks, W. B., Guenther, R. B., & Roetman, E. L. (1971). Equation of motion and continuity of fluid flow in a porous medium. *Acta Mechanica*, 12, 121–129.

Gallopoulos, E. & Saad, Y. (1992). Efficient solution of parabolic equations by krylov approximation methods. *SIAM J. Sci. Stat. Comput.*, 13, 1236–1264.

Gao, J. & Li, X. (2006). A numerical study of nozzle boundary layer thickness on axisymmetric supersonic jet screech tones. In *12th AIAA/CEAS Aeroacoustics Conference (27th AIAA Aeroacoustics Conference)*, number 2006-2675: AIAA.

Gao, J. H. & Li, X. D. (2010). A multi-mode screech frequency prediction formula for circular supersonic jets. *J. Acoust. Soc. Am.*, 127(3), 1251–1257.

Gao, J. H. & Li, X. D. (2011). Large eddy simulation of supersonic jet noise from a circular nozzle. *Int. J. Aeroacoustics*, 10(4), 465–474.

Gersborg-Hansen, A., Sigmund, O., & Haber, R. (2005). Topology optimization of channel flow problems. *Structural and Multidisciplinary Optimization*, 30, 181–192.

Geyer, T., Sarradj, E., & Fritzsche, C. (2010). Measurement of the noise generation at the trailing edge of porous airfoils. *Exp. Fluids*, 48, 291–308. 10.1007/s00348-009-0739-x.

Ghosh, S., Friedrich, R., Pfitzner, M., Stemmer, C., Cuenot, B., & El Hafi, M. (2011). Effects of radiative heat transfer on the structure of turbulent supersonic channel flow. *J. Fluid Mech.*, 677, 417–444.

Giles, M. & Pierce, N. (2000). An introduction to the adjoint approach to design. *Flow, Turb. Combust.*, 65, 393–415. 10.1023/A:1011430410075.

Giles, M. & Pierce, N. (2001). Analytic adjoint solutions for the quasi-one-dimensional euler equations. *J. Fluid Mech.*, 426, 327–345.

Giles, M. B. (2002). Discrete adjoint approximations with shocks. In T. Hou & E. Tadmo (Eds.), *Conference on Hyperbolic Problems*: Springer-Verlag.

Giles, M. B., Duta, M. C., Bijan Mohammadi, M. W., & Pierce, N. A. (2003). Algorithm developments for discrete adjoint methods. *AIAA J.*, 41(2), 198–205.

Giles, M. B. & Pierce, N. A. (1999). Improved lift and drag estimates using adjoint euler equations. In *14th Computational Fluid Dynamics Conference*, number 1999-3293: AIAA.

Glass, D. R. (1968). Effects of acoustic feedback on the spread and decay of supersonic jets. *AIAA J.*, 6(10), 1890–1897.

Goldstein, M. E. (1976). *Aeroacoustics*. McGraw-Hill International Book Company.

Griewank, A. (1992). Achieving logarithmic growth of temporal and spatial complexity in reverse automatic differentiation. *Optim. Methods Software*, 1(1), 35–54.

Guegan, A., Schmid, P., & Huerre, P. (2006). Optimal energy growth and optimal control in swept hiemenz flow. *J. Fluid Mech.*, 566, 11–45.

Guenanff, R., Sagaut, P., Manoha, E., Terracol, M., & Lewandowski, R. (2003). Theoretical aspects of a multi-domain high-order method for caa. *AIAA Paper*, 2003-3117.

Gunzburger, M. (2000). Adjoint equation-based methods for control problems in incompressible, viscous flows. *Flow, Turb. Combust.*, 65, 249–272. 10.1023/A:1011455900396.

Gutmark, E., Schadow, K. C., & Bicker, C. J. (1990). Near acoustic field and shock structure of rectangular supersonic jets. *AIAA J.*, 28(7), 1163–1170.

Gutmark, E. & Wygnanski, I. (1976). The planar turbulent jet. *J. Fluid Mech.*, 73(3), 465–495.

Hammitt, A. G. (1961). The oscillation and noise of an overpressure sonic jet. *J. Aerosp. Sci.*, 28, 673–680.

Harper-Bourne, M. & Fisher, M. (1973). The noise from shock waves in supersonic jets. In *AGARD Conference Proceedings CP-131* (pp. 1111–1113).

Hashimoto, A., Men'shov, I., & Nakamura, Y. (2004). Sound emission from the helical mode of supersonic jet. In *34th AIAA Fluid Dynamics Conference and Exhibit*, number 2004-2656: AIAA.

Hay, J. & Rose, E. (1970). In flight shock cell noise. *J. Sound Vib.*, 11, 411–420.

Hedstrom, G. (1979). Nonreflecting boundary conditions for nonlinear hyperbolic systems. *J. Comput. Phys.*, 30(2), 222–237.

Hochbruck, M. & Lubich, C. (1997). On krylov subspace approximations to the matrix exponential operator. *SIAM J. on Numer. Anal.*, 34(5), 1911–1925.

Hochbruck, M., Lubich, C., & Selhofer, H. (1998). Exponential integrators for large systems of differential equations. *SIAM J. Sci. Comput.*, 19, 1552–1574.

Hochbruck, M. & Ostermann, A. (2005). Explicit exponential runge-kutta methods for semilinear parabolic problems. *SIAM J. Numer. Anal.*, 43, 1069–1090.

Hu, T.-F. & McLaughlin, D. (1990). Flow and acoustic properties of low reynolds number underexpanded supersonic jets. *J. Sound Vib.*, 141(3), 485–505.

Imamoglu, B. & Balakumar, P. (2003). Three dimensional computation of shock induced noise in imperfectly expanded supersonic jets. In *9th AIAA/CEAS Aeroacoustics Conference and Exhibit*, number 2003-3249: AIAA.

Jameson, A. (1988). Aerodynamic design via control theory. *J. Sci. Comput.*, 3, 233–260. 10.1007/BF01061285.

Jameson, A. (1995). Optimum aerodynamic design using cfd and control theory. In *12t AIAA Computational Fluid Dynamics Conference*, number 1995-1729: AIAA.

Jones, L. E., Sandberg, R. D., & Sandham, N. D. (2010). Stability and receptivity characteristics of a laminar separation bubble on an aerofoil. *J. Fluid Mech.*, 648, 257–296.

Jordan, P., Gervais, Y., Valiére, J.-C., & Foulon, H. (2002). *Final result from single point measurement.* Technical Report G4RD-CT2000-00313, Laboratoire d′ Études Aérodynamiques.

Joslin, R. D., Gunzburger, M. D., Nicolaides, R. A., Erlebacher, G., & Hussaini, M. Y. (1995). *Self-Contained Automated Methodology for Optimal Flow Control.* Technical report, Institute for Computer Applications in Science and Engineering (ICASE).

Jungowski, W. M. (1979). Influence of closely located solid surfaces on the sound spectra radiated by gas jets. In E.-A. Mueller (Ed.), *Mechanics of Sound Generation in Flows* (pp. 116–122).

Keetels, G., D'Ortona, U., Kramer, W., Clercx, H., Schneider, K., & van Heijst, G. (2007). Fourier spectral and wavelet solvers for the incompressible navier-stokes equations with volume-penalization: Convergence of a dipole-wall collision. *J. Comput. Phys.*, 227(2), 919–945.

Kevlahan, N. K. R. & Ghidaglia, J.-M. (2001). Computation of turbulent flow past an array of cylinders using a spectral method with brinkman penalization. *Eur. J. Mech. B. Fluids*, 20(3), 333–350.

Khadra, K., Angot, P., Parneix, S., & Caltagirone, J.-P. (2000). Fictitious domain approach for numerical modelling of navier–stokes equations. *Int. J. Numer. Methods Fluids*, 34(8), 651–684.

Khan, M., Teramoto, K., Matsuo, S., & Setoguchi, T. (2008). Jet screech reduction with perforated flat reflector. *J. Therm. Sci.*, 17, 224–227. 10.1007/s11630-008-0224-5.

Khan, M. T. I., Seto, K., Xu, Z., & Ohta, H. (2004). An approach to noise reduction of a supersonic jet with a spherical reflector. *Acoust. Sci. Technol.*, 25(2), 136–143.

Kibens, V. & Wlezien, R. W. (1985). Noise reduction mechanisms in supersonic jets with porous centerbodies. *AIAA J.*, 23(5), 678–684.

Kim, J., Moin, P., & Moser, R. (1987). Turbulence statistics in fully developed channel flow at low reynolds number. *J. Fluid Mech.*, 177, 133–166.

Kim, J.-H., Kearney-Fischer, M., Samimy, M., & Gogineni, S. (2011). Far-field noise control in supersonic jets from conical and contoured nozzles. *J. Eng. Gas Turbines Power*, 133(8), 1–9.

Kim, S., Alonso, J. J., & Jameson, A. (2004). Multi-element high-lift configuration design optimization using viscous continuous adjoint method. *J. Aircraft*, 41(5), 1082–1097.

Kim, Y. & Lee, D. (2007). Acoustic properties associated with nozzle lip thickness in screeching jets. *J. Mech. Sci. Technol.*, 21, 764–771. 10.1007/BF02916354.

Kim, Y. & Nakamura, Y. (2006). Effect of nozzle lip shape on screech tone in supersonic jet. In *AIAA 2006-3706* (pp. 1–9).

Kleinman, R. & Freund, J. (2006). Adjoint-based control of the noise from a turbulent mixing layer. In *12th AIAA/CEAS Aeroacoustics Conference*.

Kolmogorov, A. N. (1962). A refinement of previous hypotheses concerning the local structure of turbulence in a viscous incompressible fluid at high reynolds number. *J. Fluid Mech.*, 13(01), 82–85.

Kolomenskiy, D. & Schneider, K. (2009). A fourier spectral method for the navier-stokes equations with volume penalization for moving solid obstacles. *J. Comput. Phys.*, 228(16), 5687–5709.

Kolomenskiy, D. & Schneider, K. (2010). Numerical simulations of falling leaves using a pseudo-spectral method with volume penalization. *Theor. Comput. Fluid Dyn.*, 24, 169–173. 10.1007/s00162-009-0171-0.

Kovasznay, L. (1953). Turbulence in supersonic flow. *J. Aero. Sci.*, 20(10), 657–682.

Kramer, J., Jecl, R., & Skerget, L. (2008). Heat and mass transfer porous medium saturated with compressible fluid with boundary domain integral method. *Defect Diffusion Forum*, 273-276, 808–813.

Krothapalli, A., Hsia, Y., Baganoff, D., & Karamcheti, K. (1986). The role of screech tones in mixing of an underexpanded rectangular jet. *J. Sound Vib.*, 106(1), 119–143.

Krothapalli, A., Soderman, P. T., Allen, C. S., Hayes, J. A., & Jaeger, S. M. (1997). Flight effects on the far-field noise of a heated supersonic jet. *AIAA J.*, 35(6), 952–957.

Krothapalli, A., Venkatakrishnan, L., Lourenco, L., Greska, B., & Elavarasan, R. (2003). Turbulence and noise suppression of a high-speed jet by water injection. *J. Fluid Mech.*, 491, 131–159.

Kurbatskii, K. (2011). Numerical simulation of three-dimensional jet screech tones using a general purpose finite-volume cfd code. In *49th AIAA Aerospace Sciences Meeting including the New Horizons Forum and Aerospace*, number 2011-1085 (pp. 1–9).: AIAA.

Kurbatskii, K. A. & Tam, C. K. W. (1997). Cartesian boundary treatment of curved walls for high-order computational aeroacoustics schemes. *AIAA J.*, 35(1), 133–140.

Kweon, Y., Tsuchida, M., Miyazato, Y., Aoki, T., Kim, H., & Setoguchi, T. (2005). The effect of reflector with sound-absorbing material on supersonic jet noise. *J. Therm. Sci.*, 14, 22–27. 10.1007/s11630-005-0035-x.

Kweon, Y.-H., Miyazato, Y., Aoki, T., Kim, H.-D., & Setoguchi, T. (2006). Experimental investigation of nozzle exit reflector effect on supersonic jet. *Shock Waves*, 15, 229–239. 10.1007/s00193-006-0021-6.

Lai, H. & Luo, K. (2008). A conceptual study of cavity aeroacoustics control using porous media inserts. *Flow, Turb. Combust.*, 80, 375–391. 10.1007/s10494-007-9129-8.

Le Moigne, A. (2002). *A discrete Navier-Stokes adjoint method for aerodynamic optimisation of BlendedWing-Body configurations.* PhD thesis, Cranfield University.

Lee, I. C., Kim, W., & Lee, D.-J. (2004). An analysis of screech tone noise and its mode change of an axisymmetric supersonic jet using an optimized compact scheme. In *10th AIAA/CEAS Aeroacoustics Conference*, number 2004-2952: AIAA.

Lele, S. K. (1992). Compact finite difference schemes with spectral-like resolution. *J. Comput. Phys.*, 103(1), 16–42.

Lepicovsky, J. & Ahuja, K. K. (1985). Experimental results on edge-tone oscillations in high-speed subsonic jets. *AIAA J.*, 23(10), 1463–1468.

Li, X. & Gao, J. (2004). Numerical simulation of axisymmetric supersonic screech tones. In *10th AIAA/CEAS Aeroacoustics Conference*, number 2004-2951: AIAA.

Li, X. & Gao, J. (2007). Prediction and understanding of three-dimensional screech phenomenon from a circular nozzle. In *13th AIAA/CEAS Aeroacoustics Conference (28th AIAA Aeroacoustics Conference)*, number 2007-3637: AIAA.

Li, X. D. & Gao, J. H. (2005). Numerical simulation of the generation mechanism of axisymmetric supersonic jet screech tones. *Phys. Fluids*, 17(8), 085105.

Lighthill, M. J. (1952). On sound generated aerodynamically. I. General theory. *Proc. R. Soc. London, Ser. A, Math. Phys. Sci.*, 211(1107), 564–587.

Lighthill, M. J. (1954). On sound generated aerodynamically. II. Turbulence as a source of sound. *Proc. R. Soc. London, Ser. A, Math. Phys. Sci.*, 222(1148), 1–32.

Lighthill, M. J. (1963). Jet noise. *AIAA J.*, 1(7), 1507–1517.

Lin, C.-J. (2007). *Projected gradient methods for non-negative matrix factorization.* Technical report, Neural Comp.

Liu, Q. & Vasilyev, O. V. (2007). A brinkman penalization method for compressible flows in complex geometries. *J. Comput. Phys.*, 227, 946–966.

Loh, C., Himansu, A., & Hultgren, L. S. (2003). A 3-d ce/se navier-stokes solver with unstructured hexahedral grid for computation of nearfield jet screech noise. In *9th AIAA/CEAS Aeroacoustics Conference and Exhibit*, number 2003-3207: AIAA.

Loh, C. & Hultgren, L. (2006). Jet screech noise computation. *AIAA J.*, 44(5), 992–998.

Love, E. S., Grigsby, C. E., Lee, L. P., & Woodling, M. J. (1959). *Experimental and Theoretical Studies of Axisymmetric Free Jets.* Technical Report NASA-TR-R-6, NASA Langley Research Center.

L'vov, V. S., Pomyalov, A., Procaccia, I., & Govindarajan, R. (2008). Random vortex-street model for a self-similar plane turbulent jet. *Phys. Rev. Lett.*, 101(9), 094503–1–4.

Maestrello, L. (1979). An experimental study on porous plug jet noise suppressor. In *5th Aeroacoustics Conference*, number AIAA 1979-0673 (pp. 1–10).: AIAA.

Manning, T. (1999). *A numerical investigation of sound generation in supersonic jet screech*. PhD thesis, Department of aeronautics and astronautics, Stanford University.

Manning, T. A. & Lele, S. K. (1998). Numerical simulations of shock-vortex interactions in supersonic jet screech. In *36th Aerospace Sciences Meeting and Exhibit*, number 1998-282: AIAA.

Manning, T. A. & Lele, S. K. (2000). A numerical investigation of sound generation in supersonic jet screech. In *6th AIAA/CEAS, Aeroacoustics Conference and Exhibit*, number 2000-2081: AIAA.

Marsden, A. L., Wang, M., & Mohammadi, B. (2001). Shape optimization for aerodynamic noise control. In *Annual Research Briefs*. Center for Turbulence Research.

Massey, K. C. (1997). *Flow/acoustic coupling in heated and unheated free and ducted jets*. PhD thesis, Georgia Institute of Technology.

Mathew, J., Foysi, H., & Friedrich, R. (2006). A new approach to les based on explicit filtering. *Int. J. Heat Fluid Flow*, 27(4), 594–602.

Mathew, J., Lechner, R., Foysi, H., Sesterhenn, J., & Friedrich, R. (2003). An explicit filtering method for large eddy simulation of compressible flows. *Phys. Fluids*, 15(8), 2279–2289.

Mclaughlin, D. K., Morrison, G. L., & Troutt, T. R. (1975). Experiments on the instability waves in a supersonic jet and their acoustic radiation. *J. Fluid Mech.*, 69(01), 73–95.

Meliga, P., Sipp, D., & Chomaz, J.-M. (2010). Open-loop control of compressible afterbody flows using adjoint methods. *Phys. Fluids*, 22(5), 054109.

Men'shov, I. & Nenashev, A. (2011). Spiral-mode instability and the screech-tone effect in supersonic jet flows. *Doklady Physics*, 56, 288–293. 10.1134/S1028335811050077.

Men'shov, I., Semenov, I., & Akhmedyanov, I. (2008). Mechanism of discrete tone generation in supersonic jet flows. *Doklady Physics*, 53, 278–282. 10.1134/S1028335808050108.

Merle, M. (1956). Sur les fréquencies des sondes émises par un jet d'air á grande vitesse. *Acad. Sci., Paris, C. R.*, 243, 490–493.

Mitchell, B. E., Lele, S. K., & Moin, P. (1995). Direct computation of the sound from a compressible co-rotating vortex pair. *J. Fluid Mech.*, 285, 181–202.

Mohammadi, B. (2004). Optimization of aerodynamic and acoustic performances of supersonic civil transports. *Int. J. Num. Methods Heat Fluid Flow*, 14(7), 893–909.

Moin, P., Squires, K., Cabot, W., & Lee, S. (1991). A dynamic subgrid scale model for compressible turbulence and scalar transport. *Phys. Fluids A*, 3(11), 2746–2757.

Moler, C. & Loan, C. V. (2003). Nineteen dubious ways to compute the exponential of a matrix, twenty-five years later. *SIAM Rev.*, 45(1), 3–49.

Morduchow, M. & Libby, P. (1949). On a complete solution of the one-dimensional flow equations of a viscous, heat conducting, compressible gas. *J. Aeronaut. Sci.*, (pp. 674–684).

Morris, P., Bhat, T., & Chen, G. (1989). A linear shock cell model for jets of arbitrary exit geometry. *J. Sound Vib.*, 132(2), 199–211.

Müller, B. (1990). Linear stability condition for explicit runge-kutta methods to solve the compressible navier-stokes equations. *Math. Methods Appl. Sci.*, 12(2), 139–151.

Munday, D., Heeb, N., Gutmark, E., Liu, J., & Kailasanath, K. (2011). Supersonic jet noise reduction technologies for gas turbine engines. *J. Eng. Gas Turbines Power*, 133(10), 101201/1–10.

Nadarajah, S. K., Jameson, A., & Alonso, J. J. (2001). An adjoint method for the calculation of non-collocated sensitivities in supersonic flow. In *1st MIT Conference on Computational Fluid and Solid Mechanics* (pp. 11–14).

Nadarajah, S. K., Kim, S., Jameson, A., & Alonso, J. J. (2003). Sonic boom reduction using an adjoint method for supersonic transport aircraft configurations. In H. Sobieczky (Ed.), *IUTAM Symposium Transsonicum IV*,

volume 73 of *Fluid Mechanics and Its Applications* (pp. 355–362). Springer Netherlands. 10.1007/978-94-010-0017-8_53.

Nagamatsu, H. T. & Horvay, G. (1969). *Supersonic Jet Noise*. Technical Report 69-C-161, GE Research and Development Center.

Nagamatsu, H. T., Sheer, R. E., J., & Horvay, G. (1969). Supersonic jet noise theory and experiments. In I. R. Schwartz (Ed.), *Basic Aerodynamic Noise Research*, number NASA SP-207 (pp. 17–51).: NASA.

Nagel, R. T., Denham, J. W., & Papathanasiou, A. G. (1983). Supersonic jet screech tone cancellation. *AIAA J.*, 21(5), 1541–1545.

Nemec, M. & Zingg, D. W. (2001). Towards efficient aerodynamic shape optimization based on the navier-stokes equations. In *15th AIAA Computational Fluid Dynamics Conference*, number 2001-2532: AIAA.

Newman, C. K. (2003). *Exponential Integrators for the Incompressible Navier-Stokes Equations*. PhD thesis, Virginia Polytechnic Institute and State University.

Norum, T. D. (1983). Screech suppression in supersonic jets. *AIAA J.*, 21(2), 235–240.

Norum, T. D. (1984). Control of jet shock associated noise by a reflector. In *9th Aeroacoustics Conference*, number AIAA-1984-2279 (pp. 1–9).

Norum, T. D. (1991). Supersonic rectangular jet impingement noise experiments. *AIAA J.*, 29(7), 1051–1057.

Norum, T. D. & Seiner, J. (1982a). *Measurements of mean static pressure and far field acoustics of shock containing supersonic jets*. Technical Report NASA-TM-84521, NASA Langley Research Center.

Norum, T. D. & Seiner, J. M. (1982b). Broadband shock noise from supersonic jets. *AIAA J.*, 20(1), 68–73.

Olesen, L. H., Okkels, F., & Bruus, H. (2004). Topology optimization of navier-stokes flow in microfluidics. In *ECCOMAS 2004*.

Othmer, C. (2008). A continuous adjoint formulation for the computation of topological and surface sensitivities of ducted flows. *Int. J. Numer. Methods Fluids*, 58(8), 861–877.

Pack, D. C. (1950). A note on prandtl's formula for the wavelength of a supersonic gas jet. *Q. J. Mech. Appl. Math*, 3, 173–181.

Panda, J. (1998). Shock oscillation in underexpanded screeching jets. *J. Fluid Mech.*, 363, 173–198.

Panda, J. (1999). An experimental investigation of sreech noise generation. *J. Fluid Mech.*, 378, 71–96.

Panda, J., Raman, G., & Zaman, K. B. M. Q. (1997). Underexpanded screeching jets from circular, rectangular, and elliptic nozzles. In *Third Aeroacoustics Conference cosponsored by the American Institute of Aeronautics and Astronautics and the Confederation of European Aerospace Societies*.

Papoutsis-Kiachagias, E., Kontoleontos, E., Zymaris, A., Papadimitriou, D., & Giannakoglou, K. (2011). Constrained topology optimization for laminar and turbulent flows, including heat transfer. In C. Poloni, D. Quagliarella, J. Periaux, N. Gauger, & K. Giannakoglou (Eds.), *Evolutionary and Deterministic Methods for Design, Optimization and Control*.

Phillips, O. M. (1960). On the generation of sound by supersonic turbulent shear layers. *J. Fluid Mech.*, 9(1), 1–28.

Pironneau, O. (1974). On optimum design in fluid mechanics. *J. Fluid Mech.*, 64(1), 97–110.

Polak, E. (1997). *Optimization: Algorithms and Consistent Approximations*. New York: Springer.

Ponton, M. K. & Seiner, J. M. (1992). The effects of nozzle exit lip thickness on plume resonance. *J. Sound Vib.*, 154(3), 531–549.

Pope, S. B. (2000). *Turbulent Flows*. Cambridge University Press.

Powell, A. (1953a). On the mechanism of choked jet noise. *Proc. Phys. Soc. B*, 66(12), 1039–1056.

Powell, A. (1953b). On the noise emanating from a two-dimensional jet above the critical pressure. *Aeronautical Quaterly*, 4, 103–122AGARD Conference Proceedings.

Powell, A., Umeda, Y., & Ishii, R. (1992). Observations of the oscillation modes of choked circular jets. *J. Acoust. Soc. Am.*, 92(5), 2823–2836.

Prandtl, L. (1904). Stationary waves in a gaseous jet. *Phys. Z.*, 5, 599–601.

Raman, G. (1996). Cessation of screech in underexpanded jets. In *2nd AIAA and CEAS Aeroacoustics Conference*, number 1996-1719: AIAA.

Raman, G. (1997a). Cessation of screech in underexpanded jets. *J. Fluid Mech.*, 336, 69–90.

Raman, G. (1997b). Screech tones from rectangular jets with spanwise oblique shock-cell structures. *J. Fluid Mech.*, 330, 141–168.

Raman, G. (1998). Advances in understanding supersonic jet screech: Review and perspective. *Pro. Aerosp. Sci.*, 34(1-2), 45–106.

Raman, G. (1999a). Shock-induced flow resonance in supersonic jets of complex geometry. *Phys. Fluids*, 11(3), 692–709.

Raman, G. (1999b). Supersonic jet screech: Half-century from powell to the present. *J. Sound Vib.*, 225(3), 543–571.

Raman, G. & Rice, E. J. (1994). Instability modes excited by natural screech tones in a supersonic rectangular jet. *Phys. Fluids*, 6(12), 3999–4008.

Raman, G., Zaman, K. B. M. Q., & Rice, E. J. (1989). Initial turbulence effect on jet evolution with and without tonal excitation. *Phys. Fluids A: Fluid Dyn.*, 1(7), 1240–1248.

Ramaprian, B. R. & Chandrasekhara, M. S. (1985). Lda measurements in plane turbulent jets. *J. Fluids Eng.*, 107(2), 264–271.

Ray, P. K. & Lele, S. K. (2007). Sound generated by instability wave/shock-cell interaction in supersonic jets. *J. Fluid Mech.*, 587, 173–215.

Reuther, J., AIonso, J. J., Rimlinger, M. J., & Jameson, A. (1996). *Aerodynamic Shape Optimization of Supersonic Aircraft Configurations via an Adjoint Formulation on Parallel Computers.* Technical report, NASA Ames Research Center (RIACS).

Rosfjord, T. J. & Toms, H. L. (1975). Recent observations including temperature dependence of axisymmetric jet screech. *AIAA J.*, 13(10), 1384–1386.

Rumpfkeil, M. P. & Zingg, D. W. (2009). Far-field noise minimization using an adjoint approach. In H. Choi, H. G. Choi, & J. Y. Yoo (Eds.), *Computational Fluid Dynamics 2008* (pp. 69–75). Springer Berlin Heidelberg. 10.1007/978-3-642-01273-0_6.

Saad, Y. (1992). Analysis of some krylov subspace approximations to the matrix exponential operator. *SIAM J. Numer. Anal.*, 29, 209–228.

Saad, Y. & Semeraro, D. (1991). Application of krylov exponential propagation to fluid dynamics equations. *RIACS Tech. Report 91.06*.

Salas, M. D. & Iollo, A. (1996). Entropy jump across an inviscid shock wave. *Theor. Comput. Fluid Dyn.*, 8, 365–375. 10.1007/BF00456376.

Sandham, N. & Luedeke, H. (2009). A numerical study of mach 6 boundary layer stabilization by means of a porous surface. *AIAA-2009-1288*.

Schaupp, C., Sesterhenn, J., & Friedrich, R. (2008). On a method for direct numerical simulation of shear layer/compression wave interaction for aeroacoustic investigations. *Comput. Fluids*, 37(4), 463–474. Turbulent Flow and Noise Generation.

Schittkowski, K. (2010). *NLPQLP: A Fortran Implementation of a Sequential Quadratic Programming Algorithm with Distributed and Non-Monotone Line Search - User's Guide, Version 3.1.* Technical report, Department of Computer Science University of Bayreuth.

Schneider, K. & Farge, M. (2005). Numerical simulation of the transient flow behaviour in tube bundles using a volume penalization method. *J. Fluids Struct.*, 20(4), 555–566. Bluff-Body/Flow Interactions.

Schulze, J. (2011). Experimental investigation of under-expanded axisymmetric jets. Unpublished.

Schulze, J., Schaupp, C., Sesterhenn, J., Friedrich, R., Berland, J., Bogey, C., & Juvé, D. (2007). Shock-induced noise in 2d sub- and supersonic mixing layers. *ESAIM: Proc.*, 16, 51–65.

Schulze, J., Schmid, P., & Sesterhenn, J. (2011). Iterative optimization based on an objective functional in frequency-space with application to jet-noise cancellation. *J. Comput. Phys.*, 230(15), 6075–6098.

Schulze, J. & Sesterhenn, J. (2010a). Numerical simulation of supersonic jet noise with overset grid techniques. In M. Deville, T.-H. Le, & P. Sagaut (Eds.), *Turbulence and Interactions*, volume 110 of *Notes on Numerical Fluid Mechanics and Multidisciplinary Design* (pp. 327–336). Springer Berlin / Heidelberg. 10.1007/978-3-642-14139-3_40.

Schulze, J. & Sesterhenn, J. (2010b). Numerical simulation of supersonic jet noise with overset grid techniques for highly parallelized computing. In *High Performance Computing in Science and Engineering, Garching/Munich 2009* (pp. 99–108). Springer Berlin Heidelberg. 10.1007/978-3-642-13872-0_9.

Schulze, J., Sesterhenn, J., Schmid, P., Bogey, C., de Cacqueray, N., Berland, J., & Bailly, C. (2009a). Numerical simulation of supersonic jet noise. In C. Brun, D. Juvé, M. Manhart, & C.-D. Munz (Eds.), *Numerical Simulation of Turbulent Flows and Noise Generation*, volume 104 of *Notes on Numerical Fluid Mechanics and Multidisciplinary Design* (pp. 29–46). Springer Berlin/Heidelberg. 10.1007/978-3-540-89956-3_2.

Schulze, J. C., Schmid, P. J., & Sesterhenn, J. L. (2009b). Exponential time integration using krylov subspaces. *Int. J. Numer. Methods Fluids*, 60(6), 591–609.

Schulze, J. C. & Sesterhenn, J. L. (2011). Optimal distribution of porous media to reduce trailing edge noise. *Computers & Fluids*. In Press.

Seiner, J. (1994). Impact of dynamic loads on propulsion integration. In *AGARD, Impact of Acoustic Loads on Aircraft Structures*, number CP-549.

Seiner, J., Manning, J., & Ponton, M. (1987). Model and full scale study of twin supersonic plume resonance. *AIAA Paper*, 244, 1–10.

Seiner, J. & Norum, T. D. (1980). Aerodynamic aspects of shock containing jet plumes. In *6th Aeroacoustics Conference*, number 1980-965: AIAA.

Seiner, J. M. (1984). Advances in High Speed Jet Aeroacoustics. *AIAA Paper*, 84-2275, 1–40.

Seiner, J. M., Manning, J., & Ponton, M. (1986a). Acoustic properties associated with rectangular geometry supersonic nozzles. In *10th Aeroacoustics Conference*, number 1986-1867: AIAA.

Seiner, J. M., Manning, J. C., & Ponton, M. (1986b). The preferred spatial mode of instability for a mach 2 jet. In *10th Aeroacoustics Conference*, number AIAA-1986-1942 (pp. 1–13).

Seiner, J. M. & Norum, T. D. (1979). Experiments of shock associated noise of supersonic jets. In *12th Fluid and Plasma Dynamics Conference*, number AIAA-1979-1526 (pp. 1–16).

Seiner, J. M., Norum, T. D., & Maestrello, L. (1980). Effects of nozzle design on the noise from supersonic jets. In *Supersonic Cruise Res. 1979, Pt. 1* (pp. 479–491). NASA Langley Research Center.

Sesterhenn, J. (2000). A Characteristic-Type Formulation of the Navier-Stokes Equations for High Order Upwind Schemes. *Comput. Fluids*, 30(1), 37–67.

Sesterhenn, J., Dohogne, J.-F., & Friedrich, R. (2005). Direct numerical simulation of the interaction of isotropic turbulence with a shock wave using shock-fitting. *Comptes Rendus Mécanique*, 333(1), 87–94.

Shen, H. & Tam, C. K. W. (1998). Numerical simulation of the generation of axisymmetric mode jet screech tones. *AIAA J.*, 36(10), 1801–1807.

Shen, H. & Tam, C. K. W. (2000). Effects of jet temperature and nozzle-lip thickness on screech tones. *AIAA J.*, 38(5), 762–767.

Shen, H. & Tam, C. K. W. (2001). Three-dimensional numerical simulation of the jet screech phenomenon. In *39th Aerospace Sciences Meeting and Exhibit*, number 2001-820: AIAA.

Shen, H. & Tam, C. K. W. (2002). Three-dimensional numerical simulation of the jet screech phenomenon. *AIAA J.*, 40(1), 33–41.

Shur, M., Spalart, P., & Strelets, M. (2010). Les-based noise prediction for shocked jets in static and flight conditions. In *16th AIAA/CEAS Aeroacoustics Conference*, number 2010-3840: AIAA.

Sidje, R. B. (1998). Expokit: a software package for computing matrix exponentials. *ACM Trans. Math. Softw.*, 24, 130–156.

Singh, A. & Chatterjee, A. (2007). Numerical prediction of supersonic jet screech frequency. *Shock Waves*, 17, 263–272. 10.1007/s00193-007-0110-1.

Spagnoli, B. & Airiau, C. (2008). Adjoint analysis for noise control in a two-dimensional compressible mixing layer. *Comput. Fluids*, 37(4), 475–486.

Spalart, P. R. (2000). Strategies for turbulence modelling and simulations. *Int. J. Heat Fluid Flow*, 21(3), 252–263.

Stromberg, J., McLaughlin, D., & Troutt, T. (1980). Flow field and acoustic properties of a mach number 0.9 jet at a low reynolds number. *J. Sound Vib.*, 72(2), 159–176.

Suzuki, T. & Lele, S. K. (2003). Shock leakage through an unsteady vortex-laden mixing layer: application to jet screech. *J. Fluid Mech.*, 490, 139–167.

Tam, C. (1987). Stochastic model theory of broadband shock associated noise from supersonic jets. *J. Sound Vib.*, 116(2), 265–302.

Tam, C. (1988). The shock-cell structures and screech tone frequencies of rectangular and non-axisymmetric supersonic jets. *J. Sound Vib.*, 121(1), 135–147.

Tam, C. (1995). Supersonic jet noise. *Annu. Rev. Fluid Mech.*, 27, 17–43.

Tam, C., Seiner, J., & Yu, J. (1986). Proposed relationship between broadband shock associated noise and screech tones. *J. Sound Vib.*, 110(2), 309–321.

Tam, C. & Tanna, H. (1982). Shock associated noise of supersonic jets from convergent-divergent nozzles. *J. Sound Vib.*, 81(3), 337–358.

Tam, C. K. W., Ahuja, K. K., & Jones, R. R. (1994). Screech tones from free and ducted supersonic jets. *AIAA J.*, 32(5), 917–922.

Tam, C. K. W., Chen, P., & Seiner, J. M. (1992). Relationship between the instability waves and noise of high-speed jets. *AIAA J.*, 30(7), 1747–1752.

Tam, C. K. W., Jackson, J. A., & Seiner, J. M. (1985). A multiple-scales model of the shock-cell structure of imperfectly expanded supersonic jets. *J. Fluid Mech.*, 153, 123–149.

Tam, C. K. W. & Webb, J. C. (1993). Dispersion-relation-preserving finite difference schemes for computational acoustics. *J. Comput. Phys.*, 107(2), 262–281.

Taylor, G. I. (1910). The conditions necessary for discontinuous motion in gases. *Proc. R. Soc. London, Ser. A*, 84(571), 371–377.

Tokman, M. (2006). Efficient integration of large stiff systems of odes with exponential propagation iterative (epi) methods. *J. Comput. Phys.*, 213, 748–776.

Trefethen, L. N. (2005). *Spectra and Pseudospectra: The Behavior of Nonnormal Matrices and Operators*. Princeton University Press.

Viswanathan, K. (2004). Aeroacoustics of hot jets. *J. Fluid Mech.*, 516, 39–82.

Wang, M., Freund, J. B., & Lele, S. K. (2006). Computational prediction of flow-generated sound. *Annu. Rev. Fluid Mech.*, 38, 483–512.

Wang, Q., Moin, P., & Iaccarino, G. (2009). Minimal repetition dynamic checkpointing algorithm for unsteady adjoint calculation. *SIAM J. Sci. Comput.*, 31(4), 2549–2567.

Wei, M. (2004). *Jet noise control by adjoint-based optimization*. PhD thesis, University of Illinois at Urbana-Champaign.

Wei, M. & Freund, J. B. (2002). Optimal control of free shear flow noise. In *40th AIAA Aerospace Sciences Meeting and Exhibit*, number 2002-0665 (pp. 1–7).: AIAA.

Wei, M. & Freund, J. B. (2006). A Noise–Controlled Free Shear Flow. *J. Fluid Mech.*, 546(-1), 123–152.

Westley, R. & Woolley, J. H. (1975). The near field sound pressures of a choked jet when oscillating in the spinning mode. In *2nd Aeroacoustic Conference*, number AIAA-1975-479 (pp. 1–9).

Williamson, J. H. (1980). Low-storage runge-kutta schemes. *J. Comput. Phys.*, 35(1), 48–56.

Wolfe, P. (1969). Convergence conditions for ascent methods. *SIAM Rev.*, 11(2), 226–235.

Wooding, R. A. (1957). Steady state free thermal convection of liquid in a saturated permeable medium. *J. Fluid Mech.*, 2(3), 273–285.

Xiong, J., Liu, F., & Papamoschou, D. (2010). Aerodynamic shape optimization of fan-flow deflectors for noise reduction using adjoint method. In *28th AIAA Applied Aerodynamics Conference*, number 2010-4675: AIAA.

Yu, J. C. & Seiner, J. M. (1983). Nearfield observations of tones generated from supersonic jet flows. In *AIAA Aeroacoustics Conference, 8th, Atlanta, GA*, number 1983-706: AIAA.

Yu, Y.-K., Chen, R.-H., & Chew, L. (1998). Screech tone noise and mode switching in supersonic swirling jets. *AIAA J.*, 36(11), 1968–1974.

Zaman, K. B. M. Q. (1999). Spreading characteristics of compressible jets from nozzles of various geometries. *J. Fluid Mech.*, 383, 197–228.